UNIVERSITY OF SOUTHAMPTON

CLIMATE CONTROL ON ALLOCHTHONOUS SEDIMENTATION IN THE DEEP SEA

Babette Agnes Antje Hoogakker

Submitted for the qualification of Doctor of Philosophy

Faculty of Science
Graduate School of the Southampton Oceanography Centre
School of Ocean and Earth Sciences

September 2003

Graduate School of the
Southampton Oceanography Centre

This PhD dissertation by

Babette Agnes Antje Hoogakker

has been produced under the supervision of the following persons

Supervisors

Dr. R.G. Rothwell

Prof. E.J. Rohling

Dr. A.P. Roberts

Prof. D.A.V. Stow

Chair of Advisory Panel

Prof. A.E.S. Kemp

I hereby declare that no part of this thesis has been submitted for a degree to the University of Southampton, or any other University at any time previously. Also that the material included is the work of the author, except where expressly stated. The co-authors' main contribution to the two papers included in the thesis was reading and editing of the material covered. Martin Palmer calculated pCO_2 for the paper submitted to Earth and Planetary Science Letters (Chapter 3). Martine Paterne contributed greyscale intensity data for the paper submitted to Marine Geology (Chapter 5).

Babette Agnes Antje Hoogakker

This thesis is dedicated to my mother and good friend
who sadly passed away.

UNIVERSITY OF SOUTHAMPTON

ABSTRACT

FACULTY OF SCIENCE

SCHOOL OF OCEAN AND EARTH SCIENCES

Doctor of Philosophy

CLIMATE CONTROL ON ALLOCHTHONOUS SEDIMENTATION IN THE DEEP SEA

by Babette Agnes Antje Hoogakker

Four giant piston cores from the Balearic Abyssal Plain have been studied in detail in order to broadly quantify the differences in advective sediment flux to the Balearic Abyssal Plain (the western Mediterranean Sea) over the last glacial/interglacial cycle. The cored Balearic Abyssal Plain sedimentary sequence (30-35 m) is dominated by turbidite deposits (90%). Intercalated hemipelagic intervals, which only make up 10% of the recovered sedimentary sequence, were used to form a tight stratigraphic framework that has been fine-tuned to the GISP2 ice core record from Greenland. This stratigraphic framework provided important constraints on individual turbidite emplacement times. Turbidite deposition on the Balearic Abyssal Plain occurred regularly and without major temporal gaps, with an average frequency of one turbidite every one to two thousand years. The highest number of turbidites occurred during periods of maximum sea-level (and climate) change. Turbidite beds from the last glacial period (Marine Isotope Stages 2-4) are much thicker than turbidite beds emplaced during interglacial periods (Marine Isotope Stages 1 and 5), which suggests that the glacial advective sediment flux to the Balearic Abyssal Plain was significantly enhanced. Sediment supply to the margins and the Balearic Abyssal Plain is estimated to have been at least doubled during the last glacial maximum, due to increased riverine sediment fluxes. Turbidite frequencies (number/ka) were also enhanced during Marine Isotope Stage 1, which is explained by anthropogenic deforestation and the subsequent increase in erosion during this period. The results presented indicate that the temporally well-constrained data do not support the hypothesis that the advective sediment flux to the basin is only high during glacials - this view is too simple and does not stand up to detailed testing.

In addition to this study a western Mediterranean oxygen isotope reference stratigraphy was developed, from a core devoid of turbidite deposits. Fourteen alternating glacial and interglacial stages were recognised that correlate well with the SPECMAP curve and is supported by geomagnetic reversal data. Stable carbon isotope records of this core (LC07) show two conspicuous long-term fluctuations from 1.00 to 0.50 and from 0.50 to 0.10 Ma, which are also observed in all major ocean basins in both surface-dwelling and deep-sea foraminifera. Both carbon isotope fluctuations are considered to result from concomitant changes in the burial fluxes of organic and inorganic carbon due to changes in bottom water ventilation.

CONTENTS

ACKNOWLEDGEMENTS

I would like to thank my supervisors Guy Rothwell, Eelco Rohling, Andy Roberts and Dorrik Stow at SOC for all the help and advice provided during the course of my PhD. Alan Kemp is acknowledged for chairing the PhD panel.

John Thomson, Trevor Clayton and Martin Palmer are thanked for stimulating discussions and advice. Mike Bolshaw, Steve Cooke, Matt Cooper and Mike Rogerson assisted with stable isotope analysis, whilst Tracey Cummins helped with sample preparation before oxygen and carbon isotope analysis. Darryl Green provided assistance with coulometric analysis. Access to the studied cores was provided by the British Ocean Sediment Core Repository (BOSCOR) located at SOC. Doug Masson is thanked for financial support and help. Furthermore I would like to thank my office-mates Stephany Arnot and Mike Rogerson for pleasant conversations and letting me use 2.5 tables out of 5 in the office.

I am very greatful for all the support and encouragement from all my friends and family. Special thanks go to Susanne Ufermann, Laura Font, Ulrike Riemenschneider, Michael Winklhofer, Ana Hilario, Sinhue Torres, Dave Lambkin, Hans Fanghor, Steffen Dransfeld, Sue Taylor, Tom Speedy, Veronique Mendel, Silvia Lucato, Marissa Motta, Luciano Pezzi, Rachel Cave, James Casford, Mark Hartl, Jane Goswell, Peter Martin, Ana Paula Spinelli, Juan Larrasoaña, Maeve Lohan, Rachel Dunk and Heike Heusel. Alex Poulton helped me through one of the most difficult periods of my life and supported me through thick and thin.

Furthermore I would like to thank everybody-else I might have forgotten, people I met at conferences, etc.

CHAPTER 1 – INTRODUCTION

1.1 THESIS OUTLINE

This chapter provides a general introduction to the study, covering background, previous research and objectives together with a short summary of the methods used. An overview of the geographic setting, geology, morphology, tectonism, physical oceanography and climatology of the western Mediterranean region and discussion of sedimentary processes that operate in the area, as reported in the literature, are presented in Chapter 2.

Turbidite beds from the Balearic Abyssal Plain sequence are intercalated with thinner hemipelagic intervals within the piston cores. These hemipelagic intervals are used to constrain a stratigraphy in Chapter 5. Part of the stratigraphic framework developed for this study is based on oxygen isotope stratigraphy (Chapter 5). For comparison a reference core was analysed for oxygen isotopes from a location where disturbance related to downslope transport is unlikely. The results of the analysis of the oxygen isotopes in this reference core are presented and discussed in Chapter 3. This record has been published in Dinarès-Turell et al. (2003). Carbon isotope records from this reference core show two conspicuous long-term fluctuations that can also be observed in many other published records from all major ocean basins. These carbon isotope fluctuations are discussed in more detail in Chapter 3 and it is proposed that the initiation of these fluctuations to lower $\delta^{13}C$ values was caused by better ventilated bottom waters, resulting in decreases in global mean organic and inorganic carbon burial fluxes.

In Chapter 4, the sedimentology of the Balearic Abyssal Plain long piston cores collected during Marion Dufresne Cruise 81 is discussed. Individual turbidites and hemipelagic intervals are identified on textural and sedimentological criteria and individual turbidite beds are characterised in terms of their sedimentology, colour, magnetic susceptibility, calcium carbonate and organic carbon contents, clay mineralogy and basal sand mineralogy.

A detailed description of turbidite deposition on the Balearic Abyssal Plain during the last 130,000 years is presented in Chapter 6. The stratigraphic records that are presented in Chapter 5 provided excellent age controls for delineating emplacement times of individual turbidite beds. Discussion of both the timing of turbidite

emplacement and turbidite thickness forms the main focus of this chapter. Furthermore, turbidite sedimentation in terms of turbidite frequency (average number of turbidites per unit time) and in terms of turbidite flux (average thickness of turbidites per unit time) is assessed.

Summaries and the conclusions of the main findings of this study, and some suggestions for future research are presented in Chapter 7.

1.2 BACKGROUND

Abyssal plains form a major deep-sea sedimentary province and can provide important records of major events in the erosional history of drainage basins. Turbidite deposits commonly dominate basin-plain sediment columns and hemipelagic intervals may make up less than 20% of the sediment sequence. Debris flow deposits are of minor importance, since most debris flows do not travel long distances over flat terrain and are mainly restricted to the continental rise and slope (Pilkey, 1987).

It is traditionally thought that deep-sea turbidite deposition is particularly dynamic during periods of low sea level (Embley, 1980; Shanmugam and Moiola, 1982; Cita et al., 1984; Caddah et al., 1998; Rothwell et al., 1998, 2000). Sea level position relative to shelf edge is a major factor in the delivery of continentally derived sediments to the deep sea (Pitman, 1978; Watts, 1982). At times when sea level falls to or below the shelf edge, many continental shelves are exposed as subaerial, coastal plains allowing rivers to dump their sediment loads closer to the shelf edge in potentially more unstable conditions. At times of high sea level, decreased stream relief and broad shelves cause river sediment loads to largely remain trapped on the continental shelf.

Global changes in sea level can be both tectonically and climatically driven (Shanmugam and Moiola, 1982). Tectonically driven changes in sea level can be caused by high sea floor spreading rates, which result in an increase in oceanic ridge volumes resulting in transgressions. Reductions in sea floor spreading rates will decrease oceanic ridge volume, thereby resulting in regressions (Russell, 1968; Valentine and Moores, 1970; Hays and Pitman, 1973; Pitman, 1979). However, computed rates for eustatic changes of sea level caused by tectonism are considerably smaller then rates caused by glaciation (Shanmugam and Moiola, 1982). Furthermore,

glaciation is probably the only mechanism that is capable of causing rapid fluctuations in sea level (Vail and Hardenbol, 1979).

Turbidites are volumetrically the most significant clastic accumulations in the deep sea (Normark et al., 1993) and make up some of the world's largest sedimentary bodies. During periods of low sea level, the frequency of turbidity currents is greatly increased (Shanmugam and Moiola, 1982). Several authors have discussed a relationship between turbidite emplacement and sea level (e.g. Weaver and Kuijpers, 1983; Cita et al., 1984; Prince et al., 1987; Caddah et al., 1998; Rothwell et al., 1998). According to Stanley (1985), emplacement of large megaturbidites during the Late Pleistocene (<1 Ma) is generally related to sea level low stands, whilst emplacement of older megabeds (>1 Ma) is mainly related to seismic events. However, little previous work has been done to quantify the differences in advective sediment flux over a glacial/interglacial cycle to show the magnitude of change of allochthonous sediment transport to the deep sea during these climatic episodes. More accurate knowledge of climate modulation of advective sediment redeposition in the deep sea basins bounding continental margins is essential if we are to better understand the sedimentary dynamics of deep sea shelves in the long term, and determine times when sediment failure on the continental shelf/slope is more likely.

Large-scale slope failures can cause damage, or failure, of seabed structures, such as cables, platforms and pipelines and they can cause tsunamis that may devastate coastal regions. In regions where the sub-ocean floor contains gas hydrates, large scale mass wasting may contribute to global warming through methane release, thereby producing important climatic impact (Paull et al., 1991; Nisbet, 1992). Allochthonous deposits are also of economic interest in that thick redeposited sands can form important hydrocarbon reservoirs, as in the North Sea. Turbidite systems form a significant component of the stratigraphic record, and, according to Weimer and Link (1991), include many of the world's most important hydrocarbon reservoirs. The region studied in this project provides a modern analogue to ancient hydrocarbon bearing sedimentary basins.

A better understanding of climatic influence on downslope sediment transport from continental margins to the deep sea and on how deep sea basins develop and fill underpins all areas of sedimentary research. Therefore, this research should provide fundamental insights into future deep-water exploration targets. The results should be

of interest to the Quaternary, sedimentological and climate change communities and to industrial exploration geologists.

1.2.1 Concept of turbidites

Systematic deep-sea sediment investigations began with the voyage of HMS Challenger (1872-1876), which established the general morphology of the ocean basins and the types of sediment they contain (Murray and Renard, 1891). In those days, and for most of the first half of the 20th century, it was generally believed that oceans had quiet, undisturbed floors where only pelagic and hemipelagic sediments were deposited. Sands and sandstones were considered to be shallow water deposits. However, the discovery of submarine canyons and the concept of turbidity currents challenged this view (Stow et al., 1996).

In 1863 the first submarine canyon was discovered by Dana and a discussion started on their origin. In 1936 Daly suggested that density currents could cause erosion of submarine canyons during periods of lowered sea level, but the role of density currents as a transporters and depositors of sands in deep water was not considered.

Since the 1880's density underflows have been known from lakes (e.g. in lakes Constance and Geneva) (Walker, 1973). It was assumed that rapid sinking of the muddy Rhine and Rhône river waters beneath the clear lake waters was due to a lower temperature of the river water and not because of a greater sediment density. In a review paper Bell (1942) emphasised the importance of density currents as agents for transporting sediment. The currents envisaged by Bell (1942) were of low density and their effectiveness, as agents of submarine erosion remained questioned. It was not until 1950, after flume experiments on turbidity currents by Kuenen and Migliorini (Kuenen, 1937, 1950), that it was recognised that turbidity currents could be responsible for the deposition of sands in the deep ocean. It was suggested that many graded sandstones in ancient successions had been deposited by high-density turbidity currents and they also interpreted flysh deposits as being a product of turbidity currents (Natland and Kuenen, 1951).

Bramlette and Bradley (1940) described cores from the Atlantic Ocean, which contained sand layers, that they interpreted as being deposited out of suspension from a submarine slump. In the late 1940's, piston cores started to be used and soon it was found that sands occur on deep-sea basin plains. The most satisfactory explanation for

the origin of these, often graded layers, was via transportation and deposition by turbidity currents (Ericson et al., 1951).

Around 1960 the word 'turbidite' was introduced to describe the deposit formed by a turbidity current (Stow et al., 1996). However, in recent reviews, Shanmugam (2000, 2002) suggests that many deep-water sands are misinterpreted as turbidite deposits that should instead be interpreted as sandy debris flow deposits. Shanmugam (2002) argues that processes other than turbidity currents can play a role in depositing sediments in deep water, including slides, slumps, debris flows, grain flows and bottom currents. Although caused by different processes, Shanmugam (2002) believes that sedimentologists also use the term 'turbidite' as a general term for deposits of deep-sea avalanches, slides, slumps and debris flows (e.g. fluxoturbidite, megaturbidite, seismoturbidite, high-density turbidite, etc.).

1.2.2 Properties of turbidity currents

Turbidity currents are a type of sediment-gravity flow with Newtonian rheology (fluid behaviour) and turbulent state from which deposition occurs through suspension settling (Shanmugam 2000). Flow turbulence is the principal sediment-support mechanism in turbidity currents (Lowe, 1982).

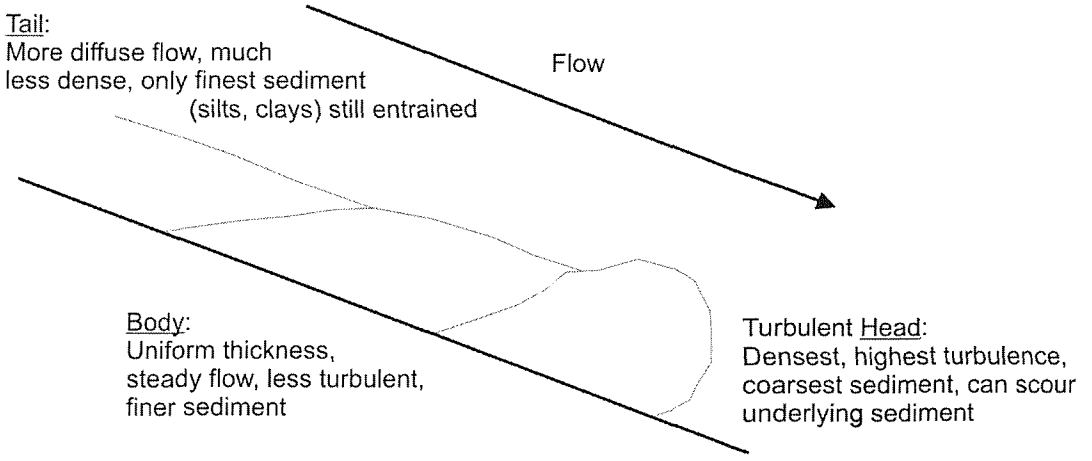

Figure 1.1 Schematic diagram of the head, neck, body and tail of a turbidity current on a slope (after Jones, University of Pittsburg, USA,: http:/mac01.eps.pitt.edu/CEJones/Geology1020/07Deltas_Turbidites.pdf).

Turbidity currents, so far, have only been observed in experimental settings. Kneller and Buckee (2000) provide an up-to-date extensive summary of experimental studies on gravity currents. Kneller and Buckee (2000) and Simpson and Britter (1979) described the physical properties of turbidity currents. They define gravity currents as having a well-defined head, body, and in some cases a tail (Figure 1.1). Turbidity current downstream velocity is extensively discussed by Middleton (1966a,b), Altinakar et al. (1996), Kneller et al. (1997, 1999) and Kneller and Buckee (2000). Garcia (1990, 1994), Altinakar et al. (1996), Kneller and Buckee (2000) and Peakall et al. (2000) discuss sediment concentration profiles in turbidity currents.

Weaver and Thomson (1993) and Mulder et al. (1998a) discuss the erosive properties of turbidity currents and entrainment of the eroded substrate sediment into the turbidity current. Weaver and Thomson (1993) found that turbidite currents emplaced on the Madeira Abyssal Plain caused only little erosion en route. Kerr (1991) pointed out that turbidity currents form an indirect mechanism for eroding stable density gradients that are common in the world's oceans and lakes.

1.2.3 Properties of turbidite deposits

A common feature in turbidite deposits is normal grading. However, reverse grading can occur at the base of thick coarse-grained beds, and multiple grading can occur in silty fine-grained beds (Stow et al., 1996), for example, through flow reflection or substrate entrainment.

Bouma (1962) showed that turbidite deposits have a characteristic sequence of sedimentary structures in each graded bed, where he defined five successive intervals (a-e) in the sequence (Figure 1.2), which are interpreted in terms of transporting, depositional and postdepositional processes (Stauffer 1967). The two uppermost of the five intervals (d, e) are products of settling from suspension; the 'c' interval reflects fallout of sand or silt from suspension while lower flow regime currents were moving on the bed; the 'b' interval results from plane bed transport in the upper flow regime and the lowest interval 'a' could be a result from flows from the upper part of the flow regime (Stow et al., 1996).

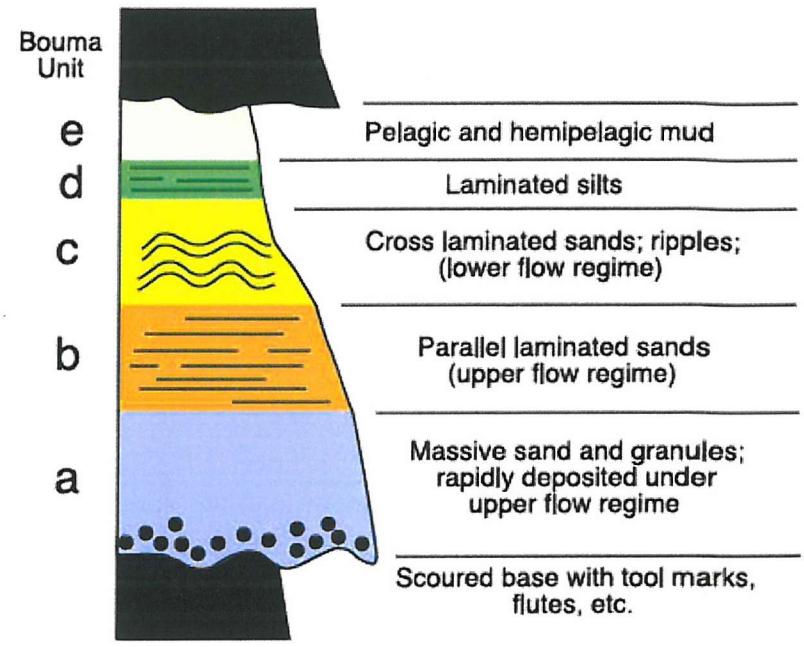

Figure 1.2 Classical Bouma sequence for medium-grained sand-mud turbidites (from: http://www.usask.ca/geology/classes/geol243/243notes/243week4b.html).

During the 1970s, it was found that this Bouma sequence is only applicable to medium-grained sand-mud turbidites. Lowe (1982) developed a sequence model for coarse-grained (conglomeratic) turbidites, whereas Stow and Shanmugam (1980) developed a sequence model for fine-grained (mud-rich) turbidites. The coarse-grained model of Lowe (1982) is an extension of the Bouma sequence with two intervals (termed R and S) that record phases of gravelly bed-load transport beneath a powerful current and two intervals that record gravel transport and deposition from suspension. The fine-grained model of Stow and Shanmugam (1980) is dominated by Bouma intervals D and E. The complete sequence of the fine-grained model is: 1) three intervals (T_0-T_2) with deposition by suspension fallout and traction, 2) three intervals (T_3-T_5) with shear-sorting of silt grains and clay flocs in the bottom boundary layer, and 3) three intervals (T_6-T_8) from suspension fallout (Figure 1.3).

1.3 OBJECTIVE

The main objective of this study is to try to broadly quantify the differences in advective sediment flux to the Balearic Abyssal Plain in the western Mediterranean Sea

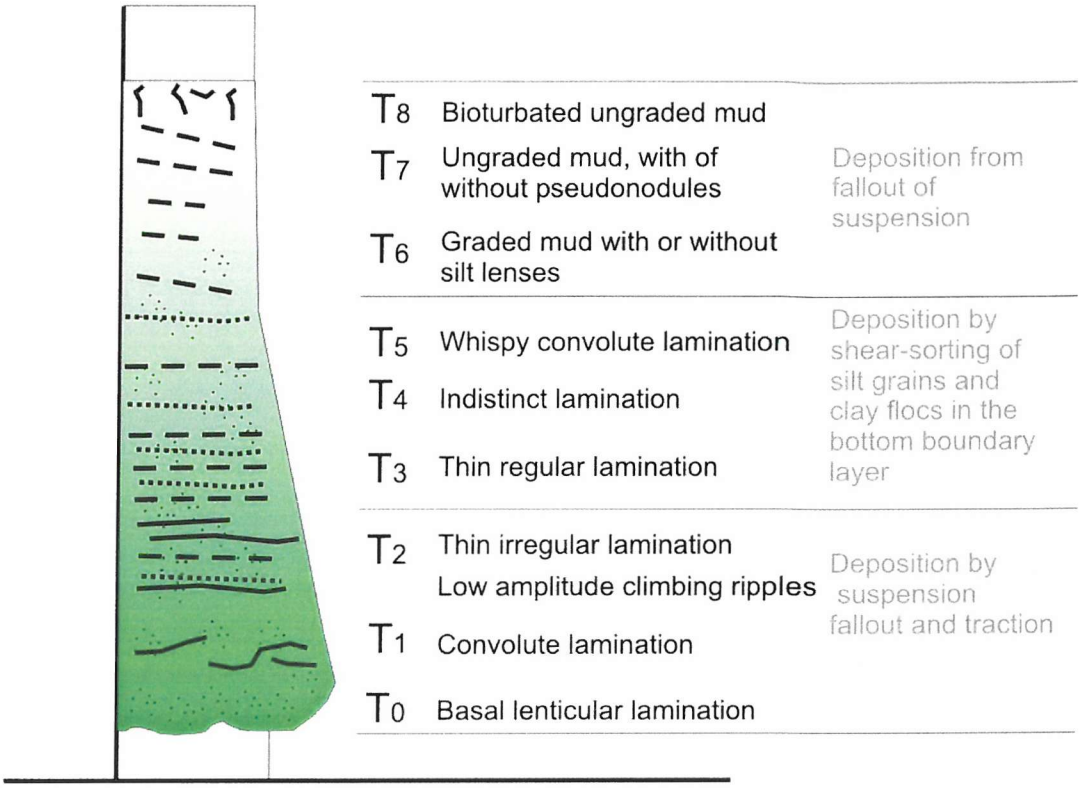

Figure 1.3 Sequence model for fine-grained (mud-rich) turbidites (after Stow and Shanmugam, 1980).

during each Marine Oxygen Isotope Stage, over the last glacial/interglacial cycle, and relate this to climate. This will enable assessment of the effects of climate changes on sediment transfer to the deep sea in this basin. The alternating occurrence of hemipelagic and turbidite beds in the Balearic Abyssal Plain cores allows reconstruction of the erosional and depositional history of this small ocean basin during the last 130,000 years – a period characterised by substantial climate changes. This study is unique in the Mediterranean Sea and represents analysis of the only suitable core material presently available from the area.

1.4 OVERALL METHODS

Four giant piston cores from the Balearic Abyssal Plain, held in BOSCOR (British Ocean Sediment Core Repository, located at SOC), were used to study the deep-sea allochthonous record. The cores extend back to ~130,000 years BP and provide a complete record of turbidite deposition from the beginning of the previous interglacial (Marine Isotope Stage 5, or MIS 5).

Individual turbidites have been identified on textural and sedimentological criteria (Chapter 4). A variety of stratigraphic and dating methods (AMS radiocarbon dating of emplacement ages of beds up to 40,000 years BP and oxygen isotope analysis of hemipelagic intervals) have been used to constrain these allochthonous units into a time-statigraphic framework (Chapters 5 and 6). In this way, a better-constrained sedimentation history for the Balearic Basin can be constructed going back to MIS 5. Provision of this time-frame, together with the estimated volumes of allochthonous sediment emplacement over time, should allow advective sediment flux to be related to the Late Pleistocene sea level curve, and hence the effects of glacial/interglacial cycles on allochthonous sediment transport to the deep sea can be determined.

CHAPTER 2 – THE WESTERN MEDITERRANEAN SEA

2.1 GEOGRAPHIC SETTING

The western Mediterranean Sea covers an area of 860×10^3 km^2 and is delimited by the Sicily-Tunis sill to the east and by the Gibraltar-Morocco sill to the west (Margalef, 1984). Within the western Mediterranean Sea, two regional seas are defined: the Alboran Sea in the west (west of the 0° median) and the Balearic Sea to the east (Figure 2.1). The Alboran Sea is rectangular in shape and is bounded by the Strait of Gibraltar to the west, the Betic Cordillera of Spain to the north and the Moroccan and Atlas Mountains to the south (Carter et al., 1972). The Balearic Abyssal Plain which floors the Balearic Basin is connected to the Alboran Sea through the Alboran Trough to the west and is bounded by Spain and France to the north and northwest, Corsica and Sardinia to the east and Algeria to the south.

2.1.1 Rivers draining into the western Mediterranean Sea

Numerous rivers of varying size drain into the western Mediterranean Sea (Figure 2.1). The most impressive deltas and fans (Rhône, Valencia and Var) that border the abyssal plain were built by rivers with the largest catchment area and highest sediment delivery (Table 2.1). These delta and fan systems may be important sediment transfer pathways to the deep-sea by sediment gravity flow processes.

2.1.1.1 Rhône and Languedocian rivers (Hérault, Aude and Têt)

The river Rhône has the largest drainage area in the western Mediterranean (97×10^3 km^2) (Table 2.1) with a sediment yield of 56×10^6 tonnes per year (Ludwig and Probst, 1998). The amount of sediment transported by the Rhône that flows out into the Gulf of Lyons is estimated at around 8.5×10^6 tonnes per year (Pont, 1993) (Table 2.1) but only 1×10^6 tonnes reaches the open sea (Martin et al., 1989). The Hérault river is 150 km long and has a medium-sized drainage basin of 2.5×10^3 km^2 (Petelet et al., 1998) (Table 2.1) which is comparable to the size of drainage basin of the Var. The river Têt is about 120 km long and has a slightly smaller drainage area (1.4×10^3 km^2) and a mean annual sediment flux at the river mouth of 53×10^3 tonnes per year

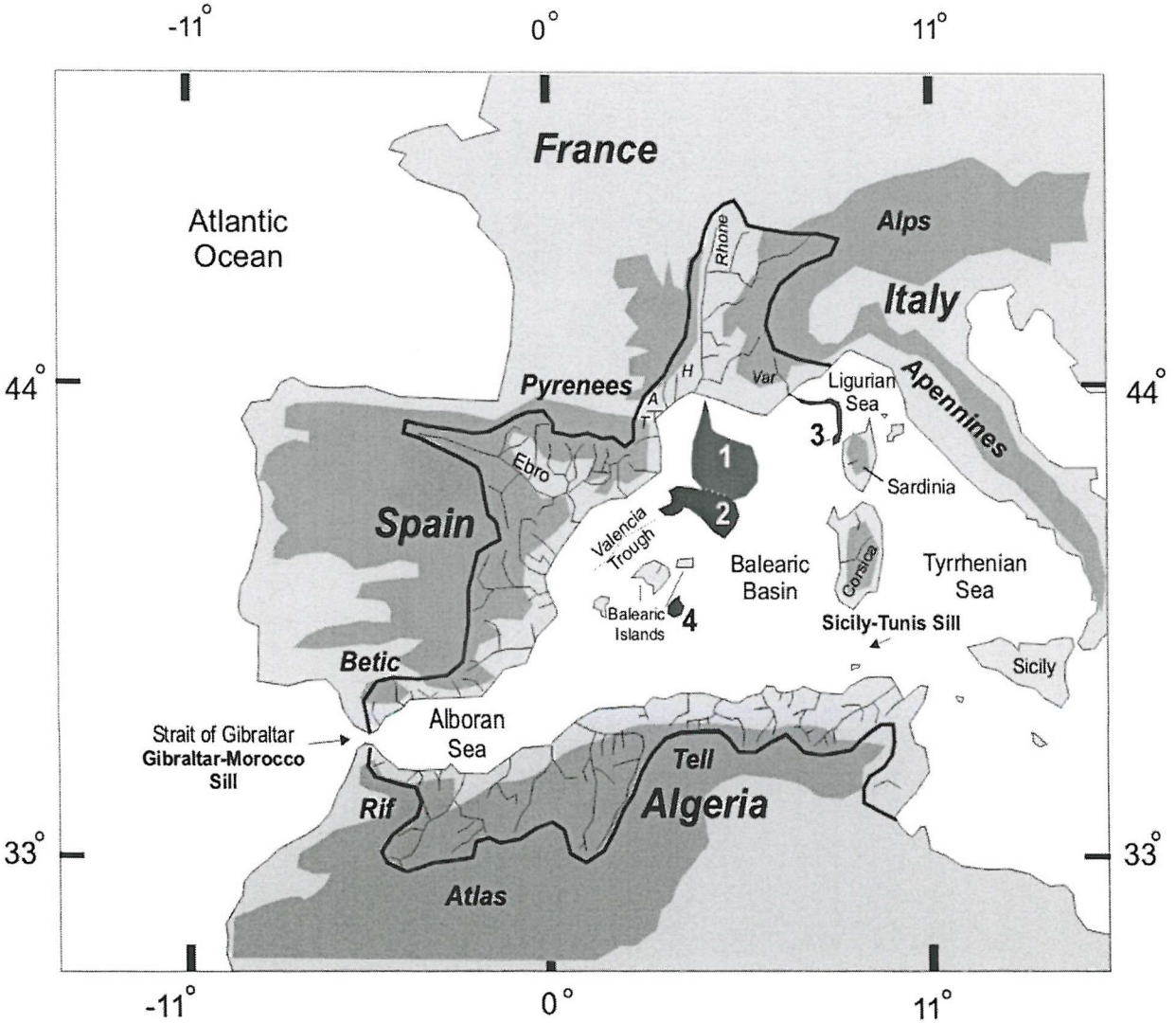

Figure 2.1 General map of the western Mediterranean Sea, showing the location of the major seas occupying the basin plus major surrounding mountain ranges and rivers, including the Rhône, Ebro, Var and Herault (H), Aude (A) and Tet (T). Also indicated are the Gibraltar-Morocco and Sicily-Tunis sills and the location of major deep-sea fans (1= Rhône fan, 2= Valencia fan, 3= Var fan and 4= Menorca fan) bordering the Balearic Abyssal Plain.

(Serrat et al., 2001) (Table 2.1).

2.1.1.2 Ebro

The Ebro, with the second largest drainage area (84×10^3 km^2), delivers around 6.2×10^6 tonnes of sediment to the continental margin per year (Nelson, 1990) (Table 2.1). The drainage area of the Ebro, however only forms 66.5% of the total main drainage area that feeds the Valencia Trough margin (Nelson, 1990). If other, smaller, rivers that drain into the Valencia Trough margin have similar sediment yields, total sediment delivery could be up to 9.3×10^6 tonnes per year.

2.1.1.3 Var and Roya

The river Var is approximately 135 km long, with a catchment area of just over 2800 km^2 (Mulder et al., 1998b) (Table 2.1). Several sources, including the tributaries Tinée and Vesubie, are located at a high altitude (~2500 m). The Var discharge regime is typical for the Alpine flank of the Mediterranean, with a broadly seasonal character. The mean annual suspended sediment load (silt and clays) of the Var was estimated by Mulder et al. (1997) at 1.3 to 1.6 $\times10^6$ tonnes (Table 2.1), whereas the gravel load is much lower, at about 0.1×10^6 tonnes (Sage, 1976). Turbidite currents at the river mouth are generated either by shallow failures through excess pore pressure during river floods or by earthquakes, the latter possibly causing more large-scale failures (Mulder et al., 1998b). The 1979 submarine landslide, which resulted in the collapse of the quay of the new port of Nice, emplaced up to 400 $\times10^6$ m^3 of sediment and reclamation fill and caused turbidity flows which destroyed underwater telegraph cables at depths of 2,500 m at distances up to 120 km offshore (Gennesseaux et al., 1980). According to Anthony and Julian (1995), no earthquake was responsible for this large landslide; instead it was largely favoured by human activities that strongly affected the sediment dynamics and geomorphology of the delta.

2.1.1.4 Corsica and Sardinia

Several small rivers, like the Taravo and Rizzanese, drain the southwestern part of Corsica. Most catchment areas in the northeastern part of the island drain into the Tyrrhenian Sea. There are numerous small river systems on Sardinia that drain into the western Mediterranean Sea. The larger river systems include the river Coghinas and

Mannu (draining the northern and north-western parts of Sardinia), the Tirso (the largest which drains the north-east and eastern part of the island) and the Cixerri /Mannu (draining the southern part of the island) (Table 2.1). To date, there is no literature available about the discharge and the sediment load of these rivers.

2.1.1.5 Menorca and Mallorca

There are only a few small rivers on the islands of Menorca and Mallorca and at present there is no information concerning their discharge or suspended sediment load.

Table 2.1 Summary of rivers and their drainage areas, sediment delivery to the continental margins and main sediment source. References: (1) Nelson (1990); (2) Andres et al. (2002); (3) Inglès and Ranos-Guerrero (1995); (4) Orr et al. (1996); (5) Ludwig and Probst (1998); (6) Pont (1993); (7) Roques et al. (1971); (8) Arnaud-Fassetta and Provansal (1999); (9) Petelet et al. (1998); (10) Hurtrez and Lucazeau (1999); (11) Serrat et al. (2001); (12) Mulder et al. (1997); (13) Anthony and Julian (1999); (14) Cornamusini et al. (2002); (15) Leclaire (1972); (16) Fourcade et al. (2001). n.i.a: no information available.

River	Drainage area (km^2)	Sediment reaching the margin (tonnes)	Main sediment source
River input from the west			
Ebro	84×10^3 (1)	6.2×10^6 (1)	Miocene carbonate rich sediments from the Central Ebro basin (2)
Menorca and Mallorca	n.i.a	n.i.a	Palaeozoic to Tertiary rocks (3, 4)
River input from the north			
Rhône	97×10^3 (5)	8.5×10^6 (6)	Palaeozoic metamorphic and igneous rocks from the Massif Central (7, 8)
Hérault	2.5×10^3 (9)	n.i.a	Palaeozoic basement, karstified Mesozoic cover and a Tertiary and Quaternary alluvial Plain (9, 10)
Aude	n.i.a	n.i.a	n.i.a
Têt	1.4×10^3 (11)	0.053×10^6 (11)	n.i.a
Var	2.8×10^3 (12)	$1.3\text{-}1.6\times10^6$ (12)	Granitic basement rocks, sandstones, limestones and schists from the Mercantour Massif (13)
River input from the east			
Coghinas (Sardinia)	n.i.a	n.i.a	Hercynian plutonics, Palaeozoic metamorphics and sedimentary calcareous clasts from the Corsica-Sardinia Massif (14)
Mannu (Sardinia)	n.i.a	n.i.a	"
Tirso (Sardinia)	n.i.a	n.i.a	"
River input from the south			
Cixerri, Mannu (Sardinia)	n.i.a	n.i.a	"
Algeria	n.i.a	$0.04\text{-}0.06\times10^6$ (15)	Palaeozoic to Tertiary sediment cover, flych deposits and sediments from the Tethyan margin (16)

2.1.1.6 Algeria

Only limited information is available about the character and the quantity of terrigenous sediment that is transported to the sea from Algeria. According to Leclaire

(1972) the present total annual suspended sediment supply to the western Mediterranean ranges between 40 and 60×10^3 tonnes (Table 2.1).

2.2 GEOLOGY AND MORPHOLOGY

The western Mediterranean Basin is surrounded by high (2000-4500 m) mountain ranges (specifically the Pyrenean and Catalan ranges, Betic Cordillera, Rif and Tell Massifs, Tertiary ranges of Sicily and Calabria, Apennines and the Western Alps). Its development is related to the converging motion of the European and African plates since the Cretaceous (Figure 2.2) (Rehault et al., 1985). The Algero-Provençal and the Tyrrhenian extensional basins developed during two major stages from the late Oligocene onwards in a geodynamic setting characterized by the nearly north-south convergence between Africa and Europe (Dewey et al., 1989) (Figure 2.3). Following a long period of rifting in the western Mediterranean area (Burrus, 1989), spreading of the Algero-Provençal basin occurred in the early-middle Miocene (Figure 2.2). This spreading occurred coeval with the rotation of the remnant volcanic arcs (Corsica-Sardinia block (Boccaletti and Guazzone, 1974; Vigliotti and Langenheim, 1995)).

Rehault et al. (1984, 1985) divide the western Mediterranean Sea into five main regional and morphological units: (1) abyssal plain, (2) continental rise and deep-sea fans, (3) continental shelf and slope, and (4) the Alboran Sea.

The Balearic Abyssal Plain (BAP) is the largest basin plain in the Mediterranean Sea, with an area of 77,000 km^2 (Rothwell et al., 1998, 2000) and is defined by the 2800 m isobath (Figure 2.1). The morphology of the BAP is flat (Figure 2.4) as a result of ponded turbidites that cover previous topography. High-resolution 3.5 kHz seismic reflection profiles across the BAP show the occurrence of a thick basin-wide acoustically transparent layer (Figure 2.4), which was interpreted by Rothwell et al. (1998) as a turbidite megabed of basin-wide extent. The layer, estimated to be 8 to 10 metres thick, lies at approximately 10 to 12 metres below the sea floor (Rothwell et al., 1998). Rothwell et al. (2000) suggested that the megabed is a ponded deposit and may have a volume of about 600 km^3. The Alboran Sea deep seafloor is divided into an eastern and western basin plain by the northeast-southwest trending Alboran Ridge (Giermann, 1962). The Western Alboran Basin is the larger, being 40 km in length and

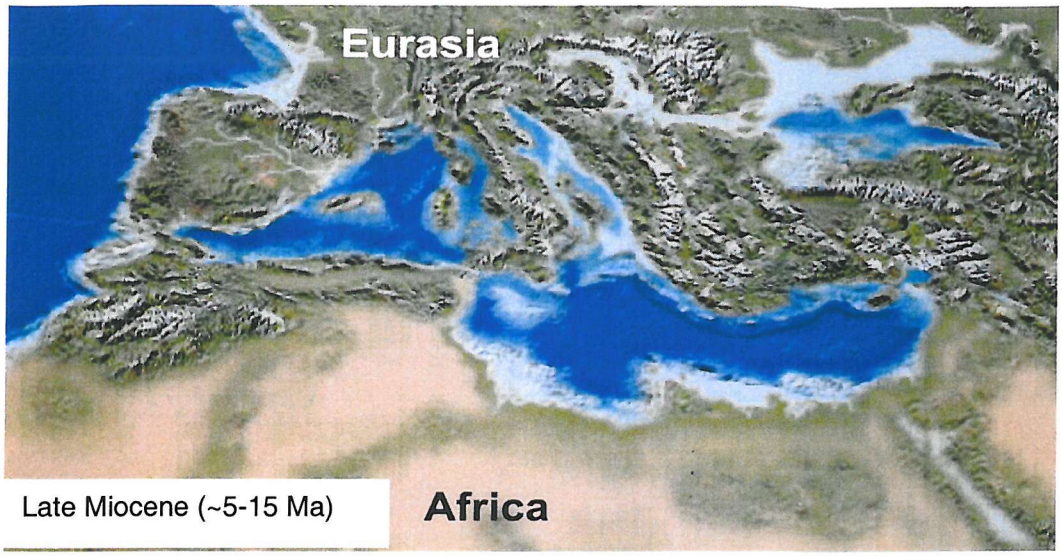

Late Miocene (~5-15 Ma)

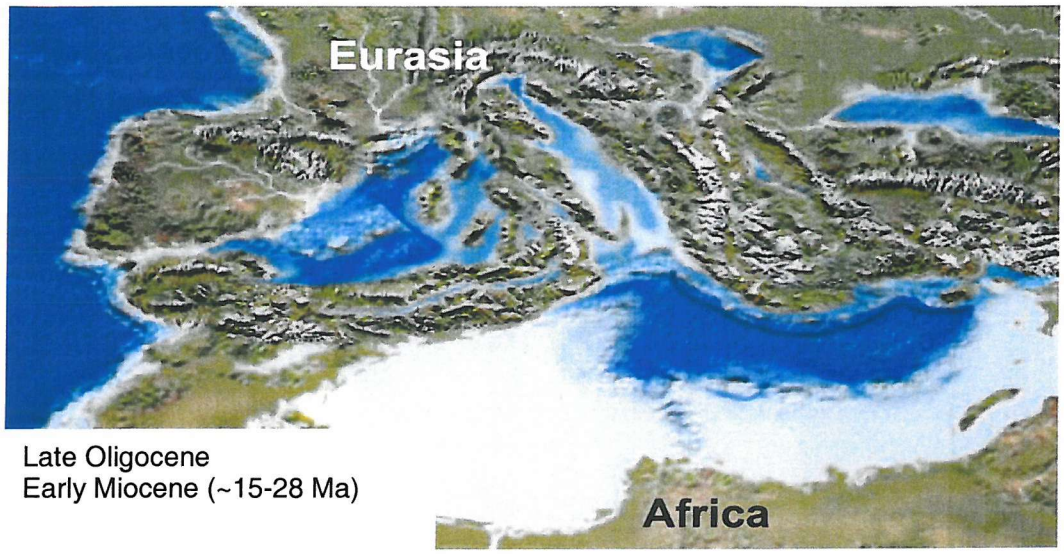

Late Oligocene
Early Miocene (~15-28 Ma)

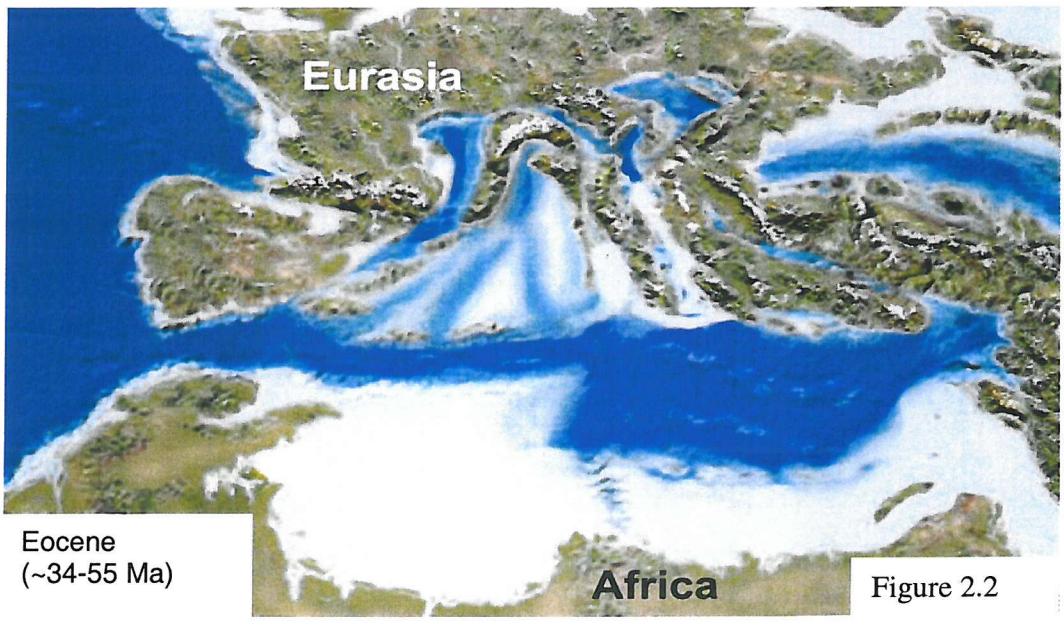

Eocene
(~34-55 Ma)

Figure 2.2

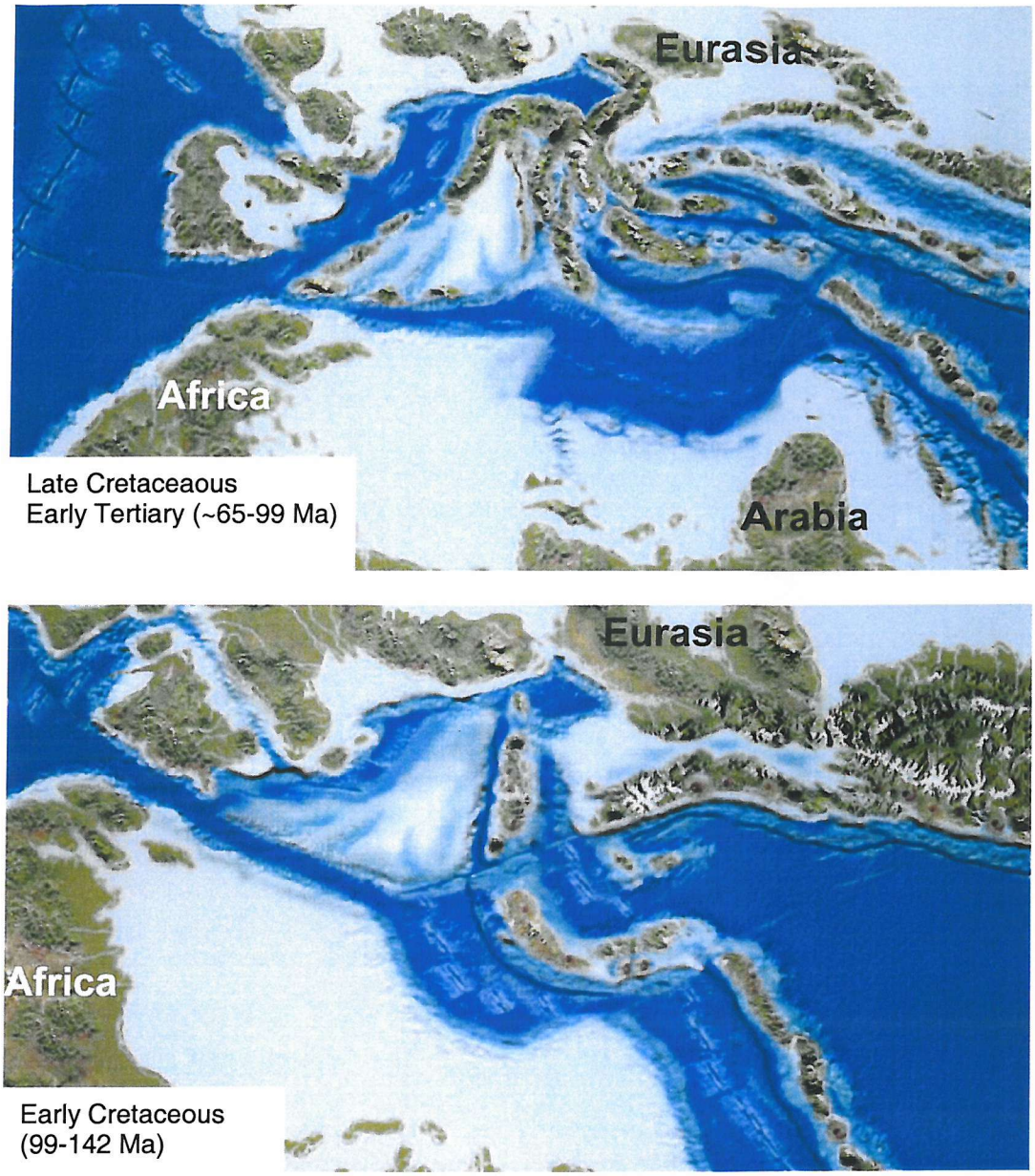

Figure 2.2 Palaeogeographic maps showing the tectonic evolution of the Mediterranean basin since the Early Cretaceous due to the converging motion of the African and Eurasian plates (adapted from http:/jan.ucc.nau.edu/~rcb7/, University of Arizona, USA).

22 km in width, whereas the Eastern Alboran Basin is approximately 13 km long and 6 km wide (Carter et al., 1972).

The continental rise and deep-sea fans in the northern part of the BAP are fed by major European river systems, specifically the rivers Roya, Var, Rhône and Ebro. Minor rivers on Corsica, Sardinia, the Balearic Islands and Algeria carry much smaller sediment loads and consequently the adjacent continental margins are considered starved of sediment (Figure 2.1, 2.5).

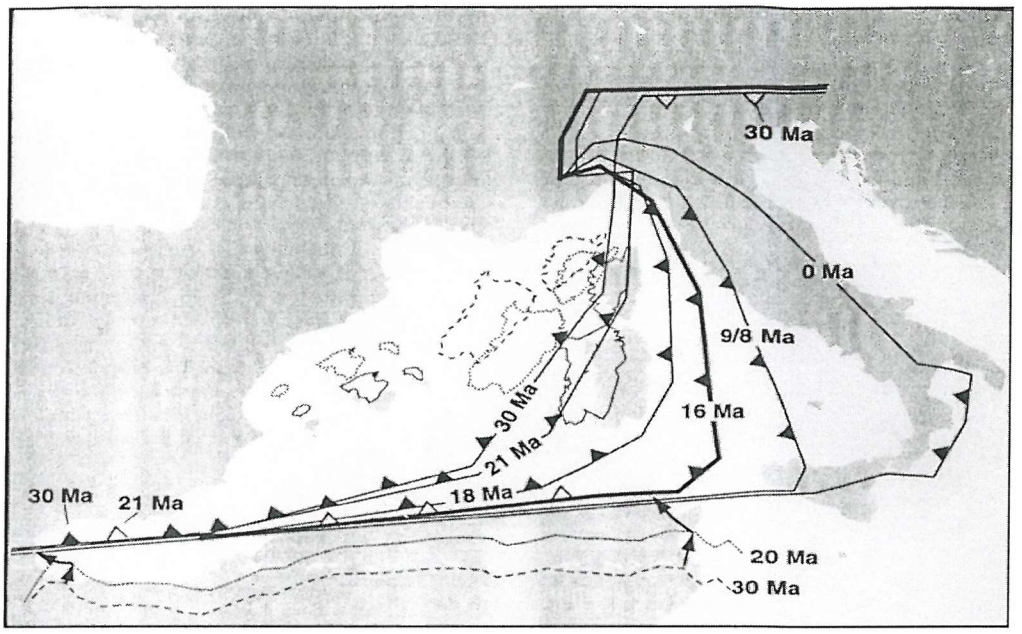

Figure 2.3 Development of the Algero-Provençal and Tyrrhenian extensional basins during two major stages of convergence in the late Oligocene (from Carminati et al., 1998). The thick line representing the 16 Ma configuration marks the transition between the first and second opening stage (Carminati et al., 1998).

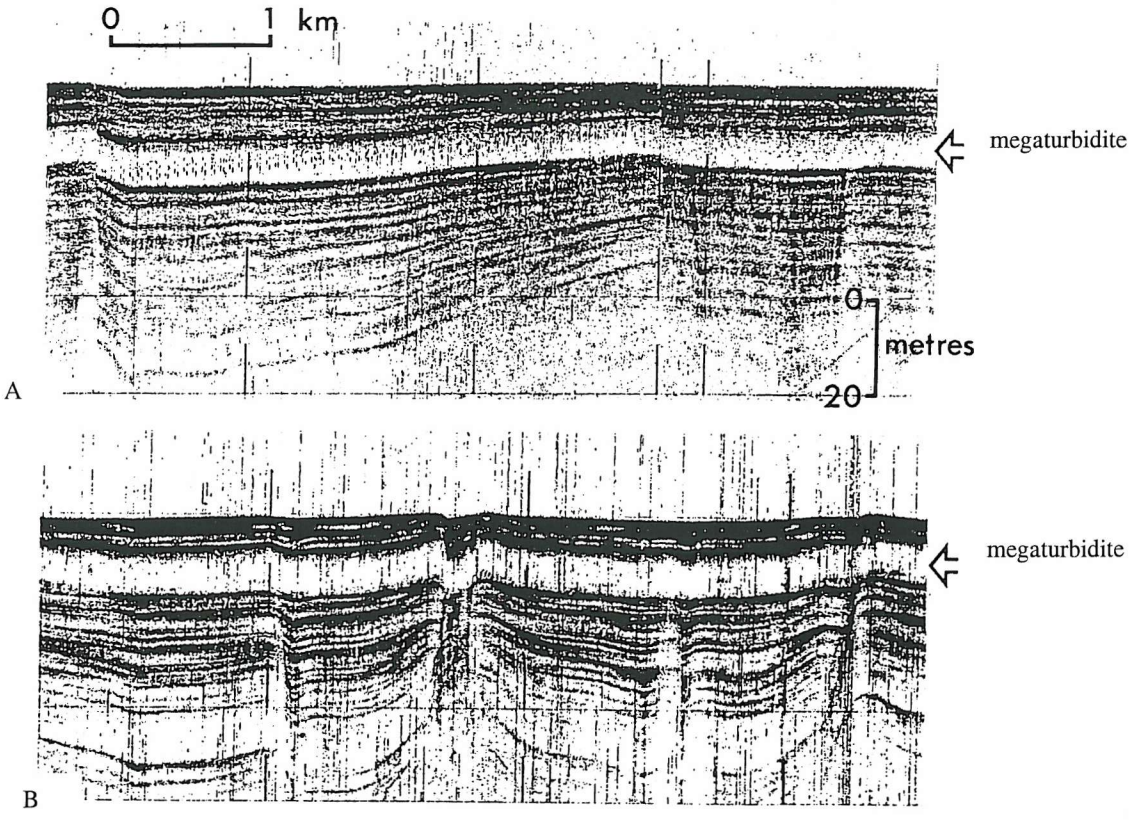

Figure 2.4 High-resolution (3.5 kHz) seismic reflection profiles across the northern (A) and central (B) BAP showing the flat morphology of the basin plain and the occurrence of the Late Glacial BAP megabed (arrow), which is now affected by salt diapirism (from Rothwell et al., 2000). The location of the profiles are shown on Figure 2.5.

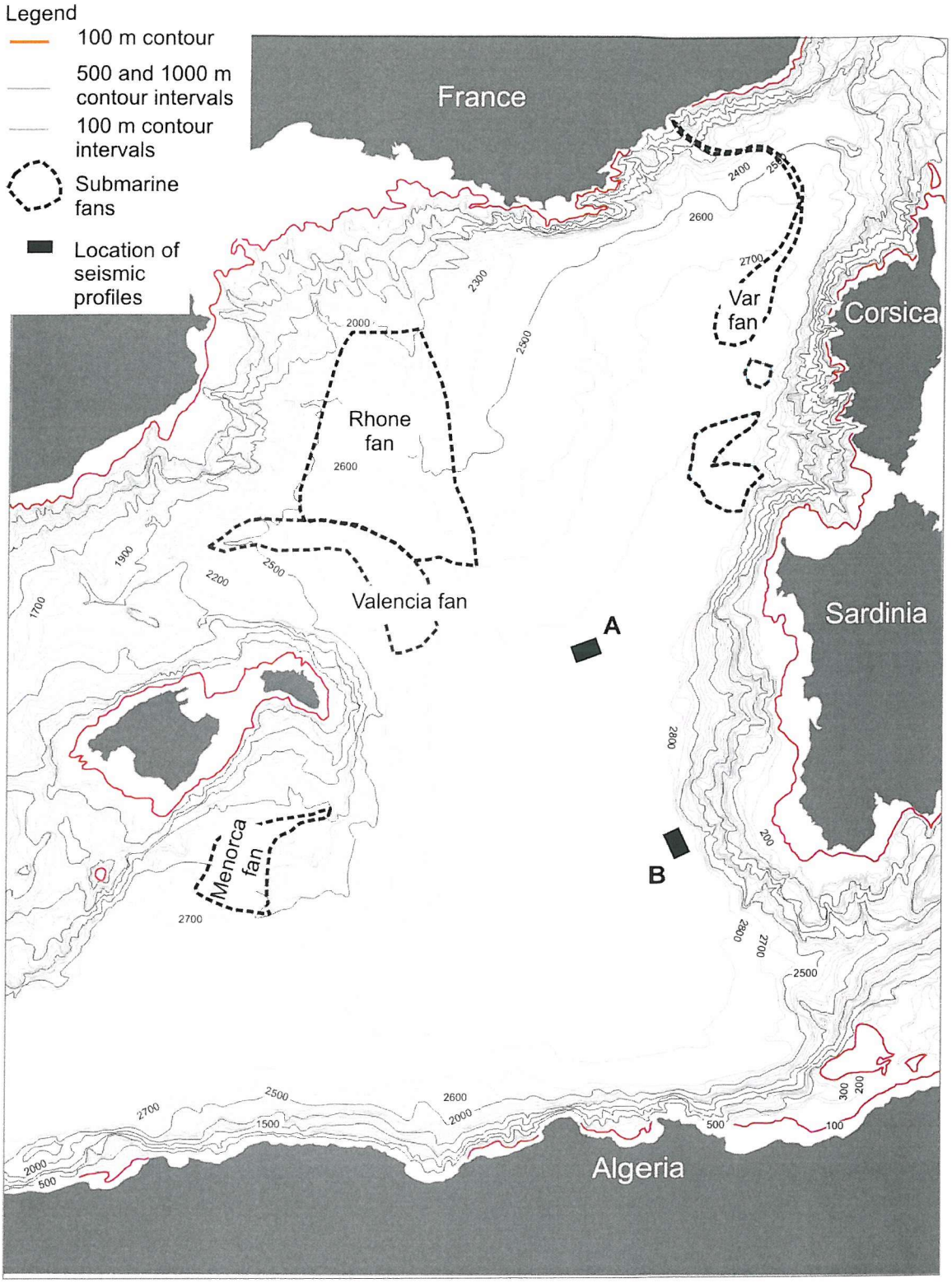

Figure 2.5 Bathymetry of the western Mediterranean Sea (source: bathymetric contour chart Mediterranean Sea - western part, Taunton Hydrographic Department, 1998) . The location of the seismic profiles from Figure 2.4 is also indicated.

2.2.1 Catchment lithology

2.2.1.1 Rhône and Languedocian rivers (Hérault, Aude and Têt)

The French Massif Central, which was uplifted during the Alpine Orogeny, is one of the major sediment source areas for the Rhône (see below) and consists of a complex of Palaeozoic metamorphic and igneous rocks (Roques et al., 1971) (Table 2.1). Holocene sands, eroded from the crystalline basement of the Massif Central are composed of quartz, plagioclase, K-feldspar (including orthoclase, microcline and perthite), biotite, muscovite, chlorite, amphibole and clinopyroxene, with granitic, metamorphic and volcanic rock samples in coarser samples (Van de Kamp et al., 1994). Heavy minerals include pyrite, magnetite, sphene, orthopyroxene, epidote, clinozoisite, garnet, kyanite, zircon and apatite (Van de Kamp et al., 1994).

The main streams and tributaries of the river Hérault drain a Palaeozoic basement (granites, schists, metalimestones and metadolomites), a karstified Mesozoic cover (consisting of Triassic clays and sandstones, some evaporitic layers and Jurassic limestones with some dolomites, clays and calcareous marls) and a Tertiary and Quaternary alluvial plain (Petelet et al., 1998; Hurtrez and Lucazeau, 1999) (Figure 2.6, Table 2.1).

The Quaternary sedimentary cover of the Gulf of Lyons continental shelf is composed of terrigenous material from the Rhône River and occasionally from the Languedocian rivers (Hérault, Aude and Têt) (Torres et al., 1995). Sedimentary deposits on the Rhône shelf mainly lie between 4 and 63 m (Added et al., 1984). Calcium carbonate contents in sediments near the river mouth are commonly higher than 25% (Added et al., 1984). Illite forms ~40% of the total clay minerals and the amount of chlorite exceeds the amount of kaolinite (Added et al., 1984).

The lower Rhône experienced a higher influx of coarse-grained sediments during the Little Ice Age (Arnaud-Fassetta and Provansal, 1999). Using heavy mineral assemblages, Arnaud-Fassetta and Provansal (1999) found that the Massif Central was a major source area of these sediments, due to its proximity to the delta. They also suggested that the sedimentary contribution from the northern and southern Alps was much lower because of the distance from the delta and the time lag affecting the down-stream transport. Due to its proximity to the delta, it is suggested here that the Massif Central most likely has been a major sediment source to the Rhône delta during the late Quaternary.

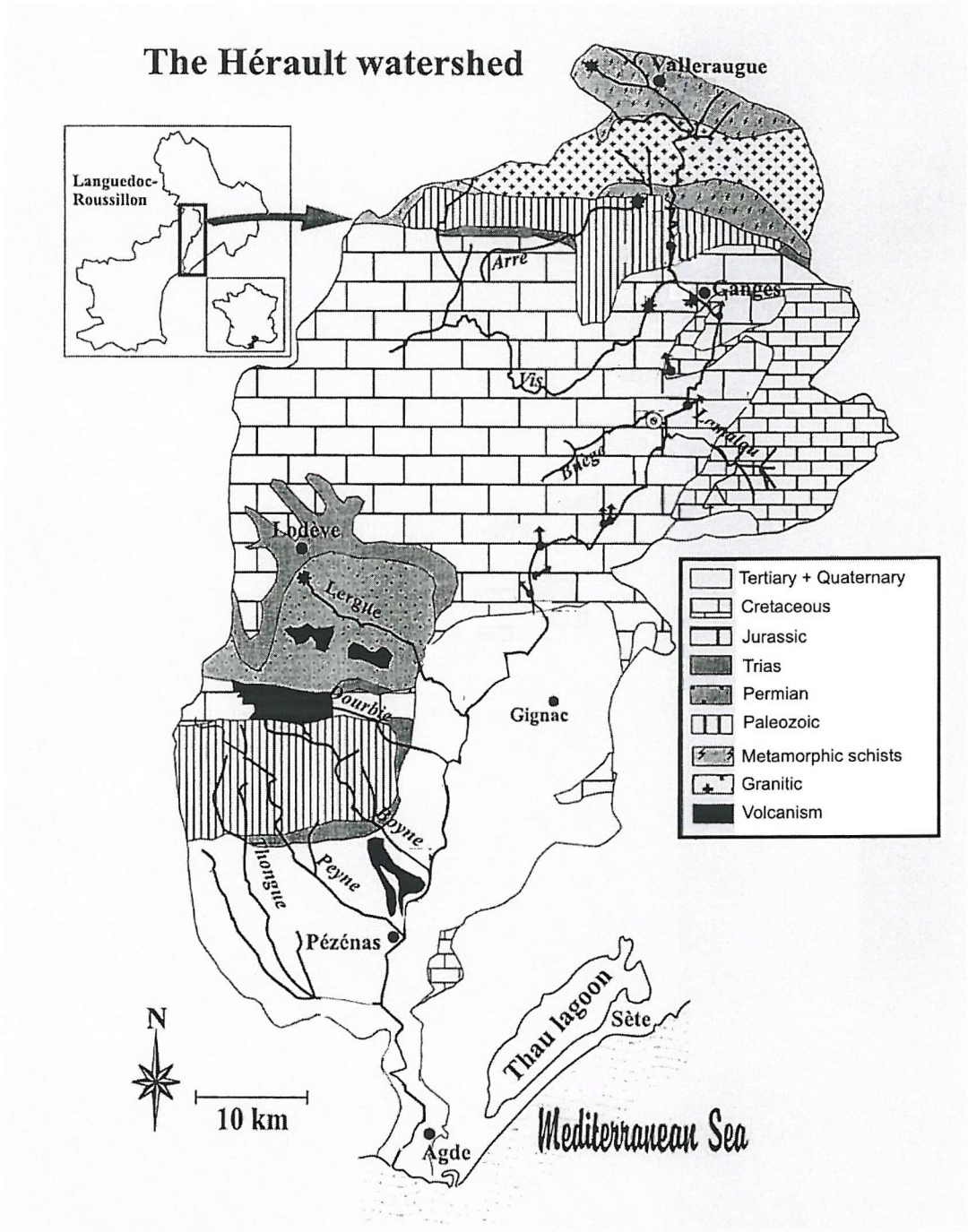

Figure 2.6 Geology of the Hérault watershed (adapted from Petelet et al., 1998).

2.2.1.2 Ebro

The major river course of the Ebro and its tributaries runs through a large Tertiary continental basin, including Tertiary conglomerates and Oligo-Miocene detrital formations (Figure 2.7) (Benito et al., 2000). Many tributaries run through Alpine settings (Pyrenees, Catalan Range and Iberian Range), folded Palaeogene

formations, calcareous platforms and evaporitic formations (Benito et al., 2000).

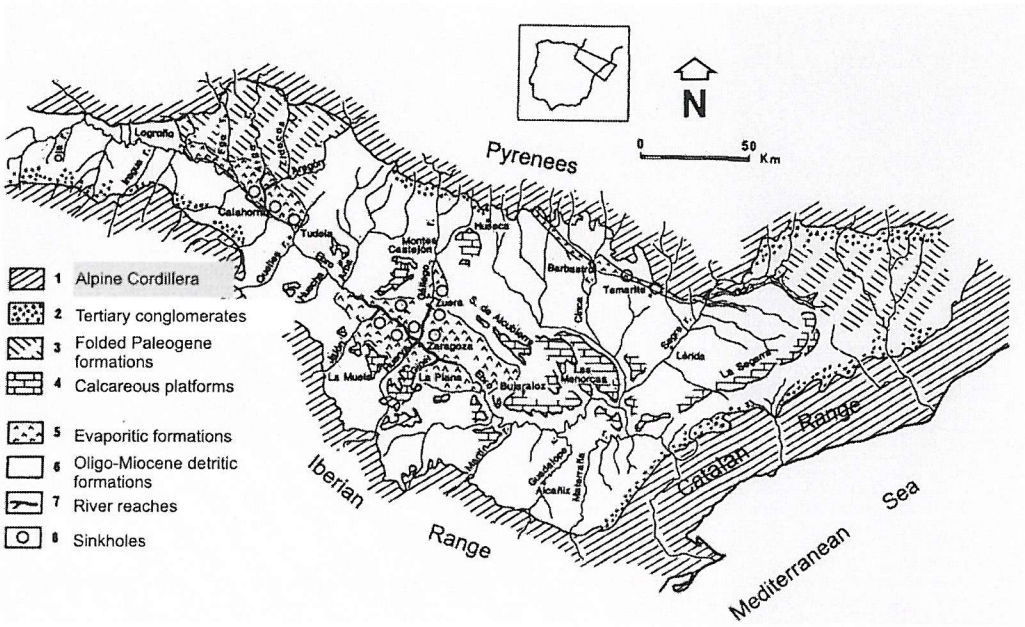

Figure 2.7 Lithological sketch map of the Ebro basin (from Benito et al., 2000).

Material derived from the Miocene sediments in the Central Ebro Basin is rich in carbonate (33-47%) (Andres et al., 2002) (Table 2.1). Bulk samples from the Ebro turbidite systems (developed between the Iberian Peninsula and the Balearic Islands on the base-of-slope off the river Ebro) and nearshore sands of the Ebro Delta contain high proportions of calcareous minerals (>38%) in the bulk samples, while quartz and feldspar predominate in the sand fraction (Maldonado, 1972; Alonso and Maldonado, 1990). The mineralogical composition of the channel sands includes: epidote, andalusite, amphiboles, tourmaline, garnet and pyroxene (Alonso, 1986). The clay mineralogical composition of turbidite deposits form the Ebro turbidite system shows a high chlorite/kaolinite ratio (1.4-1.8), a high illite/kaolinite ratio (1.2-1.6) and a low calcite/quartz ratio (0.2-0.8) (Alonso and Maldonado, 1990).

2.2.1.3 Var and Roya

The Var's main catchment area, the Mercantour Massif, is built of granitic basement rocks, Permian and Middle Eocene sandstones, various limestones and Permian schists (Anthony and Julian, 1999) (Table 2.1). The coastal reaches of the Var

consist predominantly of fine-grained sediments that would have been deposited from suspension (Anthony, 1995). These sediments are derived from marls that form extensive portions of the Var catchment area. The Var catchment area can be subject to major earthquakes (Dadou et al., 1984), due to reactivation of the passive margin through compressional movements of the European and African plates (Mascle and Rehault, 1991).

2.2.1.4 Corsica and Sardinia

The western coast of Corsica is composed of Palaeozoic granites (Conchon, 1987). Sediments from the Corsica-Sardinia Massif are derived from predominantly Hercynian plutonics (granodiorite, tonalite and S-granite), Palaeozoic metamorphics (gneiss and schist) and calcareous sedimentary clasts (Cornamusini et al., 2002). These sediments lack a high-pressure/low-temperature paragenesis in the plutonic and metamorphic clasts that is common in sediments that have been involved in the Alpine Orogeny (Cornamusini et al., 2002) (Table 2.1). In southwest Sardinia, several Tertiary clay units crop out: 1) fine-grained Cixerri clays of Eocene-Oligocene age, composed of illite, interstratified illite/smectite, quartz, kaolinite and a carbonate content of 19-24%, 2) Oligocene-Miocene Ussana clays, which consist of illite-chlorite-kaolinite with high quartz contents and variable percentages of carbonates (3-20%), and 3) Pliocene Samassi clayey silts that are rich in quartz and calcite, with a clay fraction consisting mostly of illite, smectite and chlorite (Strazzera et al., 1997).

2.2.1.5 Menorca and Mallorca

Menorca and Mallorca form part of the Balearic Islands, which rise from the submerged, northeastward extension of the alpine Betic Range of southern Spain. The islands are composed of Palaeozoic to Tertiary rocks and were folded and thrusted during the Alpine Orogeny (Inglès and Ramos-Guerrero, 1995; Orr et al., 1996).

2.2.1.6 Algeria

The northern Algerian Alpine collision belt is composed of several superimposed tectonic nappes from different palaeogeographic domains, including: 1) an internal domain corresponding to parts of the Alboran plate (including ancient basement complexes and their Palaeozoic to Tertiary sedimentary cover), 2) an internal

domain (flysch deposits) and 3) a southern external domain corresponding to the Tethyan margin of North Africa (Fourcade et al., 2001) (Figure 2.8, Table 2.1).

The coarse fraction deposited in most shallow environments (0-100/200 m) off the coast of Algeria is dominated by biogenic sediments, including marly sands, shelly sands, bryozoan sands and bioclastic sands, whereas deeper environments are dominated by terrigenous sediments, generally coarse to fine sand size quartz (Caulet, 1972). The terrigenous material present in nearshore sands comes from recent and old dunes, whose sands are derived from erosion of detrital Cretaceous and Palaeogene formations (Leclaire, 1972).

In some bays and gulfs, mud accumulates in depressions (Leclaire, 1972). This mud is dominated by clay (53%; silt and fine sand 27%) and generally has a low $CaCO_3$ content (20%) (Leclaire, 1972). The clay component is dominated by illite and mixed-layer minerals (70%) and the kaolinite content (20%) is higher than the chlorite content (10%) (Leclaire, 1972).

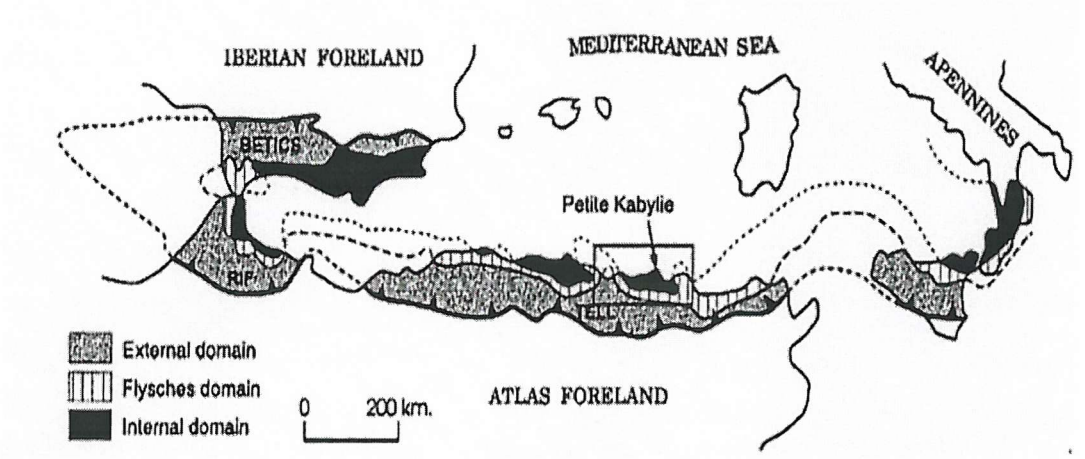

Figure 2.8 Geological sketch map of north Algeria showing the three palaeogeographic domains discussed in the text, that make up the different tectonic nappes (from Fourcade et al., 2001).

2.3 ADJACENT SEDIMENTARY SYSTEMS

2.3.1 Rhône deep-sea fan

The Rhône deep-sea fan forms the largest turbidite system in the western Mediterranean (Rehault et al., 1984, 1985) (Figure 2.5). The fan extends in a north-west to south-east direction from the lower slope seaward of the Gulf of Lyons to the

BAP (Torres et al., 1997). It has an elongated shape with maximum width of 200 km and a length of 300 km (Droz and Bellaiche, 1985; O'Connell et al., 1991). High-frequency glacio-eustatic fluctuations played a major role in the development of late Quaternary sedimentation on the shelf and slope (Tesson et al., 1990; Torres et al., 1995) and probably on the Rhône deep-sea fan (Droz and Bellaiche, 1985), which represents the main depositional deep turbidite system on the margin. According to Arnaud-Fassetta et al. (1999) the construction and evolution of the Rhône delta has been controlled by variations in sea level and sediment supply. Within the sedimentary fan-valley fill of the modern fan, Torres et al. (1997) recognised three seismic subunits. The lower unit was interpreted as a channel lag deposit, the second unit as mass-flow deposits and the third unit as turbidite overbank deposits. The characteristics of the turbidity current flows evolved from thick muddy flows during relative sea level low stands to sandy flows during the last highstand (Torres et al., 1997). Droz et al. (2001) discussed the main sedimentary events that occurred since the last glacial in the western Gulf of Lyons. From the Pliocene until the last glacial period, turbidite activity in this area was more or less continuous (Droz et al., 2001). During the last glacial maximum, the sedimentation regime changed from being characterised by deposition (event 1-3 in Figure 2.9) to being characterised by either mass movements or erosion of previously deposited sediments (Droz et al., 2001). The western debris flow (event 4 in Figure 2.9) accumulated during a period of active mass-movement processes in the western Mediterranean at around 21 ka (Droz et al., 2001), similar to the deposition time of the eastern debris flow from the eastern levee of the Rhône fan (Droz and Bellaiche, 1985), the Big'95 slide of the Ebro shelf (Berné et al., 1998) and the BAP 'megaturbidite' (Rothwell et al., 1998). Following post-glacial sea-level rise, fluvial inputs are mainly trapped in estuaries and, as a consequence, deep-sea canyons and channels are being eroded (Droz et al., 2001). Sands from the Neofan (event 5 in Figure 2.9) resulted from reshaping of the channel floor by upstream retrogressive erosion (Droz et al., 2001). Erosive currents inside and at the outlet of the Sète Canyon have resulted in downstream redeposition of sediment as a lobate unchannelized body (event 6 in Figure 2.9), whereas currents flowing inside La Fonera Canyon have removed and reshaped older sediments (event 7 in Figure 2.9), with probably minor redeposition (Droz et al., 2001).

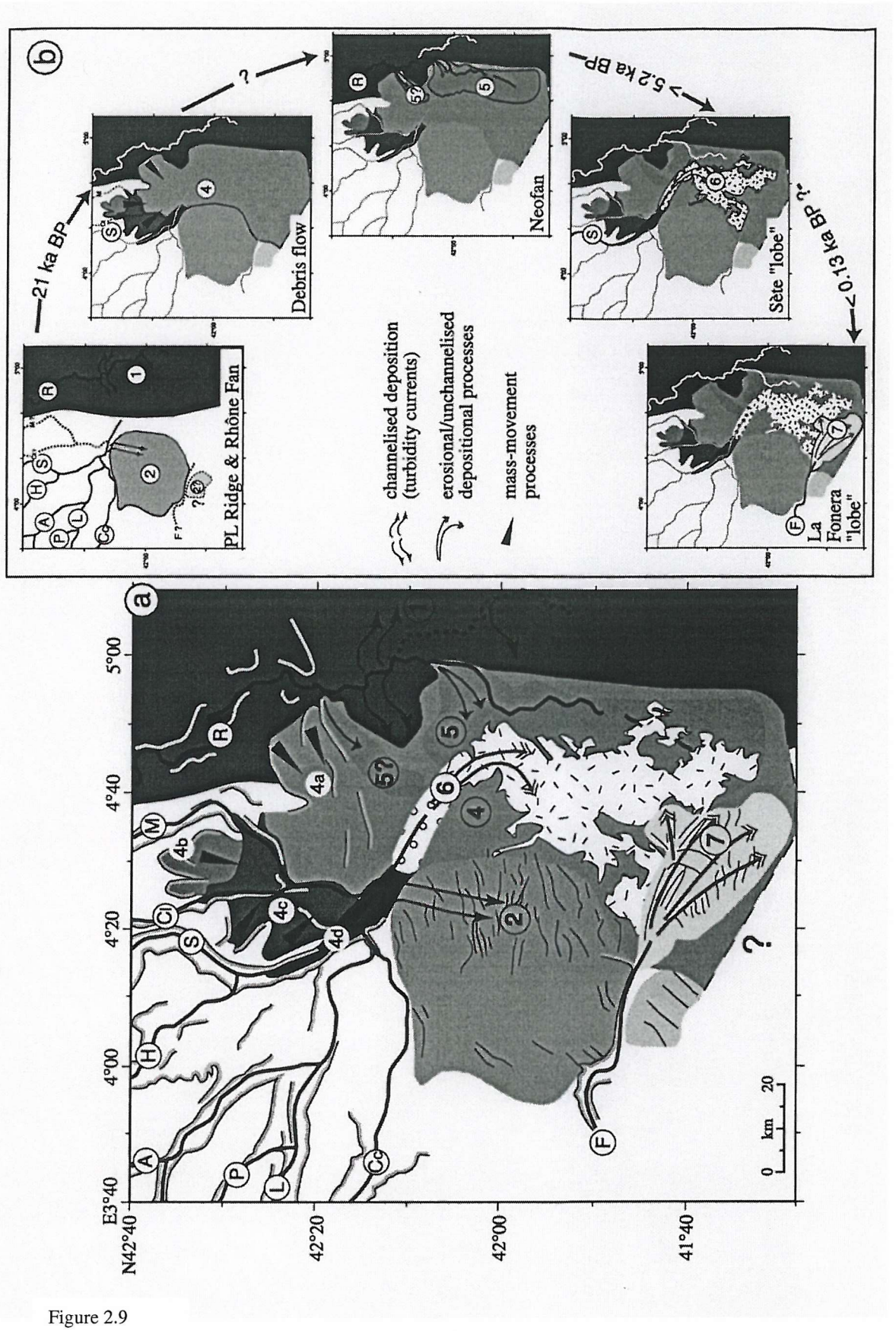
b
21 ka BP
?
Debris flow
Neofan
5.2 ka BP
Sète "lobe"
0.13 ka BP ?
La Fonera "lobe"
PL Ridge & Rhône Fan
channelised deposition (turbidity currents)
erosional/unchannelised depositional processes
mass-movement processes
a
5°00
4°40
4°20
4°00
3°40 E
42°40 N
42°20
42°00
41°40
0 km 20

Figure 2.9

Figure 2.9 Sedimentary events in the western Gulf of Lyons during the Late Pleistocene and Holocene (from Droz et al., 2001). a) Present-day superposition of units resulting from the seven main sedimentary events (numbered) as discussed in the text, including the locations of outlets of the Pyreneo-Languedocian and La Fonera canyons. **F**= La Fonera Canyon; **Cc**= Cap Creus Canyon; **L**= Lacaze Duthiers Canyon; **P**= Pruvost Canyon; **A**= Aude Canyon ; **H**= Hérault Canyon ; **S**= Sète Canyon; **Cl**= Catherine-Laurence Canyon; **M**= Marti Canyon; **R**= Rhône Canyon .

2.3.2 Valencia fan

The Valencia Fan, which is another major turbidite system in the northern part of the western Mediterranean (Figure 2.1), occurs between the deepest area of the Valencia Trough and the Balearic Basin Plain. Its structural, morphological and sedimentological patterns are controlled by the main features of the Valencia Trough (Limonov et al., 1992). The main factors controlling depositional patterns during the Plio-Quaternary were sediment supply and sea-level fluctuations related to global climatic changes (Limonov et al., 1992). The Ebro and Valencia turbidite systems were mainly built during the late Pliocene-Pleistocene (Limonov et al., 1992) and in this system, gravity flow deposits alternate with hemipelagic deposits (Alonso et al., 1991). Using seismic data, Palanques et al. (1994) related sea-level changes to phases of fan progradation and retreat resulting from changes in sediment supply to the Valencia fan system. During periods of sea level lowering, the fan system migrated downbasin and developed extensively in the deeper areas of the Valencia Trough (Palanques et al., 1994) (Figure 2.10a). However, during periods of sea-level rise the fan sedimentation migrated upstream and deeper areas of the basin were abandoned (Palanques et al., 1994) (Figure 2.10b). The Ebro canyon and many smaller submarine gullies cut a gentle submarine slope in a complex coalescent fan.

2.3.3 Var fan

In the Ligurian Sea, sediment is supplied from the Var, Roya and Paillon rivers and other canyons to build a coalescent deep-sea fan (Alinat et al., 1969; Pierot, 1972; Savoye et al., 1993; Klaucke et al., 2000). The Var submarine fan, which was constructed throughout the Pliocene and Quaternary, extends almost directly from the Var river off a steep continental slope (with an average gradient of more than 11°) and covers an area of 16,200 km^2 (Savoye et al., 1993). Savoye et al. (1993) suggested that the river Var cut a valley through older deltaic deposits during the Quaternary sea-level

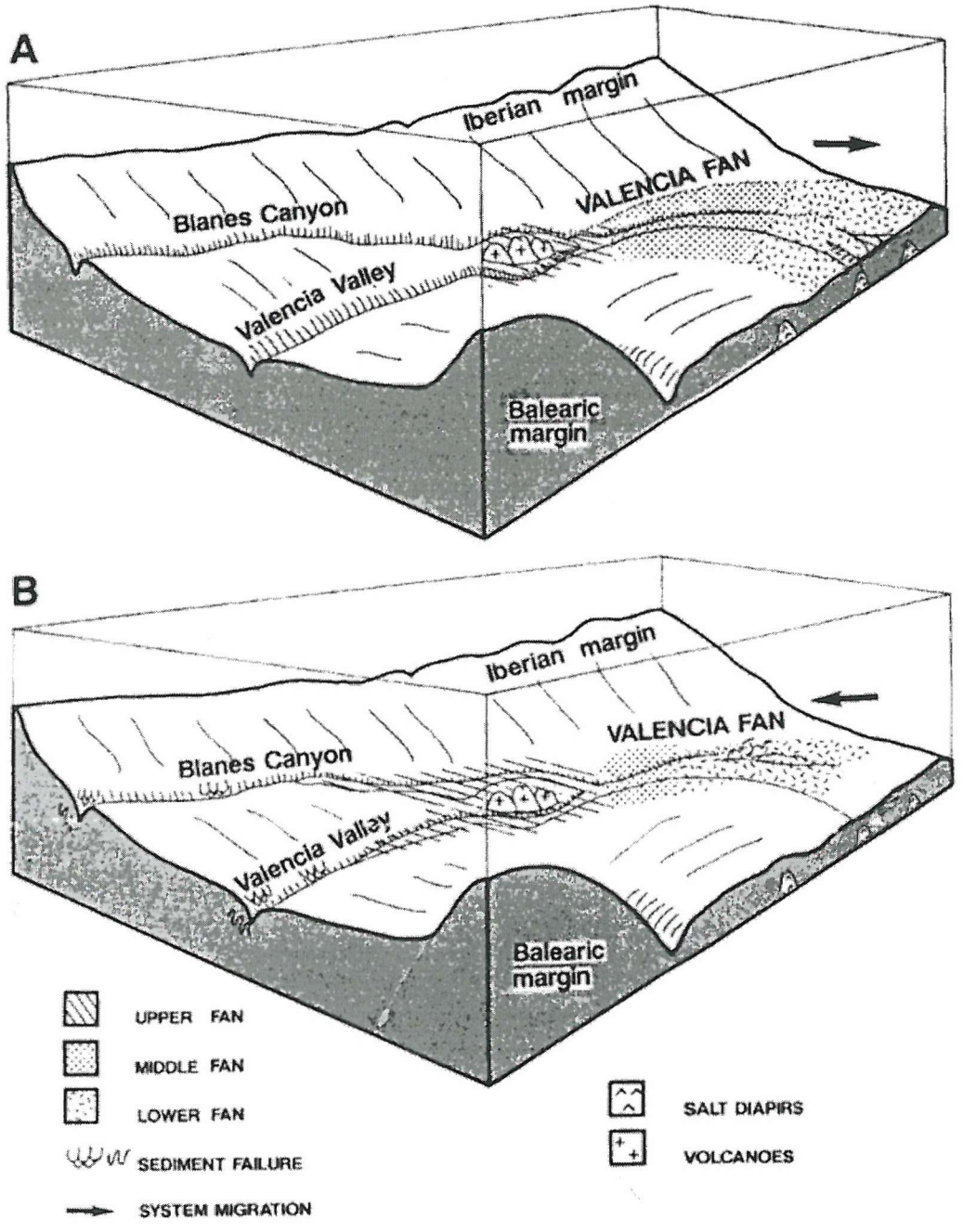

Figure 2.10 Sketch of the Quaternary Valencia fan configuration and fan lobe development during: (A) falling sea-level and periods of low stand, and (B) sea-level rise and periods of high stand (from Palanques et al., 1994). Arrows indicate direction of fan lobe migration.

lowstands, which were partially refilled during the sea-level highstands. Due to the supply of coarse sand and gravel to the fan during both sea-level highs and lows, the profile of the fan is steep concave and the gravel and pebble-floored fan valley acts as a sediment bypass zone (Savoye et al., 1993). The upper and middle fan sections of the

valley are flushed out by coarse-grained turbidity currents, thus causing partitioning of sediments (Savoye et al., 1993), with coarse sediment accumulating on the lower fan valley and basin plains, and mud accumulating as overbank deposits on the high levees.

2.3.4 Corsica and Sardinia

The continental margin off western Corsica and Sardinia is steep (~7° for the submarine slope) and is incised by numerous submarine canyons that end in small, sand-rich submarine fans at the continental slope (Bellaiche et al., 1994a, b; Kenyon et al., 2002). According to Kenyon et al. (2002), the size of the drainage basin, as a proxy for sediment input, appears to be the most important factor governing sediment distribution and overall margin architecture. Terrigenous turbidite sediments that can be found lying on the continental rise of western Corsica originate either from the Provençal margin in the north (through the Var channel) or from Sardinia in the south (Bellaiche et al., 1994a, b).

2.3.5 Menorca and Mallorca

The Mallorca-Menorca shelf to the east of the Balearic Islands has different erosion platforms, presumably related to glacio-eustatic sea-level changes (Acosta et al., 2002). Sediments of the Balearic Island shelves consist mainly of biogenic sand and gravels with a high percentage of carbonates (average $CaCO_3$ content of 77-84%) (Acosta et al., 2002). At present, sediment is being transported from the shelf to the deep basin through the Menorca Canyon, which extends down from the continental shelf off southern Menorca (Acosta et al., 2002). The Menorca fan consists of a variety of turbidite deposits (from thick coarse-grained sand turbidites close to the Menorca valley to distal thin mud turbidites) intercalated with hemipelagic mud sequences (Stanley, 1985).

2.3.6 Algeria

Studies documenting the development of deep-sea fans off northern Algieria are at present virtually non-existent.

2.4 CONTINENTAL SHELVES AND SLOPES

Most continental shelves and slopes in the western Mediterranean Sea are narrow (<20 km), except for the Gulf of Lyons, western Sardinia, the southern Menorca promontory and the Ibiza plateau (Rehault et al., 1984) (Figure 2.5). The depth of the shelf break is variable (between 90 and 130 m) and reaches the greatest depth off western Sardinia (Fanucci et al., 1976; Vanney and Gennesseaux, 1985). The prograding shelves in the Gulf of Lyons and the Catalan margin are bounded by gentle sedimentary slopes (< 4°), whereas other slopes close to mountainous hinterlands (e.g. Provence, Ligurian Alps, Corsica, Algeria, South Balearic Islands) are much steeper (6-10°) (Rehault et al., 1984). The Algerian margin in the southern part of the western Mediterranean has the steepest and narrowest margin (the continental shelf is generally only a few kilometres wide (Leclaire, 1972)) (Figure 2.5). According to Leclaire (1972), the morphology of the Algerian continental margin is distinctive and does not comprise a "normal" continental slope, but instead comprises a set of platforms and ledges with different depths and slopes. The relief of the Algerian shelf is controlled by two main processes: 1) late Cenozoic tectonic activity with varying intensity in different areas, and 2) glacio-eustatic sea-level fluctuations (Leclaire, 1972). Numerous submarine canyons cut the continental slope that bounds the western Mediterranean basin. The Algerian continental slope is also deeply incised by numerous canyons and submarine valleys, however, few of these canyons can be related to adjacent continental river valleys (Leclaire, 1972). Leclaire (1972) suggested that canyons not related to present river valleys might represent submerged traces of Cenozoic coastal drainage systems that were renewed by rivers at the end of the Pliocene or perhaps at the beginning of the middle Quaternary.

2.5 TECTONISM AND VOLCANISM

The western Mediterranean basin forms part of the boundary between the Eurasian and African plates, which follows the North African margin (Udías, 1985). The Eurasian plate has moved to the east and to the south relative to the African plate (Macklin et al., 1995).

Sedimentary deposits forming the slope, rise and basin plains have responded to concurrent extension, strike-slip, or compressive motion that has affected the

underlying basement as well as to salt tectonics (Stanley, 1985). Rehault et al. (1984) reported the occurrence of many inferred NW-SE trending transform faults and major normal faults with varying directions in the western Mediterranean Sea. Recently faulting has occurred in the Camargue coastal plain (Bonnet, 1962), in the deep Mediterranean Basin off the Balearic Islands and in the Ligurian Sea (Rehault et al., 1984).

The main concentration of recent (1910-1979) surface earthquakes in the western Mediterranean is located along the plate boundaries (Udías, 1985). Zones of seismic activity outside this boundary outline secondary plates or have intraplate character (Udías, 1985). Recent (1910-1979) intermediate and deep earthquakes are more or less confined to the central and eastern Mediterranean (Udías, 1985). The Southern Alps-Ligurian basin junction is one of the most active seismic areas among western European countries, with a high number of events (over 70 events since 1920) and with a magnitude up to 6.0 (Larroque et al., 2001).

Several volcanoes have been active in the Mediterranean area during the Quaternary (Narcisi and Vezzoli, 1999), however, most source regions (Italian and Aegean provinces) are located in the central and eastern Mediterranean basin. Between 0.8 and 0.12 Ma, a phase of volcanic activity occurred in the Logudoro district in northwestern Sardinia (Macciotta and Savelli, 1984). In the Valencia Trough, volcanism (represented by calc-alkaline andesitic and silicic pyroclastic rocks, and alkaline basaltic rocks of intraplate type) has been ongoing over the last 15 Ma, with the youngest outcrops dating between 1 and 0.3 Ma (Figure 2.11) (Martí et al., 1992).

2.6 PHYSICAL OCEANOGRAPHY AND CLIMATOLOGY

The Mediterranean Sea is a semi-enclosed basin and its only exchange with the world ocean is through the Strait of Gibraltar. The western basin is separated from the eastern basin by the shallow sill of the Strait of Sicily, which restricts the flow of water between the two basins. The main control on the physical character of the western Mediterranean Sea is the continental climates of Europe and north Africa and their seasonal variability (Kinder and Bryden, 1987; WMCE Consortium, 1989). In the northern part of the western Mediterranean, strong seasonal changes in the sea reflect the seasonal influences of the European climate (La Violette, 1994). For the southern part of the western Mediterranean, smaller seasonal variability could reflect a more

quiescent African climate, although the appearance of small seasonal changes may be due to a lack of adequate data (La Violette, 1994). At present, evaporative losses in the Mediterranean Sea exceed input from precipitation and rivers, which causes a hydrological deficit. In the Gulf of Lyons, high evaporation during winter causes the formation of dense deep water, which flows westward, to finally flow through the Strait of Gibraltar to join Atlantic waters (La Violette, 1994). Relatively fresh Atlantic water (salinity ~35 parts per thousand compared with ~38 parts per thousand for Mediterranean outflow) flows into the Mediterranean through the Strait of Gibraltar to compensate for the evaporative and dense outflow losses (La Violette, 1994).

The present climate in the western Mediterranean is characterised by high global sea level, a relatively dense vegetation cover, relatively high infiltration rates and moderate river discharges (Rose et al., 1999). The glacial western Mediterranean environment, in contrast, was characterised by a low global sea level, open vegetation with large areas of bare ground and unconsolidated sediments, soils affected by high physical stresses and highly peaked river-discharge regimes (Rose et al., 1999). Sea surface temperature (SST) estimates for the Alboran Sea, based on the relative abundances of planktonic foraminifera species, varied considerably between glacial and interglacial periods (González-Donoso et al., 2000). During interglacial times, maximum SSTs were estimated at around 20 to 23°C, whereas glacial maximum SST were much lower, between 10 and 15°C (González-Donoso et al., 2000). Alkenone-based sea surface temperature estimates give similar values of ~ 19°C during the Holocene and 11-13°C during the last glacial maximum (Cacho et al., 2001). Recent research (Rohling et al., 1998; Cacho et al., 1999, 2001; Paterne et al., 1999) has demonstrated that the western Mediterranean basin was sensitive to millennial-centennial climatic and oceanographic variability in the north Atlantic during the last glacial period.

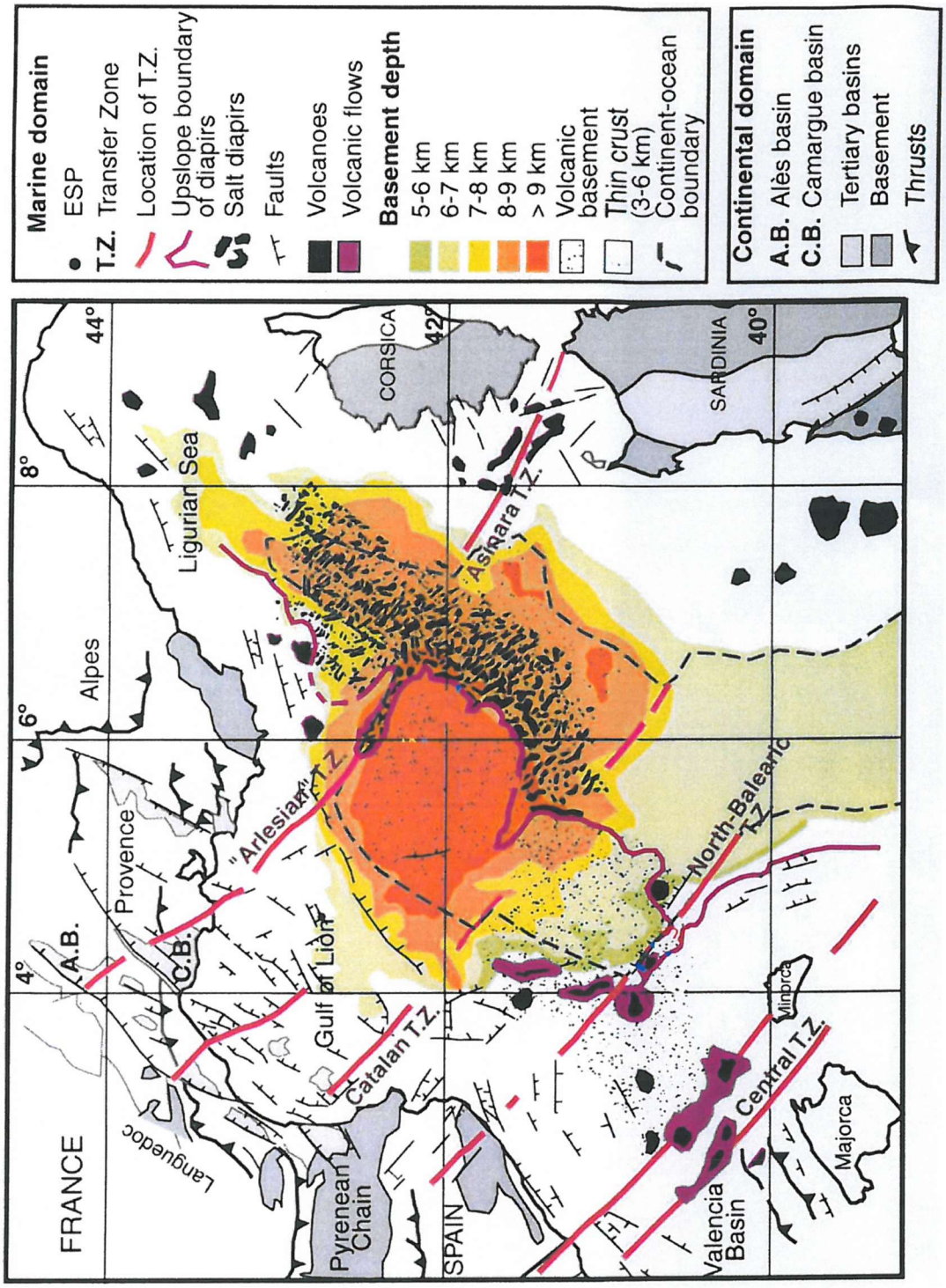

Figure 2.11 Structural map showing the locations of volcanoes and volcanic flows in the northwestern Mediterranean (from Maillard et al., 2003). Also shown are the locations of faults and the upslope boundary of the area of Messinian salt diapirs.

2.7 SEDIMENTATION PROCESSES

Stanley (1985) divided the Mediterranean margins, based on petrological, stratigraphic and seismic information, into erosion dominated areas (i.e. outer shelves, shallow ridges and upper slopes), intermittent erosional and redepositional regimes (slopes) and ponded areas (slope basins and deep, more distal basinal sectors). The main sedimentation types on the BAP are 'normal' hemipelagic background sedimentation and 'episodic' turbidite sedimentation. Gravity flow deposits, such as debris flow and slide deposits, only occur on, or close to the continental margins. Hemipelagic deposits are fine-grained sediments, with both biogenic and terrigenous components (>25%) (Stow et al., 1996). Sedimentation of the biogenic component, which is largely generated in the upper part of the water column through productivity, occurs through vertical settling. The nature and distribution of hemipelagic sediments is determined by productivity, dissolution and masking (i.e. if one component (siliceous material, calcareous oozes, or aeolian red clays) dominates the hemipelagic sediment it may mask the presence of other components) (Stow et al., 1996). The fine-grained terrigenous component in hemipelagic sediments in the western Mediterranean Sea is derived from: 1) fluvial sediment discharger, 2) reworking of shelf sediments or erosion of shorelines, and 3) wind-blown dust from arid and semi-arid areas. According to Guerzoni et al. (1999) Saharan dust input to the open western Mediterranean Sea constitutes more than 80% (~4×10^6 t/yr) of the total terrigenous (riverine + aeolian) flux.

Turbidity currents and their deposits have already been discussed in detail in Chapter 1. Sedimentary sequences from piston cores from the Balearic (western Mediterranean Sea) and Herodotus (eastern Mediterranean Sea) Abyssal Plains are dominated by turbidite muds (Rothwell et al., 2000). Rothwell et al. (2000) identified two turbidite megabeds on each plain, that were emplaced during the last sea level low stand at the height of the glacial maximum. In the eastern Mediterranean, turbidite sedimentation has been controlled by a combination of regional climate change and eustatic sea-level fluctuations (Reeder et al., 2002).

CHAPTER 3 - WESTERN MEDITERRANEAN OXYGEN AND CARBON ISOTOPE STRATIGRAPHY

3.1 INTRODUCTION

Long-term quasi-periodic changes in the Earth's orbit (eccentricity, obliquity and precession) have driven global climatic change. The driving force in global climate is the seasonal and latitudinal distribution of solar insolation (Berger, 1988). Waxing and waning of continental ice sheets during the Quaternary has been regulated by insolation variations resulting from changes in the Earth's orbit (Berger, 1988). Oxygen isotope ($\delta^{18}O$) signals from planktonic and benthic foraminifera in deep-sea cores predominantly reflect fluctuations in global ice volume and hence of global sea level, although $\delta^{18}O$ also reflects temperature and large-scale salinity variations (Shackleton and Opdyke, 1973). Numerous records from the world oceans have been stacked to form a global curve for comparison with models of astronomically forced ice volume fluctuations and to provide a detailed $\delta^{18}O$ age control (Imbrie et al., 1984; 1984; Prell et al., 1986; Martinson et al., 1987; Imbrie et al., 1992). As a result, oxygen isotope stratigraphy is now a standard technique for detailed correlation of Late Pleistocene deep-sea sediments (Prell et al., 1986). The chronology of $\delta^{18}O$ records is tied to the geomagnetic polarity time scale and can be fine-tuned using the Milankovitch theory (Shackleton et al., 1990).

For this study, four cores from the Balearic Abyssal Plain were studied to determine the timing and magnitude of turbidite sedimentation in the basin. Turbidite beds occur intercalated with thinner hemipelagic intervals within the piston cores (see Chapter 4). These hemipelagic intervals are used to form a tight stratigraphy in Chapter 5. This stratigraphy was initially based on biostratigraphy (using the nannofossil zonation scheme of Weaver, 1983), AMS radiocarbon dates and oxygen isotope stratigraphy. In order to construct a stratigraphic framework for the four cores, based on oxygen isotope stratigraphy, a reference core was analysed from a location where disturbance related to downslope transport is unlikely (i.e. a bathymetric high). Most of the methods and results discussed below, relating to the analysis of the oxygen and carbon isotopes, have been published in Dinarès-Turell et al. (2003), with B.A.A. Hoogakker as the second author (Appendix 3.1).

3.2 MATERIALS AND METHODS

Long piston core LC07 (located at 38°08.72'N, 10°04.73'E, water depth 488 m, length 23.66 m) was collected during Marion Dufresne Cruise 81 in 1995 (as part of the EU-funded MAST II PALAEOFLUX program) from a location north of the Skerki Channel on the western side of the Sicily Strait (Figure 3.1). The sediment column of core LC07 generally appears visually homogeneous and contains grey to olive grey foraminifer-rich mud and nannofossil ooze that includes an interval of foraminifer-rich sand from 15.41 to 16.08 m below sea floor (mbsf) (Figure 3.2).

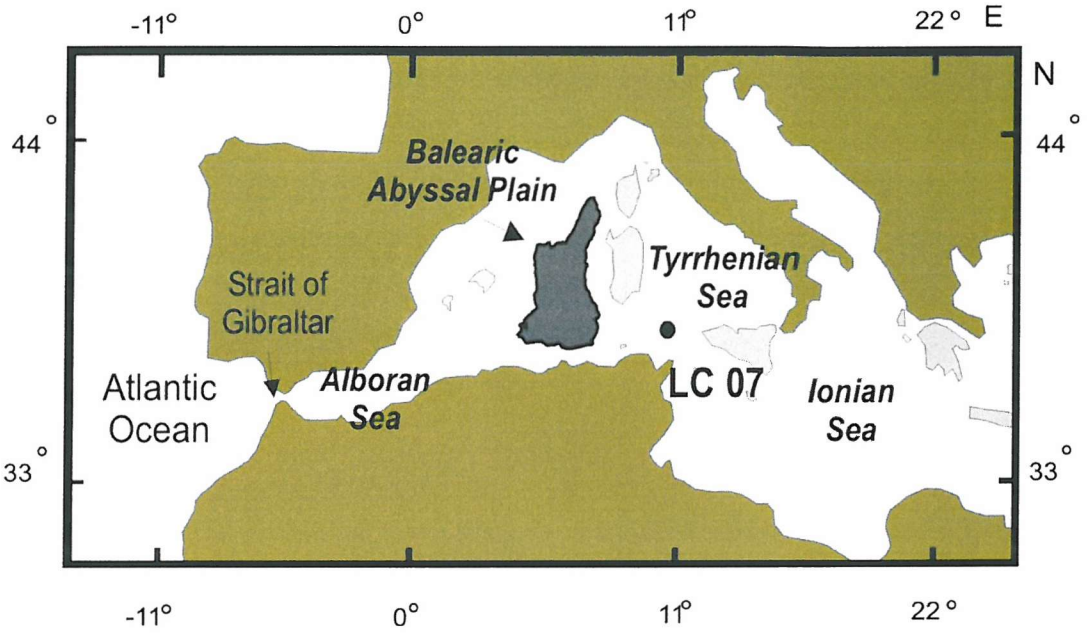

Figure 3.1 Location of core LC07 west of the Sicily Strait in the western Mediterranean Sea.

Two planktonic foraminifera species, *Neogloboquadrina pachyderma* (right coiling or dextral variety) and *Globigerinoides ruber* (white variety) were picked by hand for oxygen and carbon isotope analysis. The core was sampled at 5-cm intervals, except for the sandy interval between 15.4 and 16.08 mbsf. Fifteen to twenty specimens of *N. pachyderma* and 10 to 15 specimens of *G. ruber* were hand-picked from the 250-400 μm size fraction for analysis. *N. pachyderma* occurs almost continuously throughout core LC07, whereas *G. ruber* was less abundant and occasionally absent in certain intervals. Prior to isotopic analysis, specimens were cleaned with methanol and were dried overnight in an oven at 50°C. Oxygen and carbon isotope ratios were

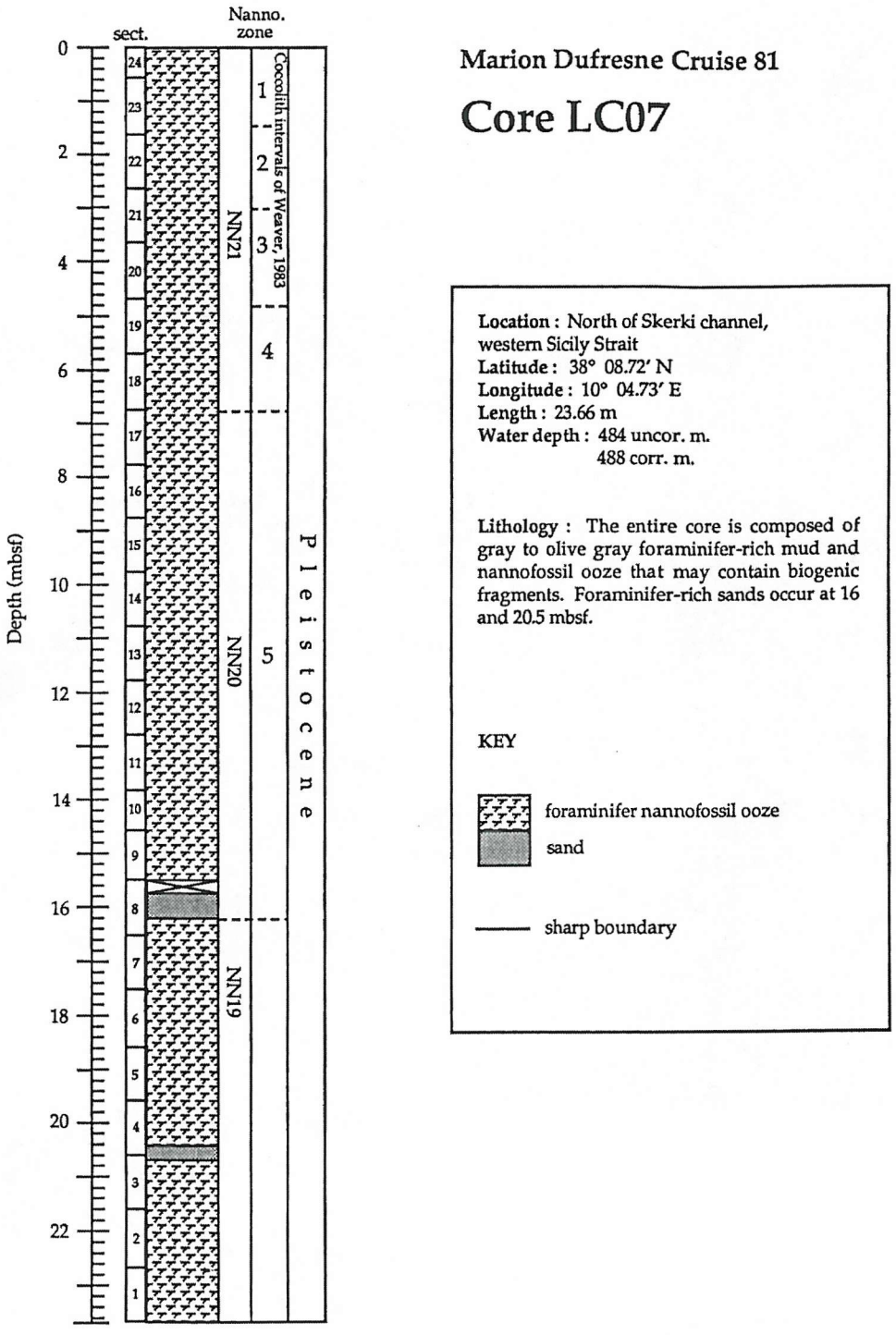

Figure 3.2 Long piston core log and sedimentological description of LC07 (from Cruise Report of Marion Dufresne Cruise 81, Rothwell et al., 1995).

measured in a stable isotope ratio mass spectrometer (model Europa GEO 20 20, manufactured by GV Instruments), with individual acid bath carbonate preparation lines. Analytical precision of powdered carbonate standards was ±0.06% for $\delta^{18}O$ and $\delta^{13}C$. Isotope data in LC07 are expressed in per mil (‰) relative to the Vienna Pee Dee Belemnite standard (V-PDB).

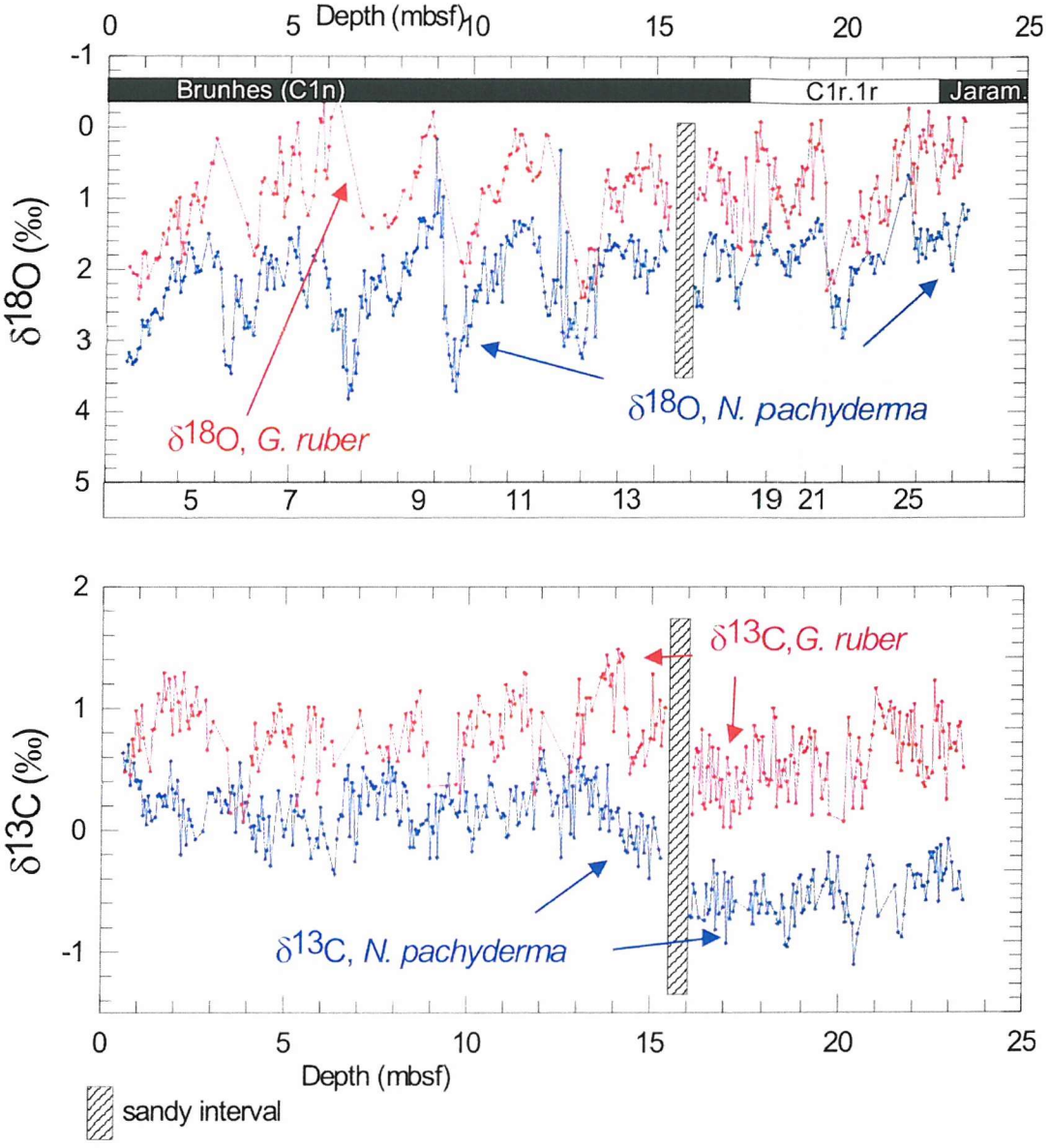

Figure 3.3 Oxygen and carbon isotope data for LC07 plotted against down-core depth (metres below sea floor). Palaeomagnetic epochs, as determined by Dinarès-Turell et al. (2003), are also shown. The $\delta^{18}O$ records are divided into the standard $\delta^{18}O$ stages (MIS) following the nomenclature of Emiliani (1955) and Shackleton and Opdyke (1973). Odd MIS (or interglacial stages) are numbered at the bottom of the upper subfigure.

A total of 388 samples was analysed for *N. pachyderma* and 287 samples for *G.ruber*. The derived $\delta^{18}O$ curve was initially divided into the standard $\delta^{18}O$ stages following the nomenclature of Emiliani (1955) and Shackleton and Opdyke (1973), where even numbered stages represent glacial intervals with heavier oxygen isotope values, and odd numbered stages represent interglacial intervals (Figure 3.3). The Marine Isotope Stages (MIS) were then further subdivided into substages and events based on the nomenclature of Imbrie et al. (1984) and Prell et al. (1986).

3.3 AGE MODEL

Fourteen alternating glacial and interglacial stages were recognised in LC07 (Figure 3.3). These correlate well with the SPECMAP curve (Dinarès-Turell et al., 2003). Ages for $\delta^{18}O$ stages and events (Table 3.1) are derived from Imbrie et al. (1984) until $\delta^{18}O$ event 15.1 and then from Shackleton et al. (1990), Bassinot et al., (1994) and Chen et al. (1995) for older stages. The Matuyama/Brunhes (M/B) boundary at 17.8 mbsf and the Upper Jaramillo (UJ) reversal at 22.4 mbsf coincide with MIS 19 and MIS 27, respectively (Table 3.1). The astronomically calibrated ages of 0.778 Ma (M/B) and 0.990 Ma (UJ) are assigned to these reversal boundaries (Shackleton et al., 1990; Tauxe et al., 1996). Because of the occurrence of a sandy interval between 15.4 and 16.08 mbsf, the core was divided into two parts for converting depth into age. The results of the two linear interpolations between age control points (Table 3.1) indicate nearly linear sedimentation rates (Dinarès-Turell et al., 2003). The sand interval is interpreted to represent a winnowed lag deposit, and, according to our age model, appears to represent a condensed section spanning part of OIS 15 and 16 and accounts for a maximum time interval of ~140 kyr.

3.4 CARBON ISOTOPES IN LC07

Carbon isotope records from LC07 based on stable isotope analysis of *G. ruber* and *N. pachyderma* show two conspicuous long-term fluctuations between 1.00 and 0.50 and between 0.50 and 0.10 Ma (Figure 3.4). Between 1.00 and 0.90 Ma carbon isotopes dropped ~0.5‰ in LC07, followed by a ~1.00‰ increase between 0.90 and 0.50 Ma. The second fluctuation started with a drop in carbon isotope values of ~0.50% between 0.50 and 0.25 Ma, followed by a ~0.70‰ increase between 0.25 and 0.10 Ma.

As part of this study other data from cores from Ocean Drilling Program cores were examined and the carbon isotope shifts were observed to have occurred in many other published records from all major basins, including the North (e.g. at ODP sites 552, 607, 502, 929, and 925) and South (e.g. at ODP site 704) Atlantic Ocean, the Indian Ocean (e.g. at ODP site 758) and the Pacific Ocean (e.g. at ODP sites 806, 847 and

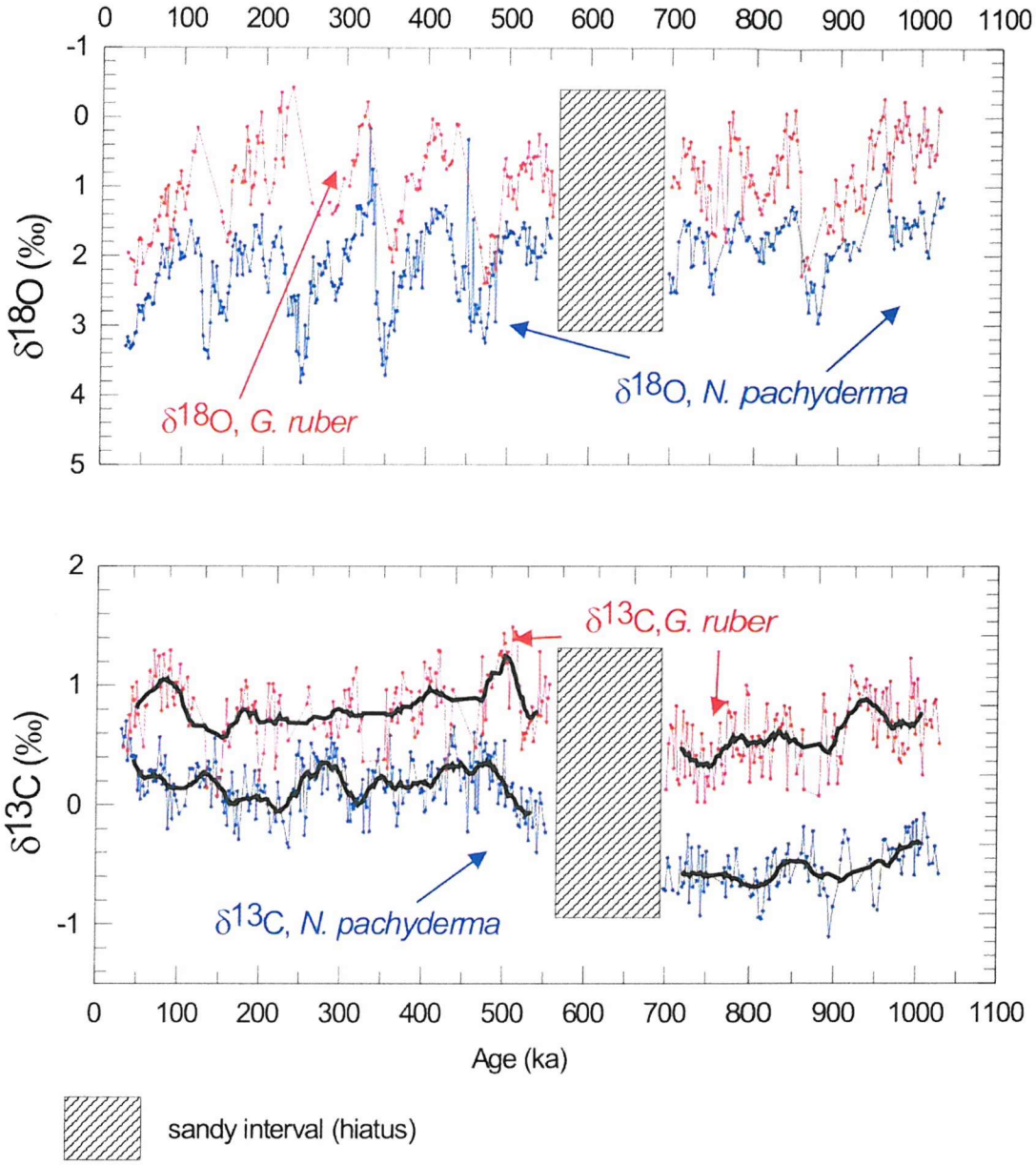

Figure 3.4 Oxygen and carbon isotope data for LC07 plotted against age (ka). A 15 point running average (thick black line) illustrates the long term fluctuations in carbon isotopic values.

849). Furthermore, these long-term fluctuations in carbon isotopic values occur in both surface-dwelling (planktonic) and deep-sea (benthic) foraminifera, which indicates the

global nature of these fluctuations. In section 3.5 these carbon isotope shifts are discussed in more detail and it is proposed that the initiation of these shifts to lower $\delta^{13}C$ was caused by better ventilated bottom waters between 1.00 and 0.90 and between 0.50 and 0.25 Ma, which resulted in decreases in global mean organic and inorganic carbon burial fluxes. Both periods coincided with insolation and eccentricity minima (Berger, 1978), at which time the effect of seasons may have been less intense and the development of monsoons was weakened (Rossignol-Strick, 1983). In the Mediterranean, strong monsoons create conditions whereby sapropel formation and preservation can occur.

Table 3.1 Depth position of oxygen isotope stages and events in LC07 and their respective ages (from Dinarès-Turell et al., 2003).

Oxygen isotope stage/event	Depth (mbsf)	Age (ka)	Oxygen isotope stage/event	Depth (mbsf)	Age (ka)
2.2	0.73	20	9.3	8.93	328
3.1	1.10	28	10.2	9.58	340
3.3	1.43	53	11.1	10.33	368
4.2	1.53	64	11.2	10.48	375
5.1	2.18	80	12.1	12.38	426
5.2	2.43	86	12.2	12.53	431
5.3	2.73	100	12.3	12.3	451
5.4	2.93	108	12.4	13.03	471
5.5	3.10	122	15.1	15.13	572
6.3	3.73	146	17	16.48	695
6.4	3.93	155	18	17.28	755
7.3	5.23	214	19	17.93	783
7.4	5.43	228	20	18.43	798
7.5	6.13	237	21	19.28	860
8.2	6.18	249	22	19.98	874
8.3	6.33	257	23	20.43	903
8.4	6.63	269	25	21.73	951
8.5	7.55	287	26	22.23	964
8.6	7.83	299	27	22.40	990
9.1	8.53	310	28	22.98	1006
9.2	8.73	320			

3.5 Long-term fluctuations in the global carbon cycle during the Pleistocene

Hoogakker, B.A.A., Rohling, E.J., Palmer, M.R., Rothwell, R.G. and Dinarès-Turell, J.[#]

Southampton Oceanography Centre, Empress Dock, Southampton SO14 3ZH, U.K.

[#]Istituto Nazionale di Geofisica e Vulcanologia, Via di Vigna Murata, 605, 00143 Rome, Italy

ABSTRACT

Pleistocene stable carbon isotope ($\delta^{13}C$) records from both surface and deep waters in all major ocean basins show two distinct carbon isotope fluctuations since 1 Ma. The first was characterised by a decrease in $\delta^{13}C$ values of 0.27‰ between 1.00 and 0.90 Ma, followed by an increase of 0.49‰ between 0.90 and 0.50 Ma. The second fluctuation started with a decrease of 0.30‰ between 0.50 and 0.25 Ma, followed by an increase of 0.25‰ between 0.25 and 0.10 Ma. Here, we evaluate evidence and existing hypotheses for these global Pleistocene $\delta^{13}C$ fluctuations and present an interpretation, where the fluctuations resulted from concomitant changes in the burial fluxes of organic and inorganic carbon due to changes in bottom water ventilation. Periods of decreasing $\delta^{13}C$ values are characterised by low preservation of organic matter and increased calcium carbonate dissolution. Our model indicates that to satisfy the long-term 'stability' of the Pleistocene lysocline (Rea and Leinen, 1985), the ratio between the amounts of change in the organic and inorganic carbon burial fluxes must have been tightly constrained to a 1:1 ratio. It is then apparent that the mid-Pleistocene climate transition, which, apart from the glacial cycles, represents the most fundamental change in the Pleistocene climate (Raymo et al., 1997), was not associated with a fundamental change in pCO_2. Our model allows a maximum variability of only 15 ppmv over the fluctuation between 1.0 and 0.5 Ma. In contrast, pCO_2 changes associated with glacial/interglacial cycles are much higher (~100 ppmv).

3.5.1 Introduction

Systematic oceanic carbon isotope ($\delta^{13}C$) shifts are commonly used indicators of change in the global carbon cycle, with research focussing on such shifts at the K/T boundary (Kump, 1991), in the Miocene (Vincent and Berger, 1985; Delaney and Boyle, 1987), and in the late Paleocene (Norris and Röhl, 1999). In this study we discuss two Pleistocene $\delta^{13}C$ fluctuations in records from both surface-dwelling (planktonic) and deep-sea (benthic) foraminifera from all major ocean basins (Table 3.2, Figure 3.5). This study is concerned with sustained long-term $\delta^{13}C$ shifts at timescales that exceed glacial/interglacial variability. In essence, the fluctuations considered here are background fluctuations that underlie the superimposed $\delta^{13}C$ variability associated with the 41 to 100-kyr glacial cycles.

Table 3.2 Location of the records and the analysed foraminiferal species used in this study, as well as similar details of eight supplementary (supporting) records (Shackleton and Hall, 1984; Ruddiman et al., 1989; Hodell and Venz, 1992; Bickert et al., 1993; Farrell et al., 1995; Bassinot et al., 1997; deMenocal et al., 1997).

Benthic records used	Species (Benthic)	Water depth (m)	Latitude/ Longitude	Planktonic records used	Species (Planktonic)	Water depth (m)	Latitude/ Longitude
Site 502, ODP Leg 68 (Caribbean)	*Cibicidoides wuellerstorfi*	3051	11°2'N 79°2'W	Site 806, ODP Leg 130 (W. Pacific)	*Globigerinoides sacculifer, Pulleniatina*	2521	0°19'N 159°22'E
Site 849, ODP Leg 138 (E. Pacific)	Mainly *Cibicidoides wuellerstorfi*	3837	0°11'N 110°31'W	Site 758, ODP Leg 121 (Indian)	*Globigerinoides sacculifer*	2924	5°23'N 90°21'E
Site 758, ODP Leg 121 (Indian)	*Cibicidoides wuellerstorfi*	2924	5°23'N 90°21'E				
Supplementary benthic records				**Supplementary planktonic records**			
Site 552, ODP Leg 81 (N. Atlantic)	*Cibicidoides wuellerstorfi*	2301	56°0'N 23°1'W	Site 847, ODP Leg 138 (E. Pacific)	*Neogloboquadrina dutertrei, Globigerinoides sacculifer*	3334	0°12'N 95°19'W
Site 929, ODP Leg 154 (N. Atlantic)	*Cibicidoides wuellerstorfi*	4358	5°59'N 43°37'W	Site 704, ODP Leg 114 (S. Atlantic)	*Neogloboquadrina pachyderma (s)*	2532	46°53'S 7°25'E
Site 607, ODP Leg 94 (Atlantic)	*Cibicidoides wuellerstorfi*	3427	41°0'N 32°57'W	Site 925, ODP Leg 154 (N. Atlantic)	*Globigerinoides ruber*	3040	4°12'N 43°29'W
Site 704, ODP Leg 114 (S. Atlantic)	*Cibicidoides wuellerstorfi*	2532	46°53'S 7°25'E	LC07, MD 81 (Mediterranean) (this Chapter)	*Neogloboquadrina pachyderma (d), Globigerinoides ruber*	480	38°09'N 10°5'E
Site 806, ODP Leg 130 (W. Pacific)	*Cibicidoides wuellerstorfi*	2521	0°19'N 159°22' E				

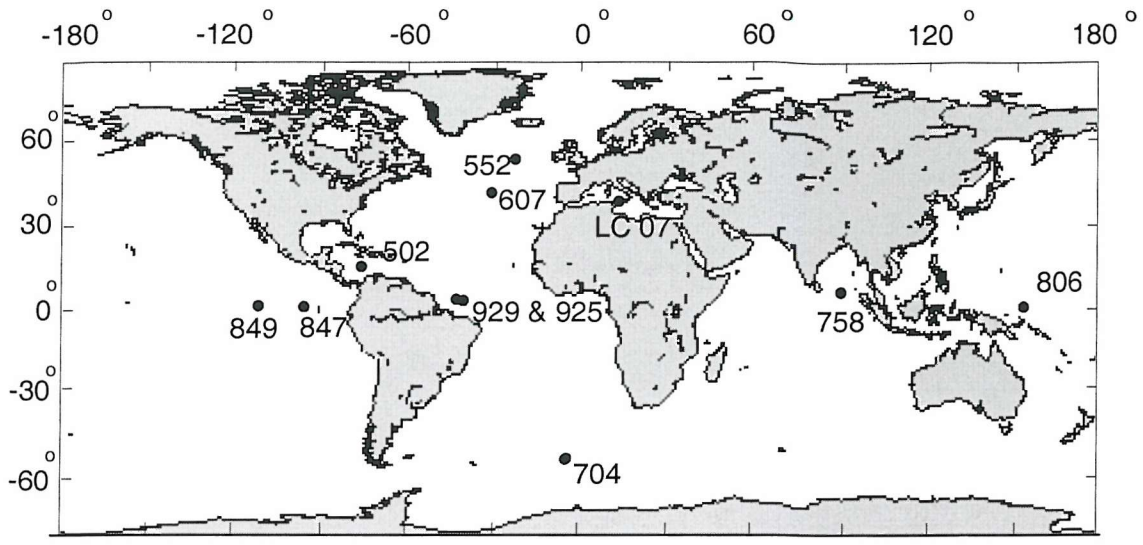

Figure 3.5 Locations of published records where the two observed Pleistocene carbon isotope fluctuations can be identified. See Table 3.2 for further details.

In order to assess the Pleistocene $\delta^{13}C$ records, the best planktonic (ODP Site 758 and 806) and benthic (ODP Site 502, 758 and 849) records are summarised in Figures 3.6A and B. These $\delta^{13}C$ records were chosen on the basis of the reliability of the respective age models and continuous coverage (0–1.5 Ma) throughout the Pleistocene. Other available records were not used because they do not fulfil both criteria.

During the last 1.5 Ma, the planktonic and benthic carbon isotope records show similar long-term trends (i.e. trends exceeding variations on times scales up to and including glacial/interglacial time scales) (Figures 3.6A, B). All three benthic $\delta^{13}C$ plots in Figure 3.6B are based on the same epibenthic foraminiferal species (*Cibicidoides wuellerstorfi*), thus avoiding possible anomalies associated with infaunal habitats. $\delta^{13}C$ differences between the three benthic sites are related to water-mass aging and mixing (Figure 3.6B). Today, the $\delta^{13}C$ value of freshly formed North Atlantic Deep Water is ~1‰, decreasing to ~0‰ en route to the North Pacific, through mixing with Southern Ocean Water and continued remineralisation of organic matter (Kroopnick, 1985). Despite these relative offsets between records from different basins, they all show the same systematic Pleistocene long-term $\delta^{13}C$ variability, thus confirming the global nature of these fluctuations (Figure 3.6B).

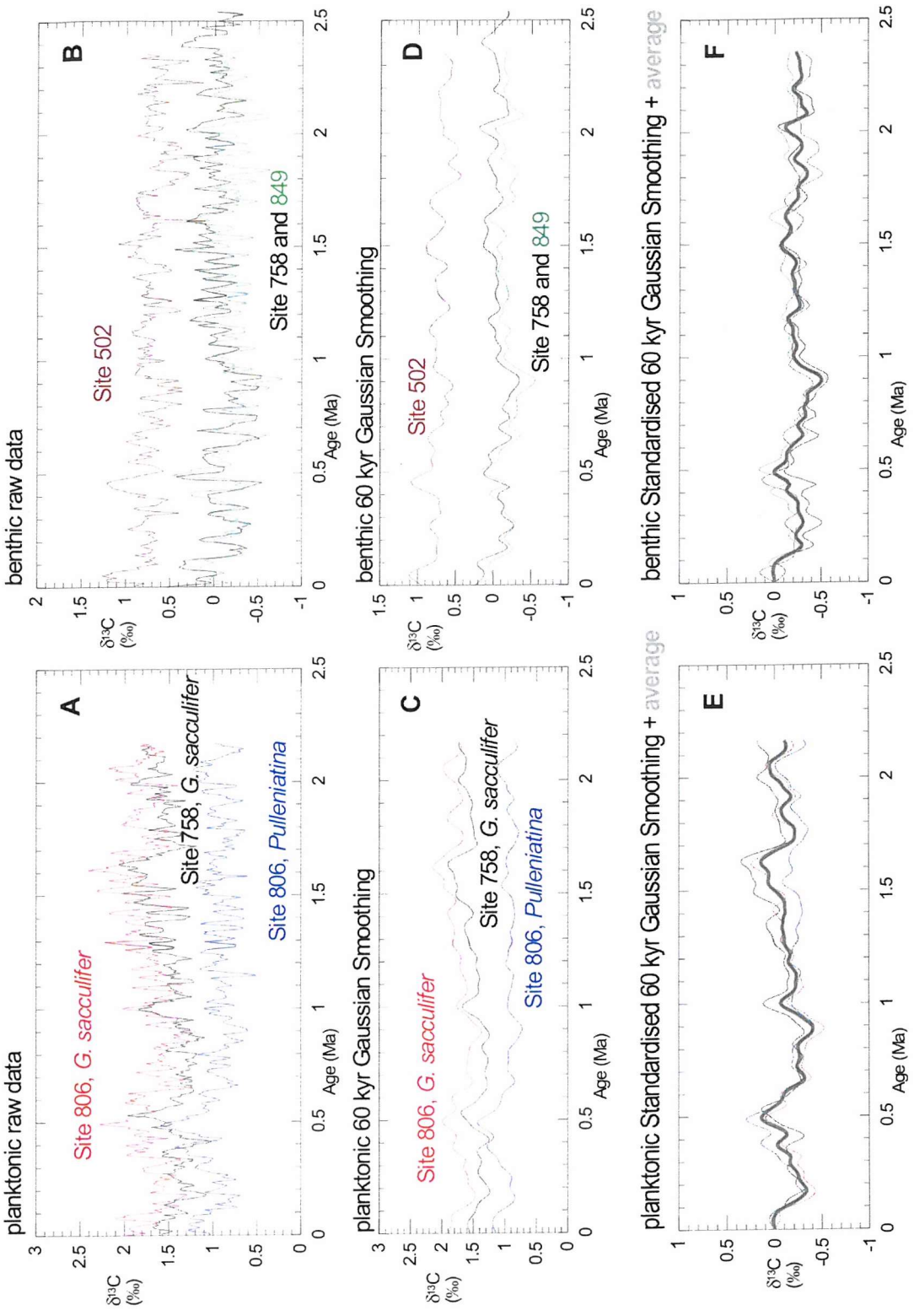
planktonic raw data
A
Site 806, G. sacculifer
Site 758, G. sacculifer
Site 806, Pulleniatina
δ13C (‰)
Age (Ma)
benthic raw data
B
Site 502
Site 758 and 849
planktonic 60 kyr Gaussian Smoothing
C
Site 806, G. sacculifer
Site 758, G. sacculifer
Site 806, Pulleniatina
benthic 60 kyr Gaussian Smoothing
D
Site 502
Site 758 and 849
planktonic Standardised 60 kyr Gaussian Smoothing + average
E
benthic Standardised 60 kyr Gaussian Smoothing + average
F

Figure 3.6

Figure 3.6 Stable carbon isotope records: (a) planktonic and (b) benthic foraminifera carbon isotope records, where planktonic records represent the Indian Ocean site 758 (Farrell and Janecek, 1991) and Pacific Ocean Site 806 (Schmidt et al., 1993), while benthic $\delta^{13}C$ records are from the Caribbean Sea Site 502 (Oppo et al., 1995), the Indian Ocean Site 758 (Chen et al., 1995) and the Pacific Ocean site 849 (Mix et al., 1995), (c, d) stable carbon isotope records represented by a 60 kyr Gaussian filter smoothing for the same planktonic and benthic foraminifera records, (e, f) standardised stable carbon isotope records for planktonic and benthic foraminifera records (thin black line) and averaged standardised stable carbon isotope records for planktonic and benthic foraminifera.

To elucidate the global trends, we constructed standardised smoothed records (Figures 3.6C, D). The individual records are first smoothed to eliminate variations on a glacial/interglacial or shorter time scale (Figures 3.6C, D). The filtered records were then standardised to a modern value of zero (Figures 3.6E, F). The very high level of agreement between the various standardised records again emphasises the systematic nature of the Pleistocene long-term $\delta^{13}C$ fluctuations, which affected both benthic and planktonic records in all major ocean basins (Figures 3.6E, F). Finally, a mean value was calculated for the records in 1000 yr increments giving the standardised 'mean' records presented in Figure 3.6E and F.

Planktonic $\delta^{13}C$ records reflect conditions in a thin surface layer with a high potential variability on regional scales, while benthic $\delta^{13}C$ records are more indicative of long-term stabilised properties in the oceanic deep-water reservoir that forms >75% of the global ocean volume. We therefore concentrate on the values of the trends given by the averaged, standardised benthic record in Figure 3.6F. This average ('stacked') benthic record was subsequently shifted so that its present-day value matches the mean $\delta^{13}C$ value for total carbonate in recent deep-sea sediments of 0.38‰ (Shackleton, 1987a) (Figure 3.7). This shift is needed because our calculations require not

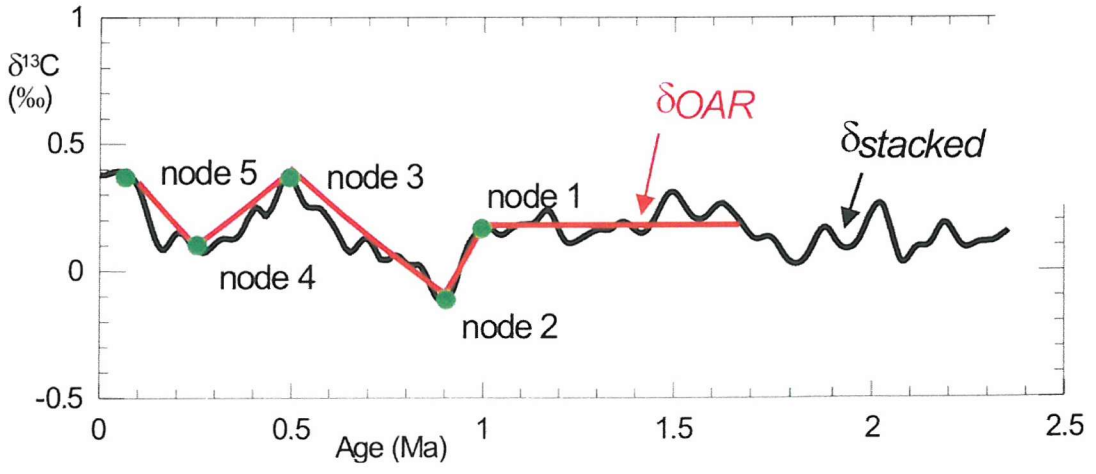

Figure 3.7 Stacked benthic carbon isotope record ($\delta_{stacked}$) plotted together with calculated carbon isotope values (δ_{OAR}). See text for further details.

only relative but also absolute values. The basis for shifting the stacked benthic $\delta^{13}C$ records is supported by the fact that the actual mean core-top value for the records used is nearly identical to the mean value for modern deep-sea sediments (~0.38‰) (Shackleton, 1987a).

Five 'nodes', marked in Figure 3.7, identify major changes in the $\delta^{13}C$ values within the stacked benthic record. The first $\delta^{13}C$ fluctuation, termed the Mid-Pleistocene $\delta^{13}C$ Fluctuation (MPCF), started with a drop in $\delta^{13}C$ of 0.27‰ between 1.00 and 0.90 Ma (nodes 1 and 2), followed by an increase of 0.49‰ between 0.90 and 0.50 Ma (nodes 2 and 3) (Figure 3.7). The second fluctuation, termed the Late Pleistocene $\delta^{13}C$ Fluctuation (LPCF), started with a drop of 0.30‰ between 0.50 and 0.25 Ma (nodes 3 and 4), followed by an increase of 0.25‰ from 0.25 to 0.10 Ma (nodes 4 and 5). The MPCF is approximately coincident with the mid-Pleistocene Climate Transition (MPT), which is marked by an increase in mean global ice volume and a shift from 41-kyr to 100-kyr ice-age cycles (Raymo et al., 1997). No such fundamental climate shift is associated with the LPCF.

3.5.2 Previous explanations

To date, only the MPCF has received any attention (Raymo et al., 1997), while the LPCF has gone unnoticed. Initial explanations of the 0.27‰ drop in $\delta^{13}C$ values at the start of the MPCF maintained that a drop in the mean ocean $\delta^{13}C$ was due to a one-time net addition of ^{12}C-enriched carbon to the world ocean (Raymo et al., 1997). This could have been caused by: (1) an increase in continental weathering and runoff; (2) an addition of organic matter to the ocean/atmosphere carbon reservoir from continental shelves; or (3) a permanent widespread ecosystem change to lower C-mass biomes due to a global increase in aridity after 0.9 Ma (Raymo et al., 1997).

The first two options can be discarded as such processes would also enhance ocean nutrient concentrations and thus increase vertical $\delta^{13}C$ gradients and the spatial $\delta^{13}C$ gradient between the Atlantic and Pacific Oceans (Boyle, 1986), whereas records suggest that these gradients remained relatively constant (Figure 3.6) (Raymo et al., 1997). Moreover, one would expect an increase in the amount of organic carbon weathering to be reflected in the osmium isotope composition of seawater, as osmium isotopes are sensitive to the ratio of organic carbon weathering to total weathering (Ravizza and Esser, 1993; Peucker-Ehrenbrink and Hannigan, 2000; Peucker-

Ehrenbrink and Ravizza, 2000). However, over the periods considered here no significant fluctuations are apparent (Ravizza, 1993). The third suggestion, that the initiation of the MPCF was driven by global aridification after 0.90 Ma (Raymo et al., 1997), is not consistent with our observation that the onset of the MPCF occurred earlier at 1.0 Ma (Figure 3.7). Hence, alternative hypotheses need to be considered for the observed Pleistocene $\delta^{13}C$ shifts.

3.5.3 Method

Here, we present a simple box model to assess the impact on global $\delta^{13}C$ of changes in the global carbon cycle on global $\delta^{13}C$ over Pleistocene time-scales (Figure 3.8). This model does not impose a steady-state solution on the size of the ocean/atmosphere carbon reservoir (V_{OAR}) and there is no partitioning of carbon between shallow and deep waters. The latter process is relevant only on ocean mixing time scales of 10^3 years, whereas the model concerns effects over time scales of $>10^4$ years. Within this system, the $\delta^{13}C$ of the ocean/atmosphere reservoir (δ_{OAR}) at time t depends on: (a) the initial value of δ_{OAR}, as indicated by $\delta_{OAR(i-1)}$ where i represents the 'nodes', so that between nodes 1 and 2 the initial value of δ_{OAR} is that observed at node 1 (Figure 3.7); (b) the amount of carbon in the ocean/atmosphere reservoir, V_{OAR}; (c) the flux of carbon into the *OAR* via weathering of mainly continental organic and inorganic carbon, F_{riv}; (d) the isotopic ratio of this riverine carbon flux, δ_{riv}; (e) the organic and inorganic oceanic carbon burial fluxes, F_{org} and F_{ino}; and (f) their isotopic ratios, δ_{org} and δ_{ino}. By varying one parameter at a time, the model is used to evaluate the observed changes in δ_{OAR} for the following six scenarios.

1. Changes in δ_{OAR} reflect changes in the input of carbon through rivers (F_{riv}). Changes in F_{riv} could result from changes in the weathering rate of organic and inorganic carbon in soils or rocks, or changes in organic and inorganic carbon content of the source rock being weathered.
2. δ_{OAR} changes are driven by changes in the carbon isotopic ratio of the river input (δ_{riv}). These changes could be caused by changes in the relative weathering rates of organic and inorganic carbon.

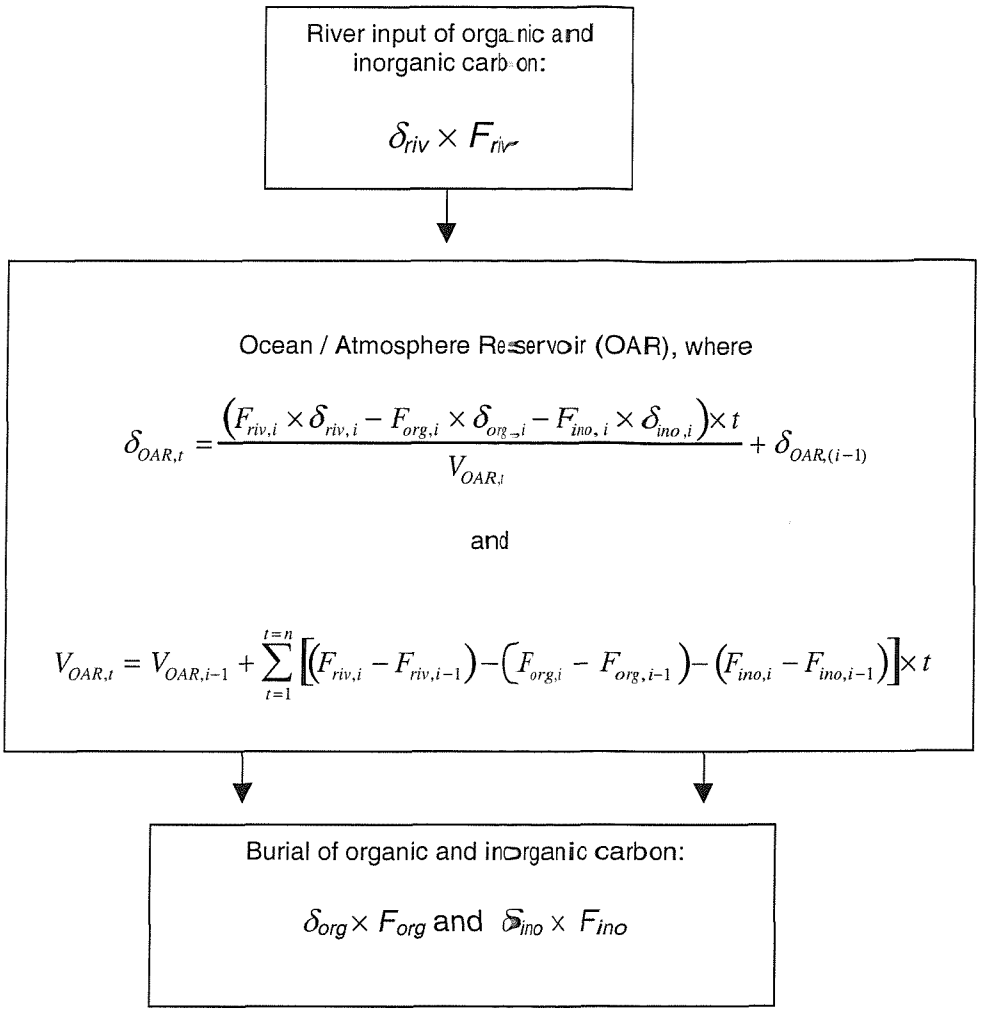

Figure 3.8 Basic box model to assess the impact of changes in the carbon cycle on global $\delta^{13}C$ over time scales > 10^4 years. F_{riv} represents the flux of carbon to the ocean/atmosphere reservoir (*OAR*) in g C yr^{-1}, from weathering of organic and inorganic carbon, and δ_{riv} represents its isotopic composition (in ‰). V_{OAR} is the volume of carbon present in the ocean/atmosphere reservoir (in g C) and δ_{OAR} its associated isotopic composition (in ‰). F_{org} and δ_{org} are the organic carbon burial flux (in g C yr^{-1}) and its isotopic ratio (in ‰). F_{ino} and δ_{ino} are the inorganic carbon burial flux (in g C yr^{-1}) and its isotope ratio (in ‰). Methane input is not considered in this model, because methane-related $\delta^{13}C$ changes observed in the past occur abruptly and within a few thousand years (Norris and Röhl, 1999). Exchange of carbon between the oceanic crust and seawater by hydrothermal activity and low temperature weathering can be considered constant on the time-scales considered in this study.

3. Changes in the δ_{OAR} reflect changes in the $\delta^{13}C$ of organic carbon buried (δ_{org}). This could be caused by changes in the $\delta^{13}C$ of terrestrial organic carbon.
4. The changes in δ_{OAR} are caused by changes in the isotopic composition of inorganic carbon buried (δ_{ino}). Possible causes for such changes could include changes in the productivity in surface waters.

5. Fluctuations in δ_{OAR} relate to variations in the organic and inorganic carbon burial fluxes (F_{org} and F_{ino}), while the changes in the organic and inorganic carbon burial fluxes follow the approximate global ratio between F_{org} and F_{ino} of 1:4 (Delaney and Boyle, 1988).
6. δ_{OAR} fluctuations are caused by variations in the organic and inorganic carbon burial fluxes (F_{org} and F_{ino}), with changes in organic and inorganic carbon burial fluxes occurring at a 1:1 ratio.

Changes in the carbon burial fluxes (scenario 5 and 6) would be likely results of changes in bottom water ventilation, and scenario 6, with ΔF_{org}:ΔF_{ino} = 1:1, in this context implies a strict adherence to the stoichiometry of the schematic equations:

$CH_2O + O_2 \Leftrightarrow CO_2 + H_2O$ and $CaCO_3 + CO_2 + H_2O \Leftrightarrow Ca^{++} + 2HCO_3^-$

Scenarios 1, 5 and 6 result in changes in the amount of carbon in the ocean-atmosphere reservoir (V_{OAR}), and would thus cause a change in ocean alkalinity and the depth of the calcite lysocline. We used the program CO2SYS, developed by Wanninkhof et al. (1999), to calculate the changes in the calcite lysocline depth resulting from the implied changes in the amount of carbon stored in the ocean-atmosphere reservoir (V_{OAR}). The present-day value for V_{OAR} is 3.85 x10^{19} g C, while the average dissolved inorganic carbon concentration in the ocean (*TC*) is 2272 μmol/kg and total alkalinity (*TA*) is 2400 μmol/kg (Broecker and Peng, 1982; Michaelis et al., 1986; Mackenzie, 1998). Both *TC* and *TA* will change when V_{OAR} changes. The model calculates the change in *TA* according to (Broecker and Peng, 1982):

$$\Delta TA = [2\Delta C_{CaCO3} / (\Delta C_{CaCO3} + \Delta C_{org}) - 0.1\Delta C_{org} / (\Delta C_{CaCO3} + \Delta C_{org})]\Delta TC$$

In this equation, ΔC_{CaCO3} and ΔC_{org} represent the change in calcium carbonate and organic carbon stored in the V_{OAR}, respectively. From the above equation it is apparent that changes in the amount of calcium carbonate within the V_{OAR} have a positive and high impact on changes in alkalinity, whilst changes in the amount of organic carbon have a negative and low influence. Once *TC* (calculated from V_{OAR}) and *TA* are established, the depth of the calcite lysocline can be calculated with CO2SYS.

3.5.4 Results

The changes that are needed in the different parameters in order to establish the observed fluctuations in δ_{OAR} are summarized in Table 3.3 for the six scenarios outlined above. Prior to 1.00 Ma, δ_{OAR} variations were negligible (Figure 3.7), the system is assumed to have been at steady state (river input equals carbon burial output), and the values used for the various parameters are: δ_{riv} = -3.8‰, δ_{org} = -23‰, δ_{ino} = 1‰, F_{riv} = 2.40x10^{14} g C yr^{-1}, F_{org} = 4.8 x10^{13} g C yr^{-1} and F_{ino} = 1.92 x 10^{14} g C yr^{-1} (Delaney and Boyle, 1988).

Table 3.3 Model values calculated for 6 different scenarios in order to explain the Mid- and Late-Pleistocene carbon isotope fluctuations (see text for full details of different scenarios).

Scenario Age (Ma)	~ 1.50 – 1.00	1.00 – 0.90 (node 1 - 2)	0.90 – 0.50 (node 2 – 3)	0.50 – 0.25 (node 3 – 4)	0.25 – 0.10 (node 4 – 5)
Scenario 1					
F_{riv} (in g C yr^{-1})	2.40 x 10^{14}	2.70 x 10^{14}	2.28 x 10^{14}	2.53 x 10^{14}	2.23 x 10^{14}
Scenario 2					
δ_{riv} (in ‰)	-3.8	-4.2	-3.69	-4.0	-3.5
Scenario 3					
δ_{org} (in ‰)	-23.0	-20.8	-24.0	-22.0	-24.3
Scenario 4					
δ_{ino} (in ‰)	1	1.5	0.8	1.2	0.7
Scenario 5					
F_{org} (1) (in g C yr^{-1})	4.8 x 10^{13}	4.2 x 10^{13}	5.0 x 10^{13}	4.5 x 10^{13}	5.1 x 10^{13}
F_{ino} (4) (in g C yr^{-1})	1.92 x 10^{14}	1.68 x 10^{14}	2.02 x 10^{14}	1.82 x 10^{14}	2.06 x 10^{14}
Scenario 6					
F_{org} (1) (in g C yr^{-1})	4.8 x 10^{13}	4.3 x 10^{13}	5.0 x 10^{13}	4.6 x 10^{13}	5.1 x 10^{13}
F_{ino} (1) (in g C yr^{-1})	1.92 x 10^{14}	1.87 x 10^{14}	1.94 x 10^{14}	1.90 x 10^{14}	1.95 x 10^{14}

The variations in the parameters calculated for scenarios 1-6 as summarised in Table 3.3 are shown in Figures 3.9-3.14. As noted above, scenarios 1, 5 and 6 invoke changes in V_{OAR} and lysocline depth, as illustrated in Figures 3.15 and 3.16 and as listed in Tables 3.4 and 3.5.

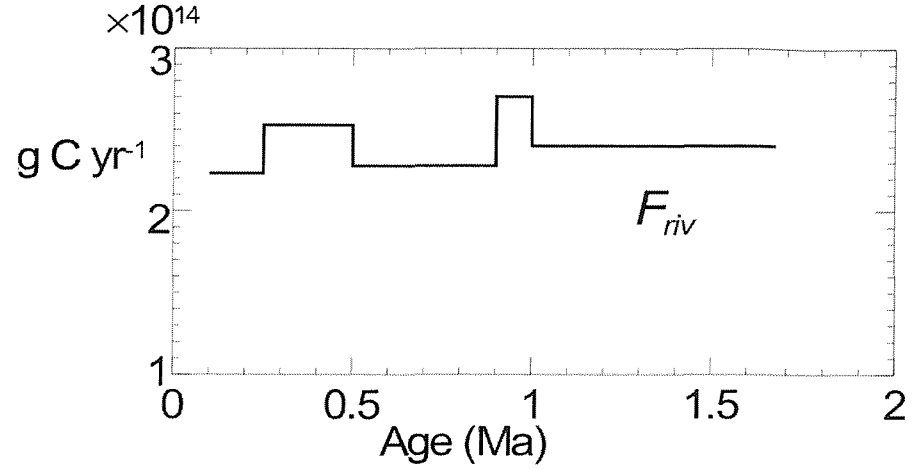

Figure 3.9 Model results for scenario 1, where changes in the river input of carbon (F_{riv}) explain the δ_{OAR} fluctuations.

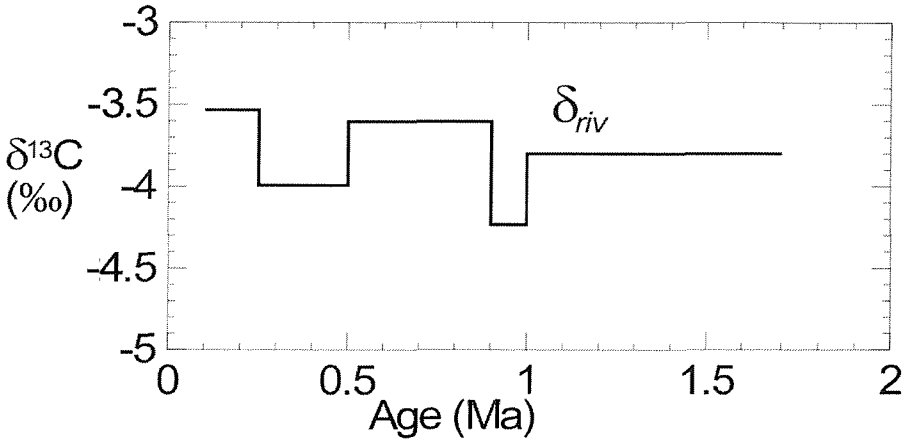

Figure 3.10 Results for scenario 2, where the changes in δ_{OAR} are explained by changes in the carbon isotopic composition of the river input (δ_{riv}).

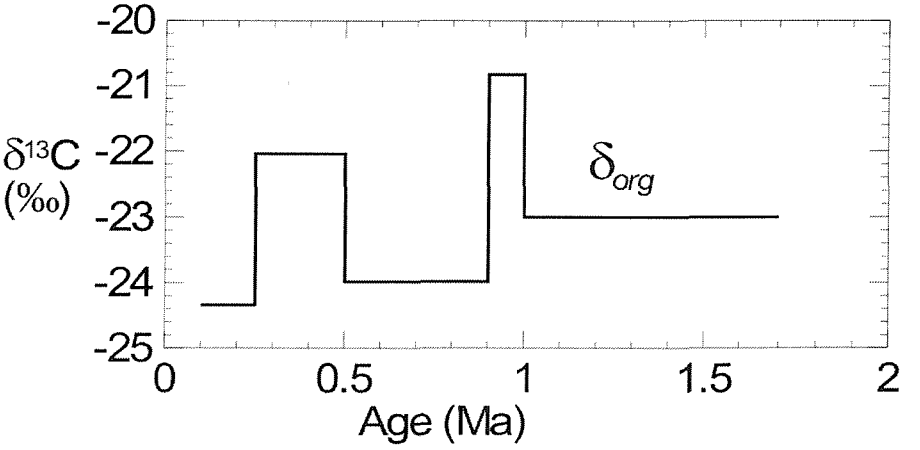

Figure 3.11 Results of the model for scenario 3, where the changes in δ_{OAR} are caused by changes in the isotopic composition of organic carbon buried (δ_{org}).

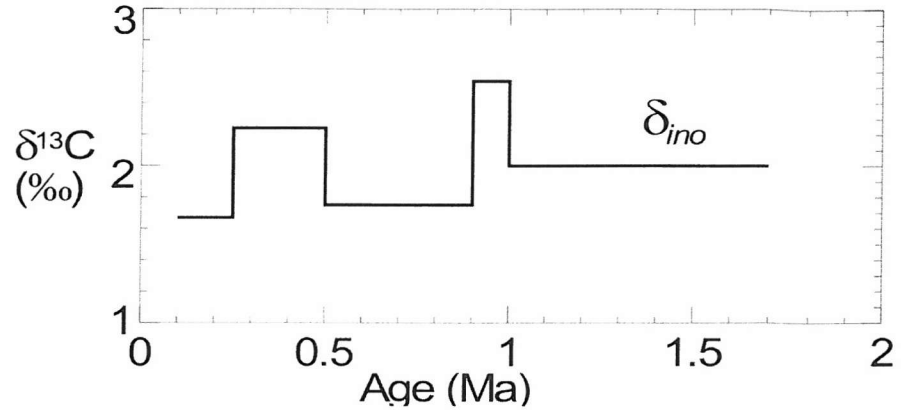

Figure 3.12 Results of the model for scenario 4, where changes in the isotopic composition of inorganic carbon buried (δ_{ino}) caused the δ_{OAR} fluctuations.

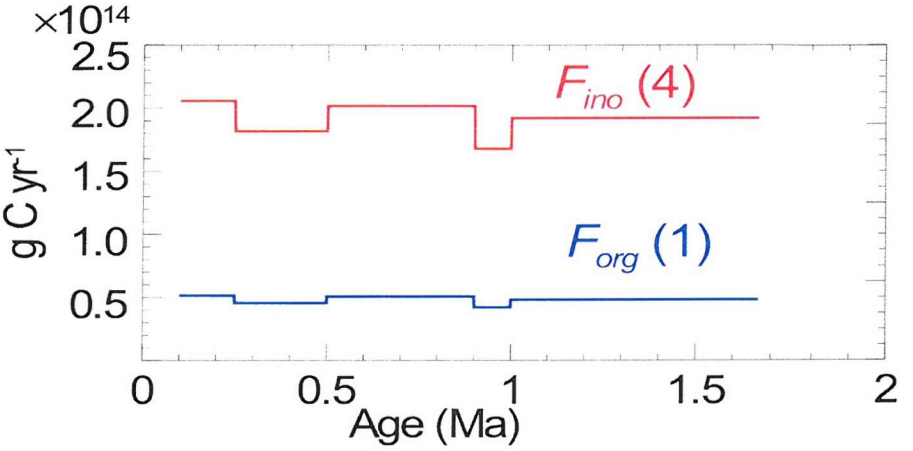

Figure 3.13 Results of the model for scenario 5, where the δ_{OAR} fluctuations are explained by changes in the carbon burial fluxes, where the ratio of change for organic and inorganic carbon burial fluxes maintain ΔF_{org}:ΔF_{ino} = 1:4.

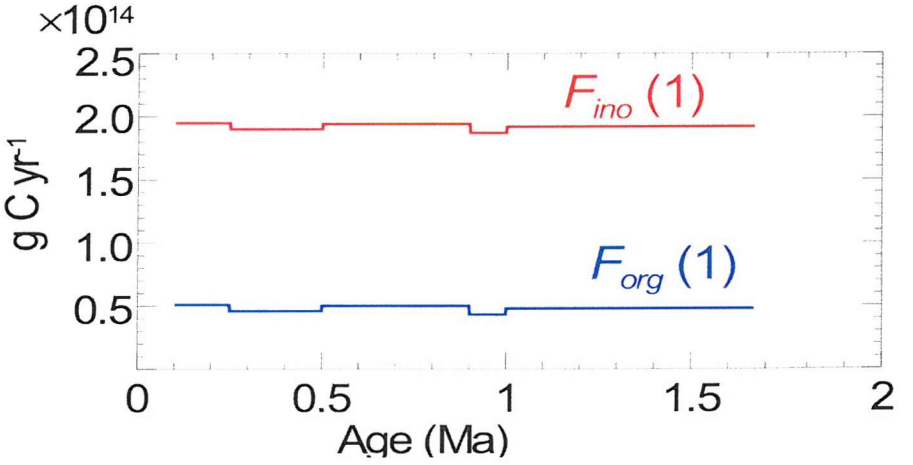

Figure 3.14 Results of the model for scenario 6, where the δ_{OAR} fluctuations are also explained by changes in the carbon burial fluxes, but the ratio of change for organic and inorganic carbon burial fluxes maintain ΔF_{org}:ΔF_{ino} = 1:1 (as defined by stoichiometry).

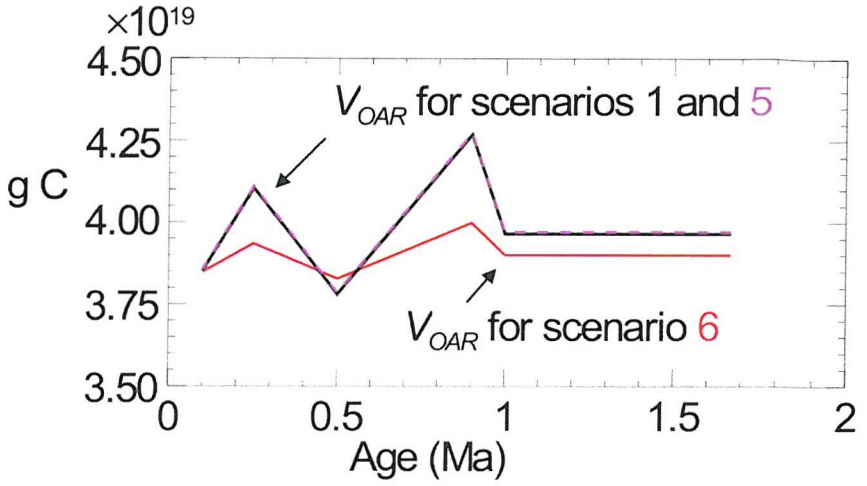

Figure 3.15 Model results for changes in V_{OAR} for scenarios 1, 5 and 6. V_{OAR} at 0.10 Ma reached the present-day volume of 3.85×10^{19} g C (Michaelis and Ittekot, 1986; Mackenzie, 1998).

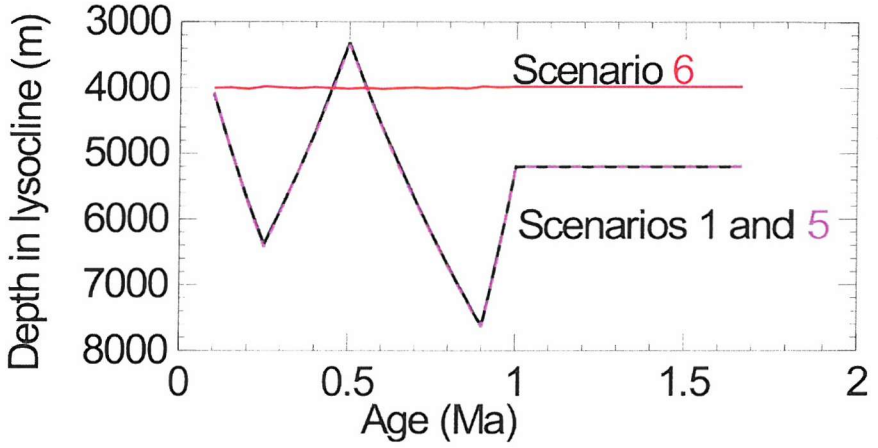

Figure 3.16 Model results for variations that occur in the depth of the calcite lysocline for scenarios 1, 5 and 6.

Table 3.4 Amount of carbon stored in the ocean-atmosphere reservoir calculated for scenarios 1, 5 and 6.

Time (Ma)	V_{OAR} for Scenario 1 (F_{nv}) in g	V_{OAR} for Scenario 5 (F_{org}:F_{ino} = 1:4) in g	V_{OAR} for Scenario 6 (F_{org}:F_{ino} = 1:1) in g
1.00 (node 1)	3.97×10^{19}	3.97×10^{19}	3.90×10^{19}
0.90 (node 2)	4.27×10^{19}	4.27×10^{19}	4.00×10^{19}
0.50 (node 3)	3.78×10^{19}	3.79×10^{19}	3.83×10^{19}
0.25 (node 4)	4.10×10^{19}	4.11×10^{19}	3.93×10^{19}
0.10 (node 5)	3.85×10^{19}	3.86×10^{19}	3.85×10^{19}

Table 3.5 Changes in the depth of the calcite lysocline calculated for scenarios 1, 5 and 6.

Time (Ma)	Lysocline depth (m) for Scenario 1	Lysocline depth (m) for Scenario 5	Lysocline depth (m) for Scenario 6
1.00 (node 1)	**5203**	**5205**	**3987**
0.90 (node 2)	**7627**	**7647**	**3985**
0.50 (node 3)	**3313**	**3345**	**4018**
0.25 (node 4)	**6388**	**6432**	**3985**
0.10 (node 5)	**4094**	**4069**	**4005**

3.5.5 Discussion

3.5.5.1 Which scenario fits best?

In scenario 1, changes of up to 16% are needed in F_{riv} to drive the observed $\delta^{13}C$ fluctuations (Table 3.3, Figure 3.9). These calculated changes in F_{riv} would imply large changes in V_{OAR} (Table 3.4, Figure 3.15), especially between 0.90 and 0.50 Ma (node 2 and 3), where a –11% change occurs in V_{OAR}, from 4.27×10^{19} to 3.78×10^{19} g C. These changes in turn invoke dramatic and untenable consequences on the calcite lysocline depth, with a calculated shift from ~7600 to 3300 m below sea level between 0.90 and 0.50 Ma (Table 3.5, Figure 3.16).

Although variations of up to ~1000 m in the calcite lysocline have been reported on glacial/interglacial time scales (Peterson and Prell, 1985; Farrell and Prell, 1991; Volbers and Henrich, 2002), on the longer time scale considered here the depth of the calcite lysocline does not vary more than ±150 m from the present ~4000 m (Broecker and Peng, 1982; Rea and Leinen, 1985). Thus, the implied variations in the depth of the lysocline resulting from the changes in input of carbon through rivers (F_{riv}) inferred in scenario 1 do not agree with observations. Scenario 1 can thus be rejected.

In scenario 2, relatively large changes in δ_{riv} are needed if they are to drive δ_{OAR} fluctuations (Table 3.3, Figure 3.10). For example, between 0.90 and 0.50 Ma (node 2 and 3), δ_{riv} would have to increase from –4.2 to –3.6 ‰. Changes in δ_{riv} would require changes in the relative weathering rates of inorganic and organic carbon. Osmium isotopes do not support this scenario, as there are no significant fluctuations over the time interval considered here (Ravizza, 1993). Hence, scenario 2 also seems to be unsupported by the available data.

The changes that would be needed in δ_{org} to explain the δ_{OAR} fluctuations (scenario 3, Figure 3.11) are considerable (between 0.90 and 1.00 Ma, (node 2 and 3), δ_{org} would need to decrease from –20.8 to 24.0‰). We know of no evidence that would support such variations, which makes scenario 3 seem unrealistic.

If changes in δ_{ino} were to explain the δ_{OAR} fluctuations (scenario 4), then large changes are needed in δ_{ino} (Figure 3.12). These should presumably be related to changes in productivity, as most inorganic carbon is synthesised in surface water. Strengthening of the biological pump would not only cause an increase of δ_{ino} but also cause an enhanced offset between benthic and planktonic $\delta^{13}C$ records (Sen Gupta,

1999). The observed covariance between these records (Figure 3.6) therefore indicates that scenario 4 can be excluded.

In scenario 5, the δ_{OAR} fluctuations are caused by changes in the carbon burial fluxes F_{org} and F_{ino}, while maintaining the ratio of change at ΔF_{org}:ΔF_{ino} = 1:4, i.e. changes in the two burial fluxes are considered to be proportional to the global F_{org}:F_{ino} ratio of 1:4 (Delaney and Boyle, 1988) (Figure 3.13). The required changes in F_{org} and F_{ino} (Table 3.3, Figure 3.13) result in large changes in the amount of carbon in V_{OAR} that are similar to those discussed above due to changes in F_{riv} (Figure 3.15). Again, such large shifts in the amount of inorganic carbon within the V_{OAR} would greatly affect the depth of the calcite lysocline (Figures 3.14, 3.16), in disagreement with long-term observations (Rea and Leinen, 1985; Peterson and Prell, 1985; Farrell and Prell, 1991).

In our final scenario (6), δ_{OAR} fluctuations are considered to be caused by changes in the carbon burial fluxes F_{org} and F_{ino}, whilst maintaining a ratio of change of ΔF_{org}: ΔF_{ino} = 1:1. The invoked changes in F_{org} and F_{ino} (Table 3.3, Figure 3.14) cause considerably less variation in V_{OAR}, with a maximum shift of ~4% (from 4.00×10^{19} to 3.83×10^{19} g C) between 0.90 and 0.50 Ma (Figure 3.15). Hence, variations in the depth of the calcite lysocline are much smaller than those for scenario 5 (where ΔF_{org}:ΔF_{ino} = 1:4) (Figure 3.16).

As noted above, sedimentary records indicate that the Pleistocene lysocline at the time scales considered in this study did not vary by more than ±150 m (Rea and Leinen, 1985; Peterson and Prell, 1985; Farrell and Prell, 1991). To satisfy this requirement, the ΔF_{org}:ΔF_{ino} ratio must have consistently remained between 50:50 and 45:55. Any change in this ratio toward increased inorganic carbon burial would have resulted in the lysocline varying by more than ±150 m. This constraint also implies that long-term changes in atmospheric pCO_2 were small (± 15 ppmv) over the past 1.5 Ma (i.e. on time scales exceeding glacial cycles).

3.5.5.2 General discussion and summary

The Pleistocene $\delta^{13}C$ stacked record ($\delta_{stacked}$) is relatively stable for ~500 kyr prior to the initial excursion of the MPCF at 1.00-0.90 Ma (Figure 3.7). A decrease in δ_{OAR} of 0.27‰ between 1.00 and 0.90 Ma (node 1 and 2), requires that the total carbon burial flux decreased from 24.0 to 23.0×10^{13} g C yr^{-1}, possibly due to increased

bottom water ventilation (Table 3.3). After 0.90 Ma, δ_{OAR} increased by 0.49‰ until 0.50 Ma. This change requires that the total carbon burial flux increased from 23.0 to 24.5×10^{13} g C yr^{-1}, possibly due to a decrease in bottom water ventilation. Similarly, the fluctuation between 0.50 and 0.10 Ma can be achieved by decreasing the total carbon burial flux by 0.9×10^{13} g C yr^{-1} between 0.50 and 0.25 Ma and then increasing it by 1.0×10^{13} g C y^{-1} between 0.25 and 0.10 Ma (Table 3.3).

The model predicts relative fluctuations in organic and inorganic carbon burial fluxes (F_{org} and F_{ino}) of up to 16 and 4% respectively. The scale of variations in F_{org} is such that one would expect them to be detectable in areas where there are substantial sedimentary C_{org} concentrations, such as the Sea of Japan, the Barents Sea, parts of the Nordic Sea, the eastern Mediterranean Sea, the Black Sea, the Arabian Sea, parts of the South Atlantic Ocean, and coastal upwelling areas (Kempe, 1977). Unfortunately, Pleistocene organic carbon burial fluxes are not generally well documented. We have found only three detailed studies, concerning the eastern Mediterranean, the Sea of Japan and the South Atlantic.

The eastern Mediterranean displays a large decrease in preserved organic-rich (sapropel) intervals between 0.98 and 0.58 Ma (Rossignol-Strick et al., 1998). As a consequence, we calculate that the amount of organic carbon buried in that basin during the mid-Pleistocene was only about half that buried during intervals with preserved sapropels, while the absence of preserved sapropels between 1.00 and 0.90 Ma defines a total "loss" of 0.6-1.5 $\times 10^{16}$ g C_{org} in the sediments (Appendix 3.2). Although this represents only 1-3% of the total 0.5×10^{18} g decrease in F_{org} projected by our model for that time interval (Table 3.3, Figure 3.14), C_{org} burial minima also occur in the Sea of Japan (Stein and Stax, 1992) and the South Atlantic (Dean and Gardner, 1985), where preserved C_{org} contents drop from ~4 to ~2% between 0.95 and 0.75 Ma and between 1.10 and 0.85 Ma, respectively. We also note that concomitant calcium carbonate minima occurred around ~1.00 to 0.90 Ma in the South Atlantic, Indian and Pacific Oceans (Farrell and Prell, 1991; Haddad et al., 1993; Bassinot et al., 1994; Schmieder et al., 2000).

Thus, all suitable available records show a broad C_{org} burial flux minimum centred around ~1.00-0.90 Ma that appears to have coincided with a period of reduced calcium carbonate burial. These observations are compatible with our hypothesis, which ascribes the initiation of the MPCF (1.00–0.90 Ma) to a global decrease in

organic and inorganic carbon burial fluxes, likely due to increased bottom water ventilation.

Similar support for our hypothesis is found in the case of the LPCF $\delta^{13}C$ shift to low values (0.50-0.25 Ma). It also coincides with a decrease in eastern Mediterranean sapropel preservation (Rossignol-Strick et al., 1998) and a ~2.5% drop in organic carbon contents in the South Atlantic (Dean and Gardner, 1985), while a global calcium carbonate low has been described as the Mid-Brunhes dissolution event (~0.4-0.3 Ma) (Peterson and Prell, 1985; Farrell and Prell, 1991; Dean and Gardner, 1985; Haddad et al., 1993; Bassinot et al., 1994; Crowley, 1985; Janssen et al., 1986; Henrich et al., 2002). We infer that enhanced remineralisation of organic matter during these events led to more corrosive conditions that caused concomitant drops in the calcium carbonate burial flux.

The mid-Pleistocene climate transition (MPT) marked an increase in mean global ice volume and a shift from 41-kyr to 100-kyr ice-age cycles (Raymo et al., 1997). The exact timing of the MPT, however, remains a matter of debate. Raymo et al. (1997) date the MPT between ~920 and 540 ka, Hall et al. (2001) report it between 860 and 450 ka, Gingele and Schmieder (2001) suggest a start at ~920 ka and termination at ~640 ka, and Henrich et al. (2002) propose an early onset at 1200 ka. Clearly, it is important that the timing relationship between the MPT and MPCF is established, since, apart from the glacial cycles themselves, the MPT represents the most fundamental change in the Pleistocene climate. The strongest pCO_2 shift inferred by our study for the MPCF is only ~15 ppmv, which suggests that whatever the timing relationship, the MPT was not driven by a CO_2 shift. The present study finds that the MPCF was most likely driven by a change in the carbon burial fluxes, with ΔF_{org}:ΔF_{ino} = 1:1, and this proportionality is highly suggestive of an underlying deep-water ventilation mechanism. Such a mechanism would more likely be a consequence of a climate transition than a cause. Therefore it may be expected that the onsets of the MPT and MPCF were closely related and coincident. Based on this argument, we would expect that further research will find the onset of the MPT narrowly constrained at ~1.0 Ma.

Although we have used the long-term stability of the calcite lysocline to constrain the burial fluxes of inorganic and organic carbon, it is equally apparent that these burial fluxes play a major role in controlling the depth of the lysocline. This

implies that significant long-term changes in the area of the seafloor covered by carbonate sediments (most obviously recorded by changes in the carbonate compensation depth (Van Andel, 1975) can only arise from processes extraneous to the ocean-atmosphere carbon system.

Finally, our hypothesis that changes in the burial fluxes of organic and inorganic carbon are tightly constrained also agrees with studies that have examined carbon burial rates and $\delta^{13}C$ excursions in the more distant geological past (Vincent and Berger, 1985; Shackleton, 1985, 1987a; Delaney and Filippelli, 1994; Compton and Mallinson, 1996; Derry and France-Lanord, 1996; Salzman et al., 2000).

3.5.6 CONCLUSIONS

- Benthic and planktonic carbon isotope records from all major ocean basins show two distinct carbon isotope fluctuations since 1 Ma, the MPCF (1.00-0.50 Ma) and the LPCF (0.50-0.10 Ma). The first $\delta^{13}C$ fluctuation (1.00-0.50 Ma), termed the MPCF, is approximately coincident with the mid-Pleistocene Climate Transition.

- A simple box model was used to asses the impact of changes in the global carbon cycle on global $\delta^{13}C$ over Pleistocene time-scales. The model results suggest that the $\delta^{13}C$ fluctuations resulted from concommitant changes in the burial fluxes of organic and inorganic carbon due to changes in bottome water ventilation.

- Sedimentary records provide additional support for this hypothesis and show decreased organic and inorganic carbon contents during periods that are associated with decreased $\delta^{13}C$ values and increased bottom water ventilation.

- Due to the 'stability' of the Pleistocene lysocline, the ratio between the amounts of change in organic and inorganic carbon burial fluxes are tightly constrained to a 1:1 ratio. As a result the model allows a maximum change in pCO_2 of only 15 ppmv during the MPCF.

CHAPTER 4 – THE BALEARIC ABYSSAL PLAIN CORES

4.1 INTRODUCTION

The Balearic Abyssal Plain (BAP) is the largest basin plain in the Mediterranean Sea (Figure 4.1). It has an area of 77,000 km^2 and is defined by the 2800 m isobath (Rothwell et al., 1998, 2000). The plain is bounded by the Var and Rhône fans to the north and north-west, the islands of Corsica and Sardinia to the east, the Balearic Island rise to the west and the North African Algerian shelf to the south (Figure 4.1). The basin plain's morphology is virtually flat (Figure 2.3) as a result of ponding by turbidites. The large European Rhône, Valencia and Var fans are important sediment source areas for these turbidites and probably only minor turbidites originate from the African continent (Vanney and Genneseaux, 1985; Bellaiche, 1993; Torres et al., 1997; Felser et al., 1998). Four giant piston cores (LC01, LC02, LC04 and LC06) were recovered from the BAP (Table 4.1, Figure 4.1) during *Marion Dufresne* Cruise 81 in 1995, using a Calypso giant piston corer. The cores, reaching 27 to 32 metres in length, were taken about 100 to 120 km apart to form an approximate North-South transect across the plain (Table 4.1, Figure 4.1).

Table 4.1 Location details of the four long piston cores used in this study (from the Cruise Report of Marion Dufresne Cruise 81, Rothwell et al., 1995).

Long piston core	Length (m)	Longitude	Latitude	Water depth (m)
LC01	26.91	6° 53.23' E	40° 15.82'N	2845
LC02	32.77	6° 22.58' E	39° 31.88' N	2860
LC04	31.83	6° 06.64' E	38° 39.01' N	2855
LC06	31.20	7° 11.09' E	38° 00.66' N	2845

Thomson et al. (2000) and Thouveny et al. (2000) have demonstrated that the upper 10 to 15 m of some Calypso cores can appear to be a factor of 1.5 to 2 times longer when compared with conventional piston cores from the same site. This difference involves stretching, over-sampling and a microfabric rotation in the vertical direction (Thouveny et al., 2000). The lithological units in the Calypso piston cores that are used in this study appear to be anomalously thick in the upper 15 m and are suspected to have been stretched during coring. To reduce this effect, the length of the involved intervals was divided by the maximum stretch factor of 2 (after Thomson et al., 2000; Thouveny et al., 2000). Data presented in Chapter 5 suggest that this

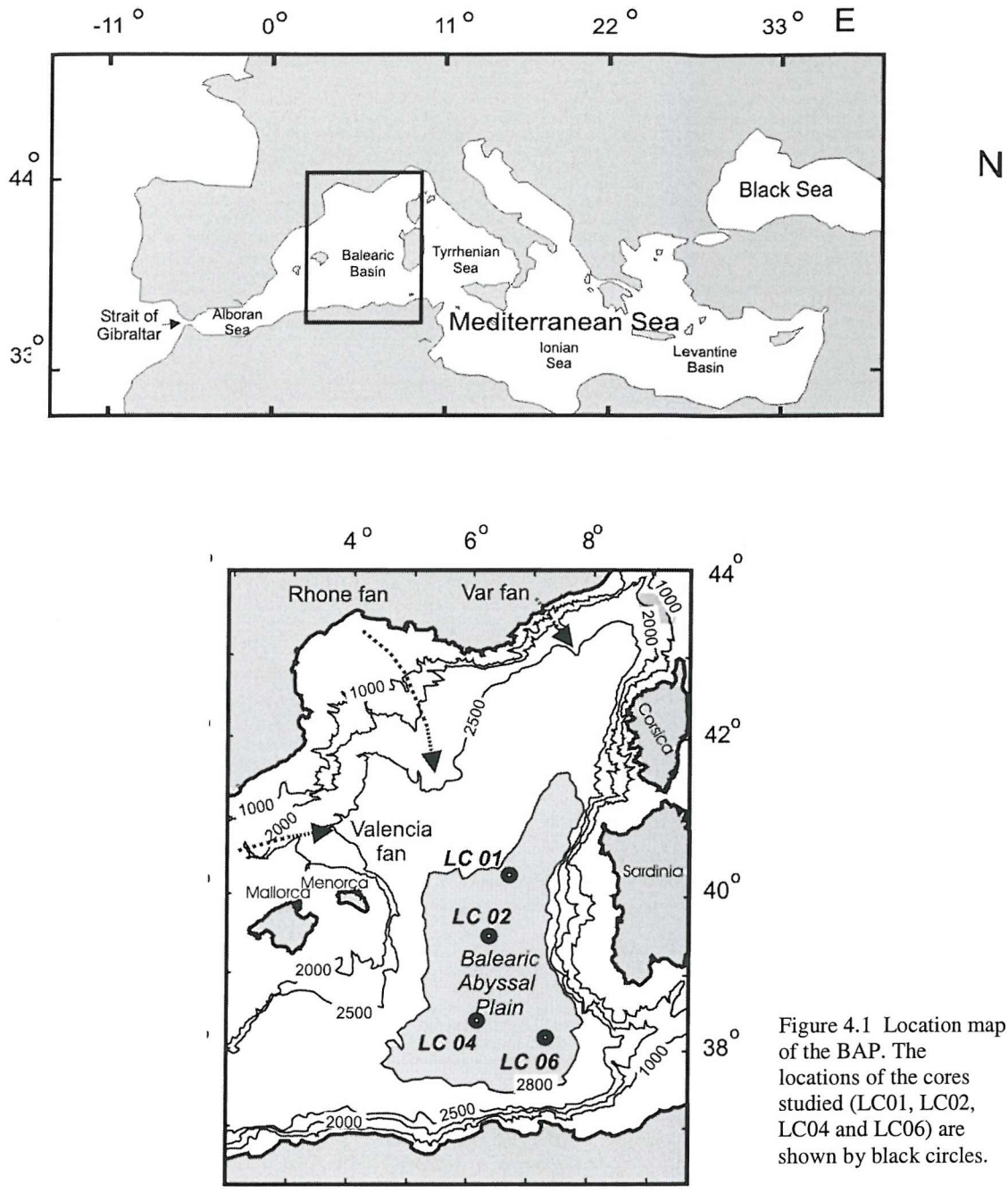

Figure 4.1 Location map of the BAP. The locations of the cores studied (LC01, LC02, LC04 and LC06) are shown by black circles.

magnitude of stretch is an appropriate estimate for these piston cores.

4.2 METHOD: CORE CHARACTERISATION

4.2.1 Sedimentological logs

Identification of individual turbidites and hemipelagic intervals in cores LC01, LC02, LC04 and LC06 was made using textural criteria following visual description of the archive half of the cores, using the guidelines from the Ocean Drilling Program 'Handbook for Shipboard Sedimentologists' (Mazzullo et al., 1987).

Table 4.2 Characteristics of turbidite beds and hemipelagic intervals

	Hemipelagic units	Turbidites
Bed organisation	The upper boundary between turbidite beds and hemipelagic interval is usually gradational.	The lower boundary between turbidite beds and hemipelagic intervals is generally planar and sharp.
Colour	Colours range from light-olive brown (5Y5/3) to olive grey (5Y 2/2) with subtle variations in hue and chroma over short segments of the core.	Colours range from uniform light-olive brown to olive grey.
Bioturbation	Minor to strong mottling occurs due to bioturbation.	Sediment is generally homogenous with bioturbation only occurring in the top 10-20 cm.
Foraminifer distribution	Foraminifera occur scattered throughout the sediment. Under hand lens the sediment appears speckled.	Foraminifera are generally rare or absent, except near the base of the turbidite. Under hand lens the sediment appears featureless.
Texture	The cut core surface frequently appears to be pitted.	The cut core surface appears to be smooth for turbidite muds.
Sedimentary structures	Apart from bioturbation, these are generally absent	Various sedimentary structures may be observed, including normal grading in sandy-based turbidites, parallel and wavy lamination (in turbidite mud and silt/sand), cross-lamination and convolute lamination (in turbidite silt/sand; convolute lamination is normally restricted close to the base of turbidites).
Physical properties (wet-bulk density, P-wave velocity and magnetic susceptibility)	Wet-bulk density, P-wave velocity and magnetic susceptibility values generally fall within a restricted range, compared to turbidite intervals.	Wide range of measurements for all three properties. Sharp turbidite bases can generally be observed by abrupt changes in all three properties. Grading is commonly observed.

Turbidite beds are distinguished from hemipelagic sediments by their sharp, normally graded bases (which can be recognised both visually and through physical property measurements made using a Multi Sensor Core Logger), colour and lack of bioturbation (except for the bioturbated top of turbidites, which is rarely more than a few decimetres thick; Stow and Piper, 1984; Jones et al., 1992; Stow and Fabrez, 1998) (Table 4.2). Additionally, turbidite beds can be distinguished from hemipelagic

sediments through the sedimentary structures present (such as normal grading and lamination) and grain size properties (Rupke and Stanley, 1974).

Lithology, core disturbance and sedimentary structures were recorded on the sedimentological logs. Other features recorded include colour, genetic unit (i.e. whether turbidite or hemipelagic interval), turbidite notation and a short description of the sedimentary unites identified. Turbidite notation is described by T_{number} for turbidites situated above the megabed, a basinwide chronostratigraphic marker described by Rothwell et al. (1998), and B_{number} for turbidites below this megabed. A comparison between the depths of lithological and genetic units from sections that were relatively unconsolidated revealed slight depth discrepancies between working and archive halfs of the cores, with a maximum displacement of 10 cm, probably due to core handling on the ship.

4.2.2 Sediment colour

A Minolta spectrophotometer (Model CM-2002) was used to quantitatively describe sediment colour in terms of Munsell colour values. Colour of most turbidite and hemipelagic intervals was measured with the spectrophotometer, except in the cases where turbidite or hemipelagic intervals were too thin (a thickness of ~1 cm is needed to get a reliable colour reading), or where the sediment was too disturbed. The recorded Munsell colour values were converted to L*, a* and b* values using Munsell Conversion Software Version 4.01 (downloaded from www.munsell.com). L* values represent psychometric lightness, which varies between black (L*=0) and white (L*=100). a* and b* represent psychometric chromaticity, with a positive value of a* corresponding to red colours, negative values of a* corresponding to green values, positive values of b* corresponding to yellow values and negative values of b* corresponding to blue values (Hunt, 1980).

4.2.3 Multi Sensor Core Logging

The archive halves of the four cores were logged using the BOSCOR Multi-Sensor Core Logger (MSCL) developed by Geotek, Ltd. This automated logging device provides non-destructive continuous measurements of gamma-ray attenuation, p-wave travel time and magnetic susceptibility (Gunn and Best, 1998).

Gamma radiation can be used to determine bulk density of sediment (Gerland and Villinger, 1995). In this case, transmission radiation was used, where the source and detector are placed on opposite sides of the material being tested. The intensity of radiation penetrating the material gives a measure of bulk density. The density and porosity of sediment are calculated by using mass weighted attenuation coefficients (Gunn and Best, 1998). P-wave profiles can be used to locate macro- and micro-scale lithological changes, e.g. turbidite layers and variations in sand, silt or clay content. For example, Weber et al. (1997a) found that terrigenous, calcareous and biogenic siliceous sediments in the Bay of Bengal differ distinctly in their acoustic properties. The magnetic susceptibility sensor was used to measure the magnetic properties of the sediment. The response of a sample to a magnetic field is a function of concentration and composition (i.e. of both mineralogy and grain size) of the sample (Thompson and Oldfield, 1986; Verosub and Roberts, 1995). The primary cause of variations in magnetic susceptibility in deep-sea sediments is changes in the amount and nature of terrigenous material reaching the site, and changes in the grain size associated with sorting by currents and/or eolian processes (Amerigian, 1974; Bloemendal et al., 1992).

4.2.4 Calcium carbonate and organic carbon content

Calcium carbonate ($CaCO_3$) and organic carbon contents in both the turbidite muds and hemipelagic intervals were measured by coulometry. Samples were oven-dried at 100°C for 48 hours in order to evaporate all water present. The dried samples were powdered and $CaCO_3$ was measured from CO_2 liberated by 10% phosphoric acid for six minutes. In order to measure organic carbon, the CO_2 liberated by acid treatment is subtracted from the CO_2 liberated by whole sample combustion at 900°C (i.e. total carbon content). The analytical precision (standard deviation) for standard bulk calcium carbonate sample was ± 1.5% and for standard bulk total carbonate ± 2.5% relative to the bulk sample mean value (see Chapter 5).

4.2.5 Clay mineralogy

The clay mineralogy of individual turbidites was determined using X-ray diffraction (XRD) which measures the relative proportion of clay minerals within a sample. Samples were oven-dried for 48 hours and then powdered. Analysis of

powders by XRD requires them to be very fine-grained (1-5 μm) in order to achieve a good signal-to noise ratio and to reduce fluctuations in intensity. Special care was taken to not excessively grind the samples since that might cause distortion of the clay lattices. Calcium carbonate analysis suggested that the samples used for XRD analysis were carbonate-rich (20 to 50% $CaCO_3$ %) (see Section 4.3.4). Carbonate was removed from the samples using 1 M acetic acid. Samples were placed in separate beakers with distilled water and the clay minerals were dispersed by adding sodium hexametaphosphate (Calgon, 1 ml of 10% solution per 100 ml) followed by ultrasound treatment for approximately 15 minutes (the optimum time for recent sediments, T. Clayton personal comm., 2002). Samples were then left to settle for approximately 3 hours. The clay mineral fraction (< 2 μm) was collected by decanting the fluids into a plastic test tube. This test tube was then centrifuged for three minutes at 750 rpm in order to remove any coarse-grained sediment. One molar $MgCl_2$ was added to the dispersed clays to facilitate clay flocculation (through cation saturation). Excess $MgCl_2$ was successively removed by (i) centrifuging; (ii) washing the sample with tap water; (iii) centrifuging; (iv) washing with tap water, and (v) centrifuging. The paste left in the tube was evenly smeared onto two labelled glass slides using a tooth pick. Samples were then analysed using an X-ray diffractometer (model Phillips Ultra-Pro) between 2θ angles of 2 to17° (air-dried, 375°C, 550°C) and of 2 to 40° (glycolated). Intensity peaks were measured using an in-house computer-based mineral identification program (XRDv3 program written by T. Clayton, University of Southampton). Clay minerals were identified on the position of their basal spacings and the changes in these spacings after the four treatments (air-dried, glycolated, 375°C and 550°C). Identification was made on the basis of the first (usually the most intense) peak using Tables 4.3 and 4.4 (after Brindley and Brown, 1984).

4.2.6 Smear slide description

The composition of selected turbidite mud intervals was assessed by microscopic examination of smear slides, which allowed classification of the lithologies (Rothwell, 1989). A small amount (1-2 mm^3) of soft mud sample was placed onto standard microscope glass slides using a toothpick. The sample was mixed with a droplet of distilled water and evenly spread over the glass slide using a wooden

Table 4.3 Guidelines for identifying common clay minerals, using X-ray diffraction.

MINERAL	Glycolated	Air-dried	Heated 550°C	Notes
Smectite	17Å	Na 12 Å Mg 15 Å	~10 Å	Strong broad 001 reflection, with all the rest of the peaks being of low intensity. In the air-dried state, the position of the 001 reflection depends on exchangeable cation and humidity.
Vermiculite	~14 Å	~14 Å	~10 Å	Vermiculite is similar to smectite but does not expand or expands only slightly on glycolation.
Chlorite	14.2 Å	14.2 Å	~14 Å	Chlorite shows peaks at approximately 14.2 Å, 7.1 Å, 4.7 Å, 3.55 Å and 2.83 Å. The 002 peak is usually the most intense. Heating to 550°C causes an increase in the intensity of the 001 peak whereas the other peaks disappear.
Paragonite	9.6 Å	9.6 Å	9.6 Å	Paragonite is Na-rich mica, which is common in low-grade metamorphic rocks. It shows peaks at 9.6 Å, 4.5 Å, and 3.2 Å, which are unaffected by glycolation and heating.
Illite	10 Å	10 Å	10 Å	Illite shows peaks at 10 Å, 5 Å, 3.33 Å and 2.5 Å. The 002 reflection is less intense than the 001 and 003 reflections.
Glauconite	10 Å	10 Å	10 Å	Glauconite shows similar peaks to illite, but can be recognised on the basis of a weak 002 reflection at 5 Å (<10% of 001 peak).
Pyrophyllite	9.2 Å	9.2 Å	9.2 Å	Pyrophyllite is rarely encountered in sediments, but is relatively common in metamorphic rocks. It shows peaks at 9.2 Å, 4.6 Å, 3.07 Å.
Kaolinite	7.2 Å	7.2 Å	-	Kaolinite peaks disappear completely on heating to 550°C. Some difficulty may be experienced in detecting kaolinite in the presence of chlorite as the 001 kaolinite peak and the 002 chlorite peak overlap. The 002 kaolinite peak has a spacing of 3.57 Å, whilst 004 chlorite has a 3.52 Å spacing.
Berthierine	7.1 Å	7.1 Å	-	Berthierine shows similar spacings to kaolinite. However, they are slightly smaller and careful measurements allows differentiation to be made. The 002 kaolinite has a 3.57 Å spacing whilst berthierine has a 3.52 Å spacing.

Table 4.4 Guidelines for identifying mixed layer clay minerals, using X-ray diffraction.

MINERAL	Glycolated	Air-dried	Heated 550°C	Notes
Illite-smectite	>10 Å <15 Å	>10 Å <17 Å	10 Å <15 Å	Peak spacings are not usually integral multiples of each other. The mineral may display a superlattice peak between 25 Å and 30 Å, indicating an ordered mixed layer structure.
Chlorite-smectite	~14 Å	~14 Å	>10 Å <14 Å	A peak between 10 Å and 14 Å on heating to 550°C is diagnostic. An ordering peak between 25-35 Å is common.

toothpick. The prepared glass slide was then dried on a hot plate and affixed with a glued coverslip (using UV-curing Norland optical adhesive). The slide was fixed using an UV exposure unit and later examined under a petrological microscope to assess relative abundance of detrital and biogenic grains as a qualitative comparison between

the discrete sedimentary types (Rothwell, 1989), which allowed sediment classification according to the scheme of Mazullo et al. (1987).

4.2.7 Mineralogical description of basal turbidite sands

The mineralogy of the sand-sized fraction from the base of some turbidites was determined with a normal binocular microscope using two steps. As a first step the whole sample (including grains from the carbonate fraction) was examined. The second step involved mineralogical description of the non-carbonate fraction. Identification of the individual common minerals was made using the guidelines of Rothwell (1989).

Before petrological analysis was conducted, samples were wet-sieved through four sieve sizes: 600, 150, 125 and 63 μm. Samples were then oven-dried for 48 hours and examined under a normal binocular microscope. Following the method of Rupke and Stanley (1974), the examined sand fractions were divided into four classes: 1) terrigenous sand, which consists of quartz, mica, lithic grains, feldspars and accessory minerals; 2) bioclastic sand, which consists of fragments or whole tests of foraminifera, pteropods and other microfossil or macrofossil debris; 3) organic sand, including wood and plant fragments, and 4) other material, such as ostracod valves and sponge spicules. Samples that contain >50% terrigenous material were classified as terrigenous sands, whereas samples with >50% biogenic material were classified as biogenic sands. Samples with >50% organic matter or other material were not observed.

During the second step, carbonate was removed from the sand fractions by acid digestion in 10% acetic acid. This digestion process lasted from several days for samples with a minor carbonate content (e.g. 25% $CaCO_3$) up to weeks for samples that had a high carbonate content (e.g. 75% $CaCO_3$). All four fractions were examined under a binocular microscope and at least 300 mineral grains were counted. Minerals were divided into individual classes: a) quartz, b) feldspar, c) lithics, d) accessory minerals, e) mica, f) plant fragments, g) sponge spicules, and h) eolian quartz. Quartz was further subdivided into angular, sub-rounded and rounded quartz, to gauge sediment maturity. Haematitic eolian sand grains were observed in all samples in low quantities (~1%).

4.2.8 Mineral identification by X-Ray Powder Diffraction

The mineralogy of sand-sized fractions (non-carbonate) has also been determined using X-Ray Powder Diffraction. Approximately 2.5 g of sand sample was finely ground so that a large number of small crystals were present for analysis. The ground sample was placed in an aluminium holder and analysed using an X-Ray Powder diffractometer (model Philips Ultra-Pro) between 2θ angles of 2 to 76°. Mineral identification was achieved using the 'Philips X'pert Graphics and Identification' program that compares measured intensity peaks with intensity peaks of known minerals from the Powder Diffraction File 2000 (International Centre for Diffraction Data, www.icdd.com).

4.3 RESULTS

4.3.1 Sedimentological logs

Sedimentological logs, for all four long piston cores, are summarised in Appendix 4.1 (see data CD). The sedimentological logs for cores LC01, LC02, LC04 and LC06 clearly show that turbidite deposits, mainly consisting of turbidite mud (although some turbidites contain silt and/or sand at their bases), dominate the lithological sequence (Figure 4.2). On average, 90% of the BAP cored sequence consists of turbidite deposits, and only 10% of the cored thickness consists of hemipelagic intervals (Table 4.5).

Table 4.5 Summary of the total thickness of the lithological units (turbidites and hemipelagic intervals) identified in the four long piston cores.

Core	**Total sediment thickness (m)**	**Total thickness of turbidites (m)**	**% of total**	**Total thickness of hemipelagic intervals (m)**	**% of total**
LC01	24.29	22.24	92%	2.05	8%
LC02	32.51	30.20	93%	2.31	7%
LC04	31.10	27.67	89%	3.43	11%
LC06	29.61	25.71	87%	3.90	13%

Core LC02 has the highest total turbidite thickness (30.20 m), whereas core LC06 has the highest total hemipelagic thickness (3.9 m) (Table 4.5). Going from the most northern core (LC01) to the south (LC02, LC04 and then LC06), the total thickness of recoverd hemipelagic sediment increases from 8% to 13% (Table 4.5).

Thicker hemipelagic intervals in the southern cores may be explained by either: 1) an increase in hemipelagic sedimentation rate, 2) thinner or fewer turbidite beds, or 3) a combination of both. Hemipelagic accumulation rates and stratigraphy are discussed in more detail in Chapter 5.

After correcting the upper 15 m of the cores by dividing the thickness of the affected turbidite and hemipelagic intervals by the maximum stretch factor of 2 (Thomson et al., 2000; Thouveny et al., 2000) as previously discussed, the total thickness of retrieved sediment, the total thickness of turbidites and the total thickness of hemipelagic intervals is much lower (see Table 4.5 & 4.6). However, the relative contributions of turbidites and hemipelagic intervals to the total sediment thickness, however, remains virtually unchanged after the correction (Tables 4.5 & 4.6).

Table 4.6 Summary of the total thickness of the lithological units identified in the four long piston cores, after correction for stretching of the piston cores (see text).

Core	**Total sediment Thickness (m)**	**Total thickness of turbidites (m)**	**% of total**	**Total thickness of hemipelagic intervals (m)**	**% of total**
LC01	18.06	16.38	91%	1.68	9%
LC02	24.87	22.96	92%	1.91	8%
LC04	23.36	20.45	88%	2.91	12%
LC06	22.25	19.14	86%	3.11	14%

A total of 238 to 257 turbidites were identified in the four cores (Table 4.7). For nineteen lithological units classified as turbidite beds, it remains unclear if they are separate turbidite beds, or if they are part of the overlying turbidite bed. This is because they display similar characteristics and are not separated by a hemipelagic interval or bioturbated turbidite top. If these units are separate turbidite beds, a total of 257 turbidites were identified in the four cores, however, if they are part of an overlying turbidite, only 238 turbidite beds were identified. Details of turbidite thickness and position in the cores are presented in Appendix 4.2.

Table 4.7 Number of turbidites (minimum and maximum numbers) in the four cores located above and below the megaturbidite described by Rothwell et al., (1998) and the total number of turbidites.

	LC01		LC02		LC04		LC06	
	min.	max.	min.	max.	min.	max.	min.	max.
Number of turbidites above megabed	20	25	8	10	6	7	37	38
Number of turbidites below megabed	11		24	32	48	50	79	80
Total number of turbidites (including the megabed)	32	37	33	43	55	58	118	119

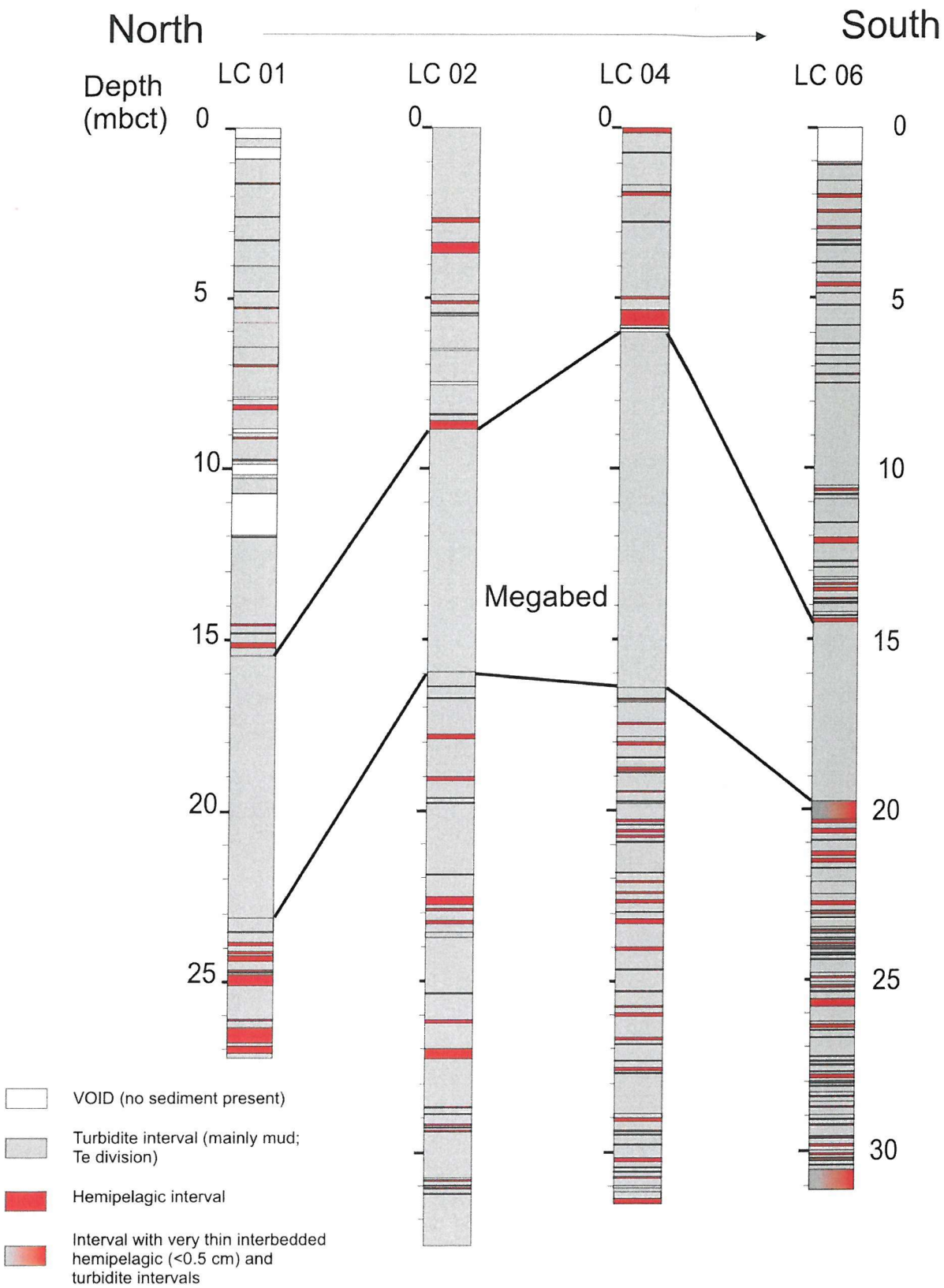

Figure 4.2 Summary of turbidite (grey) and hemipelagic (red) intervals recognised on sedimentological and textural criteria in the four long piston cores. White intervals delineate voids (i.e. contain no sediment). 'mbct' indicates metres below core top. The late Glacial megabed (Rothwell et al., 1998), which forms an important basinwide chronostratigraphic marker, is also shown.

Table 4.8 Measured thickness of basal sands in turbidites. Uncorrected thickness (Stretched) is listed on the left hand side of the Thickness column. Corrected thickness (Corr.) is listed on the right hand side (corrected by dividing by the maximum stretch factor of 2 – see discussion in text).

Sample	Thickness (cm) Stretched	Corr.	Sample	Thickness (cm) Corrected	Sample	Thickness (cm) Stretched	Corrected
LC01-T11?/T12	4	2	LC02-B7	28	LC04-B37		11
LC01_T23	104	52	LC02-B9	169	LC06-T21	255	127.5
LC01-M		77.5	LC02-B13?/B14?/B15	25	LC06-T27	4	2
LC01-B7		11	LC02-B13?/B14? /B15?/B16	3	LC06-T35	10.5	5.8
LC02-T1	12.5	6.8	LC02-B13?/B14? /B15?/B16?/B17	56.5	LC06-T36		
LC02-T8?/T9	30.5	15.3	LC02-B18	4.5	LC06-T37	3	1.5
LC02-M		80	LC02-B19	20	LC06-M		13
LC02-B1?		28.5	LC02-B20	55	LC06-B6		5
LC02-B2		9	LC02-B26	13	LC06-B38		5.5
LC02-B3		29	LC02-B30	2	LC06-B51		11
LC02-B3?/B4		20.5	LC02-B31	1	LC06-B55		4
LC02-B3?/B4?/B5		30	LC02-B31?/B32	5			
LC02-B6		64.5	LC04-M	138.5			

In total the four long piston cores contained 36 turbidites with basal sands. These basal sands are not evenly distributed throughout the cores; LC01 only contains 4 basal sands, whereas LC02 has 20. In LC04 only 2 basal sands were observed, whereas 10 were observed in LC06. The thickness of the basal sands varies between 1.5 and 169 cm (Table 4.8). The mineralogical content of these basal sands is discussed in section 4.2.7. Turbidite thickness and its relation to basin filling and geometry is discussed in more detail in Chapter 6.

4.3.2 Sediment colour

Sediment colour, measured by a spectrophotometer, is written as Munsell values on the sedimentary logs (Appendix 4.1). Munsell values were converted to L*, a* and b* using the Munsell Conversion Software Version 4.1 (www.munsell.com) and are reported in Appendix 4.2 for turbidite beds and Appendix 4.3 for hemipelagic intervals.

4.3.3 Multi-Sensor Core Logging

Multi-Sensor Core Logger data are plotted against depth and lithological unit in Figure 4.3. P-wave velocities in the cores vary between ~1530 and 2000 m/s, with high p-wave velocities commonly correlating to coarse-grained bases of turbidite beds, while low p-wave velocities commonly correlate to muddy sediments (Figure 4.3). Turbidites generally show an upward-fining textural sequence, characterised by an upward-decreasing p-wave velocity (Figure 4.3). Wet bulk density in the cores varies

between 1.15 and 2.4 g/cm^3 (Figure 4.3). Relatively higher wet bulk densities generally occur in associations with bases of turbidite layers, whereas hemipelagic intervals show lower wet bulk densities. Magnetic susceptibility varies between 0 and 35 SI (magnetic susceptibility measurements have not been corrected for density or volume). Higher magnetic susceptibilities are observed for turbidite bases containing silt- and/or sand-sized terrigenous material.

4.3.4 Calcium carbonate and organic carbon content

Calcium carbonate content was measured for almost all turbidite and hemipelagic intervals, except intervals that were too thin to sample (i.e. <0.5 cm thickness) or intervals with insufficient sample as a result of previous sampling by others. Calcium carbonate contents of turbidite muds vary between 16 and 43%, with the lowest value occurring in LC06 (16%) and the highest in LC04 (43%) (Figure 4.4, Appendix 4.2). Two broad groups of turbidites may be distinguished based on $CaCO_3$ content; the first group (Group 1) has $CaCO_3$ contents of <25%, whereas the second group (Group 2), has $CaCO_3$ contents >25%. Turbidite muds from LC01, LC02 and LC04 generally show $CaCO_3$ contents belonging to Group 2 (>25%), whereas turbidite muds from LC06 belong to both Group 2 and Group 1 (Figure 4.4, Appendix 4.2).

Calcium carbonate contents in hemipelagic mud vary between 23 and 55% (Figure 4.5). The highest $CaCO_3$ content was recorded in LC04 (55%) and the lowest in LC06 (23%). Within cores, hemipelagic $CaCO_3$ contents can be grouped in stages of relatively high (~50%) and low (~30%) values that broadly correspond to oxygen isotope stages and are further discussed in Chapter 5.

Organic carbon measurements were carried out for all the turbidite and hemipelagic intervals above the megaturbidite described by Rothwell et al. (1998). Organic carbon contents in turbidite muds are low and vary between 0.02 (detection limit) and 1.2% (Appendix 4.2). Organic carbon contents in hemipelagic intervals are also low, varying between the detection limit (0.02%) and 1.3% (Appendix 4.3).

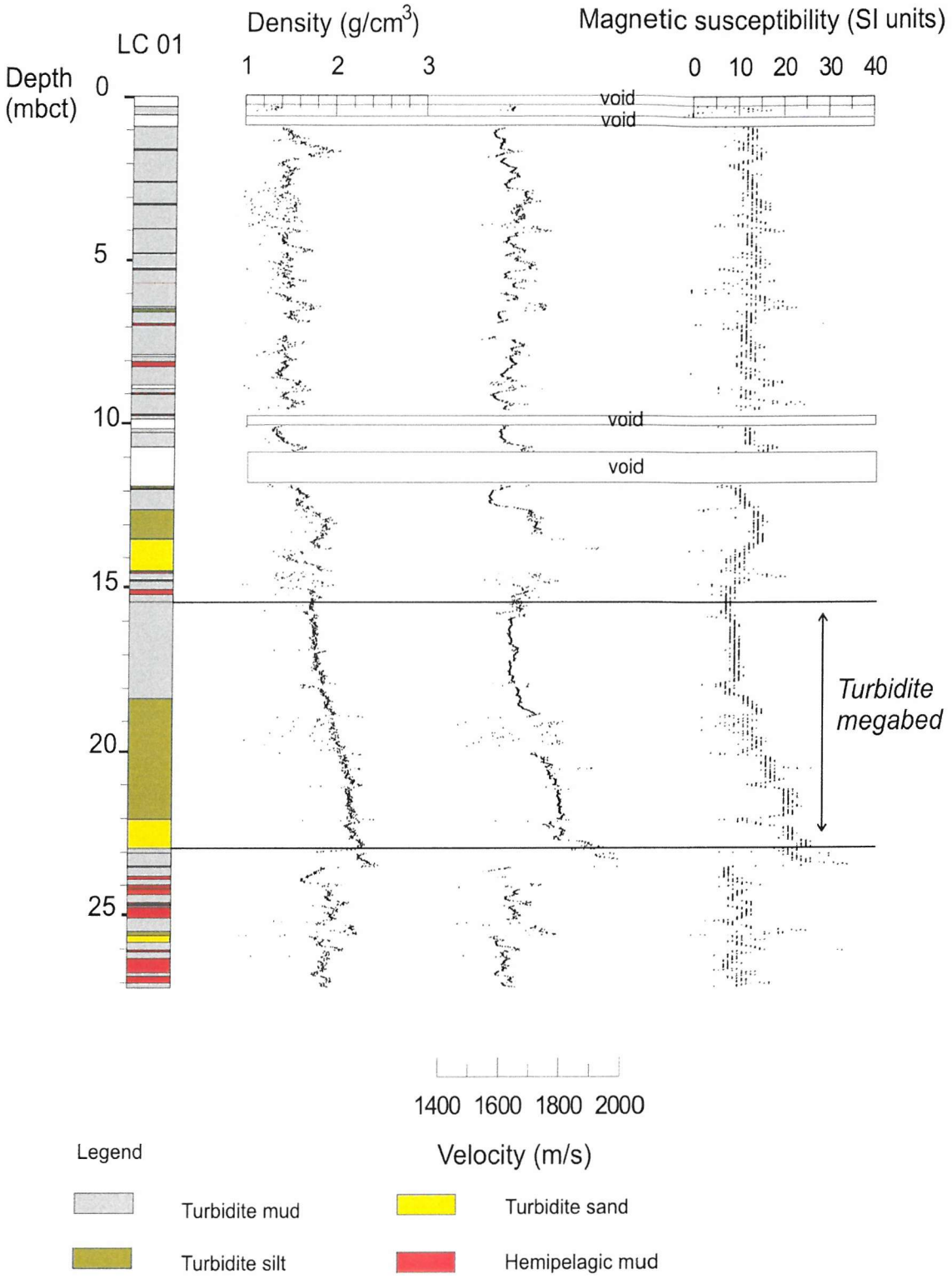

Figure 4.3A Multi-Sensor Core Logger data plotted against depth and lithological units for LC01. The position of the basinwide turbidite megabed of Rothwell et al. (1998) is also shown. Note how textural grading within turbidites is mirrored in the density, p-wave and magnetic susceptibility records.

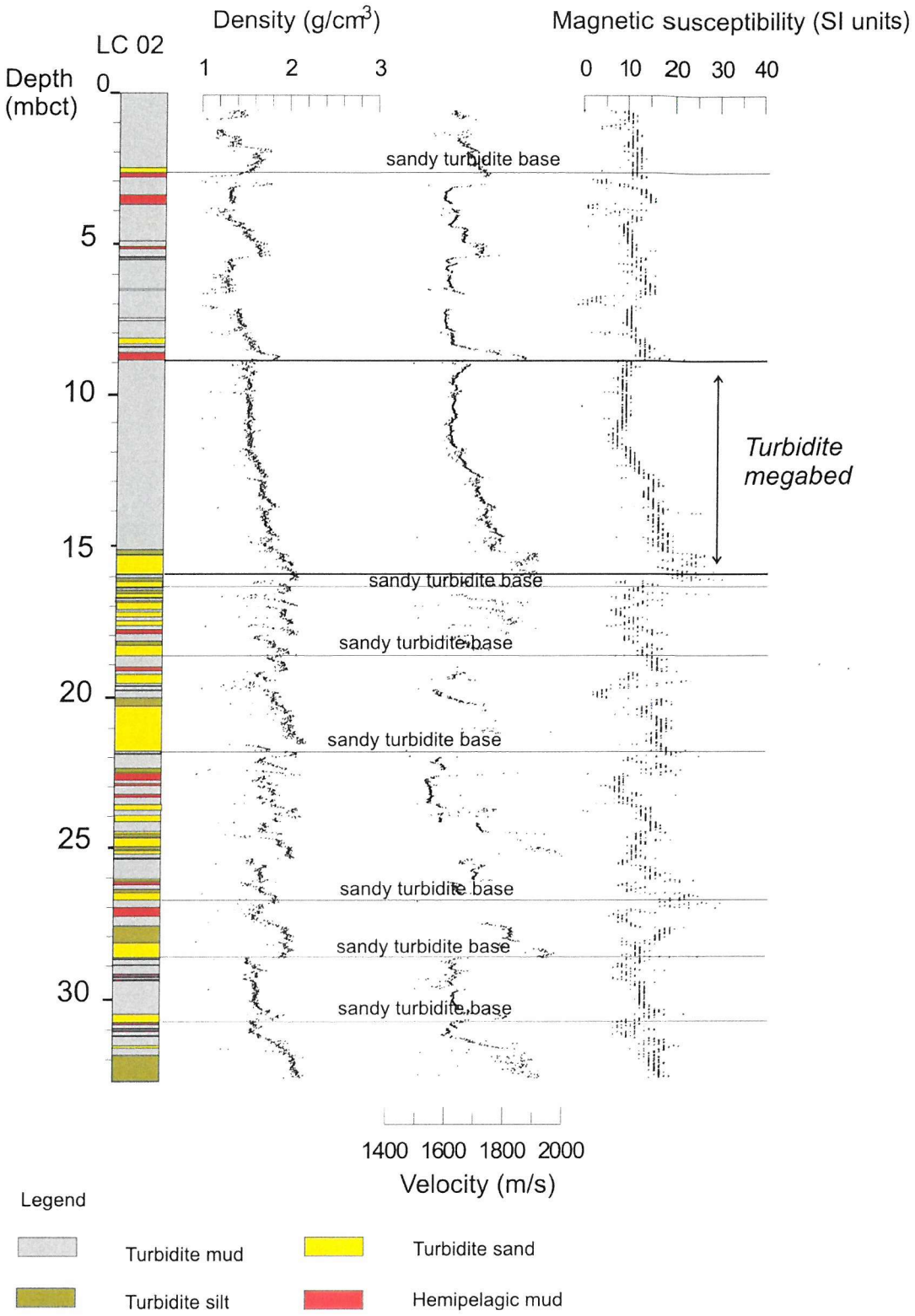

Figure 4.3B Multi-Sensor Core Logger data plotted against depth and lithological units for LC02. The position of the basinwide turbidite megabed of Rothwell et al. (1998) is also shown. Note how textural grading within turbidites is mirrored in the density, p-wave and magnetic susceptibility records. Increases in density, velocity and magnetic susceptibility that correlate with some sandy turbidite bases are also highlighted.

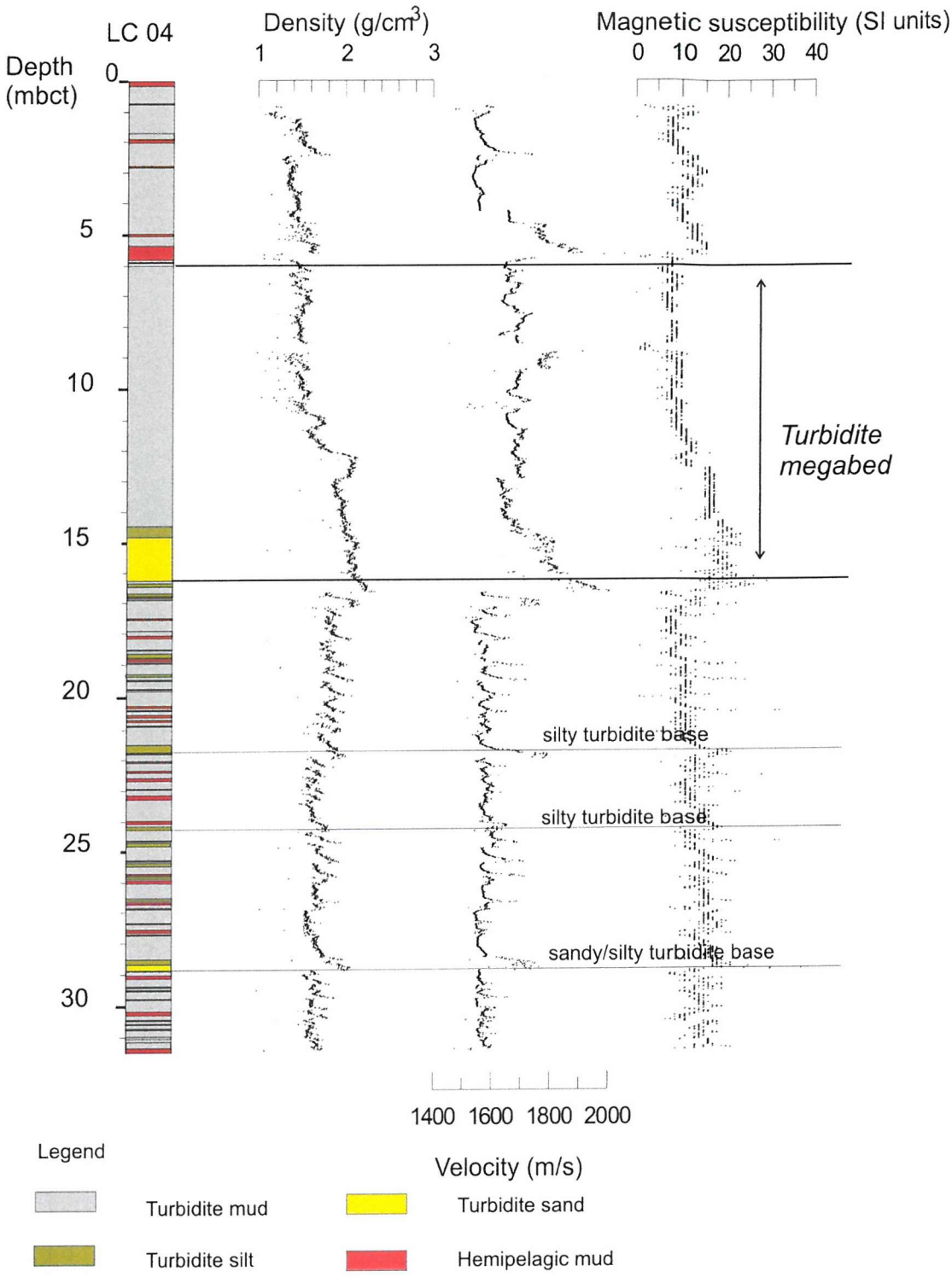

Figure 4.3C Multi-Sensor Core Logger data plotted against depth and lithological units for LC04. The position of the basinwide turbidite megabed of Rothwell et al. (1998) is also shown. Note how textural grading within turbidites is mirrored in the density, p-wave and magnetic susceptibility records. Increases in density, velocity and magnetic susceptibility that correlate with some sandy turbidite bases are also highlighted.

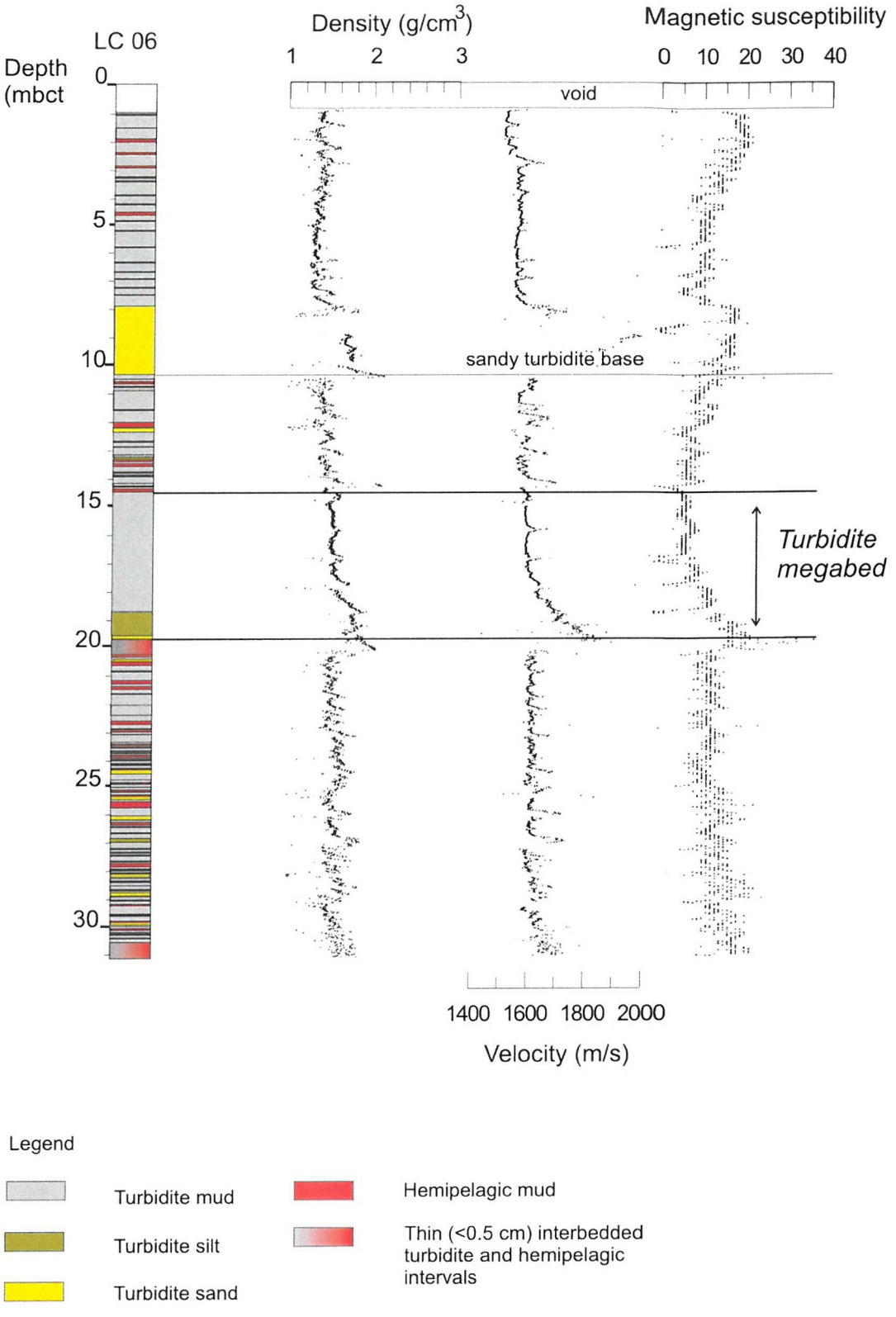

Figure 4.3D Multi-Sensor Core Logger data plotted against depth and lithological units for LC06. The position of the basinwide turbidite megabed of Rothwell et al. (1998) is also shown. Note how textural grading within turbidites is mirrored in the density, p-wave and magnetic susceptibility records. Increases in density, velocity and magnetic susceptibility that correlate with some sandy turbidite bases are also highlighted.

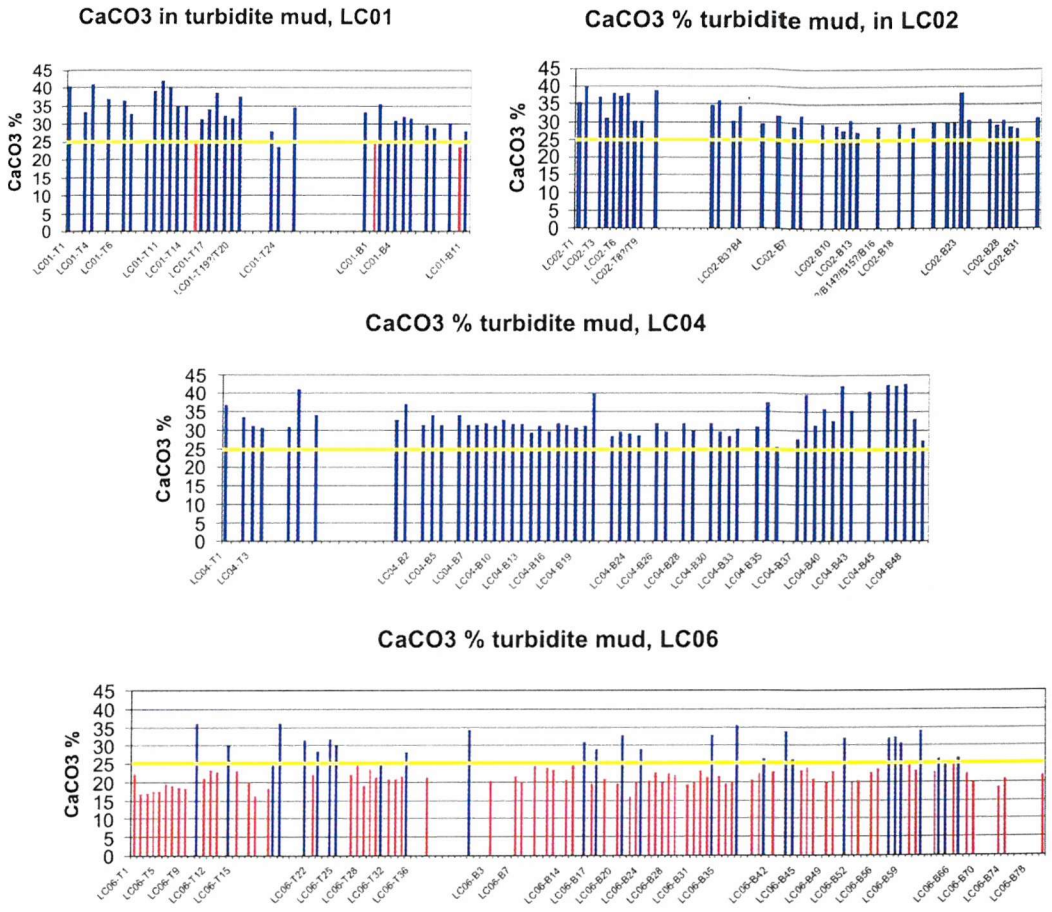

Figure 4.4 Calcium carbonate content of turbidite muds as measured by coulometry. The yellow line devides the turbidite muds into Group 1 in red ($CaCO_3$ contents <25%) and Group 2 in blue ($CaCO_3$ content >25%).

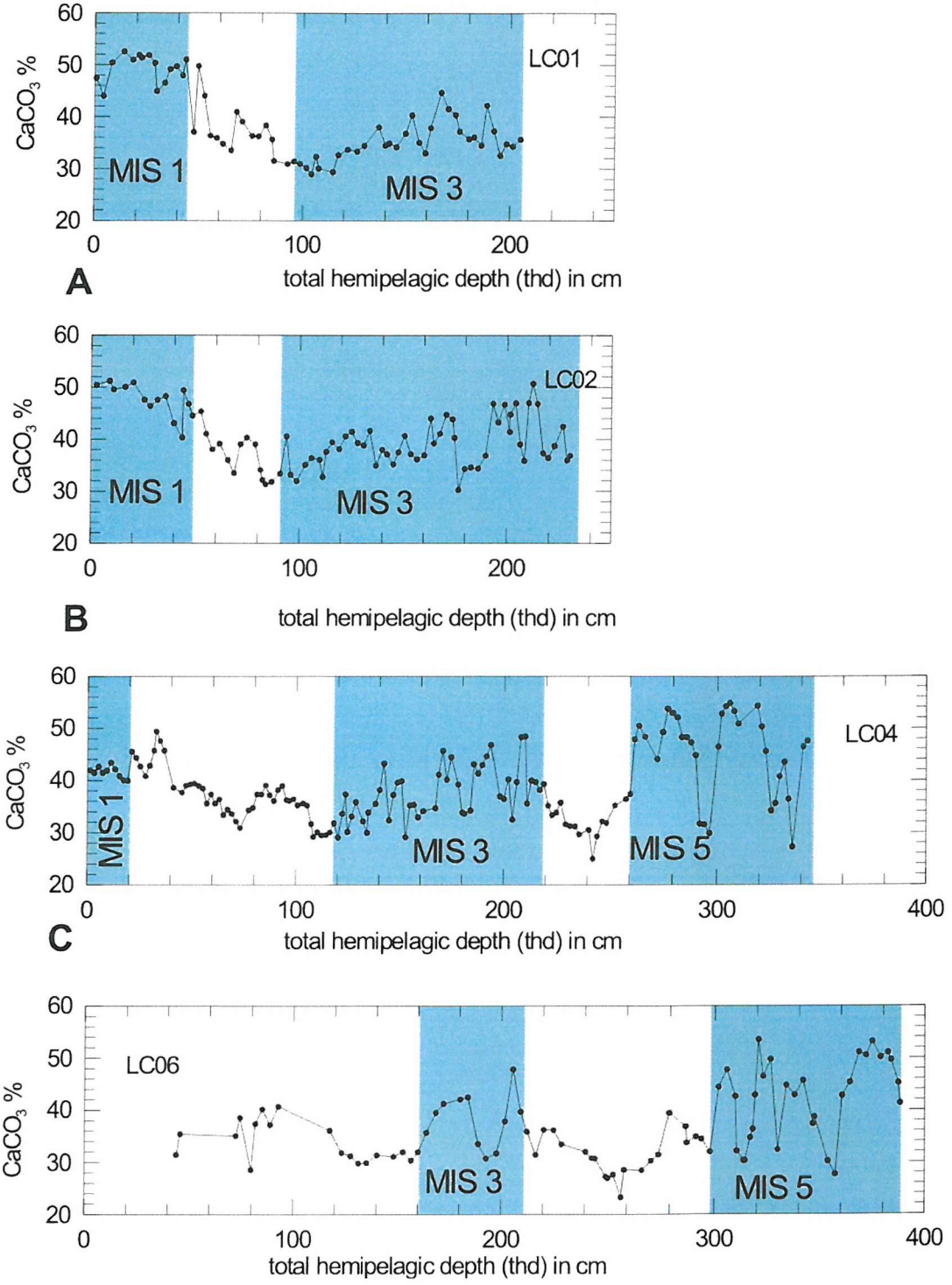

Figure 4.5 Calcium carbonate contents of the hemipelagic intervals, plotted with turbidite beds removed from the depth scale, measured by coulometry. Shaded grey areas indicate periods when hemipelagic intervals had relatively high (generally > 40%) calcium carbonate contents and correspond to interglacial intervals.

4.3.5 Clay mineralogy

The clay mineral composition of the <2 μm fraction of 40 individual turbidites was measured by X-ray diffraction (XRD). All samples contained the following clay minerals: chlorite, illite, kaolinite and expandable clay minerals (smectite and illite/ smectite) (Table 4.9, Figure 4.6). Relative contributions of clay minerals were calculated following the method of Weir et al. (1975) (Table 4.9). Some samples with expandable clay minerals contained a superlattice peak between 25 Å and 30 Å, indicating an ordered mixed layer structure (Figure 4.6, Table 4.9). The presence of this superlattice peak suggests that the expandable mixed clay mineral illite/smectite dominates, whereas samples that do not contain the superlattice peak are most likely dominated by smectite (T. Clayton, Pers. Comm., 2002). A total of 9 turbidite samples was analysed for LC01, and 5 samples showed the superlattice peak (Table 4.9). Other cores with turbidite mud samples where the superlattice peak was found include cores LC04 (3 out of 10 turbidites sampled) and LC06 (9 out of 13 turbidites sampled) (Table 4.9). Samples with a superlattice peak generally have higher contents of expandable clay minerals (most likely illite/smectite) and lower illite contributions (Table 4.9).

The seven mud samples analysed for LC02 did not show the presence of a superlattice peak (Table 4.9). Samples from LC01 and LC04 that contain the superlattice peak all have relatively lower kaolinite contributions than chlorite (samples in LC01 and LC04 that have a superlattice peak show an average kaolinite contribution of 5 and chlorite 9), whereas samples from core LC06 that have a superlattice peak show relatively higher kaolinite contributions than chlorite (kaolinite 12 and chlorite 7) (Table 4.9). One sample from LC06 has a lower kaolinite contribution than chlorite (Table 4.9). The relative ratios of kaolinite/chlorite and (smectite+illite/smectite)/illite are plotted in Figure 4.7. Most turbidite muds from LC06 with the superlattice peak have (S+I/S)/I ratios of between 0.6 and 1, whereas kaolinite/chlorite ratios are >1 (Figure 4.7, Table 4.10). All turbidite muds, with and without a superlattice peak, from LC01, LC02 and LC04 have kaolinite/chlorite ratios of <1 and (S+I/S)/I ratios varying between 0.3 and 1.2 (Figure 4.7).

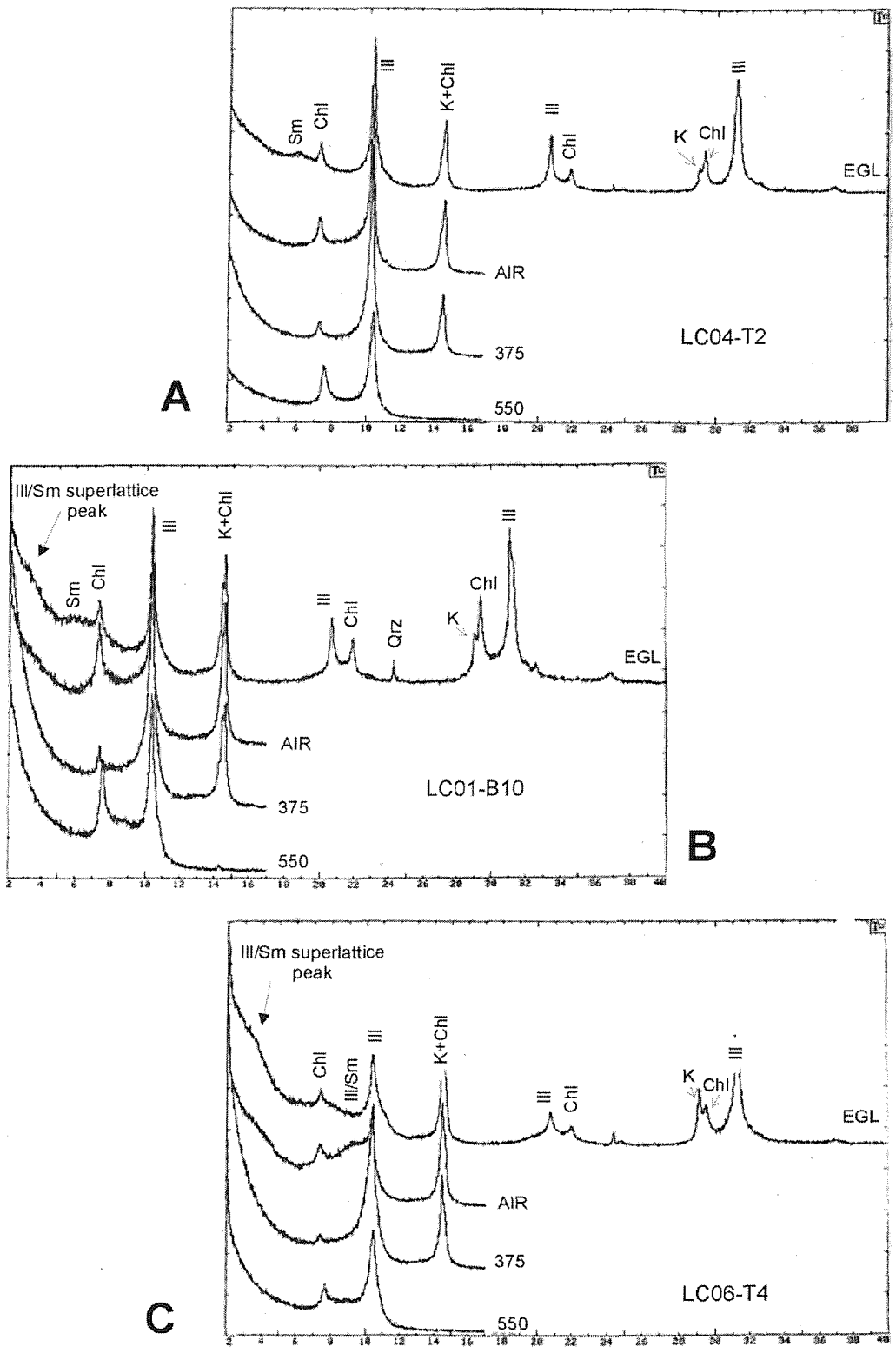

Figure 4.6 Examples of the clay mineralogical composition of turbidite muds from the BAP. Sm=smectite; Chl=chlorite; Ill=illite; K=kaolinite; Qrz=quartz. In **A** smectite is the dominant expandable clay mineral, in **B** smectite and illite/smectite (superlattice peak) are the dominant clay minerals while kaolinite is lower than chlorite and in **C** illite/smectite is the dominant expandable clay mineral and the kaolinite content is higher than the chlorite.

Table 4.9 Clay minerals identified in turbidite muds from the four long piston cores and their relative contributions in percentages. Also indicated is the presence or absence of a superlattice peak indicating the presence or absence of the mixed layer clay mineral illite/smectite.

Core LC01 Sample	Expandable clay minerals	Illite	Kaolinite	Chlorite	Superlattice
LC01-T9	35	49	5	11	Present
LC01-T11	19	63	9	9	Absent
LC01-T11?/T12	35	50	8	8	Absent
LC01-T23	42	44	5	9	Present
LC01-T24	28	56	5	10	Present
LC01-M	31	56	3	11	Absent
LC01-B7	23	61	4	12	Absent
LC01-B8	33	52	6	9	Present
LC01-B10	40	44	6	10	Present
Core LC02					
LC02-T8?/T9	30	54	5	11	Absent
LC02-M	27	60	4	9	Absent
LC02-B6	28	56	4	12	Absent
LC02-B9	22	61	4	13	Absent
LC02-B18	27	58	4	11	Absent
LC02-B26	34	51	5	10	Absent
LC02-B30	27	58	4	11	Absent
Core LC04					
LC04-T2	31	58	4	7	Absent
LC04-T4	38	48	7	7	Absent
LC04-T5	43	45	4	8	Absent
LC04-T6	28	58	5	8	Absent
LC04-M	27	57	3	13	Absent
LC04-B33	36	50	3	10	Absent
LC04-B36	42	44	6	8	Present
LC04-B42	47	40	5	7	Present
LC04-B46	35	50	8	8	Absent
LC04-B50	28	56	5	11	Present
Core LC06					
LC06-T4	41	41	11	6	Present
LC06-T8	41	43	9	7	Present
LC06-T10	30	56	5	9	Absent
LC06-T17	41	42	10	6	Present
LC06-T19	34	45	14	7	Present
LC06-T21	31	51	11	7	Present
LC06-T25	34	52	3	10	Present
LC06-T31	37	42	14	7	Present
LC06-M	22	59	5	14	Absent
LC06-B17	32	47	16	5	Present
LC06-B33	31	47	15	7	Present
LC06-B34	27	58	3	12	Absent
LC06-B55	31	46	15	8	Present

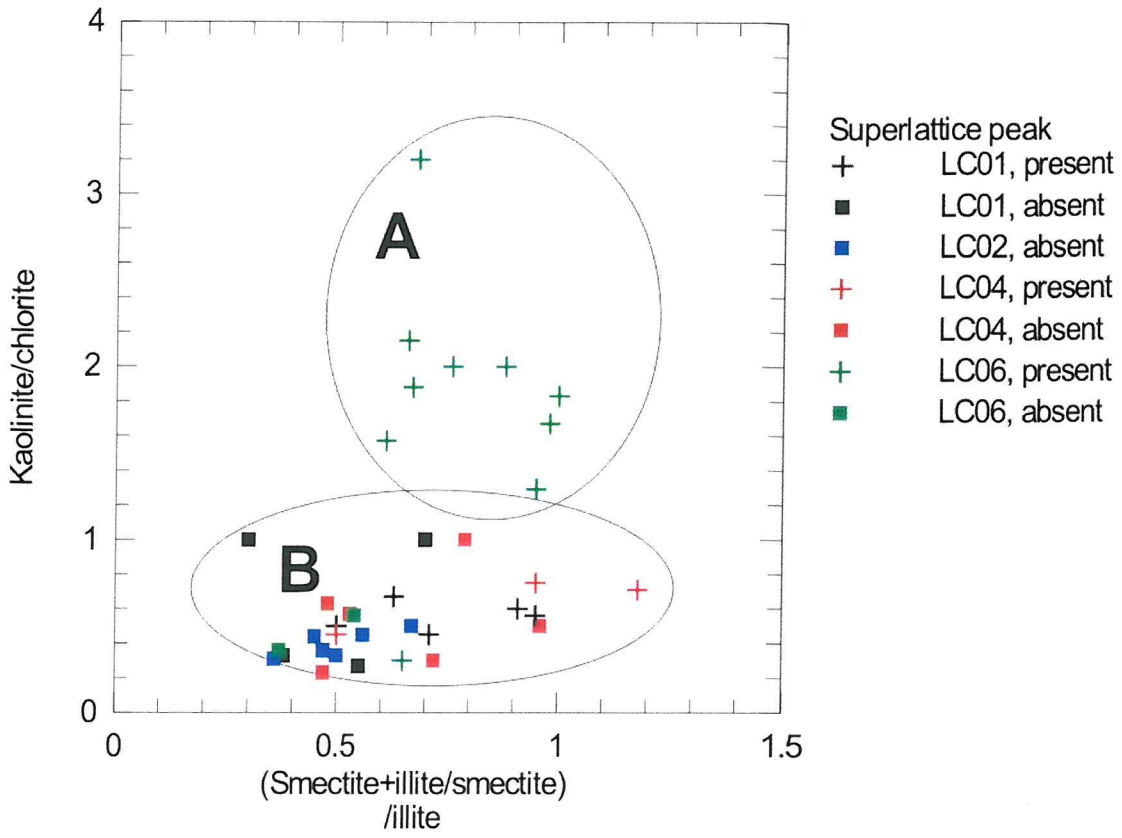

Figure 4.7 Plot of kaolinite/chlorite (K/Chl) versus (smectite+illite/smectite)/illite for all analysed samples. Crosses indicate samples that have the superlattice peak whereas squares indicate samples that lack the superlattice peak. The Figure is divided into two groupings: A (samples with kaolinite/chlorite ratio >1) and B (samples with kaolinite/chlorite ratio <1).

4.3.6 Smear slides

Smear slide examination of turbidite muds and hemipelagic intervals showed that all samples contain a substantial biogenic component (mainly coccoliths, foraminifera and foraminifer fragments) and a terrigenous component (mainly clay, quartz, feldspar and mica). Using the Mazullo et al. (1987) classification, the hemipelagic intervals are classified as clayey nannofossil oozes (>50% nannofossils and bioclasts and <50% terrigenous material, mainly clay) and nannofossil clays (<50% nannofossils and bioclast and >50% terigenous material, mainly clay) and turbidite muds are classified as nannofossil clays (~65-80% terrigenous material (of which >90% clay) and ~20-35% nannofossils and bioclasts).

Table 4.10 (Smectite+illite/smectite)/illite ratios ((S+I/S)/I) and kaolinite/chlorite ratios (K/Chl) calculated for turbidite mud samples. Highlighted samples (grey) have the mixed layer clay mineral illite/smectite with the superlattice peak.

Sample	(S+I/S)/I	K/Chl	Sample	(I+S)/I	K/Chl
LC01			LC02		
LC01-T9	0.71	0.45	LC02-T8?/T9	0.56	0.45
LC01-T11	0.30	1.00	LC02-M	0.45	0.44
LC01-T11?/T12	0.70	1.00	LC02-B6	0.50	0.33
LC01-T23	0.95	0.56	LC02-B9	0.36	0.31
LC01-T24	0.50	0.50	LC02-B18	0.47	0.36
LC01-M	0.55	0.27	LC02-B26	0.67	0.50
LC01-B7	0.38	0.33	LC02-B30	0.47	0.36
LC01-B8	0.63	0.67			
LC01-B10	0.91	0.60			
LC04			LC06		
LC04-T2	0.53	0.57	LC06-T4	1.00	1.83
LC04-T4	0.79	1.00	LC06-T8	0.95	1.29
LC04-T5	0.96	0.5	LC06-T10	0.54	0.56
LC04-T6	0.48	0.63	LC06-T17	0.98	1.67
LC04-M	0.47	0.23	LC06-T19	0.76	2.00
LC04-B33	0.72	0.30	LC06-T20	0.61	1.57
LC04-B36	0.95	0.75	LC06-T25	0.65	0.30
LC04-B42	1.18	0.71	LC06-T31	0.88	2.00
LC04-B46	0.70	1.00	LC06-M	0.37	0.36
LC04-B50	0.50	0.45	LC06-B17	0.68	3.20
			LC06-B33	0.66	2.14
			LC06-B34	0.47	0.46
			LC06-B55	0.67	1.88

4.3.7 Basal sand mineralogy

The size fractions of most basal sands fall within the very fine and medium sand grades of Wentworth (1922) (i.e. in the range 63-500 μm) and the grain sizes of a few samples fall in the silt fraction (<63 μm) (Appendix 4.4). Using the classification of Shepard (1954), the basal sands were subdivided into sands, sandy silt/clay and silt/clay (Appendix 4.4).

The mineralogical interpretations (including carbonate grains) of individual basal sands are summarised in Appendix 4.5. At least 300 grains were examined per sample under a non-polarising microscope (details are presented in Appendix 4.5).

In order to estimate proportions of sedimentary components, the comparative percentage charts of Rothwell (1989) were used. Samples that contained more than 50% of terrigenous material were classified as terrigenous sands, whereas sand samples with over 50% of biogenic grains were classified as biogenic sands (Table 4.11). Six sand samples are classified as biogenic sands, whereas the majority of basal sands (31) are terrigenous. Almost all sand samples are poorly sorted. Quartz grains in individual

samples have angular (average 35% of the quartz fraction), subrounded (average 39% of the quartz fraction) and rounded (average 26% of the quartz fraction) shapes (Appendix 4.6), suggesting that they are of mixed maturity.

Table 4.11 Mineralogical classification of the basal sands following the method of Rupke and Stanley (1974), with terrigenous sands (TERR) and biogenic sands (BIOG). Samples with a significant contribution of organic material, though not dominated by it, are denoted by ^{ORGA}. One sample (LC06-B51) is composed of equal amounts of biogenic and terrigenous sand (Appendix 4.5). The mineralogical composition of 16 basal sands was also determined using X-Ray Powder Diffraction.

Sample	Classification	dominating mineral	X-Ray Powder Diffraction	Comments
LC01-T11?/T12	BIOG	mica		contains organic material
LC01-T23	TERR	quartz	Quartz, feldspar ((P>K), mica	contains sponge spicules
LC01-M	TERR	quartz	Quartz, feldspar ((P>K), mica	
LC01-B7	BIOG	mica	Mica, Quartz, feldspar	
LC02-T1	TERR	quartz	Quartz, feldspar ((P=K), mica	>10% accessory minerals
LC02-T8?/T9	TERR/^{ORGA}	quartz and mica		
LC02-M	TERR	quartz	Quartz, feldspar ((P>K), mica	>10% feldspar
LC02-B1?	TERR	quartz		
LC02-B2	TERR	quartz		>10% accessory minerals
LC02-B3	TERR	quartz		contains siltstone fragments
LC02-B3?/B4	TERR	quartz		
LC02-B3?/B4?/B5	TERR/^{ORGA}	quartz		
LC02-B6	TERR	quartz		
LC02-B7	TERR	quartz		
LC02-B9	TERR	quartz		>10% accessory minerals
LC02-B13?/B14?/B15	TERR	quartz	Quartz, feldspar ((P>K), mica	>10% accessory minerals
LC02-B13?/B14?/B15?/B16	TERR	quartz	Quartz, feldspar (P>K), mica	contains siltstone fragments
LC02-B13?/B14?/B15?/B16?/B17	TERR	quartz		>10% feldspar, contains lithics and siltstone fragments
LC02-B18	TERR	quartz	Quartz, feldspar ((P>K), mica	
LC02-B19	TERR	quartz	Quartz, feldspar ((P>K), mica	>10% feldspar
LC02-B20	TERR	quartz		
LC02-B26	TERR	quartz		
LC02-B30	TERR	quartz	Quartz, feldspar ((P>K), mica	
LC02-B31	TERR	quartz and mica		
LC02-B31?/B32	BIOG	quartz and mica		
LC04-M	TERR	quartz	Quartz, feldspar ((P>K), mica	
LC04-B37	TERR	quartz	Quartz, feldspar ((P>K), mica	
LC06-T21	TERR	quartz	Quartz, feldspar ((P>K), mica	
LC06-T27	TERR	quartz		contains siltstone fragments
LC06-T35	BIOG	mica		contains sponge spicules and some wood fragments
LC06-T36	TERR	quartz	Quartz, feldspar ((P>K), mica	
LC06-T37	TERR	quartz		contains sponge spicules
LC06-M	TERR	quartz	Quartz, feldspar ((P>K), mica	
LC06-B6	TERR	quartz		
LC06-B38	BIOG	mica	Quartz, feldspar ((P>K), mica	
LC06-B51	BIOG/TERR	quartz		contains siltstone fragments
LC06-B55	BIOG	mica		contains sponge spicules and some wood fragments

4.3.8 Mineral identification by X-Ray Powder Diffraction

The non-carbonate mineralogical composition of basal sands was determined by X-Ray Powder Diffraction for 16 samples (Table 4.11). All samples contained quartz, feldspar (Plagioclase and K-feldspars) and mica minerals, as was also suggested by mineralogical (non-carbonate) description from visual observations with a binocular microscope (see Table 4.11).

4.4 DISCUSSION

Turbidite beds have been identified and characterised using sedimentological and geochemical analysis and using geophysical properties. Based on these analyses, it will be examined whether turbidites can be split into different groups that could possibly reflect different source areas.

4.4.1 Turbidite deposits in the four long piston cores

The number of recovered turbidites varies between the four cores (Table 4.12). The most turbidites occur in core LC06 (over 100 turbidites), whereas LC01 (32-37 turbidites) has the least (Table 4.12). Going from north (LC01) to south (to LC02 and then LC04 and LC06), the number of turbidites per core increases (Table 4.12). These differences in turbidite numbers in the cores are probably related to source area proximity and the time period covered by each core. This will be discussed in more detail in Chapters 5 and 6.

The average thickness of turbidite beds also varies between the four cores (Table 4.12), with LC02 having the highest average thickness (typically 53-70 cm) and LC06 the lowest (16-17 cm). Turbidite deposits from the two 'northern' cores LC01 and LC02 are generally thicker than turbidite deposits from the 'southern' cores LC04 and LC06 (Table 4.12), which may indicate that the northern cores have a more proximal source area with abundant sediment supply. Thinner turbidite deposits in LC04 and LC06 may indicate either more distal deposition or that the source areas had a lower sediment supply. Since LC02 contains the most turbidites with basal sands it is likely that these turbidite deposits are more proximal to a major source area.

Table 4.12 Number of turbidites per core, total turbidite thickness per core and calculated average corrected turbidite thickness (total turbidite thickness derived from Table 4.6).

Core	Total thickness of turbidites (m)	Number of turbidites	Average thickness per turbidite (cm)
LC01	15.52	32-37	42 – 49
LC02	22.95	33-43	54 – 70
LC04	20.44	55-58	35 – 37
LC06	19.44	118-119	16

4.4.2 Turbidite provenance

Not all of the analyses presented in Section 4.3 provide a clear basis for determining turbidite groups that could ultimately give an indication of turbidite provenance. Analyses that may be particularly pertinent include: 1) calcium carbonate content of turbidite muds, 2) clay mineralogy and 3) basal sand mineralogy. Characteristics of provenance areas are presented in Chapter 2 and possible relations between turbidite deposits and provenance are discussed in Chapter 6.

4.4.2.1 Turbidite provenance from turbidite muds

In Section 4.3.4 turbidite muds were divided into two groups based on $CaCO_3$ content. Groups 1 turbidite muds, which occur almost exclusively in LC06, are characterised by low $CaCO_3$ contents (< 25%) (Figure 4.11). Group 2 turbidite muds occur in all four cores and have higher $CaCO_3$ contents (> 25%) (Figure 4.4).

In Section 4.3.5, it was shown that the clay mineralogical composition of turbidite muds varies between different turbidites. Two broad groups (A and B) can be identified based on the presence (A) and absence (B) of a superlattice peak in the expandable clays. The presence of a superlattice peak suggests that the mixed layer clay mineral illite/smectite is the dominant expandable clay mineral, whereas its absence suggests that smectite is the dominant expandable clay mineral. Clays that contain the illite/smectite superlattice peak (Group A) are commonly interpreted as being derived from regions that have been subjected to burial metamorphism at temperatures of between 70-220°C. Samples that lack this superlattice peak (Group B) are more typical of recent sediments (T. Clayton pers. comm., 2002). Clay samples from Group A (with the illite/smectite superlattice peak) only occur in LC01, LC04 and LC06 (Table 4.9). Clay samples from Group B (without the superlattice peak) occur throughout all four cores. In LC01 and LC04, clay minerals with the superlattice peak have a lower kaolinite/chlorite ratio (<1), whereas in LC06 the situation is reversed and

almost all clay minerals with the superlattice peak have a higher kaolinite/chlorite ratio (>1) (Table 4.9, Figure 4.8). Thus, Group A can be subdivided into A_1 (clay minerals that show the superlattice peak with a kaolinite/chlorite ratio >1) and A_2 (almost identical to A_1, except that kaolinite/chlorite ratio <1) (Figure 4.8). Clay minerals with the superlattice peak and higher kaolinite/chlorite ratios may originate from a southern (i.e. African) source, as Guerzone et al. (1997) have shown that the clay mineralogy of Saharan dust is higher in kaolinite content than chlorite. Higher kaolinite/chlorite ratios in several clay samples from LC06 are suggestive of higher concentrations of Saharan dust in these clays.

Table 4.13 Calcium carbonate content and kaolinite/chlorite ratio (K/Chl) for turbidite mud samples that were analysed for clay mineralogy. Highlighted samples (grey) have a superlattice peak.

Sample	$CaCO_3$ content	K/Chl	Sample	$CaCO_3$ content	Chl
LC01			LC02		
LC01-T9	25.55	0.45	LC02-T8?/T9	30.29	0.45
LC01-T11	41.89	1.00	LC02-M	34.70	0.44
LC01-T11?/T12	40.09	1.00	LC02-B6	31.74	0.33
LC01-T23	27.87	0.56	LC02-B9	29.34	0.31
LC01-T24	23.33	0.50	LC02-B10	29.00	
LC01-M	33.28	0.27	LC02-B18	29.27	0.36
LC01-B7	29.50	0.33	LC02-B26	30.78	0.50
LC01-B8	28.69	0.67	LC02-B30	28.22	0.36
LC01-B10	23.34	0.60			
			LC06		
LC04			LC06-T4	17.36	1.83
LC04-T2	33.52	0.57	LC06-T8	18.45	1.29
LC04-T4	30.46	1.00	LC06-T10	35.98	0.56
LC04-T5	30.70	0.5	LC06-T17	16.22	1.67
LC04-T6	40.98	0.63	LC06-T19	25.35	2.00
LC04-M	32.86	0.23	LC06-T21	31.40	1.57
LC04-B33	30.27	0.30	LC06-T25	30.03	0.30
LC04-B36	25.50	0.75	LC06-T31	25.39	2.00
LC04-B42	27.93	0.71	LC06-M	33.81	0.36
LC04-B46	42.31	1.00	LC06-B17	19.34	3.20
LC04-B50	26.90	0.45	LC06-B33	21.11	2.14
			LC06-B34	32.56	0.46
			LC06-B55	22.53	1.88

The two broadly defined groups (Group 1 and 2 based on $CaCO_3$ content and Group A and B based on the presence or absence of a superlattice peak) can be clearly discriminated in Figure 4.8. All samples with lower $CaCO_3$ contents (<25%) from Group 1 have a superlattice peak (clay mineral Group A) (Figure 4.8, Table 4.13). Furthermore, all samples from $CaCO_3$-based Group 1 with a kaolinite/chlorite ratio <1 are from LC01 and LC04, whereas samples from Group 1 with kaolinite/chlorite ratios >1 are all from LC06 (Figure 4.8). If the separation of the two groups is also considered

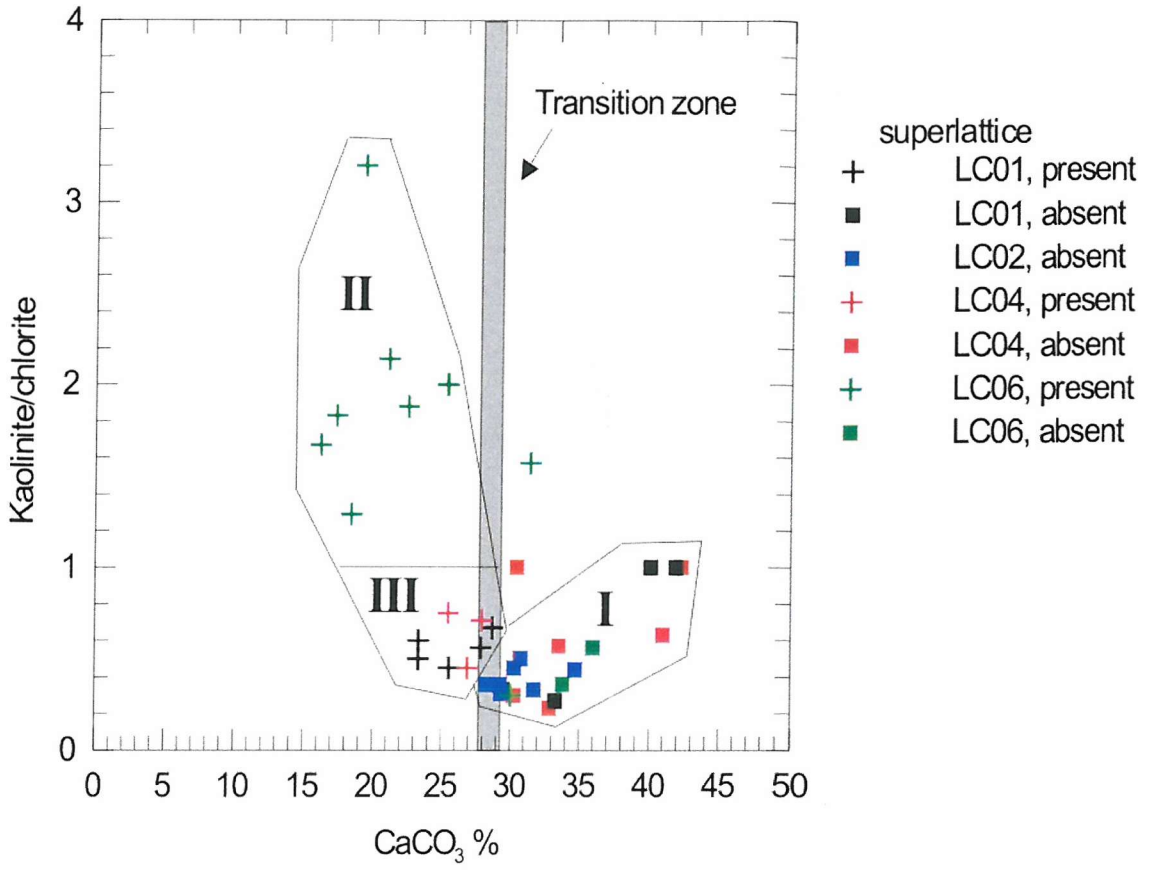

Figure 4.8 Kaolinite/chlorite ratio plotted against $CaCO_3$ percentage for 40 turbidite muds in LC01, LC02, LC04 and LC06. Several of the turbidite muds contain an illite/smectite superlattice peak. Three Groupings: I, II and III are identified on criteria that are further explained in the text.

on the basis of the presence or absence of a superlattice peak, this separation occurs at 28% $CaCO_3$ rather than at 25%, since the first sample without a superlattice peak has a $CaCO_3$ content of 28% (Table 4.13). Three samples with $CaCO_3$ contents of >28% (LC01-B8, LC06-T21 and LC06-T25) with a superlattice peak are present in Figure 4.8. The last sample (LC06-T25) has a kaolinite/chlorite ratio <1. The above suggests that $CaCO_3$ content and clay mineralogy of turbidite mud samples may be used to divide them into three groupings possibly related to source area. Turbidite Group I occurs in all the four cores and has high $CaCO_3$ contents (>28%), does not display a superlattice peak and has a kaolinite/chlorite ratio of <1. Turbidite muds from second Group II only occur in LC06 and generally have lower $CaCO_3$ contents (<28%), a superlattice peak and a kaolinite/chlorite ratio of >1. Finally, turbidite muds from Group III are present in LC01, LC04 and possibly LC06; they have low $CaCO_3$ contents (<28%) and a superlattice peak but a kaolinite/chlorite ratio of <1. On the basis of the above evidence it may be possible to interpret $CaCO_3$ contents in turbidite

muds as representing possible source areas. In Table 4.14, the contributions of the three Groups have been calculated per core based on $CaCO_3$ contents.

The BAP turbidites are dominated by turbidite muds from Group I. Turbidites from Group II only occur in LC06 and make up ~11% of the total turbidite thickness in the four cores. Turbidites from Group III, which may only occur in LC01, LC02 and LC04, only make up ~5% of the total turbidite thickness. In terms of thickness, cores LC01, LC02 and LC04 are dominated by turbidites from Group I whereas in core LC06, turbidites from Groups I and II are equally important.

Table 4.14 Contributions of each Group (as defined in the text) to the total sediment thickness in the four long piston cores. ? indicates that the contribution of samples whose $CaCO_3$ content was not measured.

	Total thickness in core (cm)/ % in core					
Group	LC01	LC02	LC04	LC06	Total	% of total
I	1380/ 84%	2103/ 92%	1839/ 90	994/ 52%	6316	80%
II				842/ 44%	842	11%
III	213/ 13%	26/ 1%	173/ 8%		412	5%
?	45/ 3%	167/ 7%	33/ 2%	79/ 4%	342	4%
Total	1651.6	2296.1	2011.8	1821.85	7781.35	100

4.4.2.1 Turbidite provenance from basal sand mineralogy

In Section 4.3.7 it was shown that basal turbidite sands can be divided into groups that are dominated by terrigenous and biogenic grains (Table 4.11). The biogenic component of the basal biogenic turbidite sands consists mainly of foraminifer and pteropod tests and test fragments. The biogenic component in biogenic turbidites is due to either: 1) long accumulation times before turbidite emplacement that caused significant quantities of hemipelagic material to accumulate carbonate that was later incorporated into the flow during emplacement, 2) emplacement from high productivity areas, or 3) through turbidity current winnowing that caused substantial amounts of hemipelagic material to be incorporated into the current during downslope transport. X-ray powder diffraction of the non-carbonate sand fractions of biogenic and terrigenous turbidites shows that almost all basal sands have similar mineralogical compositions, that are dominated by quartz (~60%) with abundant feldspar (~20%) and common mica

(~5%). The striking similarity of the mineralogy of the non-carbonate fraction does not imply that all turbidites are from one similar source, but it probably indicates that several source areas have hinterlands with similar mineralogical compositions. However, one sample, LC01-B7, is dominated by mica (~90%) with common quartz (~10%) (Table 4.11), which may possibly indicate this sample comes from a different source area or that it is a more distal deposit. In LC02 and LC06, there are several basal sands that contain similar siltstone fragments (generally well-rounded and found in the >600 μm size fraction) that may suggest that they originate from a distinct source area.

Heavy mineral analysis might prove useful in determining turbidite provenance of basal sands for turbidites in this basin. Unfortunately there has not been time to perform meaningful heavy mineral analyses in this study.

4.5 CONCLUSIONS

- Sediment cores from the BAP are dominated by turbidite deposits (mainly ponded muds (Te) some turbidites contain silt and/or sand at their bases).

- The number and thickness of turbidite beds varies between the four long piston cores. Thicker turbidites and coarse basal sands in LC01 and LC02 suggest that these cores are more proximal to their main source area, while thinner turbidite beds in LC04 and LC06 may indicate distal turbidite deposition or turbidites being deposited from a source area with a lower sediment supply.

- Based on $CaCO_3$ content and clay mineralogy, turbidite muds can be divided into three different Groups that are perhaps indicative of source areas. Group I is characterised by high $CaCO_3$ contents (>28%) and does not show the presence of a superlattice peak in clay mineralogy, suggesting that smectite is the dominant expandable clay mineral. This Group has a kaolinite/chlorite ratio of <1. Turbidite muds from Group II only occur in LC06 and generally have lower $CaCO_3$ contents (<28%), a superlattice peak, indicating that the mixed layer clay mineral illite/smectite is the dominant expandable clay mineral, and a kaolinite/chlorite ratio of >1. Finally, turbidite muds from Group III also have lower $CaCO_3$ contents (<28%) and a superlattice peak but a kaolinite/chlorite ratio <1.

- Turbidite muds from Group I dominate in LC01 and LC02 and LC04, whereas in LC06 they are as equally common as turbidite muds belonging to Group II. Turbidite muds characteristic of Group III have been identified in all four cores, but the contribution of these turbidites to the total sediment record is small (<10%).

CHAPTER 5 – ARIDITY EPISODES DURING THE LAST GLACIAL CYCLE RECORDED IN CALCIUM CARBONATE RECORDS FROM THE WESTERN MEDITERRANEAN SEA

Hoogakker, B.A.A., Rothwell, R.G., Rohling, E.J., Paterne, M.[#] and Stow, D.A.V.
Southampton Oceanography Centre, Empress Dock, Southampton, SO14 3ZH, UK
Laboratoire des Sciences du Climat et de l'Environnement, Laboratoire mixte CNRS-CEA, Domaine du CNRS, Avenue de la Terrasse, 91198 Gif sur Yvette, France

ABSTRACT

Hemipelagic intervals in four giant piston cores from the Balearic Abyssal Plain (western Mediterranean Sea) were studied in order to determine fluctuations in the supply of terrigenous sediments during the last 130,000 years. Carbonate records from hemipelagic intervals in these cores display distinct 'Atlantic' type cycles, where glacial periods show on average 20% lower calcium carbonate contents due to increased dilution with terrigenous material. Besides major calcium carbonate variations that correlate to glacial/interglacial cycles, there are also short-term minima in the calcium carbonate content that appear to reflect short-term (millennial-scale) climatic cooling events. These short-term events are also characterised by enhanced magnetic susceptibility values, especially the cold events within Marine Isotope Stage 3. We interpret these short-term events as reflecting periods of increased aridity in western Mediterranean environments, possibly correlating to Heinrich events, Dansgaard-Oeschger stadials and cold events within Marine Isotope Stage 5. Our results further indicate that about 90% of the sedimentary sequence of the Balearic Abyssal Plain consists of turbidites. These, however, did not cause significant erosion on the abyssal plain substrate, and an almost complete stratigraphy remains present in the intercalated hemipelagic intervals.

Keywords: calcium carbonate, dilution, magnetic susceptibility, western Mediterranean, last glacial cycle

5.1 INTRODUCTION

The Mediterranean Sea is a semi-enclosed basin (Figure 5.1) with anti-estuarine circulation. Its general circulation has a halo-thermal nature, controlled by the strong excess of evaporation over freshwater input and net cooling in the basin. The resultant net buoyancy loss drives surface inflow and subsurface outflow through the Strait of Gibraltar.

The major glacial/interglacial climatic oscillations of the Pleistocene had a large influence on the western Mediterranean environment (Rose et al., 1999). The development of a fixed anticyclone over the north European ice sheet and colder sea surface temperatures during glacial times resulted in colder and drier conditions (Rognon, 1987) and increased seasonality of precipitation over the Mediterranean (Prentice et al., 1992). The present climate in the western Mediterranean is characterised by a high interglacial global sea level, a relatively dense vegetation cover, relatively high infiltration rates and moderate river discharges (Rose et al., 1999). The glacial western Mediterranean environment, in contrast, was characterised by a low global sea level, open vegetation with large areas of bare ground and unconsolidated sediments, soils affected by high physical stresses and highly peaked river-discharge regimes (Rose et al., 1999). Sea surface temperature (SST) estimates for the Alboran Sea, based on the relative abundances of planktonic foraminifera species, varied considerably between glacial and interglacial periods, with interglacial maximum SST of 20 to 23°C and glacial maximum SST of 10 to 15°C (González-Donoso et al., 2000). Alkenone-based sea surface temperature estimates give similar values of ~ 19°C during the Holocene and 11-13°C during the last glacial maximum (Cacho et al., 2001). Recent research (Rohling et al., 1998; Cacho et al., 1999, 2001; Paterne et al., 1999; Combourieu-Nebout et al., 2002) has demonstrated that the western Mediterranean basin was strongly influenced by the millennial-centennial climatic and oceanographic variability observed in the north Atlantic region during the last glacial period.

The composition of deep-sea sediments reflects the climatic conditions of adjacent continental regions, and/or the oceanic and atmospheric circulation at the time of deposition (McManus, 1970; Kolla et al., 1979). For example, a higher proportion of terrigenous material accumulated in the equatorial and tropical Atlantic offshore of West Africa, during glacial times compared to interglacial times, due to higher

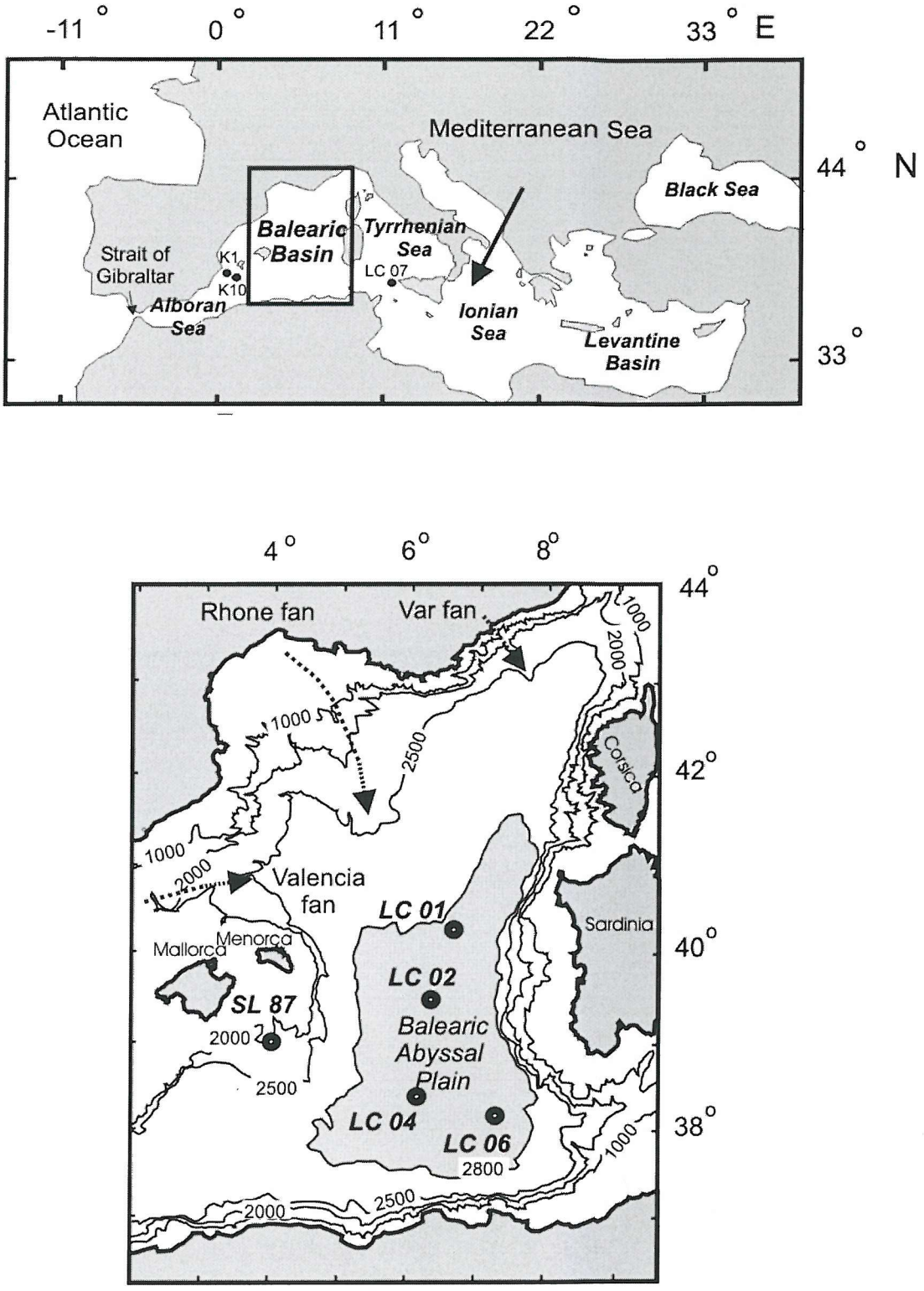

Figure 5.1 Maps of the BAP in the western Mediterranean Sea and location of the cores studied (LC01, LC02, LC04 and LC06). The locations of SL87 (Weldeab et al., 2003), K1 and K10 (Flores et al., 1997) and LC07 are also shown.

terrestrial influxes associated with higher trade wind intensities (Diester-Haas, 1976). Changes in the supply of terrigenous material to deep-sea sediments can be estimated by determining the proportion of calcium carbonate, since carbonate content in pelagic sediments is inversely related to dilution with terrigenous material (Hays and Perruzza, 1972). Higher carbonate contents in pelagic sediments of interglacial times reflect a low terrestrial input due to reduced trade wind intensities and a general decrease in aridity (Hays and Perruzza, 1972). Conversely, low carbonate contents in glacial pelagic sediments indicate enhanced terrestrial input associated with higher trade wind intensity and enhanced aridity (Hays and Perruzza, 1972). This scenario is supported by studies by Parkin and Shackleton (1973) and Parkin (1974) who showed that the Saharan desert belt expanded southward during glacial periods.

Larrasoaña et al. (2003) obtained a high-resolution proxy record of northern Sahara dust supply into the eastern Mediterranean for the last 3 Ma, based on magnetic measurements. They related dust flux minima, found at times of northern hemisphere insolation/monsoon maxima, to the northward penetration of the African summer monsoon front beyond the central Saharan watershed (~21°N). They also argued that such northward penetration of the African summer monsoon agrees with the inferred expansion of (savannah-like) vegetation cover ('greening of the Sahara' of Claussen et al., 1998 and Brovkin et al., 1998) and an increase in the soil cohesiveness throughout large areas of the northern Sahara, which resulted in a decrease in dust production, similar to present conditions in the Sahel (Middleton, 1985).

The western Mediterranean Sea is surrounded by catchment areas subject to continental, alpine and Mediterranean climate regimes in the north, and Mediterranean to semi-arid climates in the south. Weldeab et al. (2003) used Si/Al and Ti/Al ratios as well as Sr and Nd isotopes to show that the Saharan terrigenous input into the western Mediterranean Sea is predominantly from the southwest (Morocco/NW. Algeria) and southeast (Tunisia/W. Libya) during interglacial periods and from the southern Saharan/Sahelian region during glacial times. The change in sediment source reflects changes in the prevailing atmospheric circulation over the basin (Weldeab et al., 2003). These authors also found that glacial terrigenous input was much higher than during interglacial times. A high-resolution record of lithogenic fraction variability from the Alboran Sea reveals that millennial- to submillennial-scale marine oscillations, linked with Heinrich Events and Dansgaard-Oeschger stadials, were characterised by

increases in the northward Saharan dust transport, due to increased wind intensity over the Sahara (Moreno et al., 2002).

Here, we discuss the calcium carbonate content of hemipelagic sediment sequences in four giant piston cores from the BAP, to determine fluctuations in the supply of terrigenous sediments during the last 130,000 years. Supported by AMS radiocarbon dates, biostratigraphy and oxygen isotope stratigraphy, the derived calcium carbonate records are used to calculate terrigenous accumulation rates that are compared with accumulation rates reported by Weldeab et al. (2003). It has been suggested that more than 80% of the total input of terrigenous sediment (excluding gravity flow deposits) in the western Mediterranean is from Saharan dust (Loye-Pilot et al., 1986; Martin et al., 1989; Guerzoni et al., 1999). The lithogenic/terrigenous fraction of core SL87/KL66, from Marine Isotope Stage (MIS) 7 until the present is considered to consist exclusively of European and Saharan windblown dust (Weldeab et al., 2003). Most of the cores from the BAP used in this study, are located even further away from major riverine sources than SL87/KL66 (Figure 5.1) and the lithogenic/terrigenous fractions in hemipelagic intervals from these cores are therefore interpreted as windblown dust. Changes in the amount of the windblown dust in hemipelagic intervals in our four cores are likely to be accompanied by changes in magnetic susceptibility, where an increase in magnetic susceptibility reflects an increase in the amount of magnetic minerals (contained in dust). To test this hypothesis, we compare the derived calcium carbonate and magnetic susceptibility data.

5.2 CARBONATE CYCLES IN THE WESTERN MEDITERRANEAN SEA

The calcium carbonate ($CaCO_3$) content of deep-sea marine sediments is generally controlled by three factors, assuming that marine plankton forms the main carbonate component. These factors include: (i) dissolution, (ii) surface water productivity, and (iii) dilution by terrigenous sediments. Dissolution does not play a major role in the BAP, since water depths in the western Mediterranean are too shallow (<2800 m) to reach the carbonate lysocline or carbonate compensation depth (CCD). Van Os et al. (1994) attributed distinctive Pliocene $CaCO_3$ cycles in the Mediterranean to a combination of productivity variations and dilution by enhanced terrigenous input. Concerning the Quaternary, Flores et al. (1997) suggested that, after accounting for the dilution factor, production of coccolithophores appears to have been higher during

interglacial periods. Other authors disagree, suggesting instead that surface water productivity increased during glacial intervals, based on bio-mediated barium accumulation rates (Weldeab et al., 2003) and the high abundance of diatoms in sediments (Bárcena et al., 2001). The latter two studies may reflect non-coccolith productivity. Combined with the data from Flores et al. (1997), it may suggest that carbonate (coccolith) productivity was higher during interglacial times, while non-carbonate (opal, diatom) productivity was elevated during glacial times.

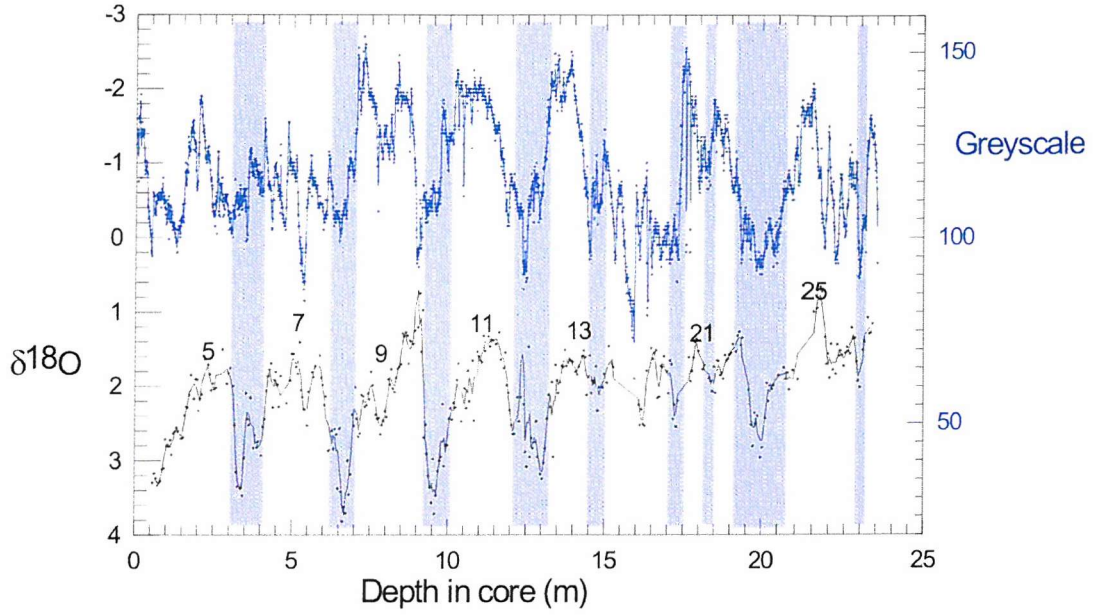

Figure 5.2 Greyscale intensity (top) and oxygen isotope data (bottom) for LC07 from the Strait of Sicily, plotted against depth. Oxygen isotope data for this core are from Dinarès-Turell et al. (2003). Grey shaded areas indicate glacial intervals. Some interglacial stages are numbered.

Greyscale intensity data from western Mediterranean piston core LC07, taken north of Skerki Channel in the Sicily Strait, at 488 metres water depth, provides a relative measure of the carbonate content through the core (Figure 5.2). Oxygen isotope data for LC07 (Dinarès-Turell et al., 2003) indicate that glacial periods coincide with low greyscale intensities (=dark shades), which represent lower $CaCO_3$ contents, whereas interglacials have higher greyscale intensities (=lighter shades) that are associated with higher $CaCO_3$ contents (Figure 5.2). In this sense, the western Mediterranean carbonate cycles of LC07 are similar in character to those observed in the Atlantic (see Ruddiman, 1971; Hays and Peruzza, 1972; Volat et al., 1980; Grützner et al., 2002).

5.3 LOCATION

The geological and geographical setting of the (BAP) (Figure 5.1) has been previously discussed in Chapter 4. Hemipelagic accumulation rates measured in nearby cores SL87/KL66 and K1 from the Balearic Rise and core K10 from the Algero-Balearic Sea (for location see Table 5.1) are around 3-4 cm/ka (Flores et al., 1997; Weldeab et al., 2003).

Table 5.1 Location and water depth of the studied long piston cores.

Core	Latitude	Longitude	Water depth (m)	Core	Latitude	Longitude	Water depth (m)
SL87/KL66	38°59.34'N	4°01.40'E	1900	LC01	40°15.82'N	6°53.23' E	2845
K1	38°57.0'N	0°50.0'E	750	LC02	39°31.88' N	6°22.58' E	2860
K10	38°03.0'N	1°00.9'E	1957	LC04	38°39.01' N	6°06.64' E	2855
LC07	38°08.72'N	10°04.73'E	488	LC06	38°00.66' N	7°11.09' E	2845

LC07 is from Dinarès-Turell et al. (2003); SL87 from Weldeab et al. (2003), K1 and K10 from Flores et al. (1997).

5.4 SEDIMENT CORES, TIME-STRATIGRAPHIC FRAMEWORK AND MAGNETIC SUSCEPTIBILITY

5.4.1 Sediment cores

Four giant piston cores (LC01, LC02, LC04 and LC06) were recovered from the BAP (Figure 5.1, Table 5.1) during *Marion Dufresne* Cruise 81 in 1995, using a Calypso piston corer. The cores, reaching 27 to 32 metres in length, were taken about 100 to 120 km apart to form an approximate North-South transect across the plain (Figure 5.1). All of the cores are dominated by sequences of thick, grey and greyish olive structureless muds (some grading down to basal sands and silts) that are underlain by foraminifer-rich mud intervals. The structureless muds and associated silts and sands are interpreted as turbidite deposits, whereas the foraminifer-rich intervals are interpreted as hemipelagic deposits. Turbidite beds are distinguished from hemipelagic sediments by their sharp bases, normal grading, relatively high terrigenous content, colour and lack of bioturbation (except for the bioturbated top of a turbidite, which is rarely more than a few decimetres thick; Stow and Piper, 1984; Jones, 1992; Stow and

Fabrez, 1998) and the presence of reworked foraminifera (Chapter 4). Additionally, it is usually possible to distinguish turbidite beds from hemipelagic sediments through the sedimentary structures present (Rupke and Stanley, 1974; Stow and Fabrez, 1998).

5.4.2 Time-Stratigraphic framework

The time-stratigraphic frameworks for LC01, LC02, LC04 and LC06 are based on the nannofossil biozones of Weaver (1983), accelerator mass spectrometry (AMS) ^{14}C dating, oxygen isotope stratigraphy (only for LC01 and LC04) and correlation based on $CaCO_3$ records. Turbidity currents that deposited on the BAP might have caused erosion of the underlying sediments, thus creating chronostratigraphic discontinuities. Furthermore, the possibility of undetected turbidites within the cored sequence should be considered. In a sufficiently detailed time-stratigraphic framework such features should show up as irregularities and can therefore be tested for.

The boundary between the Weaver (1983) coccolith zones 1 and 2 was determined in our cores by Rothwell et al. (1998) and was dated at ~50,000 years before present. Coccolith zone 1 is defined as an interval dominated by the nannofossil *Emiliania huxleyi*, whereas this species is much rarer in zone 2 where *Gephyrocapsa muellerae* becomes dominant (Figure 5.3).

Rothwell et al. (1998) reported eight radiocarbon dates for hemipelagic intervals that bracket a Late Pleistocene megaturbidite that is present in all of the cores (Table 5.2). We obtained four additional radiocarbon dates (Table 5.2). All are based on clean, handpicked planktonic foraminifera and pteropods from the >150 μm size fraction. The reported radiocarbon convention ages were calibrated using INTCAL 98 (Stuiver et al., 1998). Two radiocarbon convention ages of 23,410 and 34,380 were calibrated for variations in geomagnetic field intentsity using the curve of Laj et al. (1996).

The planktonic foraminifera species *Neogloboquadrina pachyderma* (right-coiling or dextral variety) was selected for stable oxygen and carbon isotope analysis using fifteen to twenty specimens from the 250 – 400 μm size fraction. *N. pachyderma* occurs virtually continuously throughout the hemipelagic intervals of cores LC01 and LC04. Oxygen and carbon isotope ratios were measured with a Europa GEO 20 20 stable isotope ratio mass spectrometer, with individual acid bath carbonate preparation lines.

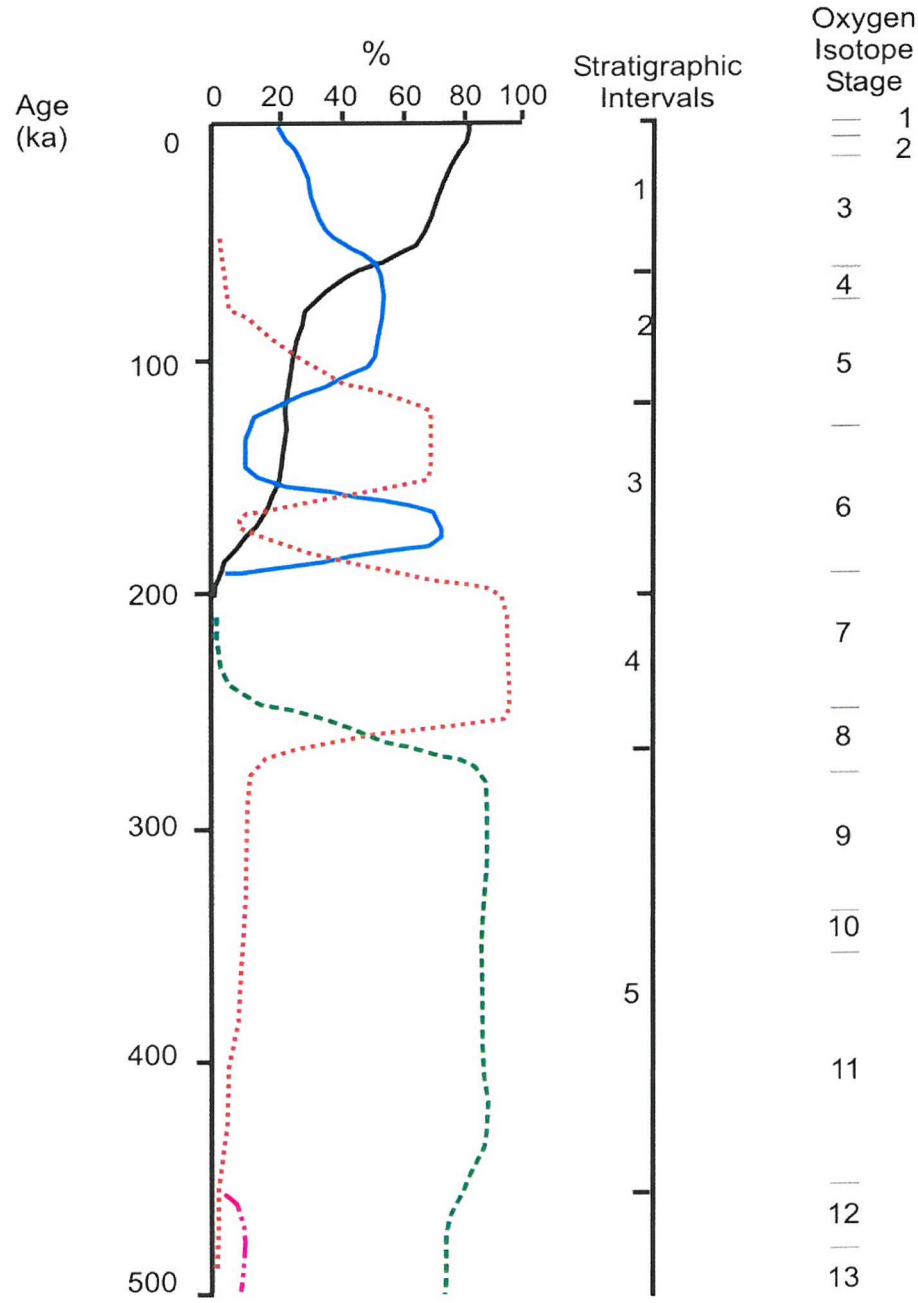

Figure 5.3 Generalized coccolith distribution through the last 500,000 years as recorded in the King's Trough area (from Kidd et al., 1983). Each coccolith interval can be defined against a time scale and various intervals relate to oxygen isotope stages.

Analytical precision of powdered carbonate standards is 0.06% for $\delta^{18}O$ and $\delta^{13}C$. The stable isotopes are expressed as $\delta^{18}O$ and $\delta^{13}C$ in per mil (‰) values relative to the Vienna Pee Dee Belemnite standard (V-PDB). A total of 42 and 60 samples were analysed for LC01 and LC04, respectively. The $\delta^{18}O$ records were initially divided into the standard $\delta^{18}O$ stages (MIS) following the nomenclature of Emiliani (1955) and Shackleton and Opdyke (1973). The oxygen isotope stages were then further subdivided into substages or events based on Imbrie et al. (1984) and Prell et al. (1986). The time-scale of Martinson et al. (1987) was applied for $\delta^{18}O$ stages and events.

$CaCO_3$ contents were measured by coulometry. Samples were collected from hemipelagic intervals at 2 to 4 cm intervals when sufficiently thick. The top 12 to 13 metres of LC06 appeared disturbed and were therefore not sampled. Samples were thoroughly oven-dried at 100°C. The dried samples were then powdered and $CaCO_3$ content was measured from CO_2 liberated by reaction with 10% phosphoric acid for six minutes. A total of 376 samples were analysed. Triplicate analyses were performed on 129 samples to determine reproducibility (Table 5.3). The analytical precision (standard deviation) for standard bulk samples was 1.50%.

5.4.3 Magnetic susceptibility

Environmental magnetic parameters such as magnetic susceptibility are useful in studies of marine and lake sediments, because they can be sensitive indicators of temporal variations in the concentration and grain size of terrigenous material deposited on the sea and lake floor (Verosub and Roberts, 1995). Fluctuations in concentration and size of magnetic grains in deep-sea cores can be climatically modulated (e.g. Amerigian, 1974; Kent, 1982; Oldfield and Robinson, 1985; Bloemendal and DeMenocal, 1989; Robinson et al., 1995). In the North Atlantic, for example, glacial periods are characterised by high concentrations of magnetic minerals, in association with low carbonate contents and increased amounts of ice-rafted detritus. In contrast, sediments from interglacial periods have low magnetic mineral concentrations and high carbonate contents (Robinson, 1986). A Bartington Instruments MS2EI point sensor was used to measure the magnetic susceptibility of the hemipelagic intervals in the four cores, at 1 cm intervals.

Table 5.2 Conventional and calibrated radiocarbon dates for 12 samples (3 in each core).

Core	Sample depth (metre below core top)	Sample number	Hemipelagic depth (cm)	^{14}C age years BP ± 1σ	Calibrated age (years BP)
LC01	**6.95-7.03** *	a	26 - 29.5	8066 ± 47	8445 – 8573
"	**14.49-14.61** #	b	71 – 77	17580 ± 120	19994 – 20674
"	**23.52-23.63** #	c	79.5 – 85.5	20340 ± 150	23092 – 23928
LC02	**3.56-3.60** *	d	26.5 – 30	9303 ± 49	9833 – 10125
"	**8.72-8.88** #	e	70 – 80.5	16900 ± 120	19223 – 19879$^{\Delta}$
"	**17.78-17.93** #	f	86.5 – 97	23410 ± 210	~26760 **
LC04	**1.97-1.99** *	g	29 – 31	11720 ± 56	13399 – 13403
"	**5.93-6.23** #	h	~102	17700 ± 130	20126 – 20818
"	**16.96-17.08** #	j	103 – 107.5	20200 ± 170	22919 – 23780
LC06	**4.66-4.69** *	k	62 - 63.5	7991 ± 43	8381 – 8481
"	**14.46-14.65** #	l	148 – 158	17730 ± 190	20126 – 20886
"	**20.17-20.19** #	m	160.5 – 165.5	34380 ± 660	~37230 **

*New dates (this paper) # from Rothwell et al. (1998). The reported conventional radiocarbon ages were calibrated using INTCAL98 (Stuiver et al., 1998) except for samples indicated with '**' which were calibrated using the magnetic curve of Laj et al. (1996).

Table 5.3 Number of $CaCO_3$ analyses per core and the calculated standard deviation (i.e. closeness of agreement between repeat analysis), repeatability (the value below which the absolute difference between two single test results may be expected to lie) and standard error.

		Repeatability				
Core	**Number of analyses**	**Number of repeat samples**	**Average $CaCO_3$ %**	**Standard Deviation**	**Repeatability**	**Standard Error**
LC01	63	19	41.71	0.29	1.74	0.17
LC02	79	27	39.40	0.35	2.79	0.21
LC04	152	54	38.84	0.41	2.59	0.24
LC06	82	29	38.15	0.70	4.49	0.41
Total	376	129				

5.5 RESULTS

5.5.1 Material

Hemipelagic intervals only make up ~10% of the total sediment thickness of the studied cores from the BAP. Turbidites account for the other ~90% of the sediment column (Figure 4.2, Table 4.6). The total hemipelagic thickness recovered increases from the northernmost core (LC01, 9%) to the southernmost core (LC06, 15%) (Table 4.6).

The upper 10 to 15 metres of some Calypso cores may appear longer by a factor of 1.5 to 2, compared with conventional piston cores, due to stretching and over sampling. This stretching is inferred to produce a microfabric rotation in the vertical plane (Thomson et al., 2000; Thouveny et al., 2000). Visual inspection revealed that all four of our cores might have been subject to such stretching (sediment down to approximately 15 metres below core top appears to be stretched). An illustration of the corrected core logs (e.g. the core intervals above 15 mbct are divided by a stretch factor of 2) is shown in Figure 5.4. This estimate corresponds to 74 cm total uncorrected hemipelagic thickness in LC01, 80 cm in LC02, 102 cm in LC04, and 158 cm in LC06.

In core LC06, two intervals have thinly bedded (<0.5 cm) intercalated hemipelagic and turbidite intervals (Figure 4.2). The first interval occurs around 20 metres below core top (mbct) and the second occurs from the bottom of the core up to 30.5 mbct. Because the hemipelagic layers in these intervals are so thin, we were unable to collect sufficient samples for $CaCO_3$ analysis and these hemipelagic intervals are not included in Table 4.6. In the following sections, the abbreviation thd is used to refer to total hemipelagic depth (cm), i.e. the total depth of hemipelagic intervals below the core top.

5.5.2 Initial Time-Stratigraphic Framework

A relatively well constrained time-stratigraphic framework was derived for each of the four cores (Figure 5.5) on the basis of identification of the nannofossil zones of Rothwell et al. (1998), existing and new AMS radiocarbon dates, stable oxygen isotope data (for LC01 and LC04 only) and calcium carbonate percentages.

In LC01, Rothwell et al. (1998) identified only coccolith stage 1 of Weaver (1983) throughout the entire core, giving the core a maximum age of 50,000 years BP (Figure 5.5). In LC02, LC04 and LC06, nannofossil zones 1 and 2 were identified, which suggested that these cores penetrated to levels older than 50,000 years BP (Figure 5.5).

Calibrated radiocarbon dates (Table 5.2) are shown in Figure 5.5 as black boxes, where the thickness of the box illustrates the thickness of the hemipelagic sample for radiocarbon analysis. Most samples were obtained from selected hemipelagic intervals, except for sample 'h' where foraminiferal tests from bioturbated

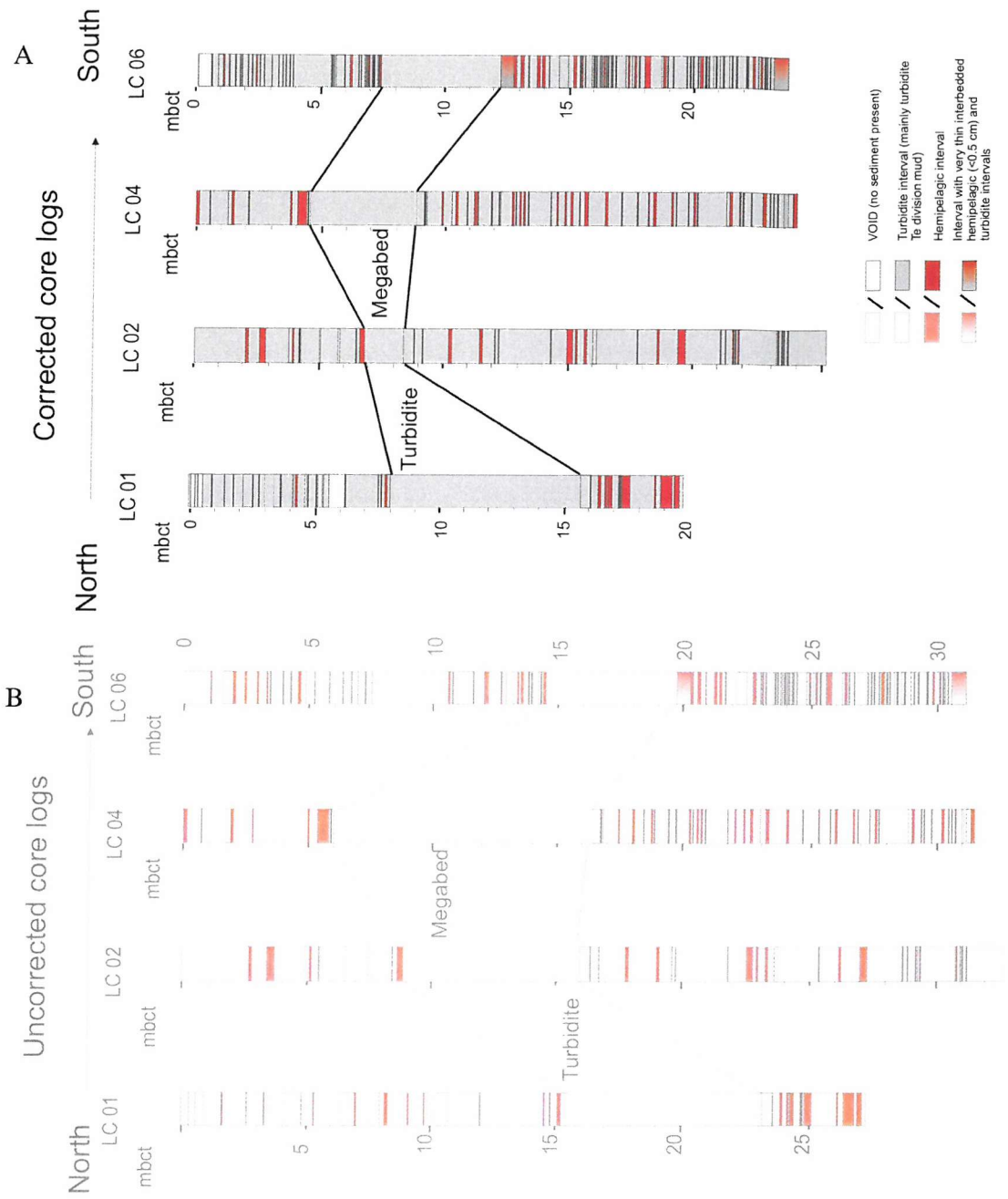

Figure 5.4 Illustration of the core logs of cores LC01, LC02, LC04 and LC06 against metres below core top (mbct). (A) Cores corrected for stretching, and (B) core logs uncorrected for stretching.

turbidite mud underlying a hemipelagic interval were also used due to the thinness of the overlying hemipelagic interval (Rothwell et al., 1998). The total hemipelagic depth used for this sample corresponds to the 'bottom' of the overlying hemipelagic interval.

Oxygen isotope measurements were made only for LC01 and LC04 (Figure 5.5). In LC01 Marine Isotope Stage (MIS) 1, 2 and (part of) 3 are apparent. LC04

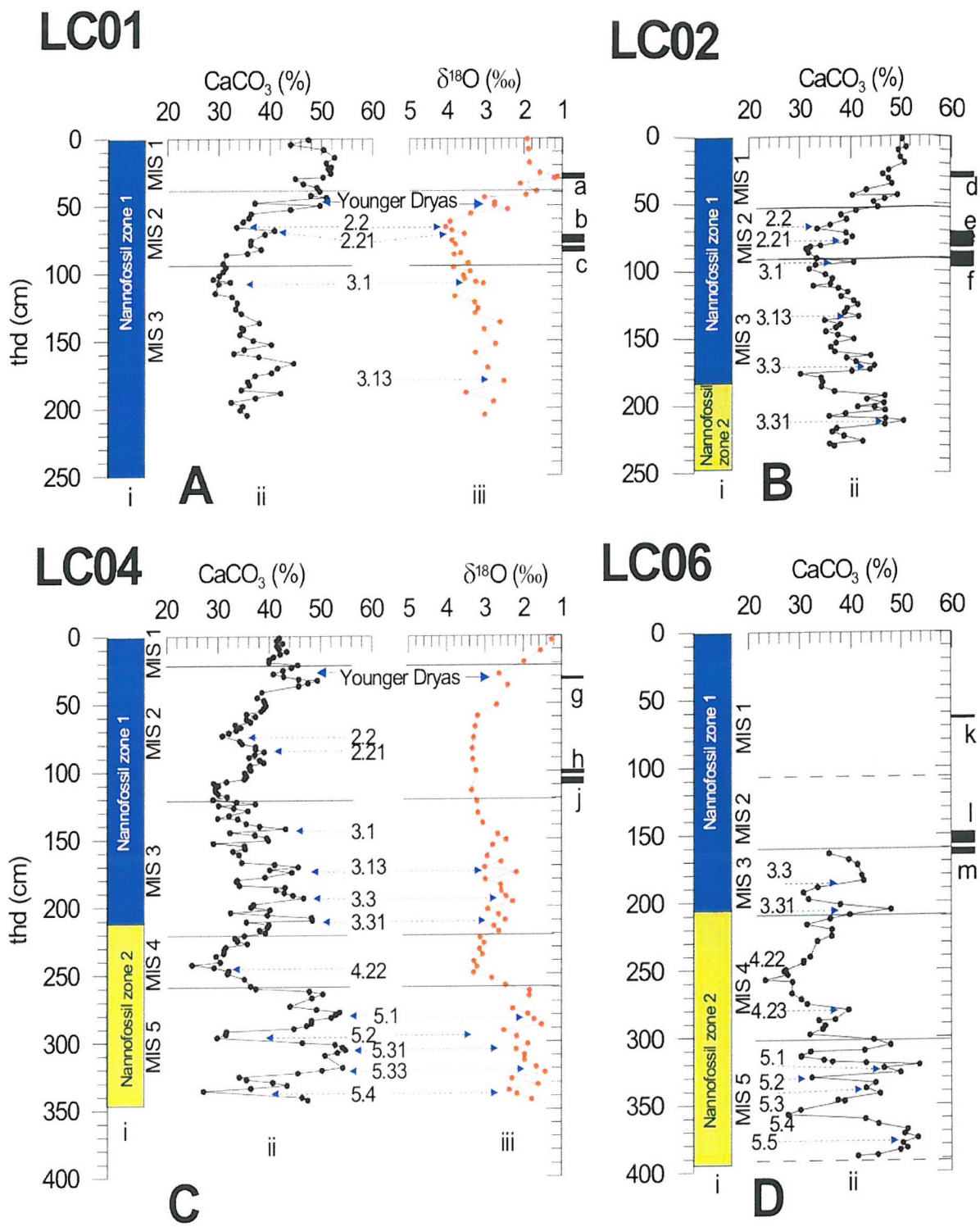
LC01
LC02
LC04
LC06
CaCO3 (%)
δ18O (‰)
thd (cm)
Nannofossil zone 1
Nannofossil zone 2
MIS 1
MIS 2
MIS 3
MIS 4
MIS 5
Younger Dryas
2.2
2.21
3.1
3.13
3.3
3.31
4.22
4.23
5.1
5.2
5.3
5.31
5.33
5.4
5.5
A
B
C
D
i
ii
iii
a
b
c
d
e
f
g
h
j
k
l
m

Figure 5.5

Figure 5.5 i) Biostratigraphy based on Quaternary nannofossil zones of Weaver (1983), ii) calcium carbonate stratigraphy and iii) oxygen isotope stratigraphy (only for cores LC01 and LC04) for the summed hemipelagic intervals in the four studied long piston cores. Nannofossil zone 1 (Weaver, 1983) is shown in blue and zone 2 shown in yellow. Boundaries of Marine Isotope Stages are delineated. Fractional numbers (e.g. 3.1) indicate the position of oxygen isotope events (after Imbrie et al. (1984) and Prell et al. (1986)). Black boxes at the right-hand side of each graph indicate the sample location of AMS radiocarbon dates. The box thickness corresponds to the thickness of the sampled interval. Radiocarbon ages are reported for each sample (lower-case letter) in Table 5.4.

Table 5.4 Tie points used for the age models: oxygen isotope stages and events derived from the $CaCO_3$ and $\delta^{18}O$ records in Figure 5.5. AMS radiocarbon dates were used where midpoints were taken from hemipelagic depths and ages. Some AMS radiocarbon ages were not used as they covered a too long depth interval.

Age control points	Depth (m)	Age (ka)	Age control points	Depth (m)	Age (ka)
Core LC01			Core LC04		
AMS Radiocarbon date 'a'	0.28	8.5	AMS Radiocarbon date 'g'	0.30	13.40
Top Younger Dryas / Boundary MIS 1 and 2	0.43	12.05	Oxygen isotope event 2.2	0.73	17.85
Base Younger Dryas	0.53	12.75	Oxygen isotope event 2.21	0.86	19.22
Oxygen isotope event 2.2	0.66	17.85	AMS Radiocarbon date 'h'	~1.02	20.47
Oxygen isotope event 2.21	0.68	19.22	AMS Radiocarbon date 'i'	1.05	23.35
AMS Radiocarbon date 'b'	0.74	20.33	Boundary MIS 2 and 3	1.22	24.11
AMS Radiocarbon date 'c'	0.83	23.51	Oxygen isotope event 3.1	1.42	25.42
Boundary MIS 2 and 3	0.95	24.11	Oxygen isotope event 3.13	1.72	43.88
Oxygen isotope event 3.1	1.08	25.42	Oxygen isotope event 3.3	1.95	50.21
Oxygen isotope event 3.13	1.81	43.88	Oxygen isotope event 3.31	2.11	55.45
Core LC02			Boundary MIS 3 and 4	2.21	58.96
AMS Radiocarbon date 'd'	0.28	9.98	Oxygen isotope event 4.22	2.44	64.09
Boundary MIS 1 and 2	0.53	12.15	Boundary MIS 4 and 5	2.61	73.91
Oxygen isotope event 2.2	0.69	17.85	Oxygen isotope event 5.1	2.79	79.25
Oxygen isotope event 2.21	0.74	19.22	Oxygen isotope event 5.2	2.98	90.95
Boundary MIS 2 and 3	0.91	24.11	Oxygen isotope event 5.31	3.07	96.21
Oxygen isotope event 3.1	0.93	25.42	Oxygen isotope event 5.33	3.20	103.29
Oxygen isotope event 3.13	1.33	43.88	Oxygen isotope event 5.4	3.37	110.79
Oxygen isotope event 3.3	1.70	50.21			
Oxygen isotope event 3.31	2.15	55.45			

Core LC06	Depth (m)	Age (ka)
AMS radiocarbon date 'k'	0.63	8.43
AMS radiocarbon date 'l'	1.53	20.51
AMS radiocarbon date 'm'	1.63	~37.23
Oxygen isotope event 3.3	1.84	50.21
Oxygen isotope event 3.31	2.05	55.45
Boundary MIS 3 and 4	2.10	58.96
Oxygen isotope event 4.22	2.57	64.09
Oxygen isotope event 4.23	2.81	68.83
Boundary MIS 4 and 5	3.00	73.91
Oxygen isotope event 5.1	3.21	79.25
Oxygen isotope event 5.2	3.30	90.95
Oxygen isotope event 5.3	3.38	99.38
Oxygen isotope event 5.4	3.57	110.79
Oxygen isotope event 5.5	3.75	123.82
Boundary MIS 5 and 6?	3.88	129.84

covers the interval from MIS 5 to the base of MIS 1. To aid chronostratigraphic assessment, we have also indicated isotopic sub-stages and events, based on Imbrie et al. (1984) and Prell et al. (1986) (Figure 5.5).

Calcium carbonate percentages are plotted against total hemipelagic depth (thd) in Figure 5.5. The $CaCO_3$ (%) and oxygen isotope records of LC01 and LC04 are similar which suggests that Mediterranean deep-sea $CaCO_3$ records can be used as a proxy for oxygen isotope records, with high $CaCO_3$ intervals correlating with interglacial stages (MIS 1 and 5); intermediate-value $CaCO_3$ intervals correspond to MIS 3; and low $CaCO_3$ intervals correspond to glacial stages (MIS 2 and 4) (Figure 5.5).

Depth-age profiles, based on various age control points (Table 5.4), for the four cores indicate a uniform background hemipelagic sedimentation (Figure 5.6). Based on the various age control points (Table 5.4), sample depths were initially converted to age (ka) through linear interpolation (Figure 5.7).

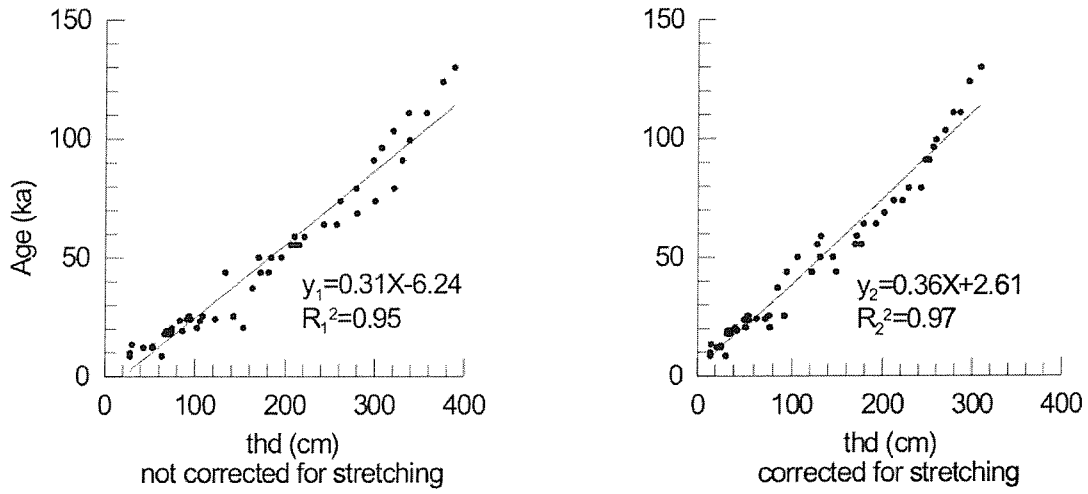

Figure 5.6 Age-depth profile through all age control points (Table 5.4). The linear regression indicates a generally uniform background hemipelagic sedimentation, at a rate of 2.78 cm/ka after correction for stretching.

5.5.3 Magnetic susceptibility

Down-core magnetic susceptibility profiles are plotted alongside the $CaCO_3$ records in Figure 5.7. Intervals characterised by high $CaCO_3$ contents generally have lower magnetic susceptibility values, whereas periods with low $CaCO_3$ contents have enhanced magnetic susceptibility values (Figure 5.7).

5.6 INTERPRETATIONS AND TUNING OF THE TIME-STRATIGRAPHIC FRAMEWORK TO GISP 2

Our hemipelagic $CaCO_3$ records for the BAP show trends that are similar to those found in the Atlantic, with low $CaCO_3$ contents (~30%) during glacial periods and high $CaCO_3$ contents (~50%) during interglacials (Figure 5.5). In the Atlantic, these $CaCO_3$ cycles are caused by increased dilution by terrigenous windblown material (Broecker et al., 1958; Ruddiman, 1971; Hays and Peruzza; 1972; Grützner et al., 2002). In the western Mediterranean, the $CaCO_3$ changes have been attributed to a combination of variations in productivity and dilution by terrigenous sediments (van Os et al., 1994; Flores et al., 1997). Our observations of generally enhanced magnetic susceptibility values during glacial intervals (Figure 5.7) support the interpretation of glacial increases in terrigenous (wind-blown) sediments.

If increased dilution by terrigenous sediments, along with constant productivity, were the main driving force causing low glacial $CaCO_3$ contents in hemipelagic sediments in the BAP, then total hemipelagic accumulation rates ought to have been enhanced during these periods. Calculated hemipelagic accumulation rates (Figure 5.8) reveal two intervals with elevated hemipelagic accumulation rates (>2.5 cm/ka) between 8 and 27 ka and between 44 and 80 ka. The highest hemipelagic accumulation rate (~20 cm/ka) was recorded between 23 and 26 ka in LC01 and LC04 (Figure 5.8), coincident with the initiation of the last glacial maximum. The termination of the last glacial maximum is also characterised by enhanced hemipelagic accumulation rates (6-8 cm/ka between 8 and 13 ka in LC01 and LC02) (Figure 5.8). In the 44-80 ka interval, hemipelagic accumulation rates rose above the average 2.5 cm/ka at around 80 ka in LC04 and LC06 (to 4 and 10 cm/ka respectively), and in LC06 elevated values were maintained until ~64 ka. At around 60 ka, hemipelagic sedimentation rates started a

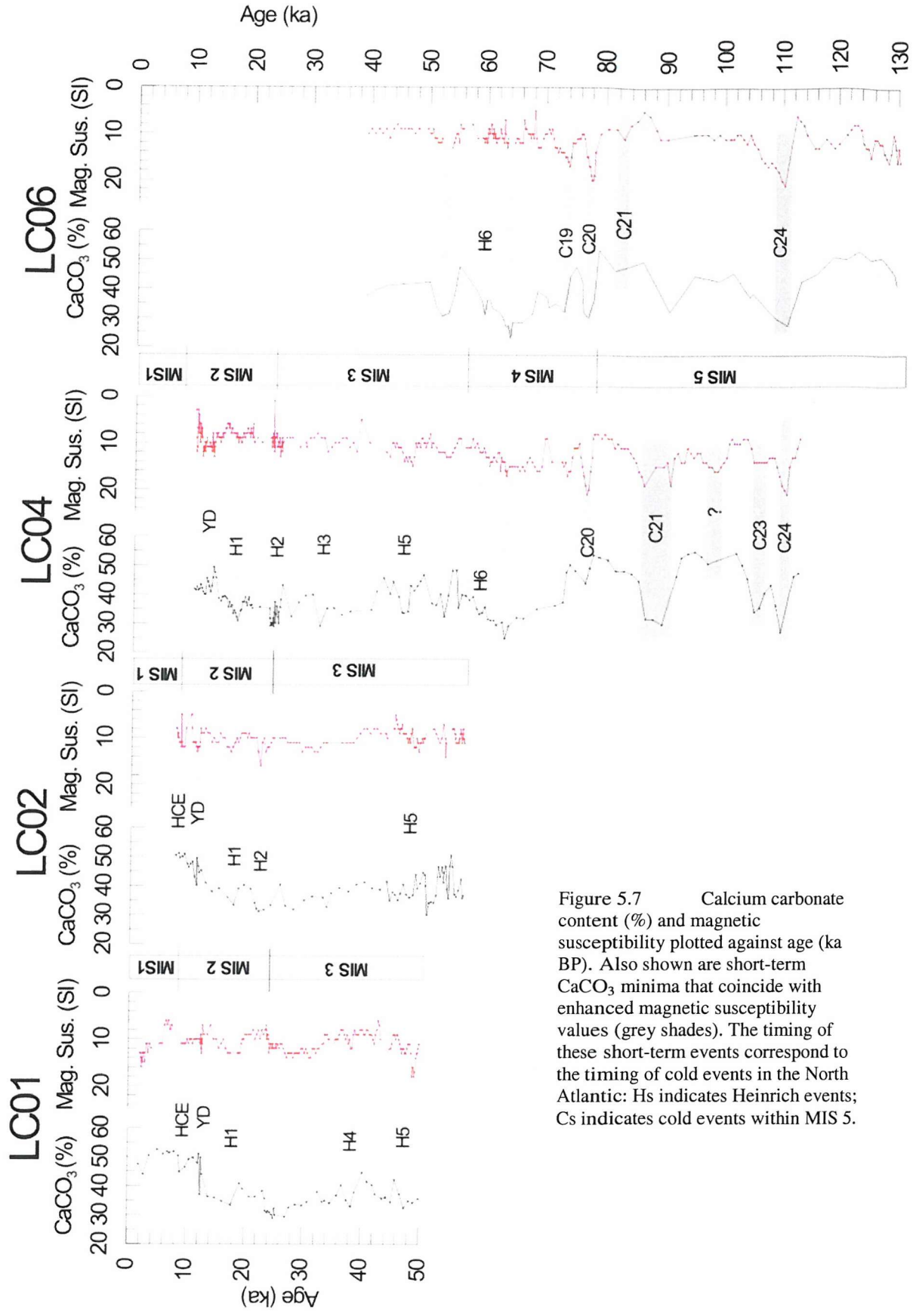

Figure 5.7 Calcium carbonate content (%) and magnetic susceptibility plotted against age (ka BP). Also shown are short-term $CaCO_3$ minima that coincide with enhanced magnetic susceptibility values (grey shades). The timing of these short-term events correspond to the timing of cold events in the North Atlantic: Hs indicates Heinrich events; Cs indicates cold events within MIS 5.

stepwise decrease until 50 ka (Figure 5.8). The variations in hemipelagic accumulation rates in LC04 were of a lower magnitude and were more gradual than in LC06, but both cores had higher hemipelagic accumulation rates between 64 and 60 ka BP (Figure 5.8).

The $CaCO_3$ content of a sample provides an estimation of the amount of terrigenous dilution, if it is assumed that the non-carbonate fraction is exclusively due to the terrigenous component. In order to compare terrigenous dilution between glacial and interglacial periods, the relative non-carbonate accumulation rate can then be calculated by dividing the non-carbonate fraction in a hemipelagic sample at a certain time with the non-carbonate fraction in a typical interglacial sample (50%). Results from these calculations show that the highest relative non-carbonate accumulation rates occur between the following time intervals: 13-30 ka, 50-55 ka, 55- 75/80 ka, 82-94 and 105-113 ka (Figure 5.9). The two broad intervals (at 8-27 and 44-80 ka) with higher hemipelagic accumulation rates, identified in Figure 5.8, correspond to periods with higher relative non-carbonate accumulation rates as identified in Figure 5.9. Between 50 and 60 ka hemipelagic accumulation rates were reduced (Figure 5.8) which corresponds to a period with lower relative non-carbonate accumulation rates (Figure 5.9). The fact that the timing of relatively high non-carbonate accumulation rates coincides with times of increased hemipelagic accumulation rates supports our hypothesis that increased dilution by terrigenous sediments can drive the Mediterranean carbonate cycles as recorded in the four studied cores, while assuming constant productivity.

Additional evidence comes from the southern flank of Menorca, where terrigenous sediment accumulation rates increased during glacial periods (MIS 2 and 4) and were about three to six times higher than during interglacial periods (MIS 1 and 5) (Figure 5.10) (Weldeab et al., 2003). Weldeab et al. (2003) also showed that the non-carbonate surface water productivity, based on bio-mediated barium accumulation rates, was possibly enhanced during MIS 2-4 compared to interglacial stages (MIS 1 and 5). An increased terrigenous flux combined with possibly enhanced non-carbonate surface water productivity during the glacial stages may increase the dilution signal. Combined, the terrigenous and biogenic Ba accumulation rates represent the non-carbonate accumulation rate that agrees well with the magnitude of our calculated non-carbonate accumulation rate, with maxima during MIS 2 and 4 (Figure 5.9).

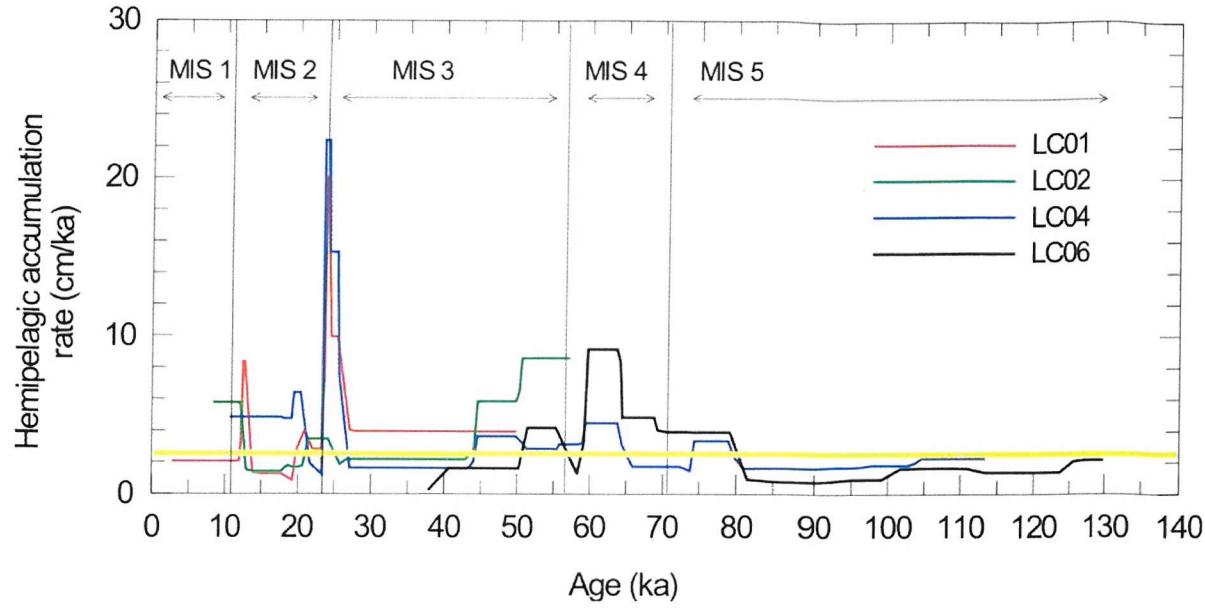

Figure 5.8 Calculated hemipelagic accumulation rates for the summed hemipelagic intervals in the four studied long piston cores. Corrected hemipelagic depths were used for this calculation. Marine Isotope Stages (MIS 1-5) are also indicated. The average hemipelagic accumulation rate (~2.5 cm/ka) is indicated by a thick yellow line.

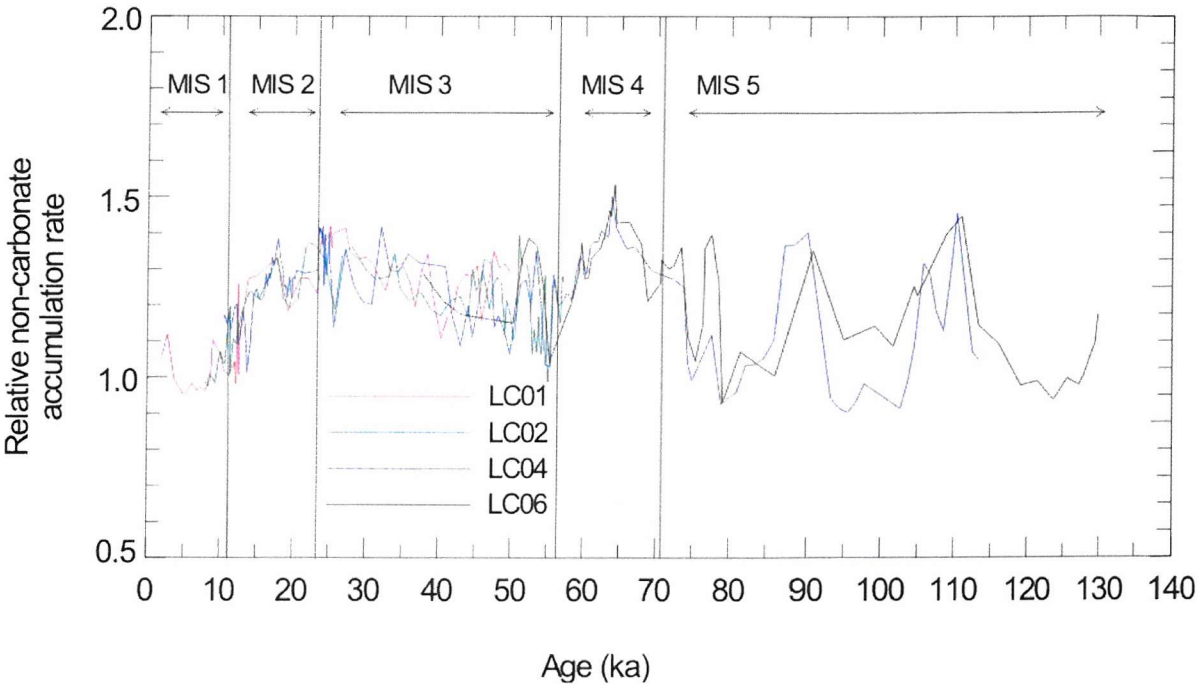

Figure 5.9 Relative terrigenous sedimentation rates (inferred from $CaCO_3$ contents) for the last 130,000 years for the four studied cores.

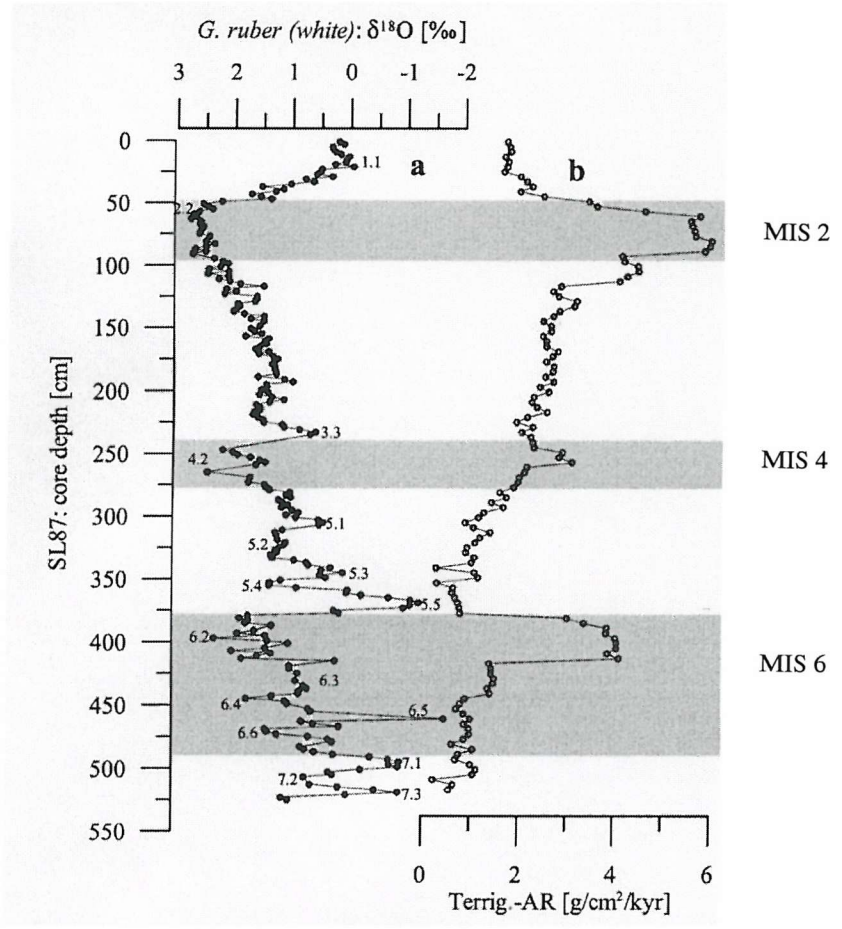

Figure 5.10 (a) Stratigraphy and (b) terrigenous sediment accumulation rate (Terrig.-AR) plotted against core depth (cm) for core SL87 (from Weldeab et al., 2003). Fractional numbers (e.g. 3.3) indicate the position of oxygen isotope events. Grey areas indicate glacial sections and Marine Isotope Stages (MIS).

Two intervals in MIS 5, which are associated with MIS substages 5.2 and 5.4, also had higher relative non-carbonate accumulation rates (Figure 5.9). The calculated hemipelagic accumulation rates for these intervals, however, did not exceed the average ~2.5 cm/ka (Figure 5.8). Were these $CaCO_3$ minima caused by changes in productivity rather than by changes in terrigenous dilution? The recorded magnetic susceptibility values during MIS 5.2 and 5.4 are elevated (almost double that of the warmer substages MIS 5.1 and 5.3, Figure 5.7), which suggests enhanced input of eolian sediments. The limited number of age control points makes it impossible to estimate time-scale variations in sedimentation rate, which makes the hemipelagic accumulation rates for this period appear almost uniform (Figure 5.8). Further evidence for enhanced eolian sediment supply to the western Mediterranean during cool substages 5.2 and 5.4 is

provided by sediment and soil sequences along the northeastern coast of Mallorca, which were characterised by eolian sand and dust deposition, in contrast to the warmer substages 5.1 and 5.3 which were characterised by more stable environments (Figure 5.11) (Rose et al., 1999).

Apart from the long term $CaCO_3$ and magnetic susceptibility variations visible in Figure 5.7, we note several 'short-term' (500 to 2000 years) $CaCO_3$ minima that correlate with short-term increases in magnetic susceptibility values (Figure 5.7). These are interpreted as the result of brief intervals of rapid environmental change and might represent periods with increased aridity and higher eolian fluxes to the western Mediterranean. The timing of almost all of these short-term events coincides with short-term cooling events such as the Younger Dryas, Heinrich Events (HE), Dansgaard-Oeschger (D/O) stadials and abrupt cooling events within MIS 5, as recorded in deep-sea sediments from the North Atlantic (Johnsen et al., 1992; Bond et al., 1993; McManus et al., 1994; Bond and Lotti, 1995; Lehman et al., 2002). In North Atlantic marine sediments, HEs are associated with massive iceberg discharges, resulting in the deposition of 'Heinrich layers' of ice-rafted debris (Heinrich, 1988). Throughout the northern hemisphere, Heinrich event-equivalent anomalies are known from palaeoclimate proxy records (Rohling et al., 2003). Climate during HEs and D/O stadials was characterised by dry, dusty and windy climatic conditions (Mayewski et al., 1997). Several sudden cooling events, which have been associated with ice rafting, have also been described within MIS 5, which was a dominantly warm time interval (McManus et al., 1994).

In the western Mediterranean Sea rapid sea surface temperature (SST) cooling and increased rates of western Mediterranean deep-water formation during the last glacial have been connected to the timing of HE and D/O stadials (Rohling et al., 1998; Cacho et al., 2000), suggesting that the Mediterranean and North Atlantic ocean-atmosphere systems are closely coupled. Similar variations in high latitude northwesterlies and low-latitude Saharan winds during the last glacial, which occurred parallel with intensification of atmospheric transport over Greenland, suggest a 'mechanistic linking' of the glacial atmospheric circulation across the high and low latitudes (Moreno et al., 2002). In the Alboran Sea, Moreno et al. (2002) showed that millennial to submillennial marine oscillations, linked with HE and D/O stadials are characterised by increases in northward Saharan dust transport associated with increases in Saharan wind intensity. Increases in Saharan wind intensity and dust

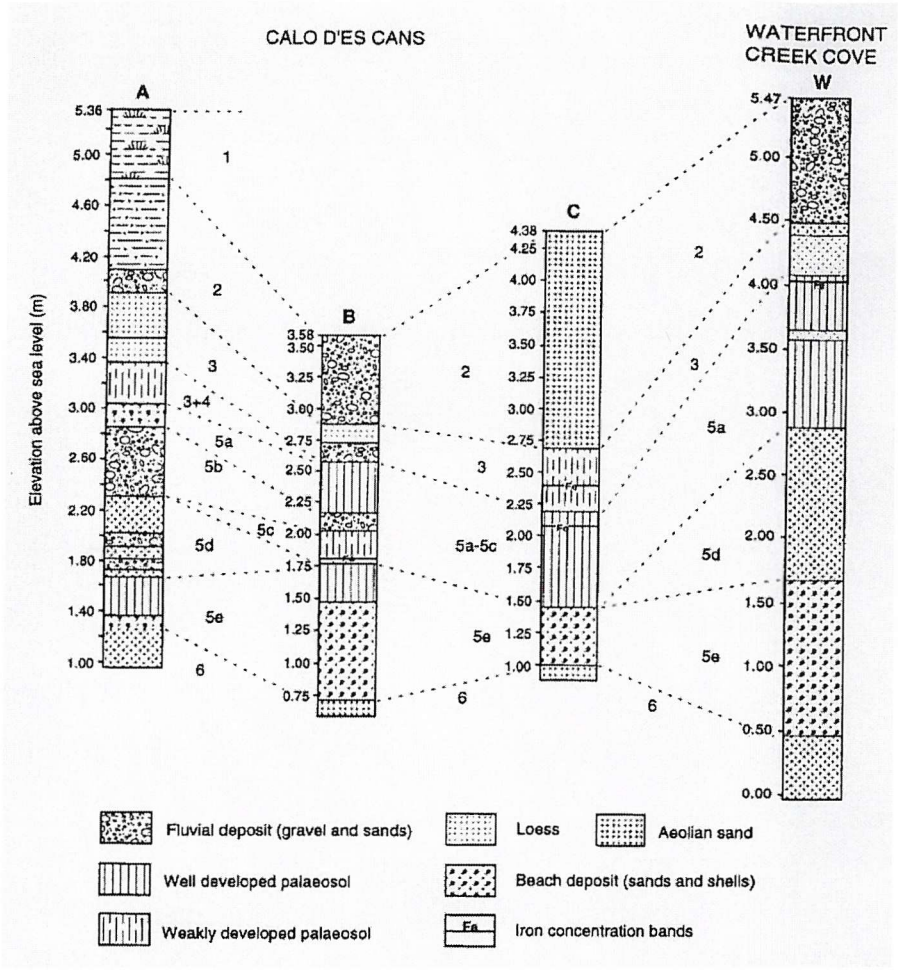

Figure 5.11 Four soil sections along the northeastern coast of Mallorca indicate enhanced eolian activity during MIS 2 and 6 and during substages 5b and d (from Rose et al., 1999). A-C are from the Calo d'es Cans sections and D is from the Waterfront Creek Cove section.

transport would be likely results of a weakened monsoonal circulation and intensified high-latitude circulation (cf. Rohling et al., 2003). Pollen records from the Alboran Sea show vegetation changes that are indicative of rapid environmental changes between cold-dry (D/O stadials) and mild-humid conditions (D/O interstadials) (Combourieu-Nebout et al., 2002), which occured in parallel with SST oscillations and indicate an almost perfect coupling between continental and marine conditions (Sánchez Goñi et al., 2002). The coldest and driest conditions in the Alboran Sea occurred during HEs (Combourieu-Nebout et al., 2002; Sánchez Goñi et al., 2002). The increased aridity and desertification in the Mediterranean during HEs is explained by prolonged wintertime anticyclonic stability associated with cooling in the North Atlantic (Combourieu-Nebout et al., 2002). Decreases in precipitation during Dansgaard-Oeschger stadials were not as severe as during HEs and have been explained by switches between the

influence of Atlantic (dominant during D/O stadials) and Scandinavian Mobile Polar Highs (dominant during HEs) (Sánchez Goñi et al., 2002). Pollen records from terrestrial lacustrine sequences at various sites in the Mediterranean confirm that continental climatic conditions in the Mediterranean during HE and D/O stadials were dry and can be linked to climatic conditions in the North Atlantic (Allen et al., 1999; Tzedakis, 1999; Allen and Huntley, 2000; Allen et al., 2000; Brauer et al., 2000). Evidence that cooling events within MIS 5 took place in the western Mediterranean is provided by the Lago Grande di Monticchio pollen record, where several intervals with a cold and dry climate (inferred from palaeovegetation and palaeoenvironment) have been reported (Allen et al., 2000).

To fine-tune the depth-age relationships for our cores, we correlate magnetic susceptibility maxima/$CaCO_3$ minima on a millennial scale to the age intervals of the main GISP2 ion series peaks from Rohling et al. (2003). The common time-scale of Lehman et al. (2002) was used for abrupt cooling events during MIS 5 that have also been related to North Atlantic ice rafting events (Chapman and Shackleton, 1999). In our cores, the short-term $CaCO_3$ minima/magnetic susceptibility maxima event dated around 8 ka BP in LC01 (Figure 5.9) is thought to represent the Holocene Cooling Event (HCE), which is associated with major dry spells in North Africa (Gasse, 2000). Several other short-term minimum $CaCO_3$/magnetic susceptibility maxima events that occurred between ~10 and 70 ka can be linked with the Younger Dryas, HE 1 to 6 and several D/O stadials (Figure 5.12). Events that have been dated before 70 ka are correlated to C19-C24 (Chapman and Shackleton, 1999) (Figure 5.12).

Almost all events identified in Figure 5.12 correspond to dry spells associated with increased dust transport to the Mediterranean Sea, as has been previously recorded in marine alkenone records, as well as in both terrestrial (lacustrine) and marine pollen records and grain-size records. Our contention that these short-term minimum $CaCO_3$/ maximum Magnetic Susceptibility events are caused by enhanced dust supplies to the western Mediterranean therefore seems justified. The co-occurrence of enhanced dust supplies to GISP2 during these events again highlights the close coupling between the Mediterranean and North Atlantic ocean-atmosphere systems.

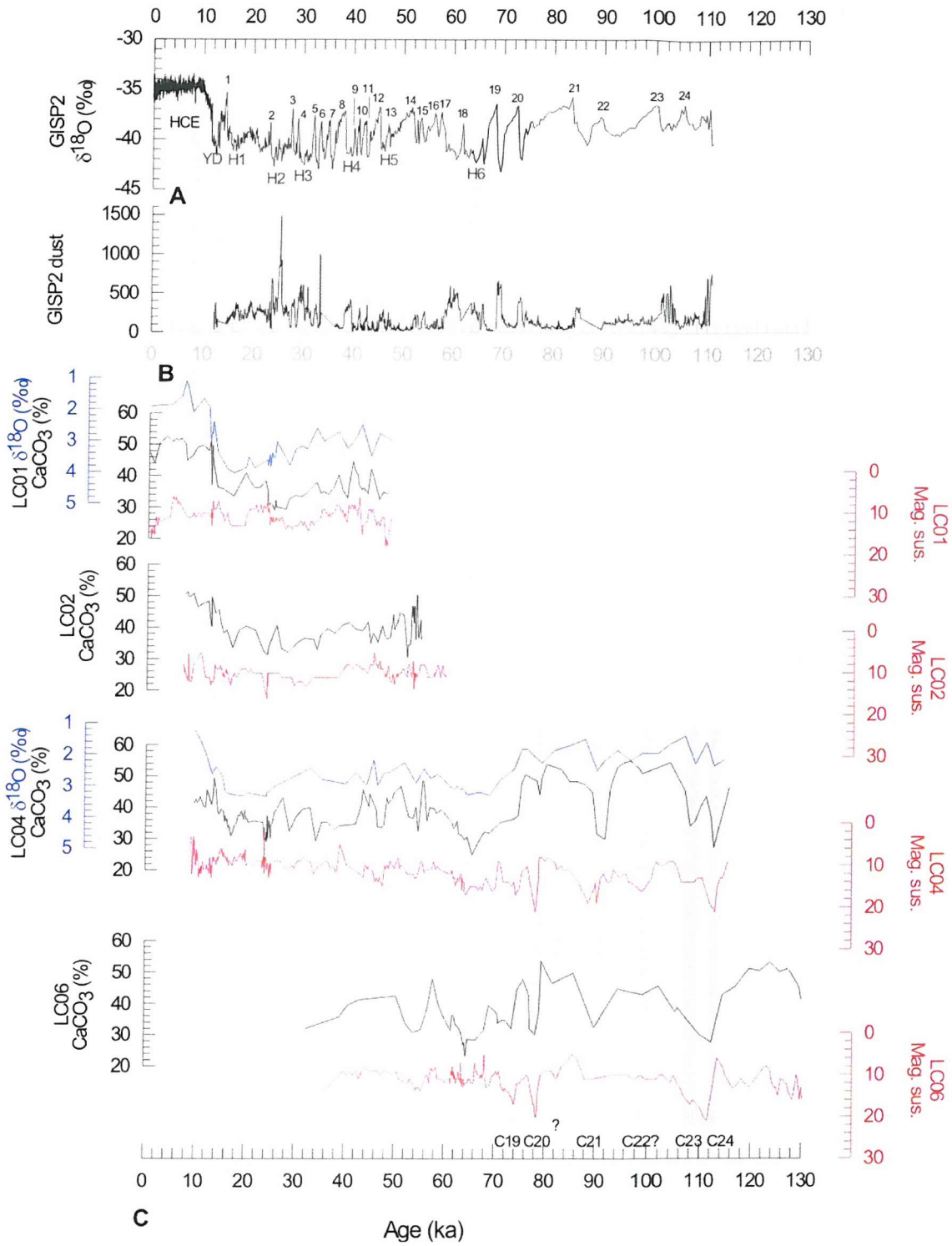

Figure 5.12 Identification of periods with enhanced dust in GISP2 and four western Mediterranean deep-sea cores, by comparison with (A) GISP2 $\delta^{18}O$, with small numbers indicating the Dansgaard-Oeschger interstadials (Dansgaard et al., 1993; Grootes et al., 1993) and Hs indicating Heinrich events, (B) GISP2 dust content as measured with laser light scattering (LLS) (Ram and Illing, 1994; Ram et al., 1995; Ram and Koenig, 1997), (C) fine-tuned $CaCO_3$ and magnetic susceptibility records from the western Mediterranean. Cold events within MIS 5 (Cs) are plotted at the bottom, since the ages used here are from Lehman et al. (2002) which deviate slightly from GISP2.

5.7 CONCLUSIONS

- Although turbidite deposits dominate late Quaternary sediments on the BAP, an almost continuous record of hemipelagic sedimentation covering the last 130,000 years is preserved in the deposits intercalated between turbidites.

- $CaCO_3$ measurements of these hemipelagic sediments reveal distinct cycles similar to 'Atlantic'-type carbonate cycles; with interglacial periods showing relatively higher $CaCO_3$ contents (~50%) and glacial periods having lower $CaCO_3$ contents (~30%). AMS radiocarbon dating, biostratigraphy (nannofossil zones) and oxygen isotope stratigraphy support the time relationship inferred from this climatic pattern in the $CaCO_3$ stratigraphy. A change in dilution with (eolian-derived) terrigenous sediment is suggested to be the main driver of these $CaCO_3$ cycles.

- Apart from the major glacial/interglacial $CaCO_3$ cycles, we detect 'short-term' intervals (duration 500-2000 year) with lower $CaCO_3$ contents and high magnetic susceptibility. Almost all of these 'short-term' events can be linked with cold events in the North Atlantic. These cold events include the Holocene cooling event, Younger Dryas, Heinrich events, Dansgaard-Oeschger stadials and cold events within MIS 5. Climate in the western Mediterranean during these events was cold, windy and dry and subsequently supported enhanced supply of dust to the BAP. This observation corroborates previous work showing similar 'short-term' oscillations in a high-resolution record of lithogenic fraction variability in the Alboran Sea and pollen records from Lago Grande di Monticchio (Italy).

CHAPTER 6 – VARIATIONS IN DEEP-SEA TURBIDITE DEPOSITION DURING THE LATE QUATERNARY

ABSTRACT

Sedimentary sequences in four long piston cores from the Balearic Abyssal Plain provide a unique opportunity to reconstruct the depositional and erosional history of the basin. The GISP2 fine-tuned time-stratigraphic framework, developed in Chapter 5, provided important constraints on individual turbidite emplacement times. Turbidite emplacement to the Balearic Abyssal Plain occurred regularly (on average one turbidite every one to two thousand years), without major temporal gaps. Highest turbidite frequencies were observed during periods of maximum sea level/climate change. During the last cold interval (Marine Isotope Stages 2-4), turbidite beds were much thicker than during interglacial periods (Marine Isotope Stage 1 and 5), which suggests that the glacial advective sediment flux to the Balearic Abyssal Plain was significantly enhanced. It is estimated that sediment supply to the margins was at least doubled during the Last Glacial Maximum, due to increases in riverine sediment fluxes and subsequent increase in sediment supply to the shelf edge. The average turbidite flux to the Balearic Abyssal Plain during Marine Isotope Stage 2 was about two to three times higher than during Stage 5, suggesting that sediment supply to the basin was also at least two to three times higher. Deforestation and subsequent increased erosion, which enhanced sediment supply during Marine Isotope Stage 1, might explain the high frequency of turbidites deposited during this period. Several periods were identified during which turbidite deposition was absent. Most of these periods correlate to times of minor sea level/climate fluctuations, whereas intervals with frequent turbidite deposition generally coincide with periods of more dynamic sea level and climate change. Basin-wide filling of the Balearic Abyssal Plain by turbidites was especially rapid during the last deglaciation and the Last Glacial Maximum. Turbidite sediment accumulation was however also increased during MIS 4, 78/80 ka and 105-115 ka. The results presented indicate that the temporally well-constrained data do not support the hypothesis that the advective sediment flux to the basin is only high during glacials - this view is too simple and does not stand up to detailed testing.

6.1. INTRODUCTION

Sedimentary sequences from the deep sea can record environmental conditions from both the overlying water masses and from adjacent landmasses. Sediment delivery to the continental margin, which controls the amount of sediment available for downslope transport, is primarily related to hinterland climate and tectonics. Changes in hinterland climate and/or tectonics can influence the amount and possibly the characteristics of sediment available for downslope transport, which is ultimately recorded in deep-sea sedimentary sequences in adjacent deep-sea basins. The main processes whereby large volumes of sediment are transported from shallow water settings to the deep sea involve sediment gravity flows (Stow et al., 1996). This mechanism is important in delivering sediment to the deep sea, however, some flow-types (like slides and debris flows) do not travel long distances over flat terrain and their deposits are primarily restricted to the continental rise and slope. Turbidity currents are the main sediment gravity flow mechanism capable of delivering large amounts of continentally derived sediment to the deep sea. Turbidite deposits commonly dominate basin-plain sediment sequences, and hemipelagic intervals may make up less than 20% of such sediment columns (Pilkey, 1987).

Turbidity currents are mainly the result of continental slope failures that can be initiated by several processes, including sedimentary overloading of the continental shelf in areas that are close to river mouths, earthquakes, volcanic eruptions and slope instability caused by the release or movement of gas hydrates. Traditionally, turbidite deposition is thought to be particularly dynamic during periods of low sea level (Embley, 1980; Shanmugan and Moiola, 1982; Cita et al., 1984; Caddah et al., 1998; Rothwell et al., 1998, 2000), as previously discussed in Chapter 1. Likewise, Shanmugam and Moiola (1982) argued that the frequency of turbidity currents is greatly increased during periods of low sea level. Several authors have discussed a relationship between turbidite emplacement and sea level (e.g. Weaver and Kuijpers, 1983; Cita et al., 1984; Prince et al. 1987; Caddah et al. 1998; Rothwell et al. 1998). Weaver and Kuijpers (1983) reported that turbidite deposition on the Madeira Abyssal Plain was more likely during marine regressions and transgressions. Recently, Prins and Postma (2000) proposed that turbidite sedimentation in the Arabian Sea was more frequent during the last glacial sea level low stand. Turbidite deposition during sea-

level rise and highstands, however, have also been recorded (Piper and Normark, 1983, Kuehl et al., 1989; Flood et al., 1991; Kolla and Perlmutter, 1993; Weber et al., 1997b).

According to Stanley (1985) emplacement of large megaturbidites during the Late Pleistocene (<1 Ma) are generally related to sea-level low stands. Mediterranean Late Pleistocene-Holocene (0-30 ka) deep-sea sedimentary sequences are dominated by turbidite mud (Rothwell et al., 2000) and in the Herodotus Basin (eastern Mediterranean), turbidite deposition was controlled by a combination of regional climatic change and eustatic sea-level fluctuations (Reeder et al., 2002). Two turbidite megabeds have been reported in the western (BAP) and eastern (Herodotus Abyssal Plain) Mediterranean Sea, which were emplaced during the last sea level low stand at the height of the Last Glacial Maximum (Rothwell et al., 2000). In the Central Mediterranean Sea (Ionian and Sirte Abyssal Plain), three thick, basin-wide turbidite beds were emplaced at around 3.5 ka (Kastens and Cita, 1981; Hieke and Werner, 2000), 235±50 ka and 650± 100 ka (Hieke, 2000). The 'Augias turbidite' (3.5 ka) has been interpreted as having been mobilised by a tsunami induced by the collapse of the Santorini caldera (Kastens and Cita, 1981; Hieke and Werner, 2000) and the two additional thick turbidite beds are interpreted to have been triggered by tsunami events related to volcanic events or earthquakes in the southern Aegean region (Hieke, 2000).

The main objective of this chapter is to broadly quantify the differences in advective sediment flux to the BAP/western Mediterranean Sea over the last glacial/interglacial cycle, and to examine any relationship with climate. The aim is to assess the effects of climate changes on sediment transfer to the deep sea in a basin whose margins were affected by profound climatic changes during the Quaternary. The alternating occurrence of hemipelagic and turbiditic sediments in the studied BAP cores, as presented in Chapter 4 and 5, allows reconstruction of the erosional and depositional history of this small ocean basin during the last 130,000 years – a period characterised by substantial climate changes.

6.2 SEDIMENT DELIVERY TO THE BASIN

An important control on the growth patterns of continental margins is sediment supply, amount, type and location (Nelson and Maldonado, 1990). The rate of sediment supply from erosional catchment to depositional basin, which can vary both in time and space, depends primarily upon climate, relief, catchment slope and lithology (Leeder et

al., 1998). The tectonic setting of the western Mediterranean basin probably has a large influence on the margin styles, depositional environments, distribution of depocentres and growth patterns. Together, climate and tectonics can influence hinterland relief and the catchment slope, through weathering and uplift/subsidence.

The continental rise and deep-sea fans in the northern part of the BAP are fed by large European rivers, including the Var, Rhône and Ebro (see Chapter 2). These rivers have the largest drainage basins and carry substantial amounts of sediment to the western Mediterranean margins (Table 6.1). Rivers from Corsica, Sardinia, the Balearic Islands and Algeria carry much smaller amounts of sediment and these continental margins are regarded as starved of sediment (e.g. Bourouba, 2003). These areas, however, might supply sediment to the abyssal plain through sliding of the continental margins.

Table 6.1 Summary of the drainage areas and sediment loads of rivers that drain into the western Mediterranean Sea.

River	Drainage area (km^2)	Sediment reaching the continental margin (tonnes)
Ebro	84×10^3 (Nelson, 1990)	6.2×10^6 (Nelson, 1990)
Rhône	97×10^3 (Ludwig and Probst, 1998)	8.5×10^6 (Pont, 1993)
Hérault	2.5×10^3 (Petelet et al., 1998)	no information available
Têt	1.4×10^3 (Serrat et al., 2001)	0.053×10^6 (Serrat et al., 2001)
Var	2.8×10^3 (Mulder et al., 1997)	$1.3\text{-}1.6\times10^6$ (Mulder et al., 1997)
Algeria	no information available	$0.04\text{-}0.06\times10^6$ (Leclaire, 1972)

6.2.1 Processes affecting sediment delivery

Two main processes affect sediment delivery to the continental margins: hinterland climate and tectonics.

6.2.1.1 Climate

It has been shown in Chapter 5 that the glacial/interglacial climate changes had a large influence on the western Mediterranean environment. The colder and dryer conditions that prevailed during the last glacial supported highly peaked river-discharge

regimes and increased physical erosion. Larger areas of bare ground and unconsolidated sediments would have increased the sediment load of rivers draining into the western Mediterranean Sea (Rose et al., 1999). In the eastern Mediterranean, Leeder et al. (1998) postulated that the glacial maximum yearly rainfall was similar to the present. Cooler temperatures and increases in winter runoff caused the widespread treeless steppe to be highly erodable (Leeder et al., 1998).

Adjacent sedimentary systems bordering the BAP, such as the Rhône, Valencia and Var fan were also affected by Pleistocene glacial/interglacial oscillations. For example, the construction and evolution of the Rhône delta was controlled by sea-level variations and the supply of sediments (Arnaud-Fassetta et al., 1999). According to Limonov et al. (1992), sediment supply and climate-induced sea-level variations were also the main factors that controlled depositional patterns of the Valencia fan during the Pliocene-Quaternary. Using seismic data, Palanques et al. (1994) related sea-level changes to phases of fan progradation and retreat resulting from changes in sediment supply to the Valencia fan system. During Quaternary sea-level lowstands, the river Var incised older deltaic deposits, which were partially refilled during sea-level highstands (Savoye et al., 1993). Different erosion platforms on the Mallorca-Menorca shelf are presumably related to glacio-eustatic sea-level changes (Acosta et al., 2002) and the relief of the Algerian shelf was also influenced by glacio-eustatic sea-level fluctuations (Leclaire, 1972).

6.2.1.2 Tectonics

The BAP is surrounded by passive continental margins (Baraza et al., 1990; Farrán and Maldonado, 1990; Tesson et al., 1990; Guennoc et al., 1994; Ercilla and Alonso, 1996), The north African margin and the eastern Spanish coast (Iberian Ranges between Amposta and Valencia) are controlled by faults and some faults are reported to be still active (Cairn, 1978; Ríoz, 1978; Robribi et al., 1985; Ben-Avraham et al., 1987). The southern coast of France between Marseille/Nice and Roussillon has been tectonically stable for the past 30,000 years (Lambeck and Bard, 2000). However, most areas draining into the western Mediterranean are at present experiencing some form of uplift, due to neotectonic compression and/or isostatic rebound. The western coast of Corsica is undergoing slow (0.15-0.3 m/ka) south to north-trending uplift (Conchon, 1987; Lenotre et al., 1996; Collina, 1998, 2002; Lambeck and Bard, 2000). Sardinia (Antonioli et al., 1999) and the Balearic Islands (Torres et al., 1993) are also

experiencing active uplift. Active faults on the north African margin (formed in response to the collision between the Eurasian and African plates (Philip and Thomas, 1977; Philip and Megraoui, 1983)) are the cause of uplift, and are evident in drainage diversions on land (Boudiaf et al., 1998; Bouhadad et al., 2003). The European Alps are at present undergoing modest rates of uplift (Fitzsimons and Veit, 2001), whereas uplift in northeast Spain has been relatively slow (~0.12 m/ka) during the late Quaternary (Macklin and Passmore, 1995).

6.3. SEDIMENT CORES, TIME-STRATIGRAPHIC FRAMEWORK AND CALCULATION OF TURBIDITE EMPLACEMENT TIME

The four studied giant piston cores and features distinguishing turbidite beds from hemipelagic intervals are discussed in detail in Chapter 4. The GISP2 fine-tuned time-stratigraphic framework for the four cores has been described in Chapter 5, where the age model is based on biostratigraphy (high-resolution nannofossil zonal scheme of Weaver (1983)), accelerator mass spectrometry (AMS) ^{14}C dating, oxygen isotope stratigraphy (only for LC01 and LC04) and calcium carbonate/magnetic susceptibility stratigraphy. This has been used to calculate the ages of hemipelagic sediments in the four cores. The emplacement time of individual turbidite beds was calculated using the ages of intercalating hemipelagic intervals (Figure 6.1). Thus, emplacement times were estimated for almost all turbidite beds.

6.4 RESULTS

Ninety percent of the total sediment thickness in the upper 30-35 m of the BAP sediment column is composed of turbidite beds (mainly T_e-division muds) (see Chapter 4). Hemipelagic accumulation rates of the four cores are similar (~2.7 cm/ka), so the cores with the highest total hemipelagic thickness (LC04 and LC06) cover the longest time intervals (see Table 6.2) (see Chapter 5).

Based on sedimentological criteria presented in Chapter 4, 238 to 257 turbidites were identified in the four cores (Tables 4.7 and 6.3; Appendix 6.1). Uncertainty concerning the precise number of turbidites is explained above (p. 70, Chapter 4).

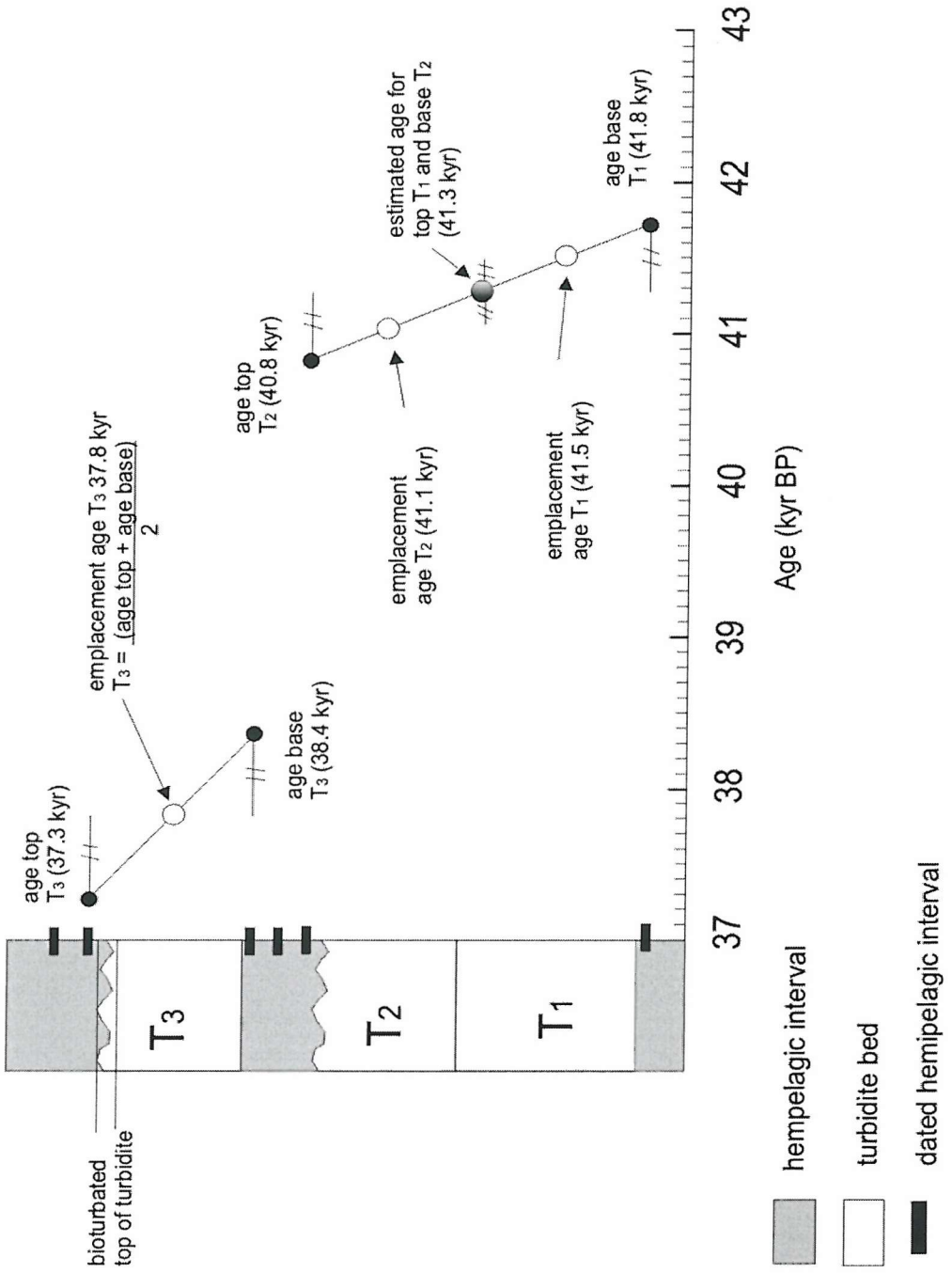

Figure 6.1 Diagram illustrating the model used to calculate turbidite emplacement times. The emplacement time of turbidite 3 (T_3) is the average of the ages of the two nearest dated hemipelagic intervals. However, not all turbidite beds are intercalated with hemipelagic intervals because the thickness of the intercalated hemipelagic interval was too thin for sampling or because turbidite beds were deposited on top of each other in a short time period, leaving no time for significant hemipelagic accumulation. Turbidites T_1 and T_2 do not occur intercalated between two dated hemipelagic intervals, instead the top of T_2 and the base of T_1 are bounded by hemipelagic sediments and dated. In order to have an indication of their respective emplacement ages, the emplacement age for the base of T_2 and the top of T_1 is first calculated as the average between the top of T_2 and the base of T_1. The estimated emplacement age for T_2 is then the average age of the ages of the top and base of T_2, whereas the estimated age for T_1 is calculated as the average between the ages of the top and of the base of T_1.

The average individual turbidite thickness is greater in the two northern cores (LC01 and LC02) whereas in the southernmost cores (LC04 and LC06) turbidite beds are generally thinner but their number is much higher (Table 6.3). The megaturbidite described by Rothwell et al. (1998) is the thickest turbidite in all of the four cores. Apart from the megabed several other thick turbidite beds (> 100 cm thick) could be identified in the four cores (Appendix 6.1). In total, the four long piston cores contain 36 turbidites with basal sand layers, of which four occurred in LC01, twenty in LC02, two in LC04 and ten in LC06 (Table 6.4).

Table 6.2 Calculated minimum and maximum ages (ka) for hemipelagic intervals in the four studied long piston cores. The GISP2 fine-tuned time-stratigraphic framework presented in Chapter 5 was used to convert depths to ages. The minimum age of LC06 is unclear, due to disturbance in the upper 12 metres of the core.

Core	Minimum age (ka)	Maximum age (ka)
LC01	0	48
LC02	7	55
LC04	9	115
LC06	0 ?	130

Table 6.3 Summary of total corrected thickness (m) of turbidite intervals, total number of turbidite beds (minimum and maximum values), and average corrected turbidite thickness (minimum and maximum, in cm) per core.

Core	Total turbidite thickness (m)	Total number of turbidites per core (min - max)			Average turbidite thickness per core (cm) (min	average	max)
LC01	16.52	32	-	37	45	48	52
LC02	22.95	33	-	43	53	61	70
LC04	20.44	55	-	58	35	36	37
LC06	19.44	118	-	119		~16	

Table 6.4 Distribution of basal sand layers in turbidite bases in the four studied long piston cores

Core	Number of basal sands	% of turbidites with basal sands	no. of basal sands/ka
LC01	3-4	8-13%	0.06-0.08
LC02	14-21	33-64%	0.24-0.37
LC04	2	3-4%	0.02
LC06	10	9%	0.09

6.4.1 Turbidite emplacement

Individual turbidites are plotted against their calculated emplacement time in Figure 6.2. It seems that turbidite deposition on the BAP occured regularly without major temporal gaps (>10 ka) in turbidite emplacement (Figure 6.2, Appendix 6.2). A few periods can be identified where turbidite deposition was more frequent, specifically between 0 and 10 ka in LC01, at 21-24 ka, at 48 ka and between 53 and 56 ka in LC02,

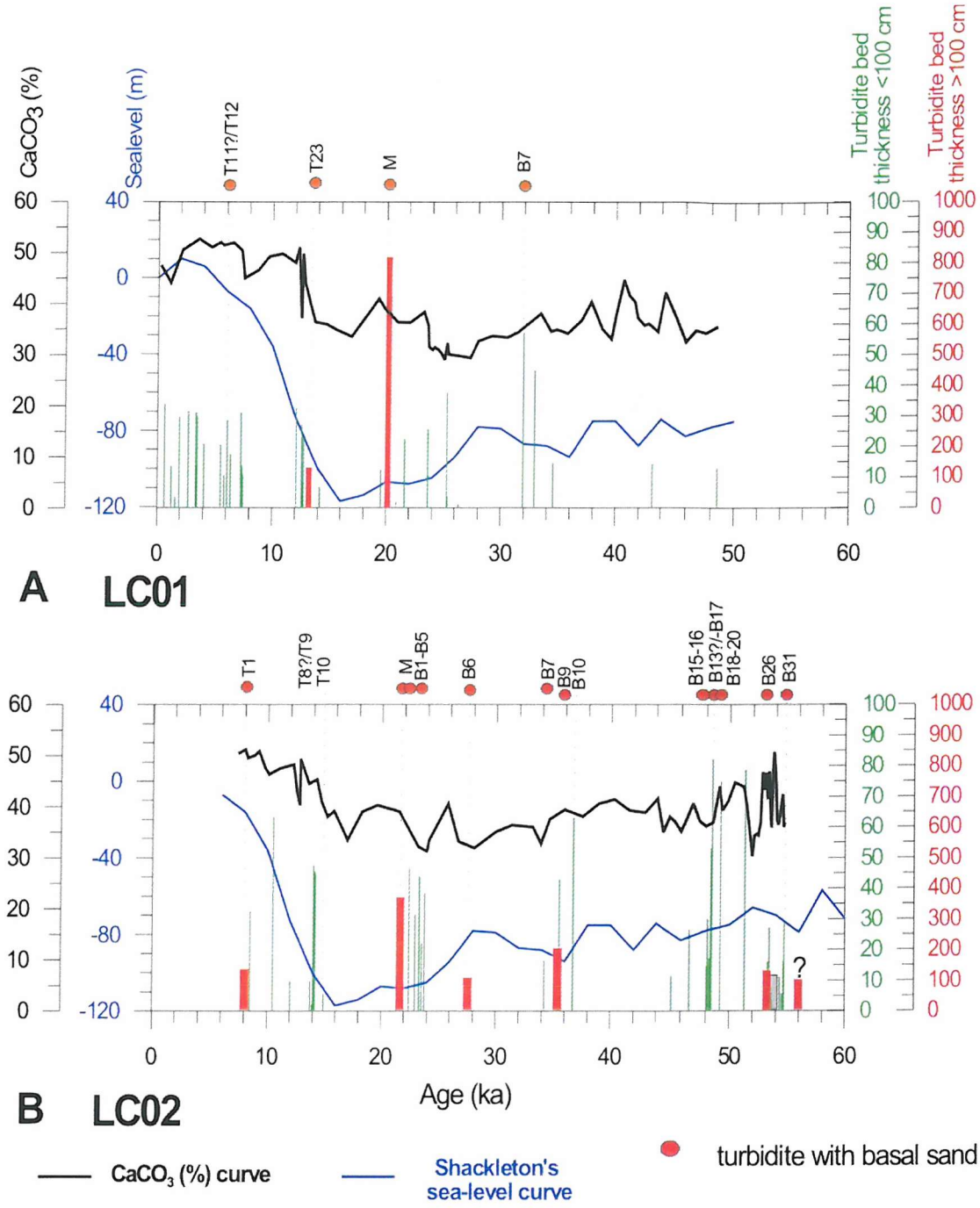

Figure 6.2 Thickness and emplacement times of turbidite beds in the four long piston cores (a-d) plotted against $CaCO_3$ curves of Chapter 5 and Shackleton's sea-level curve (Shackleton, 1987b). Turbidite beds with a thickness of <100 cm are shown in green, whereas turbidite beds > 100 cm are in red. T_{bc}-division turbidites (e.g. with a basal sand layer) are indicated with● symbol. The numbers of several turbidite beds are indicated, including the megabed (M*) described by Rothwell et al. (1998). For dating criteria see Appendix 6.2. The emplacement time of turbidite beds that appear beyond the extent of dated hemipelagic intervals is speculative; these turbidite beds (3 in LC02 and 16 in LC06) are not plotted. The calculated emplacement times for the period 0-21 ka BP in LC06 are not accurate due to uncertainties in the time-stratigraphic framework.

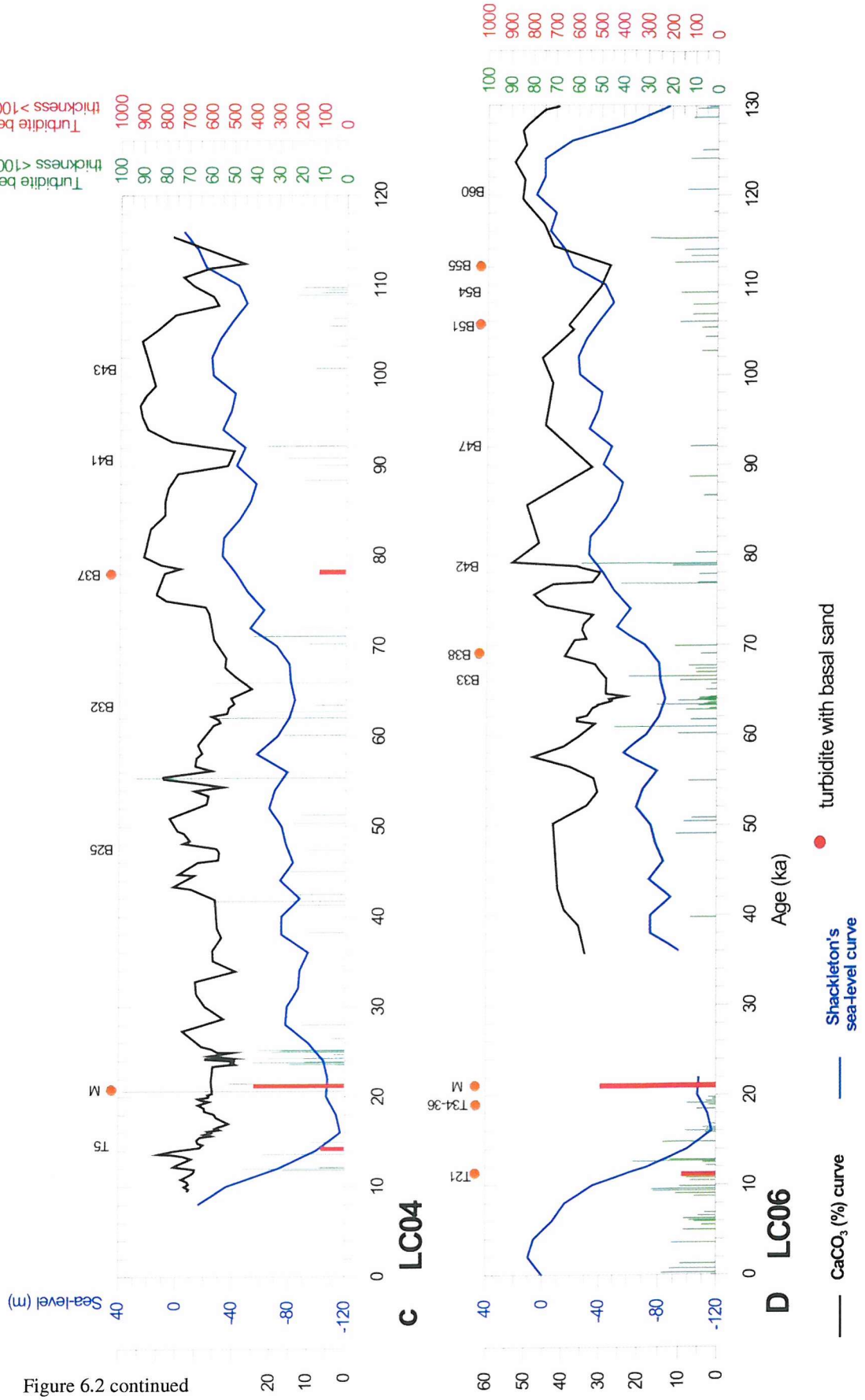

Figure 6.2 continued

at 12 ka and 23-25 ka in LC04, 0-21 ka and at 60-68 ka in LC06 (Figure 6.2). Apart from the megaturbidite, correlation of other thick turbidite beds (>1 m) from core to core is uncertain, because their emplacement times seem to vary (Figure 6.2).

Short time periods, of the order of 4 –10 ka duration during which turbidite deposition did not occur are observed in the four studied cores (Figure 6.2). The timing of these turbidite-free intervals is similar in the four cores and can be correlated with periods where sea level/climate change was minimal, except for the youngest interval, which coincides with the base of Marine Isotope Stage 1 (see Figure 6.3). The turbidite-free intervals are used as chronostragraphic markers, delineating periods when turbidite emplacement did not occur (Table 6.5). In several instances, the number of turbidites deposited during these periods was remarkably similar (for example, during periods 2, 3 and 4 in LC01 and LC02), but in others it varies significantly (compare periods 3 to 5 between LC02 and LC04 and periods 5 to 8 between LC04 and LC06) (Table 6.5). The occurence of similar numbers of turbidites within similar periods of time in different cores may either indicate that they reflect basin-wide episodes, perhaps originating from a single source, or that they comprise several events from different source areas during conditions that were particularly favourable for turbidite emplacement.

6.4.2 Turbidite frequency and fluxes

On average, turbidite frequency (i.e. number of turbidites emplaced per ka) in the four cores was quite similar and was about 1-2 turbidites every 2000 years (Table 6.6). However, the average turbidite flux (i.e. cm deposited per ka) is higher in the northern cores (Table 6.6).

Ten periods of turbidite deposition can be delineated in the four cores (Figure 6.3). Periods 1 and 8-10 are from interglacial times and are characterised by low (<1 turbidite per ka) to common (1-2 turbidites per ka) turbidite frequencies and individual turbidite beds are generally thin (<25 cm). Turbidites from the last glacial, covered by periods 2-7, have low to high (>2 turbidites per ka) turbidite frequencies and turbidites are generally of medium thickness (25-50 cm) to thick (>50 cm) (Figure 6.3, Table 6.7).

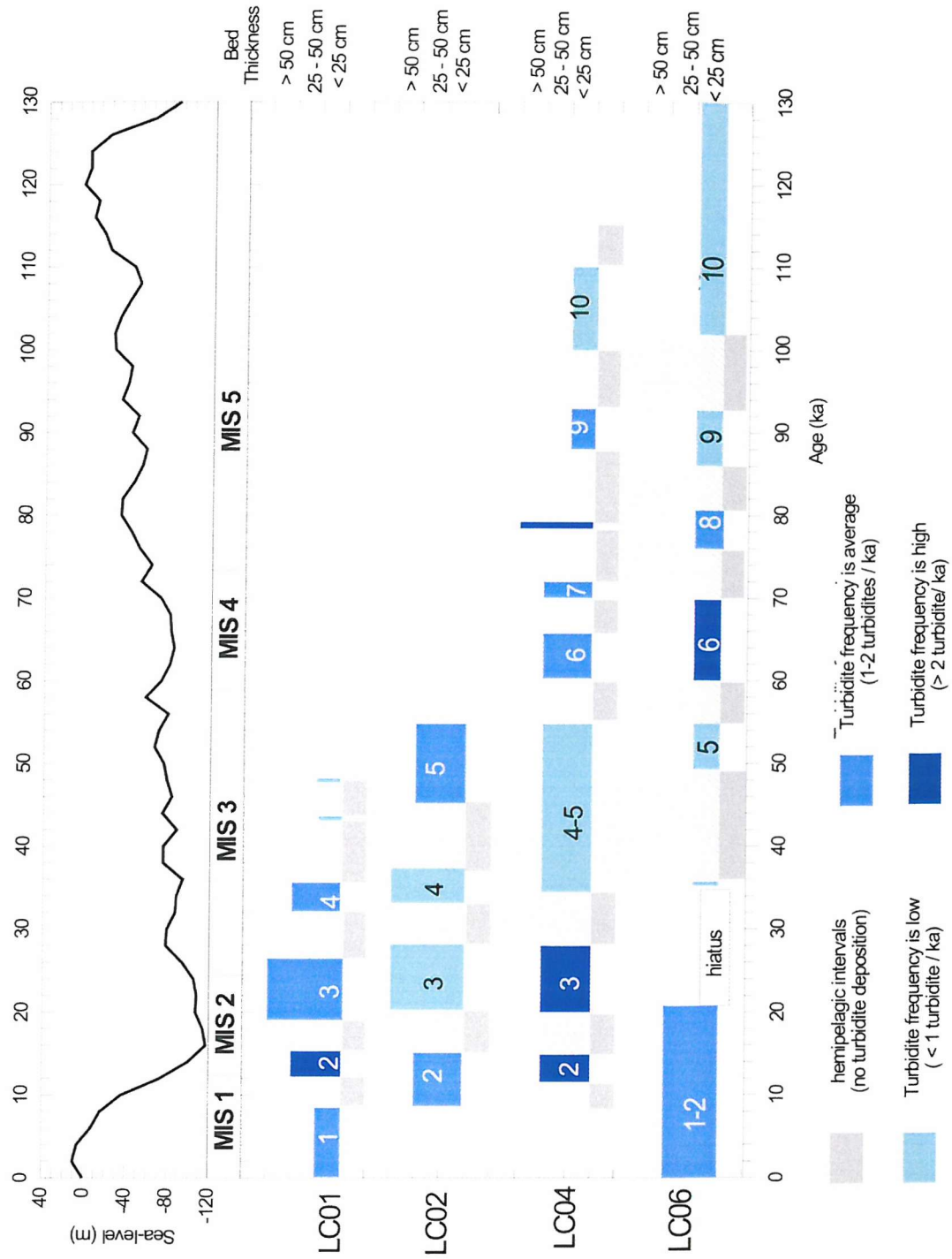

Figure 6.3 Overview of periods characterised by turbidite deposition (shades of blue) and periods with predominantly hemipelagic sedimentation (grey). Grey shaded areas in the background link hemipelagic intervals among the four cores. Turbidite frequency is divided into three groups: low (<1.0 turbidites/ka, light blue), common (1.0-2.0 turbidites/ka, medium blue) and high (>2.0 turbidites/ ka, dark blue). Average turbidite thickness is further separated into thin (<25 cm), medium thick (25-50 cm) and thick (>50 cm). Numbers in blue boxes refer to periods defined in Table 6.5. Note that most periods dominated by hemipelagic accumulation coincided with periods of minor sea level/climate fluctuations.

Table 6.5 Average number of turbidites per period* and per MIS

Core	Period 1 (ka)	Period 2 (ka)	Period 3 (ka)	Period 4 (ka)	Period 5 (ka)	Period 6 (ka)	Period 7 (ka)	Period 8 (ka)	Period 9 (ka)	Period 10 (ka)
LC01	***0 – 8***	***12 – 15***	***19 – 26***	***32 - 35***						
no.	14 – 16	6 – 8	8	3						
LC02		***8 – 15***	***20 – 28***	***32 – 37***	***45 – 55***					
no.		8 – 10	4 – 7	4	17 – 22					
LC04		***12 – 15***	***20 – 28***	***35 - 55***		***60 – 65***	***70 – 72***		***88 – 93***	***100 – 110***
no.		6	18 – 20	10		5	3		6	8
LC06	***0 – 21***				***49 – 55***	***60 – 70***		***76 – 80***	***86 – 93***	***102 – 130***
no.	37-39				4-5	24		6	3	17
Average no. per period	14-16	7-8	10-12	3-4	11-14	5	3	5	5	13
Average MIS	***MIS 1***	***MIS 2***		***MIS 3***		***MIS 4***		***MIS 5***		
no.	14-16	8-10		7-9		4		8		

* periods 1 to 10 represent the periods as defined in the text, delineated by intervals (4-10 ka) during which no turbidite deposition occurred.

Table 6.6 Number of turbidite beds per core and calculated average turbidite flux and frequency.

Core	Period (ka)	No. of turbidites	Total turbidite thickness (m)	Average turbidite frequency (number/ka)	Average turbidite flux (cm/ ka)
LC01	1.9-50.0	32 - 37	16.52	~ 0.7	34
LC02	7.8-57.2	33 – 43	22.96	~ 0.7-0.8	46
LC04	10.4-113.4	55 – 58	20.45	~ 0.5-0.6	20
LC06	0??-21 37-129.9	113-114	19.14	~ 0.8	17

6.4.3 Emplacement times of turbidites with basal sands

During marine regressions deep-sea marine sand deposition is predicted to increase according to sequence stratigraphic models (e.g. Posamentier and Vail, 1988). The assumption is that sediment, which would otherwise be deposited on the shelf, is transported across the subaerially exposed shelf by fluvial systems and deposited beyond the shelf-to-slope break into a deep marine environment (Burgess and Hovius, 1998). In the studied cores, turbidites with basal sands are common during periods of sea-level fall (Figure 6.2). However, emplacement of T_{bc}-division turbidites also occurs during sea-level rises and, in core LC02, even during periods of minor sea-level variations (Figure 6.2). Most turbidites with basal sands occur in LC02 and were deposited over a short period of time (7-55 ka) (Table 6.6) which suggests that LC02 is located closer to the source area (Chapter 4). Several turbidite beds with basal sands (T_{bc}-division turbidites) have similar emplacement times (i.e. T11/T12?* in LC01 and T8/T9?* in LC02 and T28* in LC06 were emplaced between 13 and 16 ka) (Figure 6.2, Appendix 6.2), which suggests they might reflect a basin-wide event.

6.4.4 Filling the Balearic Abyssal Plain basin floor

The pattern of turbidite filling of the BAP seafloor over the last 130 ka is illustrated in Figure 6.4. This figure has been constructed by summing the thickness of each individual turbidite bed against time. Intervals with steep gradients indicate rapid sediment accumulation compared to intervals with gentler gradients. MIS 1 in LC01 has a relatively steep gradient, which indicates that sediment accumulation during this period was rapid (Figure 6.4). During the last glacial period increased basin-wide filling of the BAP by ponded turbidites was especially marked during 12-15 and 20-28 ka; these periods coincided with the last deglaciation and the Last Glacial Maximum

Table 6.7 Calculated average turbidite frequency (numbers of turbidites per ka) and flux (cm/ka) per emplacement period per core and MIS.

Core	Period 1 (ka)	Period 2 (ka)	Period 3 (ka)	Period 4 (ka)	Period 5 (ka)	Period 6 (ka)	Period 7 (ka)	Period 8 (ka)	Period 9 (ka)	Period 10 (ka)
LC01	***0 – 8***	***12 – 15***	***19 – 26***	***32 - 35***						
freq.	1.8 - 2.0	2.0 - 2.7	0.9	1.0						
flux	22 – 25	29 – 39	115	39						
LC02		***8 – 15***	***20 – 28***	***32 – 37***	***45 – 55***					
freq.		1.1–1.4	0.5-0.9	0.8	1.9					
flux		39-49	96-168	83	39					
LC04		***12 – 15***	***20 – 28***	***35 - 55***		***60 – 65***	***70 – 72***		***88 – 93***	***100 – 110***
freq.		2.0	2.3 - 2.5	0.5		1.0	1.5		1.2	0.8
flux		41	45-50	30		40	40		45	10
LC06	***0 – 21***				***49 – 55***	***60 – 70***		***76 – 80***	***86 – 93***	***102 – 130***
freq.	1.8-2.0				0.7-0.8	2.4		1.5	0.4	0.6
flux	42				11	30		36	6	7
Ave. freq.	1.9	1.7-2.0	1.2-1.4	0.9	1.3-1.4	1.8		1.5	0.8	0.7
A. flux	24	36-43	85-111	61	25	35		36	26	9
	MIS 1	***MIS 2***		***MIS 3***		***MIS 4***		***MIS 5***		
Ave. freq.	1.9	1.5-1.7		1.1-1.2		1.8		1.0		
Ave. flux	24	61-77		43		35		24		

respectively (Figure 6.4). Sediment accumulation was also increased between 60 and 70 ka BP (MIS 4), 78/80 ka and 105-115 ka. Locally, sediment accumulation was high in the northern part of the basin (LC01, LC02) between 32- and 37 ka, and at the location of LC02 at around 48 and 55 ka (Figure 6.4). Local filling was slightly enhanced at around 42 ka at the location of LC04 (Figure 6.4).

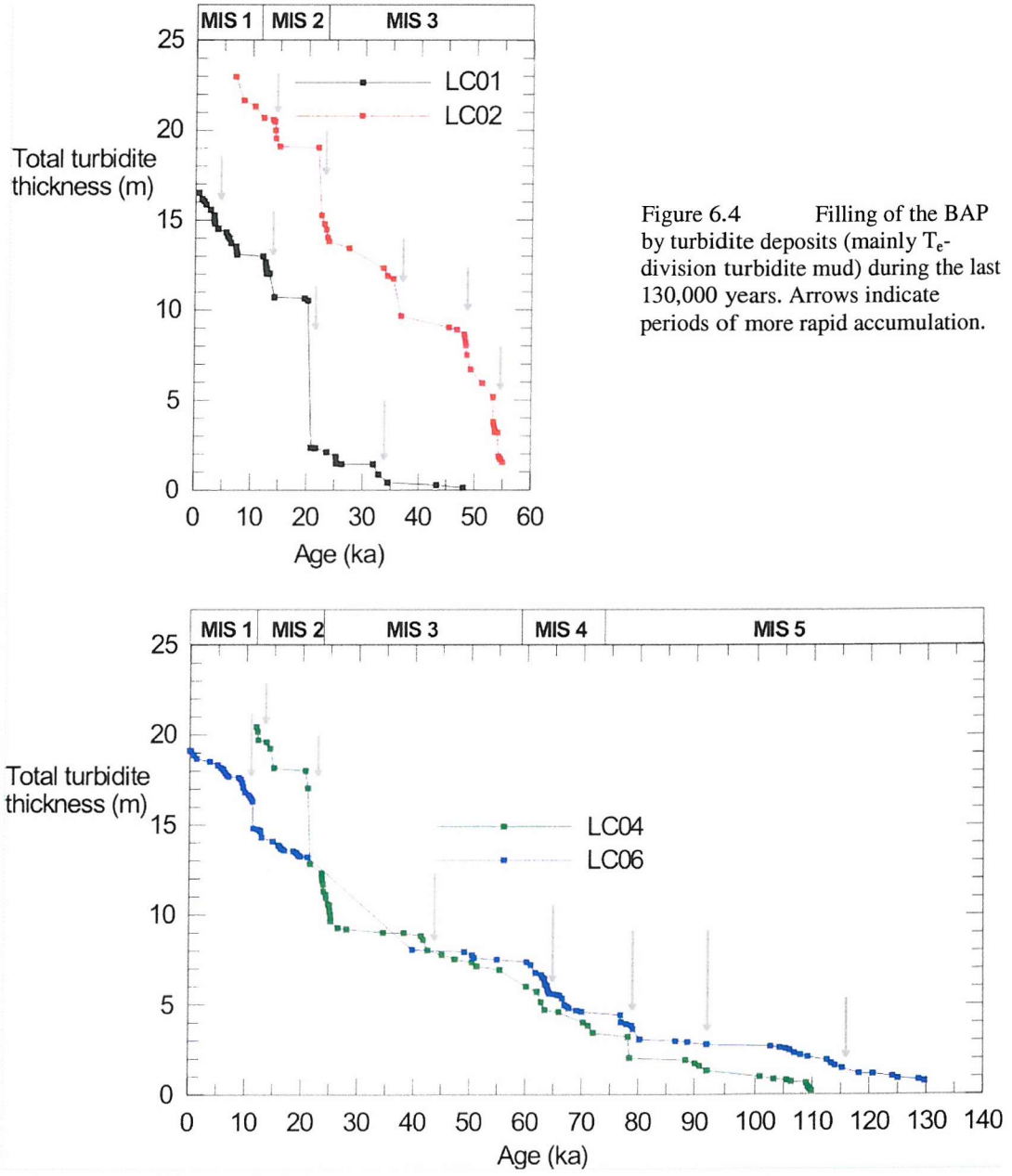

Figure 6.4 Filling of the BAP by turbidite deposits (mainly T_e-division turbidite mud) during the last 130,000 years. Arrows indicate periods of more rapid accumulation.

6.4.5 Contribution of turbidite Groups I, II and III to the Balearic Abyssal Plain sedimentary sequence

In Chapter 4, three turbidite groups (Group I, II and III) were defined, based on $CaCO_3$ content and clay mineralogy. It was suggested that Group II turbidites might originate from a southern (i.e. north African) source, since the clay mineralogy of Saharan dust is higher in kaolinite content than chlorite (Chapter 4). Group I and possibly Group III turbidites are more likely to have originated from the southern European margin. Turbidites from the two northern cores (LC01, LC02) and the southerwestern core (LC04) are predominantly from Group I (Table 6.8), which suggests a mainly southern European margin origin. Most turbidites from the south-eastern core (LC06) are from Group II and are thought to have been be transported from the north African margin, except during Marine Isotope Stage 2 during which turbidites from Group I dominated the recovered total turbidite length (Table 6.8).

6.5 CONTROLS ON TURBIDITE SEDIMENTATION IN THE WESTERN MEDITERRANEAN

Many recent studies demonstrate that turbidite deposition occurred at times of sea-level rises and highstands. For example, turbidite deposition is recorded during sea-level rises and highstands on the Amazon Fan (Flood et al., 1991), Mississippi Fan (Kolla and Perlmutter, 1993), Navy Fan (Piper and Normark, 1983) and Bengal Fan (Kuehl et al., 1989; Weber et al., 1997). Local conditions such as high fluvial discharge, headward erosion of submarine canyons and/or sediment transport into canyons by shelf-parallel currents have all been proposed as promoting sediment transport off the shelf into deep water (Palanques et al., 1994; Burgess and Hovius, 1998). On the Makran continental slope in the Arabian Sea, turbidite sedimentation during the last early sea-level rise is attributed to the narrow shelf width (Prins and Postma, 2000). On the Ebro fan, sediment supply increased significantly during sea level low stands, due to doubled river sediment discharge during the Pleistocene lowstands compared with the Holocene highstand (Nelson, 1990). The rising sea level

Table 6.8 Contributions of each turbidite Group to the total sediment thickness calculated per MIS.

	Total thickness in core (cm) per MIS/ % in core per MIS				
Core, Group	MIS 1	MIS 2	MIS 3	MIS 4	MIS 5
LC01					
Group I	370 cm/ 85%	852 cm/ 84%	158 cm/ 85%		
Group II					
Group III	21 cm/ 5%	165 cm/ 16%	27 cm/ 15%		
Not in Group	45cm/ 10%	1 cm/			
LC02					
Group I	239 cm/ 100%	693 cm/ 97%	1171 cm/ 87%		
Group II					
Group III			26 cm/ 2%		
Not in Group		22 cm/ 3%	145 cm/ 11%		
LC04					
Group I	85 cm/ 100%	845 cm/ 99%	513 cm/ 100%	258 cm/ 92%	139 cm/ 43%
Group II					
Group III					173 cm/ 54%%
Not in Group		4 cm/ 1%		22 cm/ 8%	8 cm/ 3%
LC06					
Group I	238 cm/ 49%	506 cm/ 83%	0??	128 cm/ 43%	121 cm/ 27%
Group II	246 cm/ 51%	96 cm/ 15%	56 cm/ 67%	168 cm/ 57%	276 cm/ 62%
Group III					
Not in Group		6 cm/ 2%	28 cm/ 33%		45 cm/ 11%

of the Late Pleistocene transgression coincided with high sediment discharges, which suggests that deforestation and increased erosion resulting from climatic changes influenced sediment deposition on the Ebro margin (Nelson, 1990). These studies suggest that the formation of shelf-edge deltas and consequent significant deep-marine deposition is not limited to times of relative sea-level lowstands and early transgression (Einsele, 1996; Burgess and Hovius, 1998), and that local factors may play an important role.

Turbidite sedimentation on abyssal plains is also not restricted to sea-level low-stands. For example, Weaver and Kuijpers (1983) reported that turbidite deposition on the Madeira Abyssal Plain was more likely during sea-level regressions and transgressions rather than during high- or lowstands.

In this study it is shown that turbidite deposition on the BAP was not confined to glacial (sea-level low stands) or interglacial periods (sea-level high stands) or to sea-level regressions and transgresions. Turbidite emplacement to the BAP occurred regularly (on average one turbidite every one to two thousand years), without major temporal gaps. Turbidite deposition was, however, more frequent during periods when sea-level and climate underwent profound changes. Highest turbidite frequencies occurred during periods of maximum sea-level/climate change (Figure 6.3). Average turbidite thickness was substantially greater during the last three colder Marine Isotope Stages (2-4) (Figure 6.3, Table 6.4) and, as a consequence, filling of the Balearic Basin floor was accelerated at those times (Figure 6.4).

The above discussion suggests that sediment supply to the western Mediterranean margins and the deep-sea basins, including the BAP, was greatly increased during the last glacial period. What was/were the main cause(s) of this increase in sediment supply?

The control of sea-level on riverine sediment supply to the western Mediterranean Sea has a landward limit of ~100 km for rivers with a lower gradient and higher sediment supply, whereas that of steep-gradient, low-sediment supply systems is estimated at only around 40 km (Blum and Törnqvist, 2000). Sediment supply from the lower reaches of the larger rivers (Rhône, Ebro and possibly the Var) is therefore expected to be influenced by sea-level fluctuations, whereas the upper reaches will be unaffected. Very small river systems (<40 km), on the other hand, might be completely influenced by sea-level control. The contribution of sediments from these smaller river systems to the western Mediterranean margin is, however, orders of magnitude lower compared to the larger river systems. Major changes in sea level would not change this. Moreover, most of the smaller river systems drain into areas that are characterised by narrow continental shelves and slopes, which probably act as sediment bypass zones, which would avoid substantial sediment accumulation on the continental shelf that could produce large turbidites. The larger river systems (Ebro/Valencia, Rhône and Var) have wider continental shelves and slopes, which are, thus, capable of storing substantial amount of sediment. The continental slopes and

shelves of western Sardinia, the southern Menorca promontory and the Ibiza plateau are also wide (Rehault et al., 1984) and could form areas were substantial sediment accumulation can take place. During glacial periods, the drop in sea level caused the continental shelves that lie proximal to major river systems to be subaerially exposed (Figure 6.5).

Most areas surrounding the western Mediterranean Sea are experiencing some form of uplift, due to neotectonic compression and/or isostatic rebound. Uplift due to neotectonic compression was probably constant over the period considered here. Uplift resulting from isostatic rebound mainly occurs during interglacial periods and would not promote increased sediment supply during glacials.

In the southern Pyrenees, Jones et al. (1998) concluded that the main control on river incision was climate through its influence on sediment supply. The drainage basin was less vegetated during glacial periods, which promoted catchment erosion and caused an increase in sediment supply to the river and within-channel aggradation (Jones et al., 1998). During interglacials, the climate was warmer and more humid which led to more vegetation and a reduction in sediment supply to the rivers, favouring vertical river incision (Jones et al., 1998). These observation are consistent with those of Lewin et al. (1995), Fuller et al. (1998) and Rose et al. (1999) for the western Mediterranean environment, with mainly dry and cold conditions and unvegetated surfaces during glacials and wet and humid conditions with more vegetated surfaces prevailing during interglacial periods. The cold and dry glacial conditions also promoted enhanced eolian sediment supply to the western Mediterranean environment, which was associated with higher wind intensities and enhanced aridity (see Chapter 5; also Weldeab et al., 2003).

Riverine sediment supply to the margins surrounding the western Mediterranean thus seems to be largely controlled by climate, although the influence of sea level is probably also important for the lower reaches. Isostatic uplift during the Holocene might have caused enhanced sediment supply to the margin, but could not have affected the major river systems during the last glacial.

Higher turbidite frequencies that have been calculated for the BAP basin can be related to periods with more dynamic sea-level/climate changes associated with increased sediment supply to the shelf edge. Higher turbidite fluxes during MIS 2-4 are

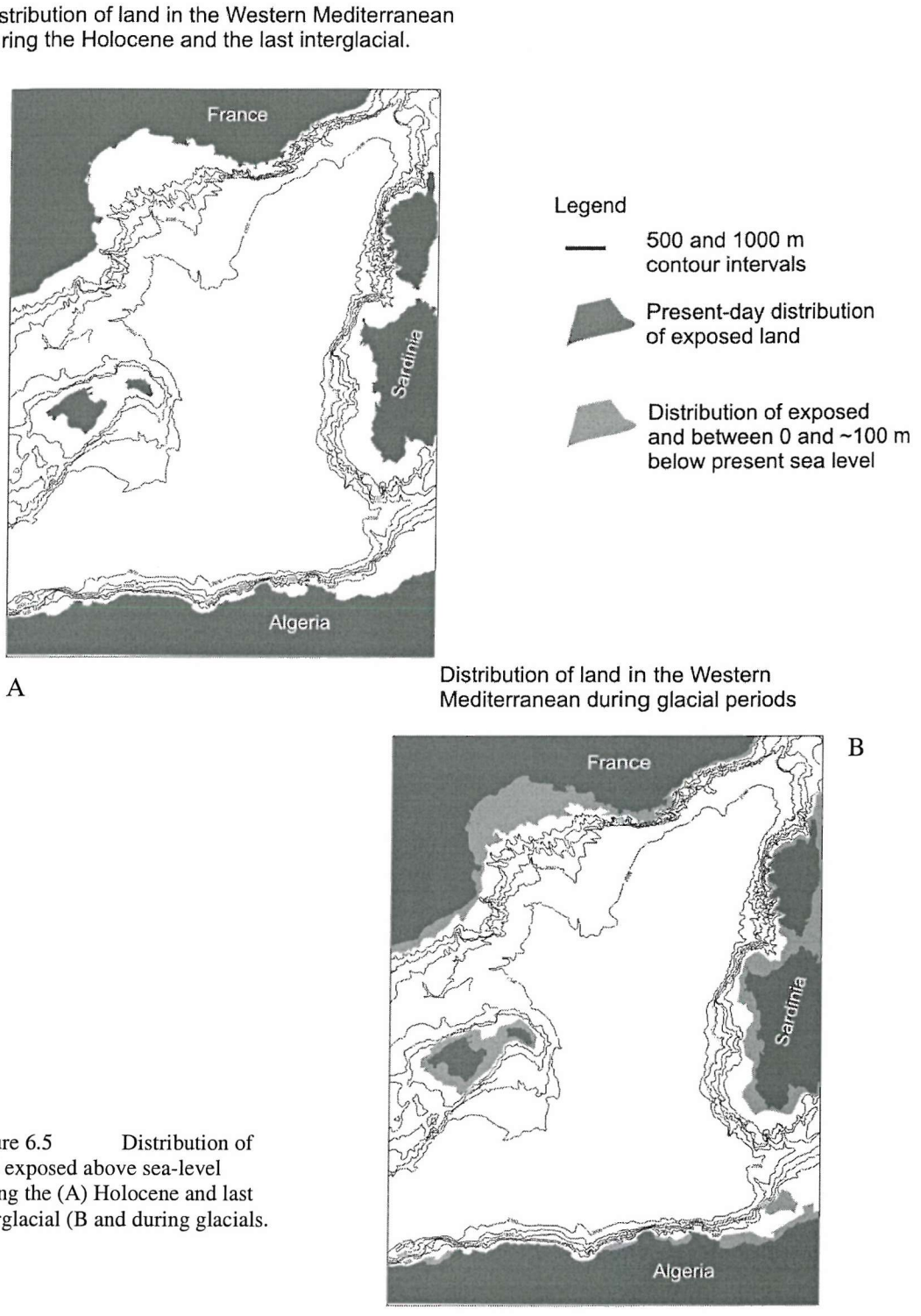

Figure 6.5 Distribution of land exposed above sea-level during the (A) Holocene and last interglacial (B and during glacials.

most likely due to an increase in supply of riverine sediment to the basin. The average turbidite flux to the BAP during MIS 2 was about two to three times higher than during

MIS 5, which suggests that the supply of riverine sediment to the abyssal plain may have at least doubled.

Compared to the last interglacial (MIS 5), the number of turbidites deposited during MIS 1 was greatly enhanced. Deforestation and increased erosion during the last sea-level rise might explain the higher number of turbidites deposited during MIS 1.

6.6 CONLUSIONS

- Sedimentary sequences in four long piston cores from the BAP provide a unique opportunity to reconstruct the depositional and erosional history of the basin. The GISP2 fine tuned time-stratigraphic framework developed in Chapter 5 has provided important contrainst for determining individual turbidite emplacement times.

- Turbidite deposition on the BAP occurred regularly and withouth major temporal gaps, with an average frequency of one turbidite every one to two thousand years.

- Periods of turbidite deposition are separated by intervals of predominantly hemipelagic sediment accumulation. These intervals of predominantly hemipelagic sedimentation coincided with times when sea-level/climate change was minimal, except for the youngest interval, which coincided with the base of MIS 1 and can possibly be attributed to low sediment delivery to the margins during the late sea level rise. Higher turbidite frequencies were recorded during periods of maximum sea-level and climate change.

- During the last glacial period, turbidite beds were much thicker and probably had larger volumes than those emplaced during interglacial periods (MIS 1 and 5). The average turbidite flux to the BAP during MIS 2 was about two to three times higher than during MIS 5, which suggests that sediment supply to the basin was also at least two to three times higher during that time. This increase in sediment supply was most likely due to increased riverine sediment fluxes as a result of the colder and drier environmental conditions and possibly to lower sea-level.

- The high number of turbidites deposited during MIS 1 may be explained by deforestation and subsequent increased continental erosion. The average turbidite flux during MIS 1 was, however, similar to that documented for MIS 5.

- Basin-wide filling of the BAP by turbidites was especially rapid during the last deglaciation and the Last Glacial Maximum. Sediment accumulation was however also increased during MIS 4, 78/80 ka and 105-115 ka.

- These results do not support the hypothesis that the advective sediment flux to the basin is only high during glacials.

CHAPTER 7 – SUMMARY, CONCLUSIONS AND FUTURE WORK

7.1 SUMMARY AND CONCLUSIONS

In this study the sedimentary sequences recovered in four giant piston cores, which make up the upper 30-35 metre of basin plain sediments from the Balearic Abyssal Plain, were described using textural and sedimentological criteria. The upper 12-15 metres of the four studied giant piston cores may haven been stretched by coring by a factor of 1.5 to 2. To reduce this effect, the length of the involved intervals was divided by a maximum estimated stretch factor of 2. The Balearic Abyssal Plain cored sequence is dominated by turbidite deposits (90% of the sediment recovered), whereas hemipelagic intervals only make up 10% of the sediments. The average thickness of turbidite beds decreases from the north of the basin plain (LC01, LC02) to the south (LC04, LC06), which suggests that the northern cores are closer to a source area with abundant sediment supply. Core LC02 received the most turbidites with basal sands during the last 55 ka, which provides further evidence that core LC02 is proximal to a major turbidite source area.

The hemipelagic intervals were used to form a tight chrono-stratigraphic framework in Chapter 5, which was initially based on biostratigraphy, AMS radiocarbon dates, oxygen isotope stratigraphy and calcium carbonate content. The hemipelagic carbonate records show distinct 'Atlantic' type cycles, where glacial periods show on average 20% lower calcium carbonate contents due to increased dilution by terrigenous material. The recognition of several possible cold events in the four cores, which have been correlated to Heinrich events, Dansgaard-Oeschger stadials and cold events within MIS 5, allowed the initial time-stratigraphic framework to be fine-tuned to GISP2. These cold events are characterised by enhanced magnetic susceptibility values and low calcium carbonate contents and are interpreted to reflect periods of increased aridity in the western Mediterranean environment. The results further indicate that although 90% of the sedimentary sequence of Balearic Abyssal Plain consists of turbidites, these events did not cause significant erosion of the sedimentary substrate.

Preceding construction of the time-stratigraphic frameworks for the Balearic Abyssal Plain piston cores, a reference core was analysed from a location (north of the

Skerki Channel) where disturbance related to downslope transport is unlikely (Chapter 3). This core, LC07, mainly consists of hemipelagic sediments. The oxygen isotope record of LC07 revealed fourteen alternating glacial and interglacial stages that correlate well with the SPECMAP curve. Moreover, the developed stable carbon isotope records show two conspicuous long-term fluctuations between 1.00-0.50 and 0.50-0.10 Ma. Both fluctuations are observed in stable carbon isotope ($\delta^{13}C$) records from both surface and deep waters in all major ocean basins. In Chapter 3, evidence and existing hypotheses for these global Pleistocene $\delta^{13}C$ fluctuations are evaluated and it is suggested that the fluctuations resulted from concomitant changes in the burial fluxes of organic and inorganic carbon due to changes in bottom water ventilation. It was found that periods of decreasing $\delta^{13}C$ values are characterised by low preservation of organic matter and increased calcium carbonate dissolution. The simple box model, presented in Chapter 3, that was developed to assess the impact of global $\delta^{13}C$ changes in the global carbon cycle over Pleistocene time-scales, indicated that to satisfy the long-term 'stability' of the Pleistocene lysocline, the ratio between the amounts of change in the organic and inorganic carbon burial fluxes must have been tightly constrained to a 1:1 ratio. It is further suggested that the mid-Pleistocene climate transition, whose timing is similar to the first $\delta^{13}C$ fluctuation (Mid-Pleistocene Carbon isotope Fluctuation, or MPCF), was not associated with a fundamental change in pCO_2.

The GISP2 fine-tuned time-stratigraphic framework developed in Chapter 5 provided important constraints on individual emplacement times of almost all turbidite beds recovered in the studied cores (Chapter 6). Turbidite emplacement to the Balearic Abyssal Plain occurred regularly (on average one turbidite every one to two thousand years), without major temporal gaps. Highest turbidite frequencies occurred during periods of maximum sea level/climate change. Turbidite beds from the last glacial period (Marine Isotope Stages 2-4) were much thicker than turbidite beds from interglacial periods (Marine Isotope Stages 1 and 5), which suggests that the glacial advective sediment flux to the Balearic Abyssal Plain was significantly enhanced (Chapter 6). Sediment supply to the continental margins and to the Balearic Abyssal Plain is estimated to have been at least doubled during the Last Glacial Maximum, due to increased riverine sediment fluxes as a result of colder and drier environmental conditions and possibly lower sea level. Turbidite

frequencies were also enhanced during Marine Isotope Stage 1, which is explained by deforestation and subsequent increase in erosion during this period. Several periods were identified during which hemipelagic sedimentation dominated. Almost all of these periods coincided with times of minor sea level/climate fluctuations, whereas intervals with frequent turbidite deposition generally occur during periods of more dynamic sea level/climate change.

It is shown that turbidite deposition on the Balearic Abyssal Plain, during the last 130,000 years, was not confined to certain time intervals. The temporally well-constrained data, developed during this study, do not support the hypothesis that the advective sediment flux to the basin is only high during glacials - this view is too simple and does not stand up to detailed testing. Basin-wide filling of the BAP by turbidites was especially rapid during the last deglaciation and the Last Glacial Maximum. However, sediment accumulation was also increased during MIS 4, 78/80 ka and 105-115 ka.

7.2 SUGGESTED FUTURE WORK

7.2.1 Turbidite sedimentation

It would be interesting to compare the temporal pattern of turbidite emplacement on the Balearic Abyssal Plain with other abyssal plains over the last 130,000 years, and see whether there are any variations in this pattern. Perhaps there are latitudinal variations that might be related to climatic variations or it might be possible that abyssal plains from open oceanic conditions show different patterns compared with a semi-enclosed basin like the Mediterranean. At the present time, however, most other turbidite-stratigraphic studies are mainly based on seismic data analyses that lack high-resolution dating. As a consequence, a comparison between results of the present study and other studies is limited. It is therefore suggested to develop similar temporally well-constrained data sets for other regions, where core material is already available, for example like the Madeira Abyssal Plain.

The results of this study span the last glacial/interglacial cycle. In order to find out about the pattern of turbidite deposition in older sequences, additional cores would be needed that go further back in time.

If more information were available on turbidite provenance, it would be possible to create a more detailed reconstruction of filling of the Balearic Abyssal Plain. To achieve this, it may be useful to compare clay mineralogy between the various source areas. Additionally it would be useful to have more information on turbidite mud chemistry. Elemental analyses could be performed by simultaneous inductively coupled plasma atomic emission spectroscopy (ICP-AES) and by XRF analysis.

7.2.2 Hemipelagic sedimentation

In order to find out more about hemipelagic mud elemental chemistry, and possible changes with depth/time it would be of interest to run XRF analysis. XRF analysis could give information on the relative amount of iron present in samples, which could reflect dust input. Si/Al and Ti/Al ratios might provide important constraints on the provenance of the lithological components of this terrestrial input.

Glacial (MIS 2) $\delta^{18}O$ values at the site of core LC01 are on average 0.5‰ higher than at the site of LC04, suggesting that the Last Glacial Maximum temperatures at the site of LC01 were up to 2°C lower than at the site of LC04 (Figure 5.5). The Holocene $\delta^{18}O$ values at both sites, on the other hand, are similar (Figure 5.5). Hence, the glacial temperature contrast between the sites of LC01 and LC04 may have been some 2°C stronger than today. Oxygen isotope measurements should also be performed for the other two cores, LC02 and LC06, in order to establish this effect for the whole basin. These results might provide important clues on past ocean and atmospheric circulation in the western Mediterranean Sea.

7.2.3 Pleistocene long-term carbon isotope fluctuations

Changes in bottom water ventilation have been proposed to drive the long-term global carbon isotope fluctuations. What are however the mechanisms that drive global

bottom water ventilation? In order to answer that question more information is needed concerning the speed, direction and intensity of ocean circulation on a global scale. Although scientist have a fairly good idea what is going on the present day, past ocean circulation reconstructions are not as well understood. Both carbon isotope fluctuations occur during periods of eccentricity and insolation minima. How, and in what manner, do the ocean and atmosphere function and interact during these times? Temperature estimates of the surface oceans (bases on relative abundances of planktonic foraminifera species and alkenones) for several key cores might give important clues on the climatic conditions during these times. The carbon isotope records that were used in this study were from both planktonic and benthic foraminifera. In order to study the possibility of changes in productivity it is vital to have carbon isotope records from both planktonic and benthic foraminifera from the same cores from the same depth intervals.

The box-model used in the present study lacks a mechanistic basis. In a follow-up study it would be useful to add carbonate chemistry to the model, to allow feedback among fluxes.

Cited References

Acosta, J., Canals, M., López-Martínez, J., Muñoz, A., Harranz, P., Urgeles, R., Palomo, C., Casamor, J.L., 2003. The Balearic Promontory geomorphology (western Mediterranean): morphostructure and active processes. Geomorphology 49, 177-204.

Added, A., Fernex, E., Ringot, J.L., Span, D., 1984. Caractères sédimentologiques et géochemiques du plateau continental devant l'embouchure de grande Rhône. In: Bizon, J.J., Burollet, P.F. (Eds.) Ecologie des microorganismes en Méditerranée occidentale. Association Française des Technicents du Pétrole, Paris, pp. 33-45.

Alinat, J., Couseau, J.Y., Giermann, G., Leenhardt, O., Perrien, Th., Pierrot, S., 1969. Lever de la carte bathymétrique de la Mer Ligure. Bulletin Institute Océanographic Monaco 69, pp. 12.

Allen, J.R.M., Brandt, U., Brauer, A., Hubberten, H.-W., Huntley, B., Keller, J., Kraml, M., Mackensen, A., Mingram, J., Negendank, J.F.W., Nowaczyk, N.R., Oberhansli, H., Watts, A., Wulf, S., Zolitschka, B., 1999. Rapid environmental changes in southern Europe during the last glacial period. Nature 400, 740-743.

Allen, J.R.M., Huntley, B., 2000. Weichselian palynological records from southern Europe: correlation and chronology. Quaternary International 73/74, 111-125.

Allen, J.R.M., Watts, W.A., Huntley, B., 2000. Weichselian palynostratigraphy, palaeovegetation and palaeoenvironment; the record from Lago Grande di Monticchio, southern Italy. Quaternary International 73/74, 91-110.

Alonso, B., 1986. El Sistema del Abanicco Profundo del Ebro. Doctoral Thesis, Universitat de Barcelona, 384 pp.

Alonso, B., Canals, M., Got, H., Maldonado, A., 1991. Sea valleys and related depositional systems in the Gulf of Lion and Ebro continental margins. American Association of Petroleum Geologists Bulletin 75, 1195-1214.

Alonso, B., Maldonado, A., 1990. Late Quaternary sedimentation patterns of the Ebro turbidite system (northwestern Mediterranean): two styles of deep-sea deposition. Marine Geology 95, 353-377.

Altinakar, M.S., Graf, W.H., Hopfinger, E.J., 1996. Flow structure in turbidity currents. Journal of Hydraulic Research 34, 713-718.

Amerigian, C., 1974. Sea-floor dynamic processes as the possible cause of correlation between paleoclimate and paleomagnetic indices in deep-sea sedimentary cores. Earth and Planetary Science Letters 21, 321-326.

Andres, W., Ries, J., Seeger, M., 2002. Pre-Holocene sediments in the Barranco de las Lenas, Central Ebro Basin, Spain, as indicators for climate-induced fluvial activities. Quaternary International 93-94, 65-72.

Anthony, E.J., 1995. Impacts gèomorphologiques côtiers les aménagements du Var et de son delta, Côte d'Azur, France, Hommes et Terres du Nord 1-2, 73-81.

Anthony, E.J., Julian, M., 1995. The 1979 Var Delta Landslide on the French Riviera: a retrospective analysis. Journal of Coastal Research 13, 27-35.

Anthony, E.J., Julian, M., 1999. Source-to-sink sediment transfers, environmental engineering and hazard mitigation in the steep Var River catchment, French Riviera, southeastern France. Geomorphology 31, 337-354.

Antonioli, F., Silenzi, S., Vittori, E., Villani, C., 1999. Sea level changes and tectonic mobility: precise measurements in three coastlines of Italy considered stable during the last 125 ky. Physics and Chemistry of the Earth Part A-Solid Earth and Geodesy 24, 337-342.

Arnaud-Fassetta, G., Bruzzi, C., L'Homer, A. Provansal, M., Sabatier, F., Suanez, S., Vella, C., 1999. Géomorphologie du Delta de Rhône. Édification Holocène et Fonctionnement Actuel, Livret Guide de l'Excursion Franco-Roumaine du 23-25 Septembre 1999. Institut de Géography, University of Aiz-Marseille I et Conseil Général des Bouches-du-Rhône, Marseille.

Baraza, J., Lee, H.J., Kayen, R.E., Hampton, M.A., 1990. Geotechnical characteristics and slope stability on the Ebro margin, western Mediterranean. Marine Geology 95, 379-393.

Bárcena, M.A., Cacho, I., Abrantes, F., Sierro, F.J., Grimalt, J.O., Flores, J.A., 2001. Paleoproductivity variations related to climatic conditions in the Alboran Sea (western Mediterranean) during the last glacial-interglacial transition: the diatom record. Palaeogeography Palaeoclimatology Palaeoecology 167, 337- 357.

Bassinot, F.C., Beaufort, L., Vincent, E., Labeyrie, L.D., Rostek, F., Müller, P.J., Quidelleur, X., Lancelot,

Y., 1994. Coarse fraction fluctuations in pelagic carbonate sediments from the tropical Indian Ocean: a 1500-kyr record of carbonate dissolution. Paleoceanography 9, 579-600.

Bassinot, F.C., Beaufort, L., Vincent, E., Labeyrie, L., 1997. Changes in the dynamics of western equatorial Atlantic surface currents and biogenic productivity at the "Mid-Pleistocene Revolution" (~930 ka). In: Shackleton, N.J. et al. (Eds.) Proceedings of the Ocean Drilling Progam, Scientific Results 154, College Station, TX (Ocean Drilling Program), pp. 269-284.

Bell, H.S., 1942. Density currents as agents for transporting sediments. Journal of Geology 50, 512-547.

Bellaiche, G., 1993. Sedimentary mechanisms and underlying tectonic structures of the northwestern Mediterranean margin, as revealed by comprehensive bathymetric and seismic surveys. Marine Geology 112, 89-108.

Bellaiche, G., Droz, L., Gaullier, V., Pautot, G., 1994a. Small submarine fans on the eastern margin of Corsica: sedimentary significance and tectonic implications. Marine Geology 117, 177-185.

Bellaiche, G., Droz, L., Gaullier, V., Pautot, G., 1994b. Morphology and sedimentation of the rise of the western margin of Corsica (France). Comptes Rendus de l'Academie des Sciences Serie II 318, 795-802.

Ben-Avraham, Z., Nur, A., Cello, G., 1987. Active transcurrent fault system along the north African passive margin. Tectonophysics 141, 249-260.

Benito, G., Gutiérrez, F., Pérez-González, A., Machado, M.J., 2000. Geomorphological and sedimentological features in Quaternary fluvial systems affected by solution-induced subsidence (Ebro Basin, NE-Spain). Geomorphology 33, 209-224.

Berger, A., 1978. Long-term variations of caloric insolation resulting from the earth's orbital elements. Quaternary Research 9, 139-167.

Berger, A., 1988. Milankovitch and climate. Review of Geophysics 26, 624-657.

Berné, S., Canals, M,m Alonso, B., Loubrie, B., Cochonat, P., the "BIG 95", "CALMAR97" shipboard parties, 1998. Recent slope failures and mass-movements in the NW Mediterranean Sea. Seafloor characterisation/mapping including swath bathymetry, side-scan sonar and geophysical surveys. Third European Marine Science and Technology Conference. Lisbon, May 23-27 (Session report) pp. 111-126.

Bickert, T., Berger, W.H., Burke, S., Schmidt, H., Wefer, G., 1993. Late Quaternary stable isotope record of benthic foraminifers: Sites 805 and 806, Ontong Java Plateau. In: Berger, W.H., Kroenke, L.W., Mayer, L.A. (Eds.) Proceedings of the Ocean Drilling Program, Scientific Results 130, College Station, TX (Ocean Drilling Program), pp. 411-420.

Bloemendal, J., DeMenocal, P., 1989. Evidence for a change in the periodicity of tropical climate cycles at 2.4 Myr from whole-core magnetic susceptibility measurements. Nature 342, 897-900.

Bloemendal, J., King, J.W., Hall, F.R., Doh, S.-J., 1992. Rock magnetism of late Neogene and Pleistocene deep-sea sediments: relationship to sediment source, diagenetic processes and sediment lithology. Journal of Geophysical Research 97, 4361-4375.

Blum, M.D., Törnqvist, T.E., 2000. Fluvial responses to climate and sea-level change: a review and look forward. Sedimentology 47 (Suppl.), 2-48.

Boccalettti, M., Guazzone, G., 1974. Remnant arcs and marginal basins in the Cainozoic development of the Mediterranean. Nature 252, 18-21.

Bond, G., Broecker, W., Johnsen, S., McManus, J., Labeyrie, L., Jouzel, J., Bonani, G., 1993. Correlations between climate records from North Atlantic sediments and Greenland ice. Nature 365, 143-147.

Bond, G.C., Lotti, R., 1995. Iceberg discharges into the North Atlantic on millennial time scales during the last glaciation. Science 267, 1005-1010.

Bonnet, A., 1962. Note sur la liaison entre les tectoniques superficielles et profondes de la Camarque. Bulletin Service de la Carte Géologique de la France, pp. 251-269.

Boudiaf, A., Ritz, J.F., Philip, H., 1998. Drainage diversion as evidence of propagating active faults: example of the El Asnam and Thenia faults, Algeria. Terra Nova 10, 236-244.

Bouhadad, Y., Nour, A., Laouami, N., Belhai, D., 2003. The Beni-Ourtilane-Tachaouaft fault and seismotectonic aspects of the Babors region (NE of Algeria). Journal of Seismology 7, 79-88.

Bouma, A.H., 1962. Sedimentology of some flysch deposits: a graphic approach to facies interpretation. Elsevier, Amsterdam, 168 pp.

Bourouba, M., 2003. A comparitive study of sediments in suspension in two intramountainous oueds of the oriental Tell (Algeria). Zeitschrift fur Geomorphologie 47, 51-81.

Boyle, E.A., 1986. Paired carbon isotope and cadmium data from benthic foraminifera: implications for

changes in oceanic phosphorus, ocean circulation, and atmospheric carbon dioxide. Geochimica et Cosmochimica Acta 50, 265-276.

Bramlette, M.N., Bradley, W.H., 1940. Geology and biology of North Atlantic deep-sea cores. U.S. Geological Survey, Professional Paper 196-A, 1-34.

Brauer, A., Mingram, J., Frank, U., Günter, C., Schettler, G., Wulf, S., Zolitschka, B., Negendank, J.F.W., 2000. Abrupt environmental oscillations during the Early Weichselian recorded at Lago Grande di Monticchio, southern Italy. Quaternary International 73/74, 79-90.

Brindley, G.W., Brown, G. (Eds), 1984. Crystal structures of clay minerals and their X-Ray identification. Mineralogical Society, London.

Britter, R.E., Simpson, J.E., 1978. Experiments on the dynamics of a gravity current head. Journal of Fluid Mechanics 99, 223-240.

Broecker, W.S., Peng, T.-H., 1982. Tracers in the sea, Lamont-Doherty Geological Observatory, Columbia University, New York, 690 pp.

Broecker, W.S., Turekian, K.K., Heezen, B.C., 1958. The relations of deep-sea sedimentation rates to variations in climate. American Journal of Science 256, 503-517.

Brovkin, V., Claussen, M., Petoukhov, V., Ganopolski, A., 1998. On the stability of the atmosphere-vegetation system in the Saharan/Sahel region. Journal of Geophysical Research 103, 31613-31624.

Burgess, P.M., Hovius, N., 1998. Rates of delta progradation during highstands: consequences for timing of deposition in deep-marine systems. Journal of the Geological Society London 155, 217-222.

Burrus, J., 1989. Review of geodynamic models for extensional basins: the paradox of stretching in the Gulf of Lions (Northwestern Mediterranean). Bulletin de la Societe Geologique de France 5, 377-393.

Cacho, I., Grimalt, J.O., Canals, M., Sbaffi, L., Shackleton, N.J., Schönfeld, J., Zahn, R., 2001. Variability of the western Mediterranean Sea surface temperature during the last 25,000 years and its connection with the Northern Hemisphere climatic changes. Paleoceanography 16, 40-52.

Cacho, I., Grimalt, J.O., Pelejero, C., Canals, M., Sierro, F.J., Flores, J.A., Shackleton, N.J., 1999. Dansgaard-Oeschger and Heinrich event imprints in the Alboran Sea palaeotemperatures. Paleoceanography 14, 698-705.

Cacho, I., Grimalt, J.O., Sierro, F.J., Shackleton, N., Canals, M., 2000. Evidence for enhanced Mediterranean thermohaline circulation during rapid climatic coolings. Earth and Planetary Science Letters 183, 417-429.

Caddah, L.F.G., Kowsmann, R.O., Viana, A.R., 1998. Slope sedimentary facies associated with Pleistocene and Holocene sea-level changes, Campos Basin, southeast Brazilian margin. Sedimentary Geology 115, 159-174.

Cairn, E., 1978. The central Mediterranean mountain chains in the alpine orogenic environment. In: Nairn, A.E.M., Kanes, W.H., Stehli, F.G. (Eds.) The ocean basins and margins 4B, The Western Mediterranean, pp. 201-256.

Carminati, E., Wortel, M.J.R., Meijer, P.Th., Sabadini, R., 1998. The two-stage opening of the western-central Mediterranean basins: a forward modelling test to a new evolutionary model. Earth and Planetary Science Letters 160, 667-679.

Carter, T.G., Flanagan, J.P., Jones, C.R., Marchant, F.L., Murchison, R.R., Rebman, J.H., Sylvester, J.C., Whitney, J.C., 1972. A new bathymetric chart and physiography of the Mediterranean Sea. In: D.J. Stanley (Ed.) The Mediterranean Sea: a natural sedimentation laboratory, Stroudsburg, PA: Dowden, Hutchinson and Ross, Inc., pp. 1-23.

Caulet, J.P., 1972. Recent biogenic calcareous sedimentation on the Algerian continental shelf. In: Stanley, D.J. (Ed.) The Mediterranean Sea: A Natural Sedimentation Laboratory, Stroudsburg, PA: Dowden, Hutchinson and Ross, Inc., pp. 261-277.

Chapman, M.R., Shackleton, N.J., 1999. Global ice-volume fluctuations, North Atlantic ice-rafting events, and deep-ocean circulation changes between 130 and 70 ka. Geology 27, 795-798.

Chen, J., Farrell, J.W., Murray, D.W., Prell, W.L., 1995. Timescale and palaeoceanographic implications of a 3.6 m.y. oxygen isotope record from northeast Indian Ocean (Ocean Drilling Program Site 758). Paleoceanography 10, 21-47.

Cita, M.B., Begi, C., Camerlenghi, A., Kastens, K.A., McCoy, F.W., Nosetto, A., Parisi, E., Scolari, F., Tomadin, L., 1984. Turbidites and megaturbidites from the Herodotus Abyssal Plain (eastern Mediterranean) unrelated to seismic events. Marine Geology 55, 79-101.

Claussen, M., Brovkin, V., Ganopolski, A., Kubatski, C., Petoukhov, V., 1998. Modelling global terrestrial

vegetation-climate interaction. Philosophical Transactions of the Royal Society of London Series B-Biological Sciences 353, 53-63.

Collina-Girard, F.J., 1998. Neotectonic observations along the western shore of Corsica using a scuba-diving method. Comptus Rendus de l'Academie des Sciences, Sciences de la Terra et des Planetes 327, 121-126.

Collina-Girard, F.J., 2002. Underwater mapping of Late Quaternary submerged shorelines in the western Mediterranean Sea and the Carribbean Sea. Quaternary International 92, 63-72.

Combourieu-Nebout, N., Turon, J.L., Zahn, R., Capotondi, L., Londeix, L., Pahnke, K., 2002. Enhanced aridity and atmospheric high-pressure stability over the western Mediterranean during the North Atlantic cold events of the past 50 k.y. Geology 30, 863-866.

Compton, J.S., Mallinson, D.J., 1996. Geochemical consequences of increased late Cenozoic weathering rates and the global CO_2 balance since 100 Ma. Paleoceanography 11, 431-446.

Conchon, O., 1987. Hydrodynamic variations and correlations with Quaternary sea-level change on a rocky coast in Corsica, western Mediterranean. Progress in Oceanography 18, 103-117.

Cornamusini, G., Elter, F.M., Sandrelli, F., 2002. The Corsica-Sardinia Massif as source area for the early northern Apennines foredeep system: evidence from debris flows in the 'Macigno costiero' (Late Oligocene, Italy). International Journal of Earth Science 91, 280-290.

Crowley, T.J., 1985. Quaternary carbonate changes in the north Atlantic and Atlantic/Pacific comparisons. In: Sundquist, E.T., Broecker, W.S. (Eds.) The Carbon Cycle and Atmospheric CO_2: Natural Variation Archean to Present, American Geophysical Union, Washington D.C., pp. 271-284.

Dadou, C., Godefroy, P., Vagneron, J.M., 1984. Evaluation probalistique de l'aléa sismique régional dans le sud-est de la France. Bureau de Recherches Geologiques et Minières Document 59, 246 pp.

Daly, R.A., 1936. Origin of submarine "canyons". American Journal of Science 312, 401-420.

Dana, J.D., 1863. A Manual of Geology. Philadephia: American Book Co., pp. 798.

Dansgaard, W., Johnson, S.J., Clausen, H.B., Dahl-Jenssen, D., Gundestrup, N.S., Hammer, C.U., Hvidberg, C.S., Steffensen, J.P., Sveinbjornsdotter, A.E., Jouzel, J., Bond, G., 1993. Evidence for general instability of past climate from a 250 kyr ice core record. Nature 364, 218-219.

Dean, W., Gardner, J., 1985. Cyclic variations in calcium carbonate and organic carbon in Miocene to Holocene sediments, Walvis Ridge, South Atlantic Ocean. In: Hsü, K.J., Weissert, H.J. (Eds.) South Atlantic Paleoceanography, pp. 61-78.

Delaney, M.L., Boyle, E.A., 1987. Cd/Ca in late Miocene benthic foraminifera and changes in the global organic carbon budget. Nature 330, 156-159.

Delaney, M.L., Boyle, E.A., 1988. Tertiary paleoceanic chemical variability: unintended consequences of simple geochemical models. Paleoceanography 3, 137-156.

Delaney, M.L., Filippelli, G.M., 1994. An apparent contradiction in the role of phosphorus in Cenozoic chemical mass balances for the world ocean. Paleoceanography 9, 513-527.

deMenocal, P., Archer, D., Leth, P., 1997. Pleistocene variations in deep Atlantic circulation and calcite burial between 1.2 and 0.6 Ma: a combined data-model approach. In: Shackleton, N.J., Curry, W.B., Richter, C., Bralower, T.J. (Eds.) Proceedings of the Ocean Drilling Program, Scientific Results (CD-ROM) 154, College Station, TX (Ocean Drilling Program), pp. 285-297.

Derry, L.A., France-Lanord, C., 1996. Neogene growth of the sedimentary organic carbon reservoir. Paleoceanography 11, 267-275.

Dewey, J.F., Helman, M.L., Turco, E., Hutton, D.H.W.,Knott, S.D., 1989. Kinematics in the western Mediterranean. In: Coward, M.P., Dietrich, D., Park, R.G. (Eds.) Alpine Tectonics, Geological Society Special Publication 45, 421-443.

Diester-Haas, L., 1976. Late Quaternary climatic variations in northwest Africa deduced from east Atlantic sediment cores. Quaternary Research 6, 299-314.

Dinarès-Turell, J., Hoogakker, B.A.A., Roberts, A.P., Rohling, E.J., Sagnotti, L., 2003. Quaternary climatic control of biogenic magnetite production and eolian dust input in cores from the Mediterranean Sea. Palaeogeography Palaeoclimatology Palaeoecology 190, 195-209.

Droz, L., Bellaiche, G., 1985. Rhône deep-sea fan: morphostructure and growth pattern. American Association of Petroleum Geologists Bulletin 69, 460-479.

Droz, L., Kergoat, R., Cochonat, P., Berné, S., 2001. Recent sedimentary events in the western Gulf of Lions (Western Mediterranean). Marine Geology 176, 23-37.

Embley, R.W., 1980. The role of mass transport in the distribution and character of deep-ocean sediment with special reference to the North Atlantic. Marine Geology 38, 23-50.

Emeis, K. –C. et al., 1996. Proceedings of the Ocean Drilling Program, Initial Reports. 160, College Station, TX (Ocean Drilling Program), 972 pp.

Emiliani, C., 1955. Pleistocene temperatures. Journal of Geology 63, 538-578.

Einsele, G., 1996. Event deposits: the role of sediment supply and relative sea-level changes – overview. Sedimentary Geology 104, 11-37.

Ercilla, G., Alonso, B., 1996. Quaternary siliciclastic sequence stratigraphy of western Mediterranean passive and tectonically active margins: the role of global versus local controlling factors. In: De Batist, M., Jacobs, P. (Eds.) Geology of Siliciclastic Shelf Seas, Geological Society of London Special Publication 117, pp. 125-138.

Ericson, D.B. Ewing, M., Heezen, B.C., 1951. Deep sea sands and submarine canyons. Geological Society of America Bulletin 62, 961-965.

Fanucci, F., Fierro, G., Gennesseaux, X., Rehault, J.P., Viaris de Lesegno, L., Ulzega, A., 1976. The continental shelf of Sardinia: structure and sedimentary characteristics. Bolletin della Societa Geologica Italy 95, 1201-1217.

Fárran, M., Maldonado, A., 1990. The Ebro continental shelf: Quaternary seismic stratigraphy and growth patterns. Marine Geology 95, 289-312.

Farrell, J.W., Janecek, T.R., 1991. Late Neogene paleoceanography and paleoclimatology of the Northeast Indian ocean (site 758), in: J. Weissel et al. (Eds.) Proceedings of the Ocean Drilling Program, Scientific Results 121, College Station, TX (Ocean Drilling Program), pp. 297-355.

Farrell, J.W., Murray, D.W., McKenna, V.S., Ravelo, A.C., 1995. Upper ocean temperature and nutrient contrast inferred from Pleistocene planktonic foraminifer $\delta^{18}O$ and $\delta^{13}C$ in the eastern equatorial Pacific. In: Pisias, N.G. et al. (Eds.) Proceeding of Ocean Drilling Program Scientific Results 138, College Station, TX (Ocean Drilling Program), pp. 289-319.

Farrell, J.W., Prell, W.L., 1991. Pacific $CaCO_3$ preservation and $\delta^{18}O$ since 4 Ma: paleoceanic and paleoclimatic implications. Paleoceanography 6, 485-498.

Felser, E., Woodside, J.M., van Hinte, J.E., 1998. Sequence boundary and salt diapirism in the Balearic abyssal plain, western Mediterranean. Geo-Marine Letter 18, 172-177.

Fitzsimons, J.J., Veit, H., 2001. Geology and geomorphology of the European Alps and the Southern Alps of New Zealand - A comparison. Mountain research and development 21, 340-349.

Flood, R., Manley, P.L., Kowsmann, R.O., Appi, C.J., Pirmez, C., 1991. Seismic facies and late Quaternary growth of the Amazon submarine fan. In: Weimer, P., Link, M.H. (Eds.) Seismic facies and sedimentary processes of modern and ancient submarine fans and turbidite systems, New York, Springer-Verlag, pp. 247-272.

Flores, J.A., Sierro, F.J., Francés, G., Vázquez, A., Zamarreño, I., 1997. The last 100,000 years in the western Mediterranean Sea: sea surface water and frontal dynamics as revealed by coccolithophores. Marine Micropaleontology 29, 351-366.

Fourcade, S., Capdevila, R., Ouabadi, A., Martineau, F., 2001. The origin and geodynamic significance of the Alpine cordierite-bearing granitoids of northern Algeria. A combined petrological, mineralogical, geochemical and isotopic (O, H, Sr, Nd) study. Lithos 57, 187-216.

Fuller, I.C., Macklin, M.G., Lewin, J., Passmore, D.G., Wintle, A.G., 1998. River response to high-frequency climate oscillations in southern Europe over the past 200 k.y. Geology 26, 275-278.

García, M.H., 1990. Depositing and eroding sediment-driven flows: turbidity currents. PhD thesis, University of Minnesota, St. Anthony Falls Hydraulic Laboratory.

García, M.H., 1994. Depositional turbidity currents laden with poorly sorted sediment. Journal of Hydraulic Engineering 120, 1240-1263.

Gasse, F., 2000. Hydrological changes in the African tropics since the Last Glacial Maximum. Quaternary Science Reviews 19, 189-211.

Gennesseaux, M., Maufret, A., Pautot, G., 1980. Les glissements sous-marine de la pente continetale Niçoise et la rupture des cables en Mer Ligure (Méditerranée occidentale). Comptes Rendus de l'Académie des Sciences Paris 290, 959-963.

Gerland, S., Villinger, H., 1995. Nondestructive density determination on marine sediment cores from gamma-ray attenuation measurements. Geo-Marine Letters 15, 111-118.

Giermann, G., 1962. Erlauterungen zur bathymetrischen Karte des westlichen Mittelmeers (zwischen 6° 40'W. L. und 1° 0'E. L.). Bulletin de l'Institute Océanographique, 1254-1324.

Gingele, F.X., Schmieder, F., 2001. Anomalous South Atlantic lithologies confirm global scale of unusual mid-Pleistocene climate excursion. Earth and Planetary Science Letters 186, 93-101.

González-Donoso, J.M., Serrano, F., Linares, D., 2000. Sea surface temperature during the Quaternary at ODP Sites 976 and 975 (western Mediterranean). Palaeogeography, Paleoclimatology, Palaeoecology 162, 17-44.

Grootes, P.M., Stuiver, M., White, J.W.C., Johnson, S., Jouzel, J., 1993. Comparison of oxygen isotope records from the GISP2 and GRIP Greenland ice cores. Nature 366, 552-554.

Grützner, J., Giosan, L., Franz, S.O., Tiedemann, R., Cortijo, E., Chaisson, W.P., Flood, R.D., Hagen, S., Keigwin, L.D., Poli, S., Rio, D., Williams, T., 2002. Astronomical age models for Pleistocene drift sediments from the western North Atlantic (ODP Sites 1055-1063). Marine Geology 189, 5-23.

Guennoc, P., Debeglia, N., Gorni, C., le Marrec, A., Mauffret, A., 1994. Anatomy of a young passive margin (Gulf of Lions – south France): contribution of geophysical data. Bulletin des centres de rechercher exploration-production ELF Aquitaine 33-57.

Guerzoni, S., Chester, R., Dulac, F., Herut, B., Loye-Pilot, M.-D., Measures, C., Migon, C., Molinaroli, E., Moulin, C., Rossini, P., Saydam, C., Soudine, A., Ziveri, P., 1999. The role of atmospheric deposition in the biogeochemistry of the Mediterranean Sea. Progress in Oceanography 44, 147-190.

Gunn, D.E., Best, A.I., 1998. A new automated nondestructive system for high resolution multi-sensor core logging of open sediment cores. Geo-Marine Letters 18, 70-77.

Haddad, G.A., Droxler, A.W., Kroon, D., Müller, D.W., 1993. Quaternary $CaCO_3$ input and preservation within Antarctic intermediate water: mineralogic and isotopic results from holes 818B and 817A, Townsville trough (north-eastern Australia margin). In: McKenzie, J.A. et al. (Eds.) Proceedings of the Ocean Drilling Program, Scientific Results 133, College Station, TX (Ocean Drilling Program), pp. 203-225.

Hall, I.R., McCave, I.N., Shackleton, N.J., Weedon, G.P., Harris, S.E., 2001. Intensified deep Pacific inflow and ventilation in Pleistocene glacial times. Nature 412, 809-812.

Hays, J.D., Perruzza, A., 1972. The significance of calcium carbonate oscillations in eastern equatorial Atlantic deep-sea sediments for the end of the Holocene warm interval. Quaternary Research 2, 355-362.

Hays, J.D., Pitman, W.C. III, 1973. Lithosperic plate motion, sea level changes and climatic and ecological consequence. Nature 246, 18-22.

Heinrich, H., 1988. Origin and consequences of cyclic ice rafting in the northeast Atlantic during the past 130,000 years. Quaternary Research 29, 142-152.

Henrich, R., Baumann, K.-H., Huber, R., Meggers, H., 2002. Carbonate preservation records of the past 3 Myr in the Norwegian-Greenland Sea and the northern North Atlantic: implications for the history of NADW production. Marine Geology 184, 17-39.

Hieke, W., 2000. Transparent layers in seismic reflection records from the central Ionian Sea (Mediterranean) – evidence for repeated catastrophic turbidite sedimentation during the Quaternary. Sedimentary Geology 135, 89-98.

Hieke, W., Werner, F., 2000. The Augias megaturbidite in the central Ionian (Central Mediterranean) and its relation to the Holocene Santorini event. Sedimentary Geology 135, 205-218.

Hodell, D.A., Venz, K., 1992. Toward a high-resolution stable isotopic record of the Southern Ocean during the Pliocene-Pleistocene (4.8 to 0.8 Ma). The Antarctic Paleoenvironment: A Perspective on Global Change, Antarctic Research Series 56, 265-310.

Hunt, R.W.G., 1980. Color terms, symbols and their usage. In: Grum, F., Bartleson, C.J. (Eds.) Optical radiation measurement. Academic Press, New York, pp. 11-31,

Hurtrez, J.-M., Lucazeau, F., 1999. Lithological control on relief and hypsometry in the Hérault drainage basin (France). Comptes Rendus Académie des Sciences, Sciences de la terre et des planetes 328A, 687-694.

Imbrie, J., Boyle, E.A., Clemens, S.C., Duffy, A., Howard, W.R., Kukla, G., Kutzbach, J., Martinson, D., McIntyre, A., Mix, A., Molfino, B., Morley, J.J., Peterson, L.C., Pisias, N.G., Prell, W., Raymo, M.E., Shackleton, N.J., Togweiler, J.R., 1992. On the structure and origin of major glaciation cycles 1. Linear responses to Milankovitch forcings. Paleoceanography 7, 701-738.

Imbrie, J., Shackleton, N.J., Pisias, N.G., Morley, J.J., Prell, W.L., Martinson, D.G., Hays, J.D., McIntyre, A., Mix, A.C., 1984. The orbital theory of Pleistocene climate: support from a revised chronology of the marine $\delta^{18}O$ record. In: Berger, A., Imbrie, I., Hays, J., Kukla, G., Salzmann, B. (Eds.), Milankovich and Climate: understanding response to astronomical forcing 1. D. Reidel Publishing Company, Dordrecht, pp. 269-305.

Inglès, M., Ramos-Guerrero, E., 1995. Sedimentological control on the clay mineral distribution in the marine and non-marine Palaeogene deposits of Mallorca (Western Mediterranean). Sedimentary Geology 94, 229-243.

Janssen, J.H.F., Kuijpers, A., Troelstra, S.R., 1986. A mid-Brunhes climatic event: long-term changes in global atmosphere and ocean circulation. Science 232, 619-622.

Johnsen, S.J., Clausen, H.B., Dansgaard, W., Fuhrer, K., Gundestrup, N., Hammer, C.U., Iversen, P., Jouzel, J., Stauffer, B., Steffersen, J.P., 1992. Irregular glacial interstadials recorded in a new Greenland ice core. Nature 359, 311-313.

Jones, K.P.N., McCave, I.N., Weaver, P.P.E., 1992. Textural and dispersal patterns of thick mud turbidites from the Madeira Abyssal Plain. Marine Geology 107, 149-173.

Jones, S.J., Frostick, L.E., Astin, T.R., 1998. Climatic and tectonic controls on fluvial incision and aggradation in the Spanish Pyrenees. Journal of the Geological Society London 156, 761-767.

Kastens, K.A., Cite, M.B., 1981. Tsunami induced sediment transport in the abyssal Mediterranean Sea. Geological Society of America Bulletin Part I 92, 845-847.

Kempe, S., 1977. Carbon in the Rock Cycle. In: Bolin, B., Degens, E.T., Kempe, S., Ketner, P. (Eds.) The Global Carbon Cycle SCOPE 13, John Wiley and Sons, Chichester, pp. 354-358.

Kent, D.V., 1982. Apparent correlation of paleomagnetic intensity and climate records in deep-sea sediments. Nature 326, 538-539.

Kenyon, N.H., Klaucke, I., Millington, J., Ivanov, M.K., 2002. Sandy submarine canyon-mouth lobes on the western margin of Corsica and Saridinia, Mediterranean Sea. Marine Geology 184, 69-84.

Kerr, R.C., 1991. Erosion of a stable density gradient by sediment-driven convection. Nature 353, 423-425.

Kidd, R.B., Searle, R.C., Weaver, P.P.E., Jacobs, C.L., Huggett, Q.J., Noel, M.J., Schultheiss, P.J., 1983. King's Trough flank: geological and geophysical investigations of its suitability for high-level radioactive waste disposal. Institute of Oceanographic Sciences Report 136, pp 1-99.

Kinder, T.H., Bryden, H.L., 1987. The 1985-1986 Gibraltar Experiment: data collection and preliminary results. EOS: Transactions American Geophysical Union 65, 786-787 and 793-795.

Klaucke, I., Savoye, B., Cochonat, P., 2000. Patterns and processes of sediment dispersal on the continental slope of Nice, SE France. Marine Geology 162, 405-422.

Kneller, B.C., Bennett, T.S.J., McCaffrey, W.D., 1997. Velocity and turbulence structure of density currents and internal solitary waves: potential sediment transport and the formation of wave ripples in deep water. Sedimentary Geology 112, 235-250.

Kneller, B.C., Bennett, S.J., McCaffrey, W.D., 1999. Velocity structure, turbulence and fluid stresses in experimental gravity currents. Journal of Geophysical Research 104, 5281-5291.

Kneller, B., Buckee, C., 2000. The structure and fluid mechanics of turbidity currents: a review of some recent studies and their geological implications. Sedimentology 47 Suppl., 62-94.

Kolla, V., Biscaye, P.E., Hanley, A.F., 1979. Distribution of quartz in late Quaternary Atlantic sediments in relation to climate. Quaternary Research 11, 261-277.

Kolla, V., Perlmutter, M.A., 1993. Timing of turbidite sedimentation on the Mississippi Fan. American Association of Petroleum Geologists Bulletin 71, 1129-1141.

Kroopnick, P.M., 1985. The distribution of ^{13}C of $\sum CO_2$ in the world oceans. Deep-Sea Research 32, 57-84.

Kuehl, S.A., Hariu, T.M., Moore, W.S., 1989. Shelf sedimentation off the Ganges-Brahmaputra river system: evidence for sediment bypassing to the Bengal Fan. Geology 17, 1132-1135.

Kuenen, P.H., 1937. Experiments in connection with Daly's hypothesis on the formation of submarine canyons. Leidse Geologische Mededelingen 8, 327-335.

Kuenen, P.H., 1950. Turbidity currents of high density. International Geological Congress 18th, London, Report. 8, 44-52.

Kump, L.R., 1991. Interpreting carbon-isotope excursions: Strangelove oceans. Geology 19, 299-302.

Laj, C., Mazaud, A., Duplessy, J.,-C., 1996. Geomagnetic intensity and ^{14}C abundance in the atmosphere and ocean during the past 50 kyr. Geophysical Research Letters 23, 2045-2048.

Lambeck, K., Bard, E., 2000. Sea-level change along the French Mediterranean coast for the last 30,000 years. Earth and Planetary Science Letters 175, 203-222.

Larrasoaña, J.C., Roberts, A.P., Rohling, E.J., Winklhofer, M., Wehausen, R. Three million years of monsoon variability over the northern Sahara. Climate Dynamics in press.

Larroque, C., Béthoux, Calais, E., Courboulex, F., Deschamps, A., Déverchère, Stéphan, J.-F., Ritz, J.-F., Gilli, E., 2001. Active and recent deformation at the Southern ALps-Ligurian basin junction. Geologie en Mijnbouw 80, 255-272.

La Violette, P.E., 1994. Overview of the major forcings and water masses of the western Mediterranean Sea. Coastal and Estuarine Studies 46 (Seasonal and interannual variability of the western Mediterranean Sea), 1-11.

Leclaire, L., 1972. Aspects of Late Quaternary sedimentation on the Algerian precontinent and in the adjacent Algiers-Balearic Basin. In: Stanley, D.J. (Ed.) The Mediterranean Sea: a natural sedimentation laboratory. Stroudsburg, PA: dowden, Hutchinson and Ross Inc., pp. 561-582.

Leeder, M.R., Harris, T., Kirkby, M.J., 1998. Sediment supply and climate change: implications for basin stratigraphy. Basin Research 10, 7-18.

Lehman, S.J., Sachs, J.P., Crotwell, A.M., Keigwin, L.D., Boyle, E.A., 2002. Relation of subtropical Atlantic temperature, high-latitude ice rafting, deep water formation, and European climate 130,000-60,000 years ago. Quaternary Science Reviews 21, 1917-1924.

Lenotre, N., Ferrandini, J., Delfau, M., Panighi, J., 1996. Present vertical movements of Corsica (France) using compared levelling data. Comptus Rendus de l'Academie des Sciences, Sciences de la Terra et des Planetes 323, 957-964.

Lewin, J., Macklin, M.G., Woodward, J.C. (Eds.), 1995. Mediterranean Quaternary River Environments, Balkema, Rotterdam.

Limonov, A.F., Woodside, J.M., Ivanov, M.K., 1992. Geological and geophysical investigations of western Mediterranean deep sea fans: initial results of the UNSECO-ESF 'Training-through –Research' cruise of RV "Gelendzhik" in the western Mediterranean (June-July 1992). Unesco Reports in Marine Science 62, 154 pp.

Lowe, D.R., 1982. Sediment gravity flows: II. Depositional models with special reference to the deposits of high-density turbidity currents. Journal of Sedimentary Petrology 52, 279-297.

Loye-Pilot, M.-D., Martin, J.-M., Morelli, J., 1986. Influence of Saharan dust on the rainfall acidity and atmospheric input to the Mediterranean. Nature 321, 427-431.

Ludwig, W., Probst, J.-L., 1998. River sediment discharge to the oceans: present-day controls and global budgets. American Journal of Science 298, 265-295.

Macciotta, G., Savelli, C., 1984. Petrology and K/Ar ages of Pliocene-Quaternary volcanites from northwestern Sardinia. Grafiche STEP, Parma, 1-45.

Mackenzie, F.T., 1998. Biogeochemical cycles of carbon, nutrients, and oxygen. In: McConnin, R.A., Dellas, K. (Eds.) Our Changing Planet: An Introduction to Earth System Science and Global Environmental Change, Prentice Hall, Upper Saddle River, pp. 155-180.

Macklin, M.G., Lewin, J., Woodward, J.C., 1995. Quaternary fluvial systems in the Mediterranean basin. In: Lewin, J., Macklin M.G. Woodward, J.C. (Eds.) Mediterranean Quaternary River environments. Balkema, Rotterdam, pp. 1-25.

Macklin, M.G., Passmore, D.G., 1995. Pleistocene environmental change in the Guadalope Basin, northeast Spain: fluvial and archeological records. In: Lewin, J., Macklin, M.G., Woodward, J.C. (Eds.) Mediterranean Quaternary environments. Balkema, Rotterdam, pp. 103-113.

Maldonado, A., 1972. El Delta del Ebro. Estudio Sedimentológico y Estratigráphico. Bol. Estrat. Universitat Barcelona 1, 486 pp.

Maillard, A., Gaullier, V., Vendeville, B.C., Odonne, F., 2003. Influence of differential compaction above basement steps on salt tectonics in the Ligurian-Provençal Basin, northwest Mediterranean. Marine and Petroleum Geology 20, 13-27.

Margalef, R., 1984. Introduction to the Mediterranean. In: Margalef, R. (Ed.) Key environments, western Mediterranean. Pergamon Press, pp. 1–16.

Martí, J., Mitjavlia, J., Roca, E., Aparicio, A., 1992. Cenozoic magmatism of the Valencia Trough (western Mediterranean): relationship between structural evolution and volcanism. Tectonophysics 203, 145-165.

Martin, J. -M, Elbaz-Poulichet, F., Guieu, C., Loye-Pilot, M. -D., Han, G., 1989. River versus atmospheric input of material to the Mediterranean Sea: an overview. Marine Chemistry 28, 159-182.

Martinson, D.G., Pisias, N.G., Hayes, D., Imbrie, J., Moore, T.C., Shackleton, N.J., 1987. Age dating and the orbital theory of the ice ages: development of a high-resolution 0 to 300,000 year chronostratigraphy. Quaternary Research 27, 1-29.

Mascle, J., R., Réhault, J.P., 1991. Le destin de la Méditerranée. La Recherche 229, 188-196.

Mayewski, P.A., Meeker, L.D., Twickler, M.S., Whitlow, S., Yang, Q., Lyons, W.B., Prentice, M., 1997. Major features and forcing of high-latitude northern hemisphere atmospheric circulation using a 110,000-year-long glaciochemical series. Journal of Geophysical Research 102, 26345-26366.

Mazzullo, J., Graham, A.G., Rabinowitz, P.D., Meyer, A.W., Garrison, L.E., 1987. Handbook for shipboard sedimentologists. Texas A & M University Ocean Drilling Program Technical Note 8, 67 pp.

McManus, D.A., 1970. Criteria of climatic change in the inorganic components of marine sediments. Quaternary Research 1, 72-102.

McManus, J.F., Bond, G.C., Broecker, W.S., Johnson, S., Labeyrie, L., Higgins, S., 1994. High-resolution climate records from the North Atlantic during the last interglacial. Nature 371, 326-339.

Michaelis, W., Ittekkot, V., Degens, E.T., 1986. River inputs into oceans. In: Larasse, P., Martin, J.M. (Eds.) Biogeochemical Processes at the Land-Sea Boundary, Elsevier, Amsterdam, pp. 37-52.

Middleton, N.J., 1985. Effect of drought on dust production in the Sahel. Nature 316, 431-434.

Middleton, G.V., 1966a. Experiments on density and turbidity currents; [Part 1], Motion of the head. Canadian Journal of Earth Science 3, 523-546.

Middleton, G.V., 1966b. Experiments on density and turbidity currents; [Part 2], Uniform flow of density currents. Canadian Journal of Earth Science 3, 627-637.

Mix, A.C., Pisias, N.G., Rugh, W., Wilson, J., Morey, A., Hagelberg, T.K., 1995. Benthic foraminifer stable isotope record from Site 849 (0–5 Ma): Local and global climate changes. In: Pisias, N.G. et al. (Eds.) Proceedings of the Ocean Drilling Program, Scientific Results 138, College Station, TX (Ocean Drilling Program), pp. 371-412.

Moreno, A., Cacho, I., Canals, M., Prins, M.A., Sánchez Goñi, M.-F, Grimalt, J.O., Weltje, G.J., ., Sánchez-Goñi, M., 2002. Saharan dust transport and high-lattitude glacial climatic variability: the Alboran Sea record. Quaternary Research 58, 318-328.

Mulder, T., Savoye, B., Piper, D.J.W., Syvitsji, J.P.M., 1998b. The Var submarine sedimentary system: understanding Holocene sediment delivery processes and their importance to the geological record. In: Stoker, M.S., Evans, D., Cramp, A. (Eds.) Geological processes on continental margins: sedimentation, mass wasting and stability. Geological Society Special Publication 129, pp.145-166.

Mulder, T., Savoye, B., Syvitski, J.P.M., Parize, O., 1997. Hyperpycnal turbidite currents at the head of the Var Canyon? Hydrological data and geological observations. Oceanologica Acta 20, 607-626.

Mulder, T., Syvitski, J.P.M., Skene K.I., 1998a. Modelling of erosion and deposition by turbidity currents generated at river mouths. Journal of Sedimentary Research 68, 124-137.

Murray, J., Renard, A.F., 1891. Report on deep-sea deposits based on specimens collected during the voyage of HMS Challenger on the years 1873-1876. In: 'Challenger' Reports. Her Majesty's Stationary Office London, 525 pp.

Narcisi, B., Vezzoli, L.,1999. Quaternary stratigraphy of distal tephra layers in the Mediterranean - an overview. Global and Planetary Change 21, 31-50.

Natland, M.L., Kuenen, P.H., 1951. Sedimentary history of the Ventura Basin, California, and the action of turbidity currents. In: Hough J.L. (Ed.) Turbidity currents and the transportation of coarse sediments to deep water. Society of Economic Paleontologist and Mineralogist Special Publication 2, pp. 76-107.

Nelson, C.H., 1990. Estimated post-Messinian sediment supply and sedimentation rates on the Ebro continental margin, Spain. Marine Geology 95, 395-418.

Nelson, C.H., Maldonado, A., 1990. Factors controlling late Cenozoic continental margin growth from the Ebro delta to the Western Mediterranean deep sea. Marine Geology 95, 419-440.

Nisbet, E.G.,1992. Sources of atmospheric CH_4 in early postglacial time. Journal of Geophysical Research 97, 12859-12867.

Normark, W.R., Posamentier, H., Mutti, E., 1993. Turbidite systems: state of the art and future directions. Reviews of Geophysics 31, 91-116.

Norris, R.D., Röhl, U., 1999. Carbon cycling and chronology of climate warming during the Palaeocene/Eocene transition. Nature 401, 775-778.

O'Connell., S., Normark, W.R., Ryan, W.B.F, Kenyon, N.H., 1991. An entrenched thalweg channel on the Rhône Fan: interpretation from a Seabeam and Seamarc I Survey. In: Osborne, R.H. (Ed.) From Shoreline to Abyss – Contributions in marine geology in honor of Francis Parker Shepard. Society Economic Paleontologist and Mineralogist Special Publication 46, 259-270.

Oldfield, F., Robinson, S.G., 1985. Geomagnetism and palaeoclimate. In: Tooley, M.J. and Sheil, G. (Eds.), The climatic scene. Allen and Unwin, Winchester, Mass., pp. 186-205.

Oppo, D.W., Raymo, M.E., Lohman, C.P., Mix, A.C., Wright, J.D., Prell, W.L., 1995. A $\delta^{13}C$ record of Upper North Atlantic Deep Water during the past 2.6 million years. Paleoceanography 10, 373-394.

Orr, P.J., Benton, M.J., Trewin, N.H., 1996. Deep marine trace fossil assemblages from the Lower

Carboniferous of Menorca, Balearic Islands, western Mediterranean. Geological Journal 31, 235-258.

Palanques, A., Alonso, B., Farrán, M., 1994. Progradation and retreat of the Valencia fanlobes controlled by sea-level changes during the Plio-Pleistocene (northwestern Mediterranean). Marine Geology 117, 195-205.

Parkin, D.W., Shackleton, N.J., 1973. Trade wind and temperature correlations down a deep-sea core off the Saharan coast. Nature, 245, 455-457.

Parkin D.W., 1974. Trade winds during glacial cycles. Proceedings of the Royal Society 337, 73-100.

Paterne, M., Kallel, N., Labeyrie, L., Vautravers, M., Duplessy, J.C., Rossignol-Strick, M., Cortijo, E., Arnold, M., Fontugne, M., 1999. Hydrological relationship between the North Atlantic Ocean and the Mediterranean Sea during the past 15-75 kyr. Paleoceanography 14, 626-638.

Paull, C.K., Ussler, W., Diller, W.P., 1991. Is the extent of glaciation limited by marine gas hydrates? Geophysical Research Letters 18, 432-434.

Peakall, J., McCaffrey, W.D., Kneller, B.C., 2000. A process model for the evolution, morphology and architecture of sinuous submarine channels. Journal of Sedimentary Research 70, 434-448.

Perry, A., 1981. Mediterranean climate_ a synoptic reappraisal. Progress in Physical Geography 5, 107-113.

Petelet, E., Luck, J.-M., Othman, D.B., Negrel, P., Aquilina, L. 1998. Geochemistry and water dynamics of a medium-sized watershed: the Hérault, southern France. 1. Organisation of the different water reservoirs as constrained by Sr isotopes, major, and trace elements. Chemical Geology 150, 63-83.

Peterson, L.C., Prell, W.L., 1985. Carbonate preservation and CO_2: natural variations Archean to Present. In: Sundquist, E.T., Broecker, W.S. (Eds.), The Carbon Cycle and Atmospheric CO_2: Natural Variation Archean to Present, American Geophysical Union, Washington D.C., pp. 251-269.

Peucker-Ehrenbrink, B., Hannigan, R.E., 2000. Effects of black shale weathering on the mobility of rhenium and platinum group elements. Geology 28, 475-478.

Peucker-Ehrenbrink, B., Ravizza, G., 2000, The marine osmium isotope record. Terra Nova 12, 205-219.

Philip, H., Megraoui, M., 1983. Structural analysis and interpretation of the surface deformation of the El Asnam earthquake of October 10, 1980. Tectonics 2, 17-49.

Philip, H., Thomas, G., 1977. Détermination de la direction de raccourcissement de la phase de compression quaternaire en Oranie (Algérie). Revue Géographique Physique Géologique et Dynamique 19, 315-324.

Pierot, S., 1972. Carte bathymétrique de la Mer Ligure. Musee Océanographique Monaco.

Pilkey, O.H., 1987. Sedimentology of basin plains. In: Weaver, P.P.E., Thomson, J. (Eds) Geology and Geochemistry of Abyssal Plains. Geological Society Special Publication 31, pp. 1-12.

Piper, D.J.W., Normark, W.R., 1983. Turbidite depositional patterns and flow characteristics, Navy submarine fan, California Borderland. Sedimentology 30, 681-691.

Pitman, W.C. III, 1978. Relationship between eustacy and stratigraphic sequences of passive margins. Bulletin of the Geological Society of America 89, 1389-1403.

Pitman, W.C., III, 1979. The effect of eustatic sea level change on stratigraphic sequences at Atlantic margins. American Association of Petroleum Geologists Memoir 29, 453-460.

Pont, D., 1993. Vers une Meilleures Connaissance des Apports du Rhône à la Méditerranée. Les rencontres de l'Agence Régionale Pour l'Environment, Région PACA (Provence, Alpes Côte d'Azur), pp 16-24.

Posamentier, H.W., Vail, P.R., 1988. Eustatic controls on clastic deposition II – sequence and system tract models. In: Wilgus, C.K. et al. (eds.) Sea level changes: An integrated approach. SEPM Special Publications 42, 125-154.

Prell, W.L., Imbrie, J., Martinson, D.G., Morley, J.J., Pisias, N.G., Shackleton, N.J., Streeter, H.F., 1986. Graphic correlation of oxygen isotope stratigraphy: application to the late Quaternary. Paleoceanography 1, 137-162.

Prentice, I.C., Guiot, J., Harrison, S.P., 1992. Mediterranean vegetation, lake levels and palaeoclimate at the last glacial maximum. Nature 360, 658-660.

Prince, C.M., Elmore, R.D., Ehrlich, R., Pilkey, O.H., 1987. Areal and lateral changes in a major trailing margin turbidite – the Black Shell Turbidite. Geo-Marine Letters 7, 103-112.

Prins, M.A., Postma, G., 2000. Effects of climate, sea level, and tectonics unraveled for last deglaciation turbidite records of the Arabian Sea. Geology 28, 375-378.

Ram, M., Illing, M., 1994. Polar ice stratigraphy from laser-light scattering: scattering from meltwater. Journal of Glaciology 40, 504-508.

Ram, M., Illing, M., Weber, P., Koenig, G., Kaplan, M., 1995. Polar ice stratigraphy from laser-light scattering: scattering from ice. Geophysical Research Letters 22, 3525-3527.

Ram, M., Koenig, G., 1997. Continuous dust concentration profile of pre Holocene ice from the Greenland Ice Sheet Project 2 ice core: dust stadials, interstadials, and the Eemian. Journal of Geophysical Research 102, 26641-26648.

Ravizza, G., 1993. Variations of the $^{187}Os/^{186}Os$ ratio of seawater over the past 28 million years as inferred from metalliferous carbonates. Earth and Planetary Science Letters 118, 335-348.

Ravizza, G., Esser, B.K., 1993. A possible link between the seawater osmium isotope record and weathering of ancient sedimentary organic matter. Chemical Geology 107, 255-258.

Raymo, M.E., Oppo, D.W., Curry, W., 1997. The mid-Pleistocene climate transition: a deep-sea carbon isotopic perspective. Paleoceanography 12, 546-559.

Rea, D.K., Leinen, M., 1985. Neogene history of calcite compensation depth and lysocline in the South Pacific Ocean. Nature 316, 805-807.

Reeder, M.S., Stow, D.A.V., Rothwell, R.G., 2002. Late Quaternary turbidite input into the east Mediterranean basin: new radiocarbon constraints on climate and sea-level control. In: Jones, S.J., Frostick, L.E. (Eds.) Sediment flux to basins: causes, controls and consequences. Geological Society London, Special Publication 191, 267-278.

Rehault, J.,-P., Boillot, G., Mauffret, A., 1984. The western Mediterranean Basin geological evolution. Marine Geology 55, 447-477.

Rehault, J.,-P., Boillot, G., Mauffret, A., 1985. The western Mediterranean Basin. In: D.J. Stanley, D.J., F.-C. Wezel (Eds.) Geological Evolution of the Mediterranean Basin. Springer-Verlag, pp 101-129.

Ríos, J.M., 1978. The Mediterranean coast of Spain and the Alboran Sea. In: Nairn, A.E.M., Kanes, W.H., Stehli, F.G. (Eds.) The ocean basins and margins 4B, The Western Mediterranean, pp. 1-65.

Robinson, S.G., 1986. The late Pleistocene palaeoclimatic record of North Atlantic deep-sea sediments revealed by mineral magnetic measurements. Physics of the Earth and Planetary Interiors 42, 22-57.

Robinson, S.G., Maslin, M.A., McCave, I.N., 1995. Magnetic susceptibility variations in Upper Pleistocene deep-sea sediments of the NE Atlantic: implications for ice rafting and paleocirculation at the last glacial maximum. Paleoceanography 10, 221-250.

Robrini, M.E.L., Genneseaux, M., Mauffret, A., 1985. Consequences of the El-Asnam earthquakes: turbidite currents and slumps on the Algerian margin (western Mediterranean). Geo-Marine Letters 5, 171-176.

Rognon, P., 1987. Aridification and abrupt climatic events on the Saharan northern and southern margins, 20,000 years BP to present. In: Berger, W.H., and Labeyrie, C.D. (Eds.), Abrupt Climatic Change: Evidence and Implications. D. Reidel Publishing Company, Dordrecht, pp. 209-220.

Rohling, E.J., Hayes, A., de Rijk, S., Kroon, D., Zachariasse, J.W., Eisma, D., 1998. Abrupt cold spells in the northwest Mediterranean. Paleoceanography 13, 316-322.

Rohling, E.J., Mayewski, P.A., Challenor, P., 2003. On the timing and mechanism of millennial-scale climate variability during the last glacial cycle. Climate Dynamics 20, 257-268.

Roques, M., Vachette, M., Vialette, Y., 1971. Géochronologie du Socle du Massif Central. In: Jung, J. (Ed.) Géology, Géomorphology et Structure Profonde du Massif Central Français: plain Air Service, Clemont-Ferrand, pp 269-289.

Rose, J., Meng, X., Watson, C., 1999. Palaeoclimate and palaeoenvironmental responses in the western Mediterranean over the last 140 ka: evidence from Mallorca, Spain. Journal of the Geological Society London 156, 435-448.

Rossignol-Strick, M., 1983. African monsoons, an immediate climate response to orbital insolation. Nature 304, 46-49.

Rossignol-Strick, M., Paterne, M., Bassinot, F.C., Emeis, K.C., De Lange, H.J., 1998. An unusual mid-Pleistocene monsoon period over Africa and Asia. Nature 392, 269-272.

Rothwell, R.G., 1989. Minerals and mineraloids in marine sediments: an optical identification guide. Elsevier Applied Science, London, 279 pp.

Rothwell, R.G., et al., 1995. Marion Dufresne Cruise 81 Cruise Report – Mediterranean Giant Piston Coring Transect (unpublished manuscript), 120 pp.

Rothwell, R.G., Reeder, M.S., Anastasakis, G., Stow, D.A.V., Thomson, J., Kähler, G., 2000. Low sea-level stand emplacement of megaturbidites in the western and eastern Mediterranean Sea. Sedimentary Geology 135, 75-88.

Rothwell, R.G., Thomson, J., Kähler, G., 1998. Low-sea-level emplacement of a very large Late Pleistocene

'megaturbidite' in the western Mediterranean Sea. Nature 392, 377-380.
Ruddiman, W.F., 1971. Pleistocene sedimentation in the equatorial Atlantic: Stratigraphy and faunal paleoclimatology. Geological Society of America Bulletin 82, 283-302.
Ruddiman, W.F., Raymo, M.E., Martinson, D.G., Clement, B.M., Backman, J., 1989. Pleistocene evolution: northern hemisphere ice sheets and North Atlantic Ocean. Paleoceanography 4, 353-412.
Rupke, N.A., Stanley, D.J., 1974. Distinctive properties of turbidite and hemipelagic mud layers in the Algéro-Balearic Basin, western Mediterranean Sea. Smithsonian Contributions to the Earth Science 13, 1-40
Russell, K.L., 1968. Oceanic ridges and eustatic changes in sea level. Nature 218, 861-862.
Sage, L., 1976. La sédimentation à l'embouchure d'un fleuve côtier méditerranéen: le Var, Thesis doctorat de 3éme Cycle, Université de Nice, 243 pp.
Salzman, M.R., Ripperdan, R.L., Brasier, M.D., Lohmann, K.C., Robison, R.A., Chang, W.T., Peng, S., Ergaliev, E.K., Runnegar, B., 2000. A global isotope excursion (SPICE) during the Late Cambrian: relation to trilobite extinctions, organic-matter burial and sea level. Palaeogeography, Palaeoclimatology, Palaeoecology 162, 211-223.
Sánchez Goñi, M.F., Cacho, I., Turon, J.-L., Giuot, J., Sierro, F.J., Peypouquet, P.-P., Grimalt, J.O., Shackleton, N.J., 2002. Synchroneity between marine and terrestrial responses to millennial scale climatic variability during the last glacial periods in the Mediterranean region. Climate Dynamics 19, 95-105.
Savoye, B., Piper, D.J.W., Droz, L., 1993. Plio-Pleistocene evolution of the Var deep-sea fan off the French Riviera. Marine and Petroleum Geology 10, 550-571.
Schmieder, F., von Dobeneck, T., Bleil, U., 2000. The Mid-Pleistocene climate transition as documented in the deep South Atlantic Ocean: initial, interim state and terminal event. Earth and Planetary Science Letters 179, 539-549.
Schmidt, H., Berger, W.H., Bickert, T., Wefer, G., 1993. Quaternary carbon isotope record of pelagic foraminifers: Site 806, Ontong Java Plateau. In: Berger, W.H. et al. (Eds.) Proceedings of the Ocean Drilling Program, Scientific Results 130, College Station, TX (Ocean Drilling Program), pp. 397-409.
Sen Gupta, B.K., 1999. Modern Foraminifera. Kluwer Academic, Dordrecht, 371 pp.
Serrat, P., Ludwig, W., Navarro, B., Blazi, J.L., 2001. Spatial and temporal variability of sediment fluxes from a coastal Mediterranean river, the Tet (France). Comptes Rendus de l'Academie des Sciences, Sciences de la terre et des planetes 333, 389-397.
Shackleton, N.J., 1985. Oceanic carbon isotope constraints on oxygen and carbon dioxide in the Cenozoic atmosphere. In: Sundquist, E.T., Broecker, W.S. (Eds.), The Carbon Cycle and Atmospheric CO_2: Natural Variation Archean to Present, American Geophysical Union, Washington D.C., pp. 412-417.
Shackleton, N.J., 1987a. The carbon isotope record of the Cenozoic: history of organic carbon burial and of oxygen in the ocean and atmosphere. In: Brooks, J., Fleet, A.J. (Eds.) Marine Petroleum Source Rocks, Geological Society Special Publication 26, pp. 423-434.
Shackleton, N.J., 1987b. Oxygen isotopes, ice volume and sea level. Quaternary Science Reviews 6, 183-190.
Shackleton, N.J., Berger, A., Peltier, W.R., 1990. An alternative astronomical calibration of the lower Pleistocene timescale based on ODP Site 677. Transactions of the Royal Society of Edinburgh: Earth Sciences 81, 251-261.
Shackleton, N.J., Hall, M.A., 1984. Oxygen and carbon isotope stratigraphy of deep sea drilling project 552A: Plio-Pleistocene glacial history. In: Bailey, M.G., Orlofski, S., Whalen, E. (Eds.) Initial Reports of the Deep Sea Drilling Project 81, Washington, pp. 599-609.
Shackleton, N.J., Opdyke N.D., 1973. Oxygen isotope and paleomagnetic stratigraphy of equatorial Pacific Core V28-238: oxygen isotope temperatures and ice volumes on a 10^5 year and 10^6 year scale. Quaternary Research 3, 39-55.
Shanmugam, G., 2000. 50 years of the turbidite paradigm (1950s-1990s): deep-water processes and facies models-a critical perspective. Marine and Petroleum Geology 17, 285-342.
Shanmugam, G., 2002. Ten turbidite myths. Earth-Science Reviews 58, 311-341.
Shanmugam, G., Moiola, R. J., 1982. Eustatic control of turbidites and winnowed turbidites. Geology 10, 231-235.
Shepard, J., 1954. Nomenclature based on sand-silt-clay ratios. Journal of Sedimentary Petrology 24, 151

-158.
Simpson, J.E, Britter, R.E., 1979. The dynamic of the head of a gravity current advancing over a horizontal surface. Journal of Fluid Mechanics 94, 477-495.
Stanley, D.J., 1985. Mud redepositional processes as a major influence on Mediterranean margin- basin sedimentation. Rapports et Proces-Verbaux des Reunions Commission Internationale pour l'Exploration Scientifique de la Mer Mediterranee 29, 213-216.
Stauffer, AP.H., 1967. Grain flow deposits and their implications, Santa Ynez Mountains, California. Journal of Sedimentary Petrology. 37, 487-508.
Stein, R., Stax, R., 1992. Late Cenozoic changes in flux rates and composition of organic carbon at Site 798, 799 (Sea of Japan). In: Pisciotto, K.A. et al. (Eds.) Proceedings of the Ocean Drilling Program, Scientific Results 127/128, Part I, College Station, TX (Ocean Drilling Program), pp. 423-437.
Stow, D.A.V., Piper, D.J.W., 1984. Deep-water fine-grained sediments: facies models. In: Stow, D.A.V., Piper, D.J.W. (Eds.), Fine-grained Sediments: Deep-water Processes and Facies. Geological Society, London, Special Publication 15, pp 611-645.
Stow, D.A.V., Reading, H.G., Collinson, J.D., 1996. Deep seas. In: Reading H.G. (Ed.) Sedimentary environments: processes, facies and stratigraphy. Oxford, Blackwell Science, pp. 395-453.
Stow, DA.V., Shanmugam, G., 1980. Sequence of structures in fine-grained turbidites; comparison of recent deep-sea and ancient flysch sediments. Sedimentary Geology 25, 23-42.
Stow, D.A.V. Tabrez, A.R., 1998. Hemipelagites: processes, facies and model. In: Stoker, M.S., Evans, D., Cramp, A. (Eds.), Geological processes on continental margins: sedimentation, mass-wasting and stability. Geological Society, London, Special Publication 129, pp. 317-337.
Strazzera, B., Dondi, M., Marsigli, M., 1997. Composition and ceramic properties of Tertiary clays from southern Sardinia. Applied Clay Science 12, 247-266.
Stuiver, M., Reimer, P.J., Bard, E., Beck, J.W., Burr, G.S., Hughen, K.A., Kromer, B., McCormac, G., Van der Plicht, J., Spurk, M., 1998. INTCAL98 radiocarbon age calibration 24,000 - 0 cal BP. Radiocarbon 40, 1041-1083.
Tauxe, L., Herbert, T., Shackleton, N.J., Kok, Y.S., 1996. Astronomical calibration of the Matuyama-Brunhes boundary: consequences for magnetic remanence acquisition in marine carbonates and the Asian Loess sequences. Earth and Planetary Science Letters 140, 133-146.
Tesson, M., Gensous, B., Allen, G.P., Ravenne, C., 1990. Late Quaternary deltaic lowstand wedges on the Rhône continental shelf, France. Marine geology 91, 325-332.
Thompson, R., Oldfield, F., 1986. Environmental Magnetism. Allen and Unwin, London, pp. 25
Thomson, J., Nixon, S., Summerhayes, C.P., Rohling, E.J., Schönfeld, J., Zahn, R., Grootes, P., Abrantes, F., Gaspar, L., Vaqueiro, S., 2000. Enhanced productivity on the Iberian margin during glacial/interglacial transitions revealed by barium and diatoms. Journal of the Geological Society 157, 667-677.
Thouveny, N., Moreno, E., Delanghe, D., Candon, L., Lancelot, Y., Shackleton, N.J., 2000. Rock magnetic detection of distal ice-rafted debris: clue for the identification of Heinrich layers on the Portuguese margin. Earth and Planetary Science Letters 180, 61-75.
Torres, J., Bois, C., Burrus, J., 1993. Initiation and evolution of the Valencia Trough (western Mediterranean): constraints from deep seismic profiling and subsidence analysis. Tectonophysics 228, 57-80.
Torres, J., Droz, L., Savoye, B., Terentieva, E., Cochonat, P., Kenyon, N.H., Canals, M., 1997. Deep-sea avulsion and morphosedimentary evolution of the Rhône Fan Valley and Neofan during the late Quaternary (north-western Mediterranean Sea). Sedimentology 44, 457-477.
Torres, J., Savoye, B., Cochonat, P., 1995. The effects of the later Quaternary sea-level changes on the Rhône slope sedimentation (northwestern Mediterranean), as indicated by seismic stratigraphy. Journal of Sedimentary Research 65, 368-387.
Tzedakis, C., 1999. The last climatic cycle at Kopais, central Greece. Journal of the Geological Society London 156, 425-434,
Udías, A., 1985. Seismicity of the Mediterranean basin. In: D.J. Stanley and F.-C. Wezel (Eds.) Geological evolution of the Mediterranean Basin Raimondo Selli commemorative volume. Springer-Verlag, New York, pp 56-63.
UK hydrographi office., 2002. Bathymetric contour chart Mediterranean Sea, Central Part C7825, UK Hydrographic Office, Taunton.
Vail, P.R., Hardenbol, J., 1979. Sea-level changes during the Tertiary. Oceanus 22, 71-79.

Valentine, J.W., Moores, E.M., 1970. Plate-tectonic regulation of faunal diversity and sea level: a model. Nature 228, 657-659.

Van Andel, T.J., 1975. Mesozoic-Cenozoic calcite compensation depth and the global distribution of calcareous sediments. Earth and Planetary Science Letters 26, 187-194.

Vanney, J. -R., Genneseaux, M., 1985. Mediterranean seafloor features: overview and assessment. In: Stanley, D.J. and Wezel, F.-C. (Eds.), Geological evolution of the Mediterranean Basin: Raimondo Selli commemorative volume. Springer-Verlag, New York, pp. 2-32.

Van de Kamp, P.C., Helmold, K.P., Leake, B.E., 1994. Holocene and Paleogene arkoses of the Massif Central, France: mineralogy, chemistry, provenance and hydrothermal alteration of the type arkose. Journal of Sedimentary Research 64, 17-33.

Van OS, B.J.H., Lourens, L.J., Hilgen, F.J., de Lange, G.J., Beaufort, L., 1994. The formation of Pliocene sapropels and carbonate cycles in the Mediterranean: diagenesis, dilution and productivity. Paleoceanography 9, 601-617.

Verosub, K.L., Roberts, A.P., 1995. Environmental magnetism: past, present and future. Journal of Geophysical Research 100, 2175-2192.

Vigliotti, L., Langenheim, V.E., 1995. When did Sardinia stop rotating? New paleomagnetic results. Terra Nova 7, 424-435.

Vincent, E., Berger, W.H., 1985. Carbon dioxide and polar cooling in the Miocene: the Monterey hypothesis. In: Sundquist, E.T., Broecker, W.S. (Eds.) The Carbon Cycle and Atmospheric CO_2: Natural Variation Archean to Present. American Geophysical Union, Washington D.C., pp. 455-468.

Volat, J.-L., Pastour, L., Vergnaud-Grazzini, C., 1980. Dissolution and carbonate fluctuations in Pleistocene deep-sea cores: a review. Marine Geology 34, 1-28.

Volbers, A.N.A., Henrich, R., 2002. Late Quaternary variations in calcium carbonate preservation of deep-sea sediments in the northern Cape Basin: results from a multiproxy approach. Marine Geology 180, 203-220.

Walker, R.G., 1973. Mopping up the turbidite mess. In: Ginsburg R.N. (Ed.) Evolving concepts in sedimentology, Baltimore: John Hopkins University Series in Geology 21, pp 1-37.

Wanninkhof, R., Lewis, E., Feely, R.A., Millero, F.S., 1999. The optimal carbonate dissociation constants for determining surface water pCO2 for alkalinity and total inorganic carbon. Marine Chemistry 65, 291-301.

Watts, A.B., 1982. Tectonic subsidence and global sea level. Nature 297, 469-474.

Weaver, P.P.E., 1983. An integrated stratigraphy of the Upper Quaternary of the King's Trough flank area NE Atlantic. Oceanologica Acta 6, 451-456.

Weaver, P.P.E., Kuijpers, A., 1983. Climatic control of turbidite deposition on the Madeira Abyssal Plain. Nature 306, 360-363.

Weaver, P.P.E., Thomson, J., 1993. Calculating erosion by deep-sea turbidity currents during initiation and flow. Nature 364, 136-138.

Weber, M.E., Niessen, F., Kuhn, G., Wiedicke, M., 1997a. Calibration and application of marine sedimentary physical properties using a multi-sensor core logger. Marine Geology 136, 151-172.

Weber, M.E., Wiedicke, M.H., Kudrass, H.R., Hübschner, C., Erlenkeuser, H., 1997b. Active growth of the Bengal Fan during sea-level rise and highstand. Geology 25, 315-318.

Weimer, P., Link, M.H., 1991. Global petroleum occurrences in submarine fans and turbidite systems. In: Weimer, P., Link, M.H. (Eds) Frontiers in sedimentary geology, seismic facies and sedimentary processes of submarine fans and turbidite systems, Springer Verlag, New York, pp. 9-67.

Weir, A.H., Ormerod, E.C., El Mansey, I.M.I., 1975. Clay mineralogy of sediments of the western Nile delta. Clay Minerals 10, 369-386.

Weldeab, S., Siebel, W., Wehausen, R., Emeis, K-, C., Schmiedl, G., Hemleben, C., 2003. Late Pleistocene sedimentation in the Western Mediterranean Sea: implication for productivity changes and climatic conditions in the catchment areas. Palaeogeography Palaeoclimatology Palaeoecology 190, 121-137.

Wenthworth, C.K., 1922. A scale of grade and class terms for clastic sediments. Journal of Geology 30, 377-392.

WMCE Consortium. 1989. Western Mediterranean Circulation Experiment: a preliminary review of results. EOS: Transactions American Geophysical Union, 70-746.